

---

## Methods in Modern Biophysics

Bengt Nölting

# Methods in Modern Biophysics

Second Edition  
With 267 Figures

 Springer

Dr. Bengt Nölting  
Prussian Private Institute  
of Technology at Berlin  
Am Schlosspark 30  
D-13187 Berlin  
Germany  
nolting@pitb.de

Library of Congress Control Number: 2005929410

ISBN-10 3-540-27703-X 2nd Edition Springer Berlin Heidelberg New York  
ISBN-13 978-3-540-27703-3 2nd Edition Springer Berlin Heidelberg New York  
2nd edition 2006.

ISBN 3-540-01297-4 1st Edition Springer Berlin Heidelberg New York

This work is subject to copyright. All rights reserved, whether the whole or part of the material is concerned, specifically the rights of translation, reprinting, reuse of illustrations, recitation, broadcasting, reproduction on microfilm or in any other way, and storage in data banks. Duplication of this publication or parts thereof is permitted only under the provisions of the German Copyright Law of September 9, 1965, in its current version, and permission for use must always be obtained from Springer. Violations are liable for prosecution under the German Copyright Law.

Springer is a part of Springer Science+Business Media  
springeronline.com

© Springer-Verlag Berlin Heidelberg 2003, 2006  
Printed in Germany

The use of general descriptive names, registered names, trademarks, etc. in this publication does not imply, even in the absence of a specific statement, that such names are exempt from the relevant protective laws and regulations and therefore free for general use.

Product liability: The publisher cannot guarantee the accuracy of any information about dosage and application contained in this book. In every individual case the user must check such information by consulting the relevant literature.

Patents: A number of methods mentioned in this book are covered by patents. Nothing in this publication should be construed as an authorization or implicit license to practice methods covered by any patents.

The instructions given for carrying out practical experiments do not absolve the reader from being responsible for safety precautions. Liability is not accepted by the authors.

Safety considerations: Anyone carrying out these methods will encounter pathogenic and infectious biological agents, toxic chemicals, radioactive substances, high voltage and intense light radiation which are hazardous or potentially hazardous materials or matter. It is required that these materials and matter be used in strict accordance with all local and national regulations and laws. Users must proceed with the prudence and precaution associated with good laboratory practice, under the supervision of personnel responsible for implementing laboratory safety programs at their institutions.

Typesetting: By the Author  
Production: LE- $\text{\TeX}$ , Jelonek, Schmidt & Vöckler GbR, Leipzig  
Coverdesign: KuenkelLopka, Heidelberg

Printed on acid-free paper 2/YL - 5 4 3 2 1 0

*To*      *Alan R. Fersht*  
*Robert Huber*  
*Manfred Eigen*  
*Kurt Wüthrich*

# Preface

This second edition presents new chapters on (a) the utilization of mutants as high-resolution nanosensors of short-living protein structures and protein nanophysics (Chap. 11) and (b) the recently developed method of evolutionary computer programming (Chap. 12), respectively. In the latter method, computer programs evolve themselves towards a higher performance. In contrast to simple self-learning programs, the code of the evolved program differs significantly from that of the original "wild-type" program. In applications on protein folding and structure, evolutionary programming has been shown to yield results many orders of magnitude faster and more efficient than traditional methods. The method is applicable on a wide range of complex problems, e.g., in the fields of nanooptics and adaptive optics (Sects. 12.4, 12.5).

The author gratefully acknowledges Max F. Perutz († 2002) for many inspiring discussions regarding methods for the study of the extreme efficiency of protein folding. These discussions were the strong inspiration for the development of the self-evolving computer programs.

Berlin, June 2005

Bengt Nölting

## Preface to the first edition

In the recent years we have seen a remarkable increase of the interest in biophysical methods for the investigation of structure-function relationships in proteins, cell organelles, cells, and whole body parts. Biophysics is expected to answer some of the most urgent questions: what are the factors that limit human physical and mental abilities, and how can we expand our abilities. Now a variety of new, faster and structurally higher-resolving methods enable the examination of the mysteries of life at a molecular level. Examples are X-ray crystallographic analysis, scanning probe microscopy, and nanotechnology. Astonishingly large molecular complexes are structurally resolvable with X-ray crystallography. Scanning probe microscopy and nanotechnology allow to probe the mechanical properties of individual biomolecules. Near-field optical microscopy penetrates Abbe's limit of diffraction and enables sub-200 nm resolution. Electron microscopy closes the gap between methods with molecular resolution and cellular resolution. Other methods, such as proteomics, mass spectrometry and ion mobility spectrometry, help us to study highly heterogeneous analytes and to understand extremely complex biological phenomena, such as the function of the human brain. Detailed mechanistic knowledge resulting from the application of these physical and biophysical methods combined with numerous interdisciplinary techniques will further aid the understanding of biological processes and diseases states and will help us to find rational ways for re-designing biological processes without negative side effects. This knowledge will eventually help to close the gap between humans and machines under consideration of all drawbacks, and to find cures for diseases and non-native declines of performance.

This book was mainly written for advanced undergraduate and graduate students, postdocs, researchers, lecturers and professors in biophysics and biochemistry, but also for students and experts in the fields of structural and molecular biology, medical physics, biotechnology, environmental science, and biophysical chemistry. The book is largely based on the lecture "Biophysical Methods" given by the author at the occasion of a visiting professorship at Vienna University of Technology. It presents a selection of methods in biophysics which have tremendously progressed in the last few years.

Chap. 1 introduces fundamentals of protein structures. Proteins have evolved to become highly specific and optimized molecules, and yet the class of proteins may be seen as the biomolecule class with the largest variety of functions. Surely the understanding of biological systems much depends on the understanding of protein structure, structure formation, and function. The next chapter (Chap. 2)

presents important chromatographic methods for the preparation of proteins and other biomolecules. Many biophysical studies require this form of sample preparation and often a lot of time can be saved by using optimized procedures of sample purification. Mass spectrometry (Chap. 3) is important for the quality control in preparations of biomolecules, but also has a variety of further analytical applications. Chaps. 4–7 focus on methods for the chemical and structural characterization of biomolecules. X-ray crystallography (Sect. 4.1.2) probably offers the highest resolving power for large biomolecules and biomolecular complexes, but it requires the preparation of high-quality crystals. Cheaper is infrared spectroscopy (Chap. 5) which may also comparably easily be applied in the fast time scale. Electron microscopy (Chap. 6) is particularly suitable for the structural resolution of complex biological systems at the size level of cells, cell organelles, and large molecular complexes. Different types of scanning probe microscopes (Chap. 7) can generate images of geometrical, mechanical, electrical, optical, or thermal properties of biological specimens with up to sub-nm resolution. In Chap. 8 (biophysical nanotechnology) we find novel methods for the mechanical characterization of individual biomolecules and for the engineering of novel nanotechnological structures and devices. The next two chapters (proteomics, Chap 9; and ion mobility spectrometry, Chap. 10) concentrate on two types of analytical methods for the characterization of complex samples such as human cells or bacteria. Finally Chap. 11 deals with some novel developments regarding the interaction of electromagnetic radiation with humans. Kinetics methods in biophysics were not much emphasized throughout the book since many of them can be found in the monograph "Protein Folding Kinetics" (Nölting, 2005). The reader may refer to this monograph for more information on protein structure, transitions state theory in protein science, and on a variety of kinetic methods for the resolution of structural changes of proteins and other biomolecules.

Prof. Dr. Alan R. Fersht supported the development of a variety of modern biophysical methods in our extremely fruitful collaboration at Cambridge University. Prof. Dr. Robert Huber and Prof. Dr. Max F. Perutz initiated highly inspiring discussions regarding modern applications of protein X-ray crystallography. I am particularly indebted to Prof. Dr. Calvin F. Quate, Prof. Dr. Steven G. Sligar, and Prof. Dr. Joseph W. Lyding for an introduction into the AFM technology.

I am indebted to Prof. Dr. Joachim Voigt, Prof. Dr. Martin H. W. Gruebele, Prof. Dr. Kevin W. Plaxco, Dr. Gisbert Berger, and Dr. Min Jiang for proof-reading the manuscript, and to Dr. Marion Hertel for processing the manuscript within Springer-Verlag.

# Contents

1	The three-dimensional structure of proteins .....	1
1.1	Structure of the native state .....	1
1.2	Protein folding transition states .....	9
1.3	Structural determinants of the folding rate constants .....	12
1.4	Support of structure determination by protein folding simulations .....	20
2	Liquid chromatography of biomolecules .....	23
2.1	Ion exchange chromatography .....	23
2.2	Gel filtration chromatography .....	28
2.3	Affinity chromatography .....	31
2.4	Counter-current chromatography and ultrafiltration .....	33
3	Mass spectrometry .....	37
3.1	Principles of operation and types of spectrometers .....	37
3.1.1	Sector mass spectrometer .....	38
3.1.2	Quadrupole mass spectrometer .....	39
3.1.3	Ion trap mass spectrometer .....	39
3.1.4	Time-of-flight mass spectrometer .....	40
3.1.5	Fourier transform mass spectrometer .....	43
3.1.6	Ionization, ion transport and ion detection .....	44
3.1.7	Ion fragmentation .....	45
3.1.8	Combination with chromatographic methods .....	46
3.2	Biophysical applications .....	49
4	X-ray structural analysis .....	59
4.1	Fourier transform and X-ray crystallography .....	59
4.1.1	Fourier transform .....	59
4.1.2	Protein X-ray crystallography .....	69
4.1.2.1	Overview .....	69
4.1.2.2	Production of suitable crystals .....	69
4.1.2.3	Acquisition of the diffraction pattern .....	71



---

4.1.2.4	Determination of the phases: heavy atom replacement .....	76
4.1.2.5	Calculation of the electron density and refinement .....	83
4.1.2.6	Cryocrystallography and time-resolved crystallography .....	84
4.2	X-ray scattering .....	85
4.2.1	Small angle X-ray scattering (SAXS) .....	85
4.2.2	X-ray backscattering .....	88
5	Protein infrared spectroscopy .....	91
5.1	Spectrometers and devices .....	92
5.1.1	Scanning infrared spectrometers .....	92
5.1.2	Fourier transform infrared (FTIR) spectrometers .....	92
5.1.3	LIDAR, optical coherence tomography, attenuated total reflection and IR microscopes .....	96
5.2	Applications .....	102
6	Electron microscopy .....	107
6.1	Transmission electron microscope (TEM) .....	107
6.1.1	General design .....	107
6.1.2	Resolution .....	109
6.1.3	Electron sources .....	110
6.1.4	TEM grids .....	112
6.1.5	Electron lenses .....	112
6.1.6	Electron-sample interactions and electron spectroscopy .....	115
6.1.7	Examples of biophysical applications .....	117
6.2	Scanning transmission electron microscope (STEM) .....	118
7	Scanning probe microscopy .....	121
7.1	Atomic force microscope (AFM) .....	121
7.2	Scanning tunneling microscope (STM) .....	133
7.3	Scanning nearfield optical microscope (SNOM) .....	135
7.3.1	Overcoming the classical limits of optics .....	135
7.3.2	Design of the subwavelength aperture .....	138
7.3.3	Examples of SNOM applications .....	142
7.4	Scanning ion conductance microscope, scanning thermal microscope and further scanning probe microscopes .....	143
8	Biophysical nanotechnology .....	147
8.1	Force measurements in single protein molecules .....	147
8.2	Force measurements in a single polymerase-DNA complex .....	150

---

8.3	Molecular recognition .....	152
8.4	Protein nanoarrays and protein engineering .....	155
8.5	Study and manipulation of protein crystal growth .....	158
8.6	Nanopipettes, molecular diodes, self-assembled nanotransistors, ..... nanoparticle-mediated transfection and further biophysical nanotechnologies	159
9	Proteomics: high throughput protein functional analysis .....	165
9.1	Target discovery .....	166
9.2	Interaction proteomics .....	168
9.3	Chemical proteomics .....	172
9.4	Lab-on-a-chip technology and mass-spectrometric array scanners .....	173
9.5	Structural proteomics .....	174
10	Ion mobility spectrometry .....	175
10.1	General design of spectrometers .....	175
10.2	Resolution and sensitivity .....	180
10.3	IMS-based “sniffers” .....	183
10.4	Design details .....	184
10.5	Detection of biological agents .....	193
11	$\Phi$ -Value analysis .....	197
11.1	The method .....	197
11.2	High resolution of six protein folding transition states .....	199
12	Evolutionary computer programming .....	203
12.1	Reasons for the necessity of self-evolving computer programs .....	203
12.2	General features of the method .....	203
12.3	Protein folding and structure simulations .....	206
12.4	Evolution of nanooptical devices made from nanoparticles .....	207
12.4.1	Materials and methods .....	207
12.4.2	Results and discussion .....	208
12.5	Further potential applications .....	210
13	Conclusions .....	213
	References .....	215
	Index .....	247

# Symbols

→	arrow indicating a process or a coordinate axis	eV	electron volt ( $1.6022 \times 10^{-19}$ J)
➔	arrow pointing to a label or indicating a distance	FPLC	fast performance liquid chromatography
Å	ångström ( $10^{-10}$ m; 0.1 nm)	FTIR	Fourier transform infrared
AC	alternating current	FTMS	Fourier transform mass spectrometer
ADC	analog-to-digital converter	GC	gas chromatography
AFM	atomic force microscope	GPS	global positioning system
ATP	adenosine triphosphate	$h$	Planck constant ( $6.6261 \times 10^{-34}$ J s)
BESSY	(Berlin Electron Synchrotron Storage Ring)	HPLC	high pressure liquid chromatography
bp	base pair	$i$	imaginary number ( $i \equiv \sqrt{-1}$ )
BSA	bovine serum albumin	IHF	integration host factor
BSE	bovine spongiform encephalopathy	IMS	ion mobility spectrometer
°C	degree Celsius (kelvin-273.15)	IMU	inertial measurement unit
$c$	speed of light in vacuum ( $2.99792 \times 10^8$ m s <sup>-1</sup> )	IR	infrared
CBMS	chemical-biological mass spectrometer	$k_B$	Boltzmann constant ( $1.3807 \times 10^{-23}$ J K <sup>-1</sup> )
CCD	charge coupled device	KBr	potassium bromide
CD	circular dichroism	kDa	kilodalton (kg mol <sup>-1</sup> )
CJD	Creutzfeldt-Jacob disease	kJ	kilojoule (1 kJ = 240 cal)
cm	centimeter ( $10^{-2}$ m)	kp	kilopond (9.8066 N)
CM	carboxy methyl	kV	kilovolt ( $10^3$ V)
CNS	central nervous system	kW	kilowatt ( $10^3$ W)
CO	carbon monoxide	l	liter ( $10^{-3}$ m <sup>3</sup> )
CsI	cesium iodide	Laser	light amplification by stimulated emission of radiation
CTP	chain topology parameter	LD	linear dichroism
Da	dalton (g mol <sup>-1</sup> )	LIDAR	light detection and ranging (measurement of light backscatter)
DC	direct current	μm	micrometer ( $10^{-6}$ m)
dCTP	2'-deoxycytidine 5'-triphosphate	MΩ	megaohm ( $10^6$ V A <sup>-1</sup> )
DSC	differential scanning calorimetry	MALDI	matrix-assisted laser desorption ionization
DEAE	diethyl-amino-ethyl	MCT	mercury cadmium telluride
DNA	deoxyribonucleic acid	$m_e$	electron rest mass ( $9.1094 \times 10^{-31}$ kg)
dsDNA	double-stranded DNA		
DTGS	deuterated triglycine sulfate		
$e$	elementary charge ( $1.6022 \times 10^{-19}$ C)		

---

ml	milliliter ( $10^{-6} \text{ m}^3$ )	RNAse	ribonuclease
mM	millimolar ( $6.0221 \times 10^{20} \text{ liter}^{-1}$ )	$\mu\text{s}$	microsecond ( $10^{-6} \text{ s}$ )
mol	$6.0221 \times 10^{23}$	SAXS	small angle X-ray scattering
mV	millivolt ( $10^{-3} \text{ V}$ )	SDOCT	spectral domain optical coherence tomography
$M_w$	molecular weight	SICM	scanning ion conductance microscope
$m/z$	mass-to-charge ratio	SNOM	scanning near-field optical microscope
nA	nanoampere ( $10^{-9} \text{ A}$ )	SPM	scanning probe microscope
nm	nanometer ( $10^{-9} \text{ m}$ )	ssDNA	single-stranded DNA
NMR	nuclear magnetic resonance	STEM	scanning transmission electron microscope
nN	nanonewton ( $10^{-9} \text{ kg m s}^{-2}$ )	SThM	scanning thermal microscope
NSOM	near-field scanning optical microscope – <i>see</i> SNOM	STM	scanning tunneling microscope
OCT	optical coherence tomography	TEM	transmission electron microscope
ORF	open reading frame	TGS	triglycine sulfate
pA	picoampere ( $10^{-12} \text{ A}$ )	TIR	total internal reflection
PCR	polymerase chain reaction	TNT	trinitrotoluene
pg	picogram ( $10^{-12} \text{ g}$ )	TOF	time-of-flight mass spectrometer
pI	isoelectric point	UV	ultra-violet
pN	piconewton ( $10^{-12} \text{ kg m s}^{-2}$ )	VIS	visible
ppbv	part per billion volume ( $10^{-9}$ )	VUV	vacuum ultra-violet
PVC	polyvinyl chloride		
PyMS	Py-MS, pyrolysis mass spectrometry		
rms	root mean square		
RMSD	root mean square deviation		

# 1 The three-dimensional structure of proteins

## 1.1 Structure of the native state

The human body contains the astonishing number of several 100,000 different proteins. Proteins are “smart” molecules each fulfilling largely specific functions such as highly efficient catalysis of biochemical reactions, muscle contraction, physical stabilization of the body, transport of materials in body fluids, and gene regulation. In order to optimally fulfill these functions, highly specific protein structures have evolved. The performance of humans, animals, and plants crucially depends on the integrity of these structures. Already small structural errors can cause diminishings of performance or even lethal diseases.

Proteins generally consist of thousands of atoms, such as hydrogen (H), carbon (C), nitrogen (N), oxygen (O), and sulfur (S). The van-der-Waals radii are about 1.0–1.4 Å for H, 1.6–2.1 Å for  $-\text{CH}_3$ , 1.4–1.8 Å for N, 1.4–1.7 Å for O, and 1.7–2.0 Å for S. Typical sizes of proteins range from a few nm to 200 nm. Since representations with atomic resolution of the whole molecule (Fig. 1.1a), or only its backbone (Fig. 1.1b), would be quite confusing for most proteins, it has become common to represent the protein structure as a ribbon of the backbone (Fig. 1.1c).

Multiple levels of structure are distinguished (see Nölting, 2005): The most basic is the primary structure which is the order of amino acid residues. The 20 common amino acids found in proteins can be classified into 3 groups: nonpolar, polar, and charged. Some physical properties of amino acids are given in Table 1.1. For the hydrophobicity of amino acids see Nölting, 2005. A typical protein contains 50–1000 amino acid residues. An interesting exception is titin, a protein found in skeletal muscle, containing about 27,000 residues in a single chain. The next level, the secondary structure, refers to certain common repeating structures of the backbone of the polypeptide chain. There are three main types of secondary structure: helix, sheet, and turns. That which cannot be classified as one of these three types is usually called “random coil” or “other”. Long connections between helices and strands of a sheet are often called “loops”. The third level, the tertiary structure, provides the information of the three-dimensional arrangement of elements of secondary structure in a single protein molecule or in a subunit of a protein molecule. The tertiary structure of a protein molecule, or of a subunit of a protein molecule, is the arrangement of all its atoms in space, without regard to its relationship with neighboring molecules or subunits. As this definition implies, a protein molecule can contain multiple subunits. Each subunit

consists of only one polypeptide chain and possibly co-factors. Finally, the quaternary structure is the arrangement of subunits in space and the ensemble of its intersubunit contacts, without regard to the internal geometry of the subunits. The subunits in a quaternary structure are usually in noncovalent association. Rare exceptions are disulfide bridges and chemical linkers between subunits.

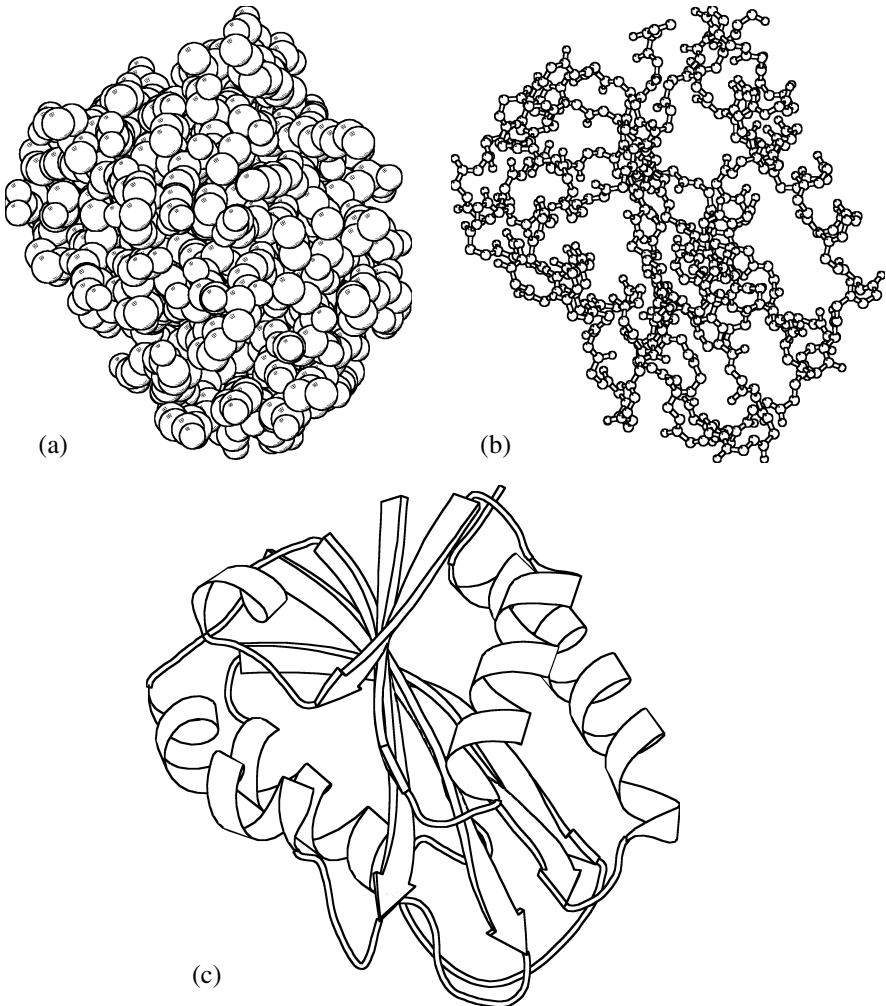


**Fig. 1.1** The three-dimensional structure of the saddle-shaped electron transport protein flavodoxin from *Escherichia coli* (Hoover and Ludwig, 1997). (a) Space-filling representation of the complete molecule. (b) Ball-and-stick representation of the protein backbone. (c) Ribbon representation: ribbons, arrows, and lines symbolize helices, strands, and other, respectively. Coordinates are from the Brookhaven National Laboratory Protein Data Bank (Abola et al., 1997). The figure was generated using MOLSCRIPT (Kraulis, 1991)

Most proteins have only a marginal stability of 20–60 kJ mol<sup>-1</sup> and can undergo conformational transitions (Nölting, 2005). Small reversible conformational changes on a subnanometer scale occur very frequently. Reversible or irreversible molecular movements in the subnanometer or nanometer scale are essential for the function of many proteins. However, occasionally proteins irreversibly misfold into a non-native conformation. This can have dramatic consequences for the organism, especially when misfolded protein accumulates in the cell. A well known example of such a process is the misfolding of the prion protein (Figs. 1.2 and 1.3; Riek et al., 1996, 1998; Hornemann and Glockshuber, 1998). According to the “prion-only” hypothesis (Prusiner, 1999), a modified form of native prion protein can trigger infectious neurodegenerative diseases, such as Creutzfeldt-Jacob disease (CJD) in humans and bovine spongiform encephalopathy (BSE).

**Table 1.1** Physical properties of natural amino acids

Amino acid	Molecular mass (Da) <sup>a</sup>	Partial molar volume (cm <sup>3</sup> mol <sup>-1</sup> ) <sup>b,c</sup>	Partial molar volume of residue in protein (cm <sup>3</sup> mol <sup>-1</sup> ) <sup>b</sup>
Alanine	89.09	60.4	54.7
Arginine	174.20	126.9	121.2
Asparagine	132.12	77.3	71.6
Aspartic acid	133.10	74.3	68.6
Cysteine	121.16	73.5	67.7
Glutamic acid	147.13	89.7	84.0
Glutamine	146.15	93.9	88.2
Glycine	75.07	43.2	37.5
Histidine	155.16	98.8	93.1
Isoleucine	131.17	105.6	99.9
Leucine	131.17	107.7	101.9
Lysine	146.19	111.4	105.7
Methionine	149.21	105.4	99.6
Phenylalanine	165.19	121.8	116.1
Proline	115.13	82.2	74.8
Serine	105.09	60.7	55.0
Threonine	119.12	76.9	71.1
Tryptophan	204.23	143.9	138.2
Tyrosine	181.19	123.7	118.0
Valine	117.15	90.8	85.1

<sup>a</sup> (Dawson et al., 1969; Richards, 1974; Coligan et al., 1996; Nölting 2005)

<sup>b</sup> At 25 °C in water (Kharakoz, 1989, 1991, 1997)

<sup>c</sup> For the standard zwitterionic state

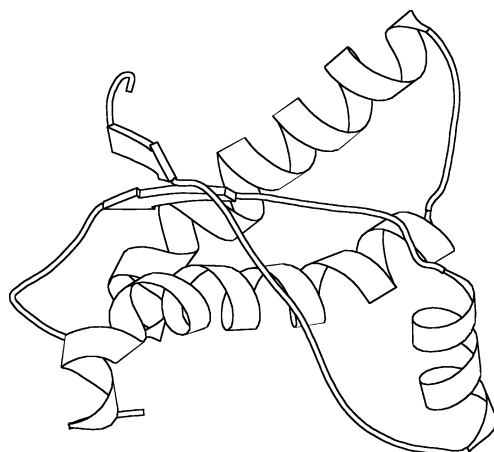


**Fig. 1.2** Structure of the mouse prion protein fragment PrP(121–231) (Riek et al., 1996). The displayed secondary structure is strand<sub>1</sub> (128–131), helix<sub>1</sub> (144–153), strand<sub>2</sub> (161–164), helix<sub>2</sub> (172–194), helix<sub>3</sub> (200–224), coil (124–127, 132–143, 154–160, 165–171, 195–199). The figure was generated using MOLSCRIPT (Kraulis, 1991)

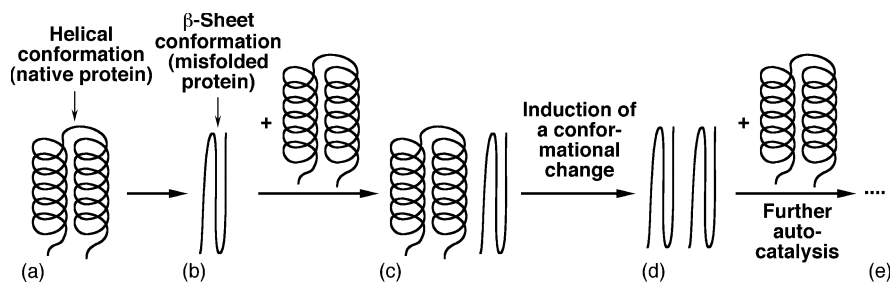


**Fig. 1.3** A hypothetical mechanism of autocatalytic protein misfolding: with a low rate, the native helical conformation (a) spontaneously changes (misfolds) into a  $\beta$ -sheet conformation (b); contact of the misfolded protein with further correctly folded protein molecules (c) catalyzes further misfolding (d, e)

In soluble proteins, hydrophilic sidechains (that of aspartic acid, glutamic acid, lysine, arginine, asparagine, glutamine) have a higher preference for a location at the surface. Hydrophobic sidechains (that of alanine, valine, leucine, isoleucine, phenylalanine, tryptophan) are preferentially located inside the so-called hydrophobic core (Fig. 1.4). In contrast, the surface of membrane proteins often contains hydrophobic patches (Fig. 1.5).

Examples of the astonishing diversity of protein tertiary structure are shown in Figs. 1.6–1.8. Many proteins attain complicated multimeric structures. Fig. 6.18 in Chap. 6 shows an example of a complex assembly, the GroEL. For further details on the structures of proteins see Nölting, 2005.



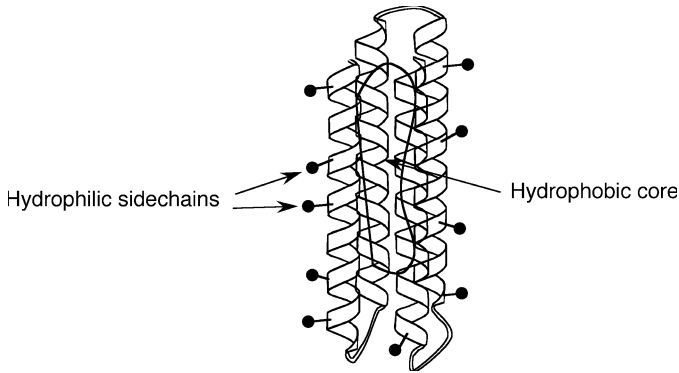


**Fig. 1.4** In soluble proteins, charged and polar sidechains prefer a location at the surface. The sidechains of hydrophobic amino acids do not like to reside in an aqueous environment. That is why these sidechains are preferentially buried within the hydrophobic core

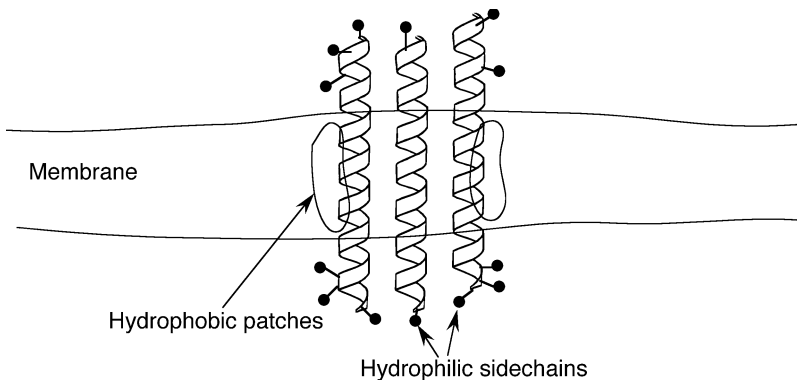
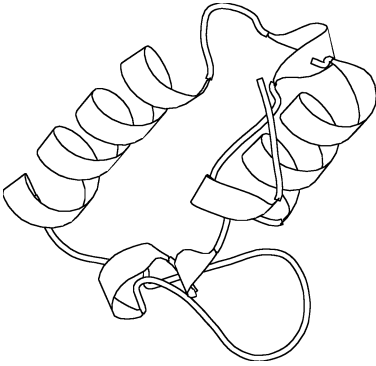
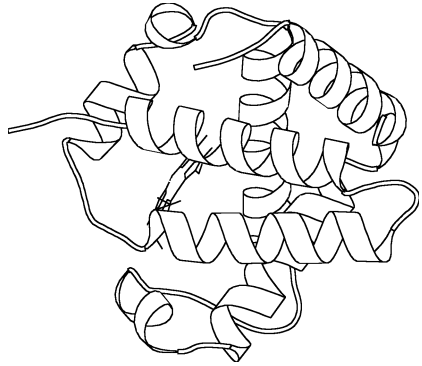


**Fig. 1.5** Typical distribution of hydrophobic and hydrophilic sidechains in membrane proteins. The sidechains of hydrophobic amino acids are preferentially buried within the lipid portion of the membrane. Hydrophilic sidechains prefer contact with the bulk water outside the membrane

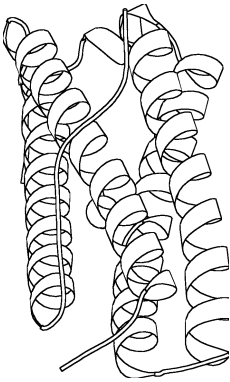
*Next page: Fig. 1.6* Examples of proteins with mainly helical secondary structure. (a) 1ACP: acyl carrier protein (Kim and Prestegard, 1990); (b) 1HBB: human hemoglobin A (Fermi et al., 1984); (c) 1BCF: iron storage and electron transport bacterioferritin (cytochrome  $b_1$ ) (Frolow et al., 1994); (d) 1MGN: sperm whale myoglobin (Phillips et al., 1990); (e) 1QGT: assembly domain of human hepatitis B viral capsid protein (Wynne et al., 1999); (f) 2ABD: acyl-coenzyme A binding protein (Andersen and Poulsen, 1992); (g) 1FUM: the *Escherichia coli* fumarate reductase respiratory complex comprising the fumarate reductase flavoprotein subunit, the fumarate reductase iron-sulfur protein, the fumarate reductase 15-kDa hydrophobic protein, and the fumarate reductase 13-kDa hydrophobic protein (Iverson et al., 1999). Coordinates are from the Brookhaven National Laboratory Protein Data Bank (Abola et al., 1997). The figure was generated using MOLSCRIPT (Kraulis, 1991).



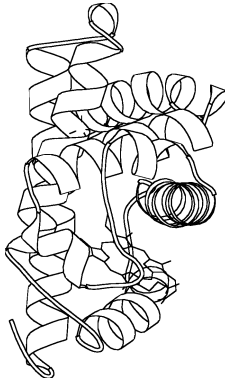
(a) acyl carrier protein



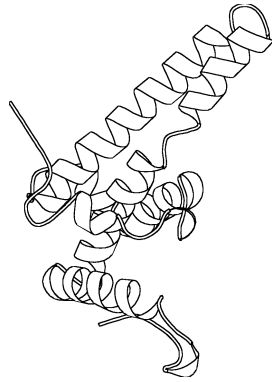
(b) hemoglobin A



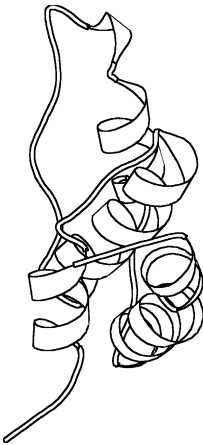
(c) cytochrome b<sub>1</sub>



(d) myoglobin



(e) viral capsid protein domain



(f) acyl-coenzyme A  
binding protein



(g) fumarate reductase respiratory complex

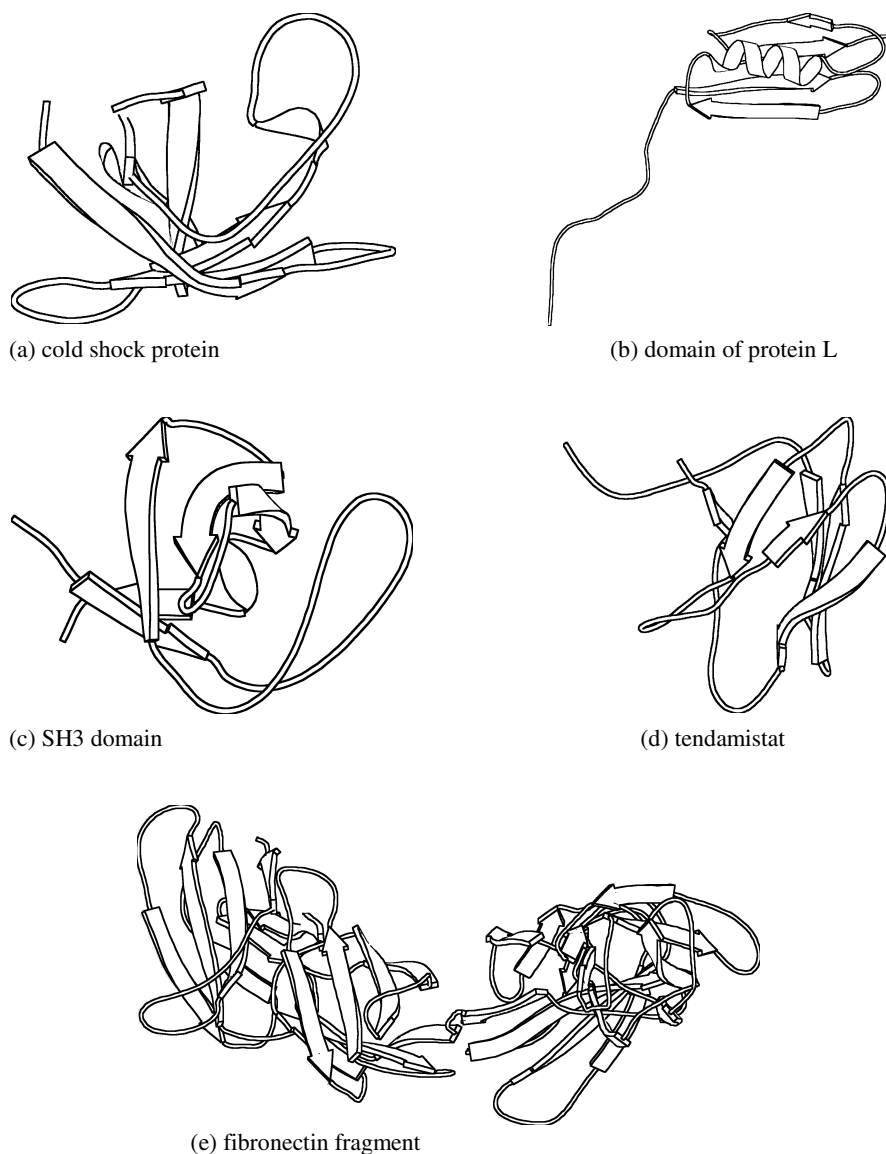
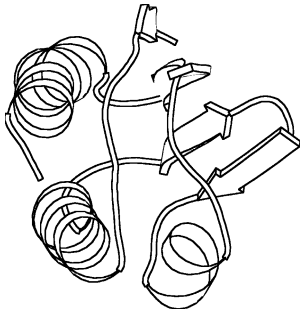
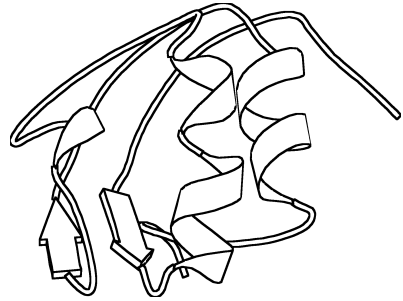


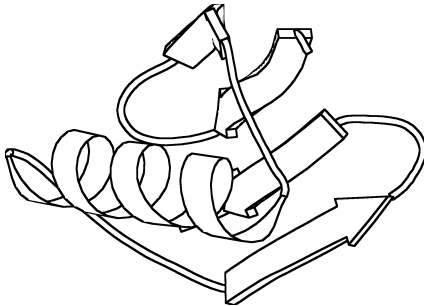
**Fig. 1.7** Examples of proteins with mainly sheet-shaped secondary structure. **(a)** 1CSP: major cold shock protein (CSPB) from *Bacillus subtilis* (Schindelin et al., 1993); **(b)** 2PTL: an immunoglobulin light chain-binding domain of protein L, (Wikström et al., 1995); **(c)** 1NYF: SH3 domain from fyn proto-oncogene tyrosine kinase (Morton et al., 1996); **(d)** 2AIT:  $\alpha$ -amylase inhibitor tendamistat, (Kline et al., 1988); **(e)** 1FNF: fragment of human fibronectin encompassing type-III (Leahy et al., 1992). Coordinates are from the Brookhaven National Laboratory Protein Data Bank (Abola et al., 1997). The figure was generated using MOLSCRIPT (Kraulis, 1991)



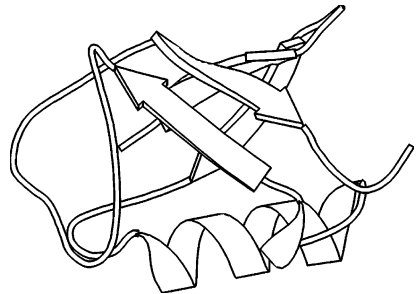
(a) HPR protein



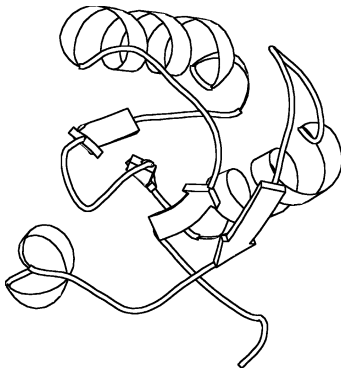
(b) domain of procarboxypeptidase B



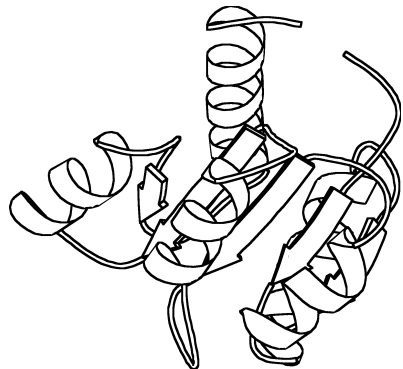
(c) domain of streptococcal protein G



(d) ubiquitin



(e) domain of the U1A protein



(f) signal transduction protein CheY

**Fig. 1.8** Examples of proteins with significant amounts of helical and sheet-shaped structure. (a) 1HDN: histidine-containing phosphocarrier protein, (van Nuland et al., 1994); (b) 1PBA: activation domain from porcine procarboxypeptidase B, (Vendrell et al., 1991); (c) 1PGB: B1 immunoglobulin-binding domain of streptococcal protein G (Gallagher et al., 1994); (d) 1UBQ: human erythrocytes ubiquitin, (Vijay-Kumar et al., 1987); (e) 1URN: RNA-binding domain of the U1A spliceosomal protein complexed with an RNA hairpin, (Oubridge et al., 1994); (f) 3CHY: signal transduction protein CheY, (Volz and Matsu-mura, 1991). Coordinates are from the Brookhaven National Laboratory Protein Data Bank (Abola et al., 1997). The figure was generated using MOLSCRIPT (Kraulis, 1991)

## 1.2 Protein folding transition states

A considerable number of studies has been devoted to the resolution of folding transition states, see, e.g., Nölting, 2005. The structure of the folding transition

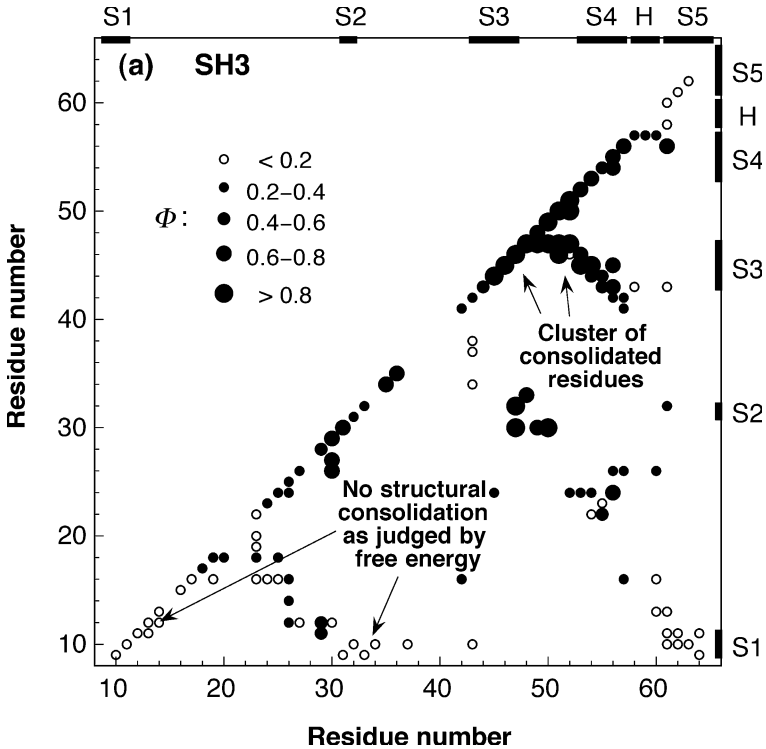


**Fig. 1.9a** Inter-residue contact map for the main folding transition state of the monomeric protein src SH3 domain (Nölting and Andert, 2000). The sizes and fillings of the circles indicate the magnitudes of structural consolidation, measured by the so-called  $\Phi$ -value (Nölting, 2005). The diagonal of the plot displays secondary structure contacts, and tertiary structure contacts are contained in the bulk of the diagram. Usually, high  $\Phi$ -values (large full circles) indicate a high degree of consolidation of structure and about native interaction energies, and  $\Phi \approx 0$  (small open circles) are diagnostic of little, if any, formation of stable structure at the individual positions in the inter-residue contact space. Moderate magnitudes of  $\Phi$  ( $\approx 0.2-0.8$ ) suggest different probabilities of the consolidation of structure. Because of the possibility of the occurrence of non-native interactions in the transition state, only clusters of several contacts (for  $\Phi$  around 0.5 usually at least 5 contacts) may be used to draw statistically significant conclusions about the presence or absence of a significant degree of structural consolidation. The positions of helices and strands of  $\beta$ -sheets in the native state are indicated by bars, H1, H2, ... , and bars, S1, S2, ... , respectively. For further details on transition state structures see also Chap. 11

state is the structure of which formation represents the rate-limiting step in the folding reaction, i.e., the reaction of formation of the native conformation which usually starts with the unfolded polypeptide chain. Knowledge of transition state structures is important to understand the high efficiency of such folding reactions. The structures of many transition states of monomeric and also some dimeric and multimeric proteins provide evidence for a nucleation-condensation mechanism of folding in which structure growth starts with the formation of a diffuse folding nucleus which catalyzes further structure formation (Nölting, 2005; Chap. 11).

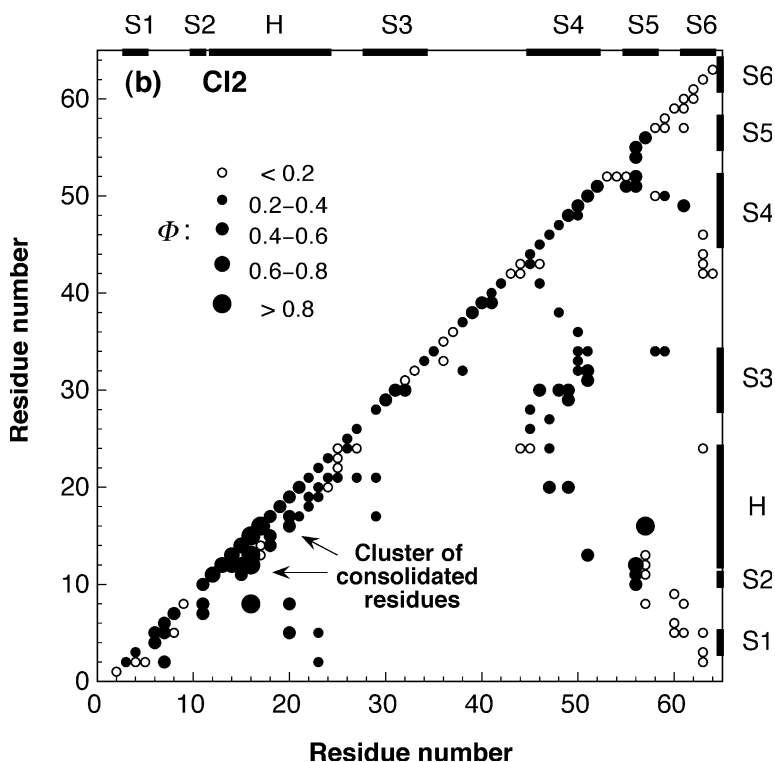


**Fig. 1.9b** Inter-residue contact map for the main folding transition state of chymotrypsin inhibitor 2 (CI2) (Nölting and Andert, 2000). The sizes and fillings of the circles indicate the magnitudes of structural consolidation, measured by the so-called  $\Phi$ -value (Nölting, 2005; Chap. 11). For further explanation see the legend for Fig. 1.9a on p. 9

Fig. 1.9 a–d displays the structural consolidation of the transition states of four proteins. In these maps, the magnitudes of  $\Phi$ -values are a measure or probability of structure formation at the corresponding locations in the inter-residue contact space. For example, large filled circles on the diagonal indicate consolidation of

secondary structure contacts, and large filled circles in the bulk of the diagrams indicates consolidated tertiary structure contacts in the transition state (Nölting, 1998). The high structural resolution of the main transition states for the formation of native structure of these four small monomeric proteins (src SH3 domain, chymotrypsin inhibitor 2, barstar, barnase) and of the dimeric Arc repressor (not shown here) reveals that the most consolidated parts of each protein molecule in the transition state cluster together in the tertiary structure, and these clusters contain a significantly higher percentage of residues that belong to regular secondary structure than the rest of the molecule (Nölting and Andert, 2000). For many small monomeric and some dimeric proteins, the astonishing speed of protein folding can be understood as caused by the catalytic effect of the formation of clusters of residues which have particularly high preferences for the early formation of regular secondary structure in the presence of significant amounts of tertiary structure interactions (Nölting and Andert, 2000).

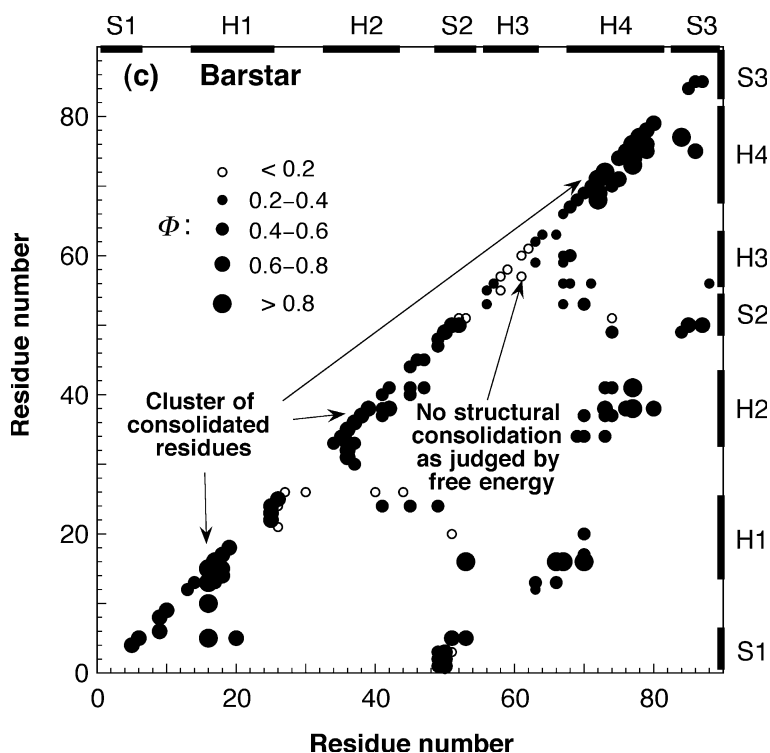


**Fig. 1.9c** Inter-residue contact map for the main folding transition state of barstar (Nölting and Andert, 2000). The sizes and fillings of the circles indicate the magnitudes of structural consolidation, measured by the so-called  $\Phi$ -value (Nölting, 2005; Chap. 11). For further explanation see the legend for Fig. 1.9a on p. 9





1999; Forge et al., 2000; Griko, 2000; Niggemann and Steipl, 2000; Nölting and Andert, 2000; Nölting, 2005).

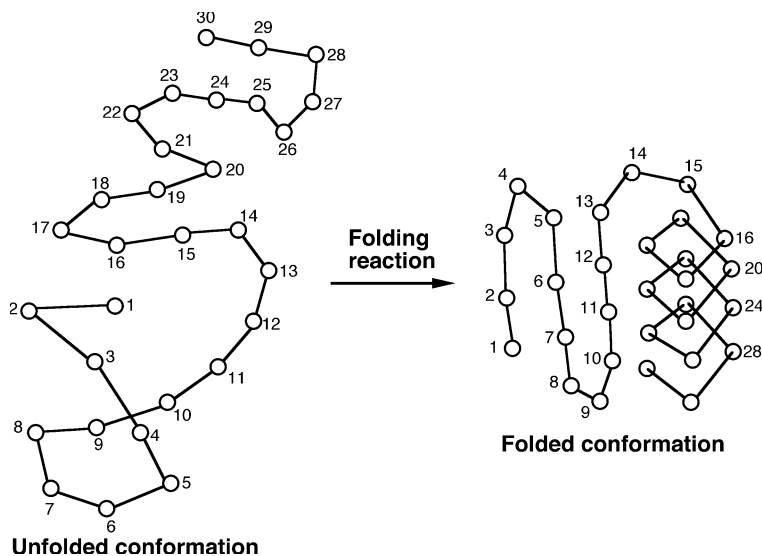


**Fig. 1.10** Example for the formation of intramolecular contacts. Here the contacting residues in the folded conformation with the largest sequence separation are residues number 10 and 30. The set of distance separations in sequence between all contacting residues in space is called chain topology. It is an important determinant of the folding rate constant of the protein (Nölting et al., 2003)

One of the key questions is about the interplay between local and non-local interactions in the folding reaction (Tanaka and Scheraga, 1975, 1977; Gromiha and Selvaraj, 1997, 1999; Goto et al., 1999). In a number of studies it has been shown that the folding rate constants,  $k_f$ , of proteins depend on the contact order which is a measure of the complexity of the chain topology of the protein molecule (Fig. 1.10; Doyle et al., 1997; Chan, 1998; Jackson, 1998; Plaxco et al., 1998; Alm and Baker, 1999; Baker and DeGrado, 1999; Muñoz and Eaton, 1999; Riddle et al., 1999; Baker, 2000; Grantcharova et al., 2000; Koga and Takada, 2001). Proteins with a complicated chain topology, i.e., of which the native structure and the structure of the transition state contains many contacts of residues remote in sequence (Figs. 1.11 a, b; 1.12 a, b) have orders of magnitude lower folding rate constants,  $k_f$ , than proteins with a simple chain topology, i.e., of which the native structure and the structure of the transition state is dominated by contacts of residues near in sequence (Figs. 1.11 c, d; 1.12 c, d). Within the range of  $10^{-1} \text{ s}^{-1} \leq k_f \leq 10^8 \text{ s}^{-1}$ ,  $-\log k_f$  correlates well with the so-called chain topology parameter, *CTP*, with a correlation coefficient of up to  $\approx 0.87$ :

$$-\log k_f \sim CTP, \quad CTP = \frac{1}{L \cdot N} \sum \Delta S_{i,j}^2, \quad (1.1)$$

where  $L$  is the number of residues of the protein (chain length),  $N$  the number of inter-residue contacts in the protein molecule,  $\Delta S_{i,j}$  the separation in sequence between the contacting residue number  $i$  and  $j$ , and “ $\sim$ ” marks a linear correlation (Fig. 1.13; Nölting et al., 2003).

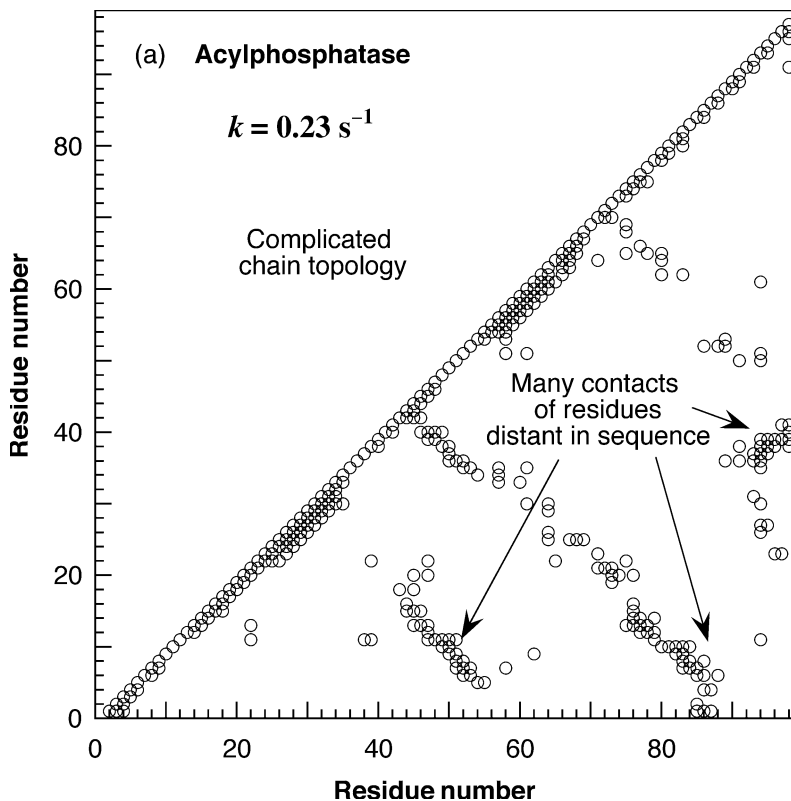


**Fig. 1.11a** Chain topologies (Nölting et al., 2003) of three proteins and a peptide with vastly different folding times: (a) acylphosphatase (Pastore et al., 1992), (b) FK506 binding protein (FKBP-12) (van Duyne et al., 1991), (c)  $\lambda$ -repressor dimer bound to DNA (Beamer and Pabo, 1992), and (d) the hairpin forming peptide from protein G (41–56) GEWYDDATKTFVTE (Achari et al., 1992; Muñoz and Eaton, 1999). Coordinates are from the Brookhaven National Laboratory Protein Data Bank (Abola et al., 1997). *Continued on the following pages*

The only important difference of the definition of *CTP* to the definition of the contact order is the quadratic dependence on  $\Delta S_{ij}$ , and yet the fit is more stable and valid over a much larger range of rate constants and valid for both  $\alpha$ -helix proteins and  $\beta$ -sheet proteins. The relation  $-\log k_f \sim CTP$  can also reasonably well predict folding times of peptides. For various cut-off distances from 3.5 Å to 8.5 Å, the correlation coefficient,  $R$ , for  $-\log k_f \sim CTP$  is 0.80–0.87 (Nölting et al., 2003; Fig. 1.14). Ignoring the inter-residue contacts involving hydrogen atoms which generally have less precisely known or fluctuating positions in the protein molecule causes only little if any effect on  $R$  (Nölting et al., 2003). When ignoring the data points for the small peptides, the  $R$  for  $-\log k_f \sim CTP$  is still 0.75–0.81 for this range of cut-off distances.

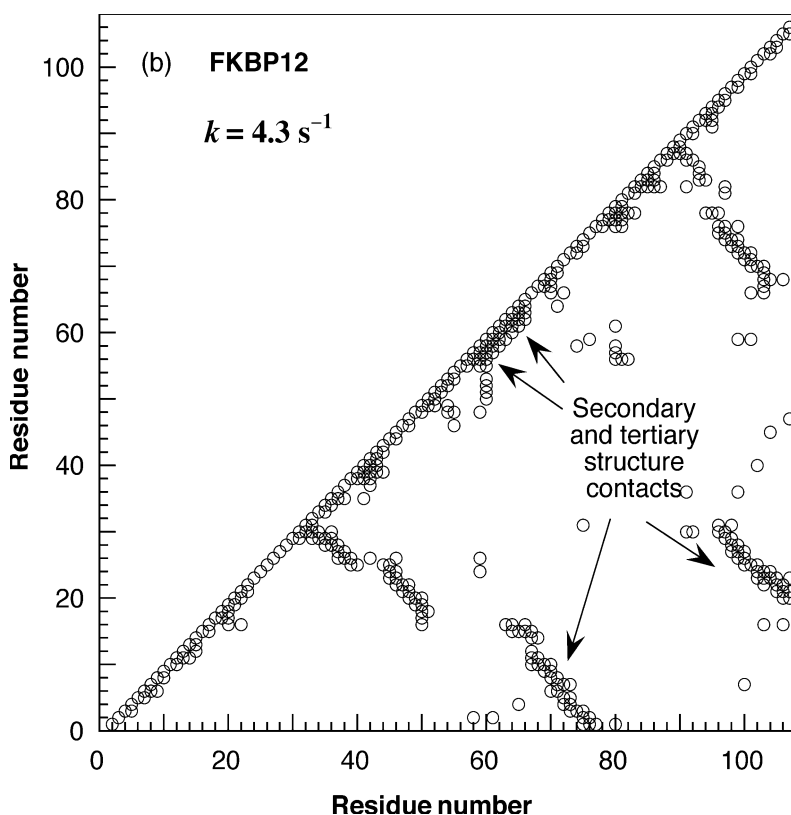


**Fig. 1.11b** Chain topology (Nölting et al., 2003) of FK506 binding protein (FKBP-12). Coordinates are from the Brookhaven National Laboratory Protein Data Bank (Abola et al., 1997). For further chain topologies see pp. 14, 16, and 17

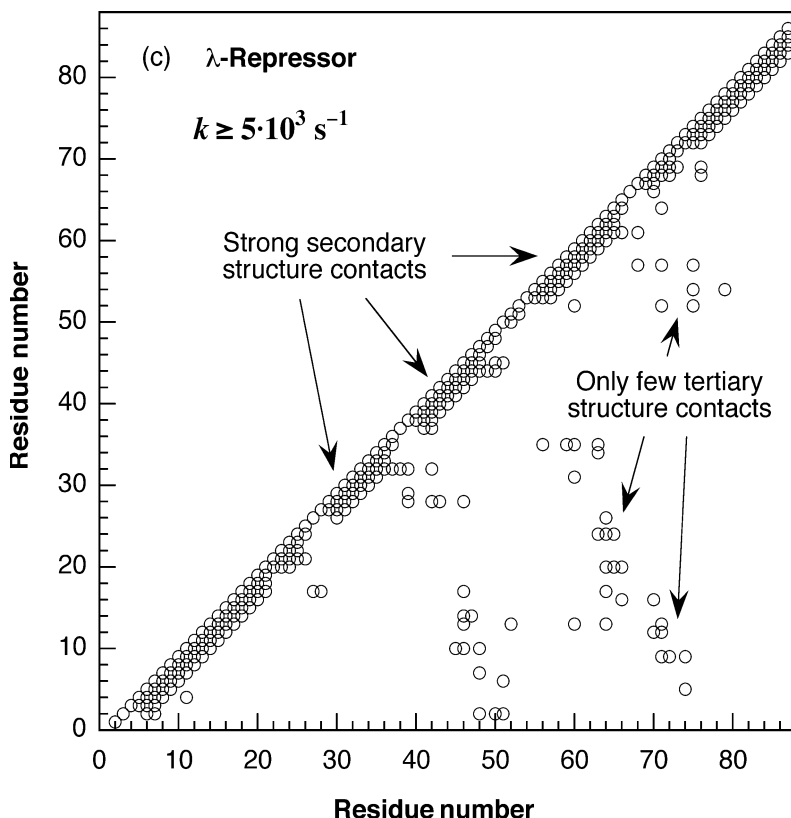


**Fig. 1.11c** Chain topology (Nölting et al., 2003) of  $\lambda$ -repressor dimer bound to DNA. Coordinates are from the Brookhaven National Laboratory Protein Data Bank (Abola et al., 1997). For further chain topologies see pp. 14, 15, and 17

A further important determinant of the speed of folding is the occurrence of some single strong interactions in the protein molecule. For example, some fast-folding proteins of thermophilic organisms contain a relatively large content of asparagine residues and salt bridges. These interactions can affect the rate of folding by a couple of orders of magnitude.  $-\log k_f$  correlates also with the number of residues belonging to  $\beta$ -sheets. This may be due to the larger number of long-range secondary structure contacts in sheets than in helices.

The  $-\log k_f \sim CTP$  is inconsistent with a zipper-like model for folding where the time of folding would be roughly proportional to the zipper length (sequence separation between zipper beginning and end). Obviously this relation is also inconsistent with a random-search mechanism where  $-\log k_f [s^{-1}] \approx L - 9$ .

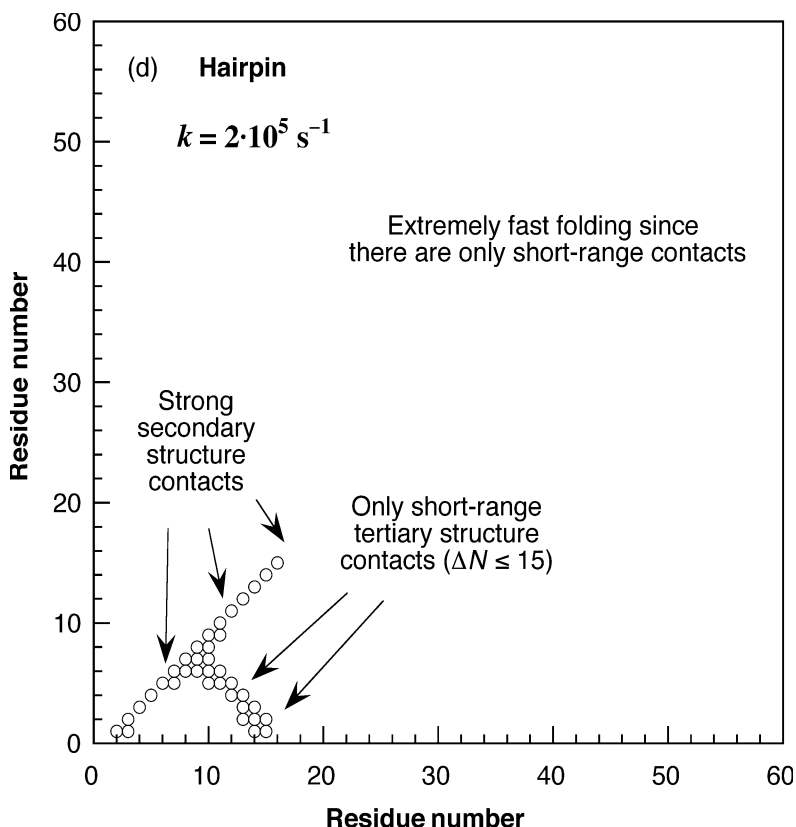
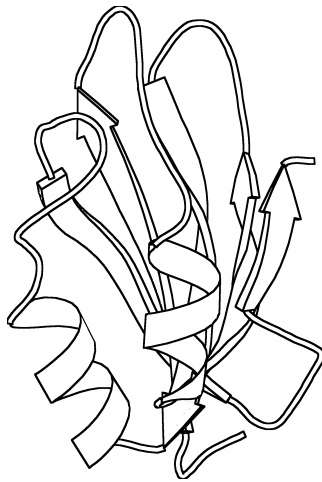
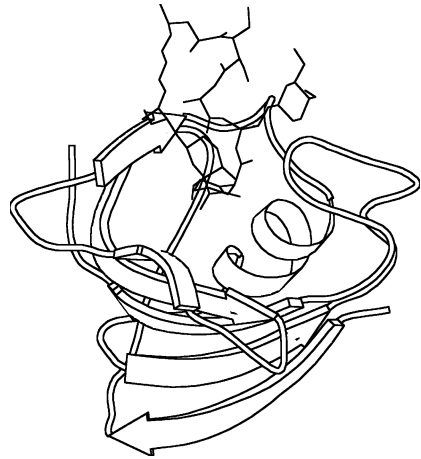


**Fig. 1.11d** Chain topology (Nölting et al., 2003) of the hairpin forming peptide from protein G (41–56) GEWTYDDATKTFTVTE. Coordinates are from the Brookhaven National Laboratory Protein Data Bank (Abola et al., 1997). For further chain topologies see pp. 14–16

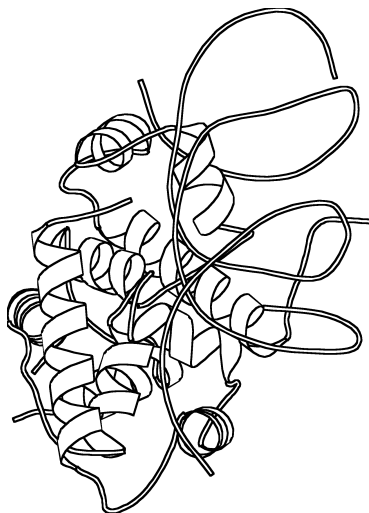
The protein folding problem, i.e., the understanding of the astonishing speed, complexity and efficiency of folding (Nölting et al., 1995, 1997a; Nölting and Andert, 2000; Nölting, 2005) has gained a large and still increasing importance in the context of folding-related diseases (Bellotti et al., 1998; Ironside, 1998; Brown et al., 1999; Gursky, 1999; Kienzl et al., 1999; Brown et al., 2000; Gursky and Alekhov, 2000), but also in the context of a variety of other exciting questions, such as macromolecular crowding inside the cell (Ellis and Hartl, 1999; van den Berg et al., 2000), high level expression of proteins (Hardesty et al., 1999; Kohno et al., 1999; Kramer et al., 1999), thermostability (Backmann et al., 1998; Williams et al., 1999) and packing problems (Efimov, 1998; Grigoriev et al., 1998, 1999; Efimov, 1999; Clementi et al., 2000a, 2000b).



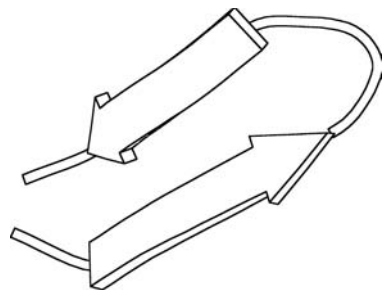
(a) acylphosphatase;  $k_f = 0.23 \text{ s}^{-1}$



(b) FKBP-12;  $k_f = 4.3 \text{ s}^{-1}$



(c)  $\lambda$ -repressor;  $k_f = 5,000\text{--}100,000 \text{ s}^{-1}$   
(bound DNA is also shown)



(d) hairpin;  $k_f = 200,000 \text{ s}^{-1}$

**Fig. 1.12** Structures of the three proteins and a peptide with vastly different folding rate constants,  $k_f$ : (a) acylphosphatase (Pastore et al., 1992), (b) FK506 binding protein (FKBP-12) (van Duyne et al., 1991), (c)  $\lambda$ -repressor dimer bound to DNA (Beamer and Pabo, 1992), and (d) the hairpin forming peptide from protein G (41–56) GEWTYDDATKTFVTVE (Achari et al., 1992; Muñoz and Eaton, 1999). Coordinates are from the Brookhaven National Laboratory Protein Data Bank (Abola et al., 1997). The figure was generated using MOLSCRIPT (Kraulis, 1991)

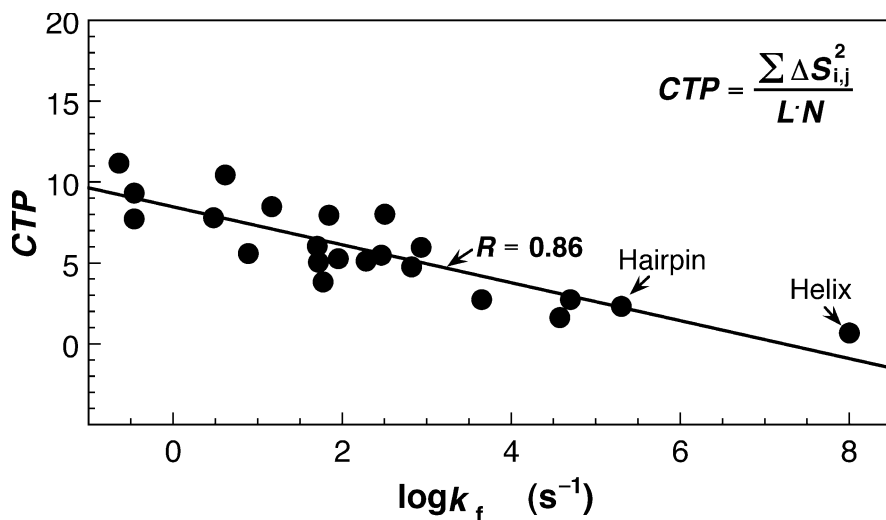


**Fig. 1.13** The measured folding rate constants,  $k_f$ , of 20 proteins, a 16-residue  $\beta$ -hairpin and a 10-residue helical polyalanine peptide as a function of the chain topology expressed by the chain topology parameter,  $CTP = L^{-1} N^{-1} \sum \Delta S_{i,j}^2$ , where  $L$  is the number of residues of the macromolecule,  $N$  the total number of inter-residue contacts in the macromolecule, and  $\Delta S_{i,j}$  the sequence separation between the contacting residues  $i$  and  $j$  (Nölting et al., 2003). The fit provides  $\log k_f = 7.56 - 0.895 \cdot CTP$  with a correlation coefficient of 0.86. Within the range of  $10^{-1} \text{ s}^{-1} \leq k_f \leq 10^8 \text{ s}^{-1}$ , predictions of the folding rate constants of peptides and proteins are accurate to typically a couple of orders of magnitude. The relation between structure and rate of folding is so important because it tells us a lot about the mechanism of protein folding and helps to solve the so-called folding paradox (see Nölting et al., 2003; Nölting, 2005). Inter-residue contacts were calculated at a cut-off distance of 4 Å, and no contacts of hydrogen atoms were included in the calculations. Coordinates of the proteins and the  $\beta$ -hairpin were taken from the Brookhaven National Laboratory Protein Data Bank (Abola et al., 1997). For the choice of coordinates see Nölting et al., 2003. Coordinates of the 10-residue helical polyalanine peptide were calculated with the program FoldIt (Jésior et al., 1994). 18 rate constants from ref. (Jackson, 1998) and the  $k_f$  of the 16-residue  $\beta$ -hairpin were chosen as previously selected in ref. (Muñoz and Eaton, 1999). The  $k_f$  of the 10-residue helical polyalanine peptide was estimated using data in (Williams et al., 1996; Gruebele, 1999; Zhou and Karplus, 1999; Nölting, 2005). Embedded in a lipid membrane, similar helices in folded proteins undergo intense vibrations with a frequency of  $10^7 \text{ s}^{-1}$  and several 0.1 Å elongation (e.g., Voigt and Schrötter, 1999). The  $k_f$  for the thermostable variant of  $\lambda$ -repressor and for the engrailed homeodomain,  $\approx 50,000 \text{ s}^{-1}$ , and  $37,000 \text{ s}^{-1}$  are from (Burton et al., 1996, 1997), and (Mayor et al., 2000), respectively (Nölting et al., 2003)

Studies on protein folding have contributed to the better understanding of hydrophobic interaction (Drablos, 1999; Garcia-Hernandez and Hernandez-Arana, 1999; Chan, 2000; Czaplowski et al., 2000), hydrophilic interaction (Jésior, 2000),

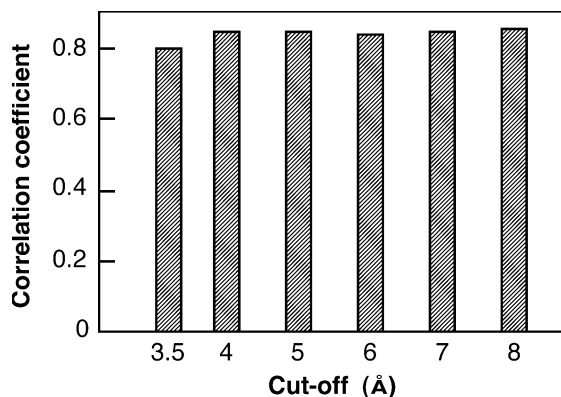


**Fig. 1.14** Correlation coefficient for  $-\log k_f \sim CTP$  for different cut-off distances for the calculation of the contacts, as indicated. No contacts of hydrogen atoms were included in the calculations. Including these contacts leads to a slightly higher correlation coefficient (Nölting et al., 2003)

charge interaction (Åqvist, 1999; de Cock et al., 1999), sidechain association (Galzitskaya et al., 2000), and disulfide formation (Chang et al., 2000a, 2000b).

Speeding up folding was achieved by design of sequences with good folding properties (Irbäck et al., 1999) and facilitating folding with helper molecules, so-called chaperones (Csermely, 1999; El Khattabi et al., 1999; Itoh et al., 1999; Kawata et al., 1999; Yamasaki et al., 1999; Gutsche et al., 2000a, 2000b), and taking carbohydrates as templates for *de novo* design of proteins (Brask and Jensen, 2000).

Protein folding has gained interest also regarding RNA folding energy landscapes (Chen and Dill, 2000), the interpretation of multi-state kinetics (Bai, 1999, 2000; Goldbeck et al., 1999), interpretation of differential scanning calorimetry (DSC) data towards cooperative formation of a folding nucleus (Honda et al., 1999; Honda et al., 2000), the evolution of structure formation (Chan, 1999; D'Alessio, 1999a, 1999b), protein secretion (Chambert and Petit-Glatron, 1999; Berks et al., 2000), and protein structure prediction (Crawford, 1999).

## 1.4 Support of structure determination by protein folding simulations

Theoretically, the structure of the native state of a protein can be determined by calculating the energies of all conformations of the molecule. This is true even if the native conformation does not correspond to the global energy minimum. For example, with a few additional experimentally obtained distance constraints one could decide which is the native structure. Unfortunately, the number of possible



conformations of a polypeptide chain is astronomically large. For example, as judged by the entropy, for a protein comprising 100 residues it is of the order of  $10^{100}$  (Nölting, 2005). There are some more optimistic estimates which are based on mechanistic considerations, but still the number of conformations is astronomically large. A further problem is that there are large positive and negative contributions to the protein stability: The stability of the molecule is given by the difference of two large almost equal numbers (Nölting, 2005). In order to calculate the global energy minimum or a folding pathway with sufficient precision, these two numbers would need to be known with about 3–4 significant digits. Currently the theory of molecular energies is not precise enough to meet this requirement. That is why it has not yet been possible to calculate the global energy minimum of an average-sized protein without significant approximations and profound simplifications. Only recently, groundbreaking molecular dynamics simulations on a 23-residue mini-protein found the energy minimum in 700  $\mu\text{s}$  of simulation (Snow et al., 2002).

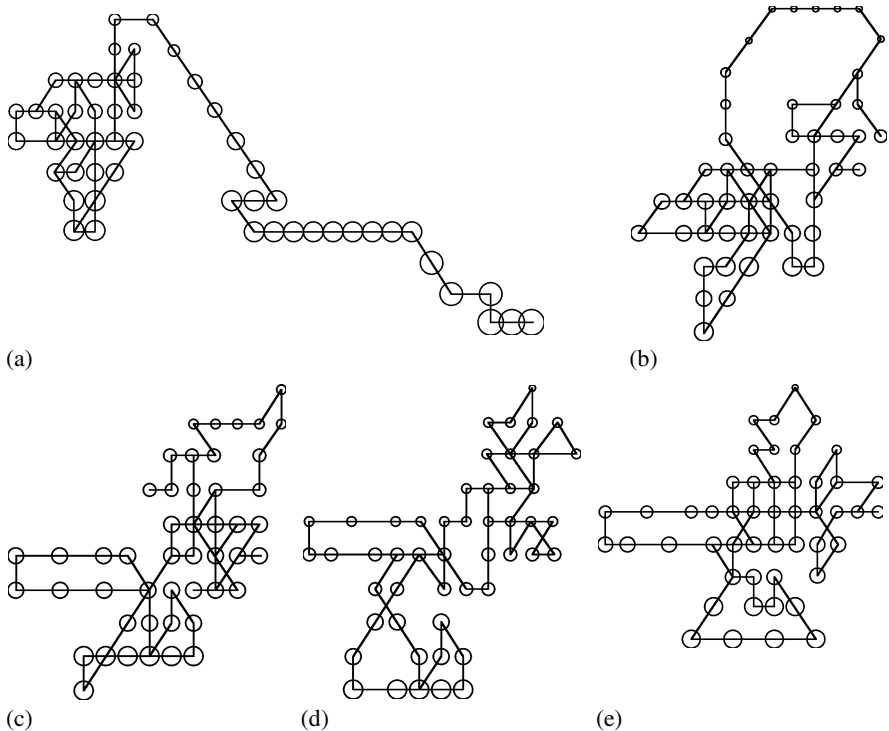


**Fig. 1.15** Support of structure determination by simulation of protein folding. (a) Step 100 of the simulation: initial collapse to a non-native conformation. (b) Step 400: formation of a molten-globule-like state. (c) Step 4,480 and (d) step 17,990: further condensation and reorganization of the molten-globule intermediate. (e) Step 38,174: formation of a native-like state. Each circle represents an amino acid residue of the protein

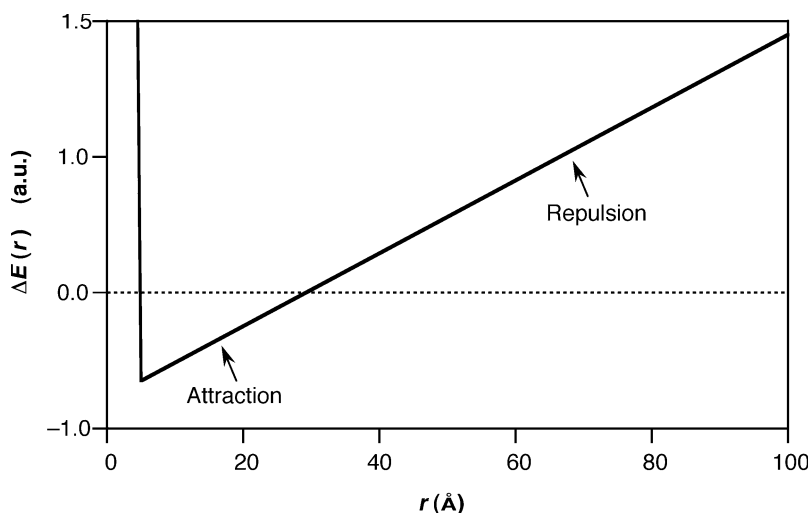


**Fig. 1.16** Hydrophobic potential used for the folding simulation shown in Fig. 1.15

Due to their extreme simplicity, lattice models for the protein structure and statistical energies have become especially prominent (see, e.g., Shakhnovich et al., 1996; Shakhnovich 1997; Mirny and Shakhnovich, 2001). In these models, often the amino acid residues are represented by spheres and the possible angles of the backbone are significantly restricted, e.g., only  $0^\circ$  and  $\pm 90^\circ$  are allowed. Surprisingly, these simple approaches often yield reasonable results.

Fig. 1.15 exemplarily shows lattice simulations which could fold small proteins into native-like structures. The hydrophobic potential used for these simulations is similar to the potential described by Casari and Sippl (1992), but has a strong repulsion at very short distances (Fig. 1.16). For the attractive component, the same relative factors for pairs of amino acids were used as given by Casari and Sippl (1992) in Table 2. The start conformations are random combinations of the structural elements helix, sheet and random coil. The use of not purely random start conformations, but start conformations that contain fluctuating secondary structure elements speeds up the simulation by several orders of magnitude. The aim was not to calculate a unique native structure, but is to find a set of low-energy conformations. Experimental constraints are then used to rule out the wrong conformations and to determine the native conformation. Important features of the folding reaction are resembled: the initially expanded conformation collapses to a molten-globule-like state after 400 simulation steps (Fig. 1.15b) which reorganizes after a total of 38,174 simulation steps to a native-like conformation (Fig. 1.15e).

## 2 Liquid chromatography of biomolecules

Proteins, peptides, DNA, RNA, lipids, and organic cofactors have various characteristics such as electric charge, molecular weight, hydrophobicity, and surface relief. Purification is usually achieved by using methods that separate the biomolecules according to their differences in these physical characteristics, such as ion exchange (Sect. 2.1), gel filtration (Sect. 2.2), and affinity chromatography (Sect. 2.3).

### 2.1 Ion exchange chromatography

In ion exchange chromatography, the stationary solid phase commonly consists of a resin with covalently attached anions or cations. Solute ions of the opposite charge in the liquid, mobile phase are attracted to the ions by electrostatic forces. Adsorbed sample components are then eluted by application of a salt gradient which will gradually desorb the sample molecules in order of increasing electrostatic interaction with the ions of the column (Figs. 2.1–2.3). Because of its excellent resolving power, ion exchange chromatography is probably the most important type of chromatographic methods in many protein preparations.

The choice of ion exchange resin for the purification of a protein largely depends on the isoelectric point,  $pI$ , of the protein. At a  $pH$  value above the  $pI$  of a protein, it will have a negative net charge and adsorb to an anion exchanger. Below the  $pI$ , the protein will adsorb to a cation exchanger. For example, if the  $pI$  is 4 then in most cases it is advisable to choose a resin which binds to the protein at a  $pH > 4$ . Since at  $pH > 4$  this protein is negatively charged, the resin has to be an anion ion exchanger, e.g., DEAE. One could also use a  $pH < 4$  and a cation exchanger, but many proteins are not stable or aggregate under these conditions. If, in contrast, the protein we want to purify has a  $pI = 10$ , it is positively charged at usually suitable conditions for protein ion exchange chromatography, i.e., at a  $pH$  around 7. Thus, in general for this protein type we have to choose a cation ion exchange resin, e.g., CM, which is negatively charged at neutral  $pH$ .

The capacity of the resin strongly depends on the  $pH$  and the  $pI$  of the proteins to be separated (Fig. 2.4; Table 2.1), but also on the quality of the resin, the applied pressure, and the number of runs of the column (Fig. 2.5). To improve the life of the resin, it should be stored in a clean condition in the appropriate solvent and not be used outside the specified  $pH$  range and pressure limit.

For the separation of some enzymes which may lose their activity by contact with metals in the wall of stainless steel columns, glass-packed columns may be more appropriate. The chromatographic resolution mainly depends on the type of biomolecules, type and quality of the resin, ionic strength gradient during elution, temperature, and the geometry of the column.

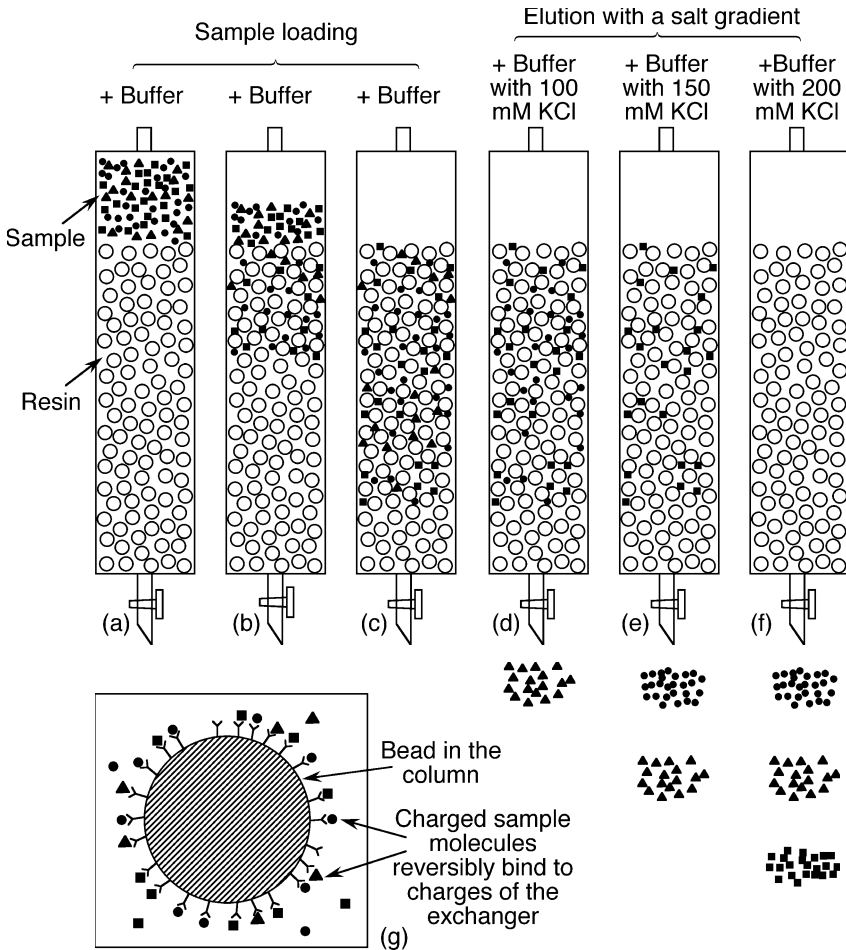


**Fig. 2.1** Example of ion exchange chromatography. (a)–(c) Loading the column: mobile anions (or cations) are held near cations (or anions) that are covalently attached to the resin (stationary phase). (d)–(f) Elution of the column with a salt gradient: the salt ions weaken the electrostatic interactions between sample ions and ions of the resin; sample molecules with different electrostatic properties are eluted at different salt concentrations, typically between 0–2 M. (g) Interaction of sample molecules with ions attached to the resin: at a suitable pH and low salt concentration, most of the three types of biomolecules to be separated in this example reversibly bind to the ions of the stationary phase

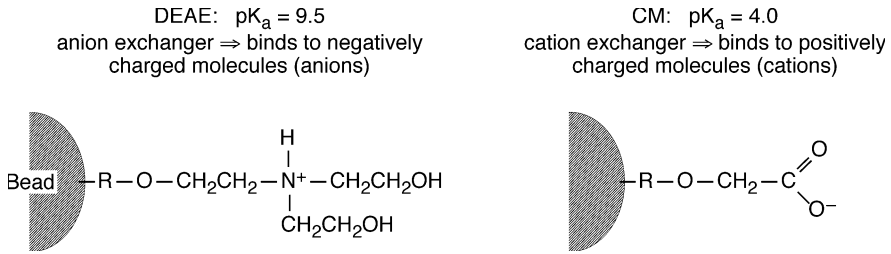


**Fig. 2.2** Two ion exchangers: diethyl-amino-ethyl (DEAE) and carboxy methyl (CM). The positive charge of DEAE attracts negatively charged biomolecules. CM is suitable for purification of positively charged biomolecules

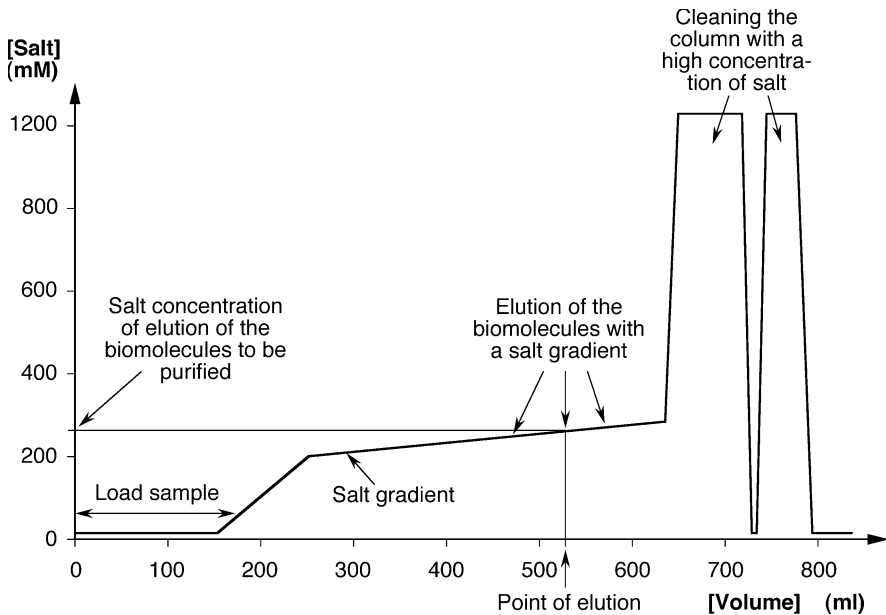


**Fig. 2.3** Example for the salt concentration during adsorption of a sample to an ion exchange column, subsequent elution of the sample, and cleaning of the column. Example of a purification protocol: First the solution of biomolecules and impurities in buffer contained in a syringe is loaded onto the column. The biomolecules and some of the impurities bind to the ions attached to the resin. Loading is completed and non-binding molecules are partly rinsed through the column with some further buffer. The next step is to apply a salt gradient with a programmable pump which mixes buffer with extra salt-containing buffer. The steep salt gradient at the beginning elutes most of the weakly binding impurities. At a certain salt concentration, the biomolecules to be purified elute from the column. Elution is monitored with an absorption detector at 280 nm wavelength and the sample fraction collected. After each run the column is cleaned with 1–2 M KCl. This removes most of the strongly binding sample impurities

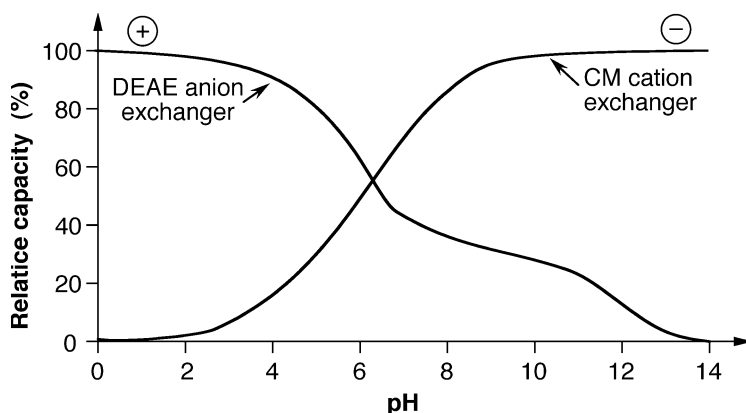


**Fig. 2.4** Charge properties of anion and cation exchangers. DEAE has a significant capacity at low and medium pH; CM is highly capacious at high and medium pH

**Table 2.1** Properties of some important ion exchangers

Functional group	Type of exchanger	pH range
$\begin{array}{c} \diagup \\ -\text{N}^+-\text{CH}_3 \\ \diagdown \end{array}$	Quaternary amine (strong anion)	1 – 11
$-\text{NH}_2$	Primary amine (weak anion)	1 – 8
$-\text{NH}-$	Secondary amine (weak anion)	1 – 7
$\begin{array}{c} \diagup \\ -\text{N} \\ \diagdown \end{array}$	Tertiary amine (weak anion)	1 – 6
$-\text{COO}^-$	Carboxylic acid (weak cation)	6 – 14
$-\text{SO}_3^-$	Sulfonic acid (strong cation)	1 – 14

The experimental set-up (Fig. 2.6) often just consists of a bottle with buffer, a bottle with buffer with salt, a programmable FPLC or HPLC pump, the column, a detector and recorder of absorption at 280 nm, or occasionally at 220 nm, and a sample collector. If the right conditions for protein preparation are unknown, a pre-run is performed with a small fraction of the sample. Attention should be paid not to overload the column in preparative runs since this can shift peak positions and lead to substantial sample losses. In many cases of modern high expression of recombinant proteins, it is possible to obtain a protein with 99% purity with a

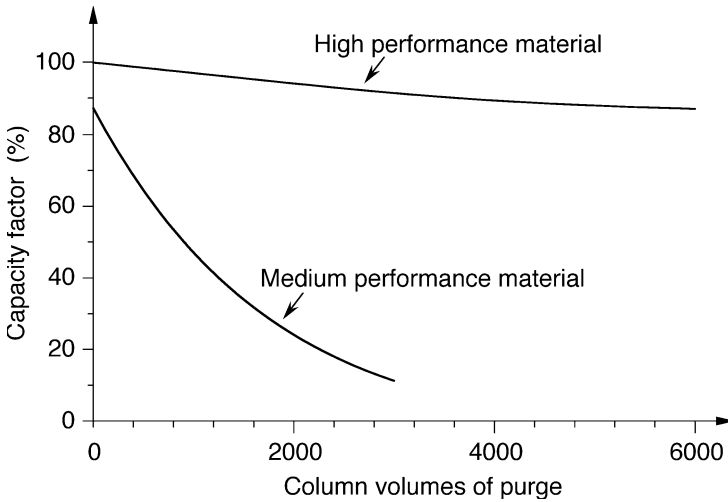


**Fig. 2.5** Change of the capacity of ion exchange columns due to usage. High performance columns operated at the appropriate pressure and pH can last many 1000 runs

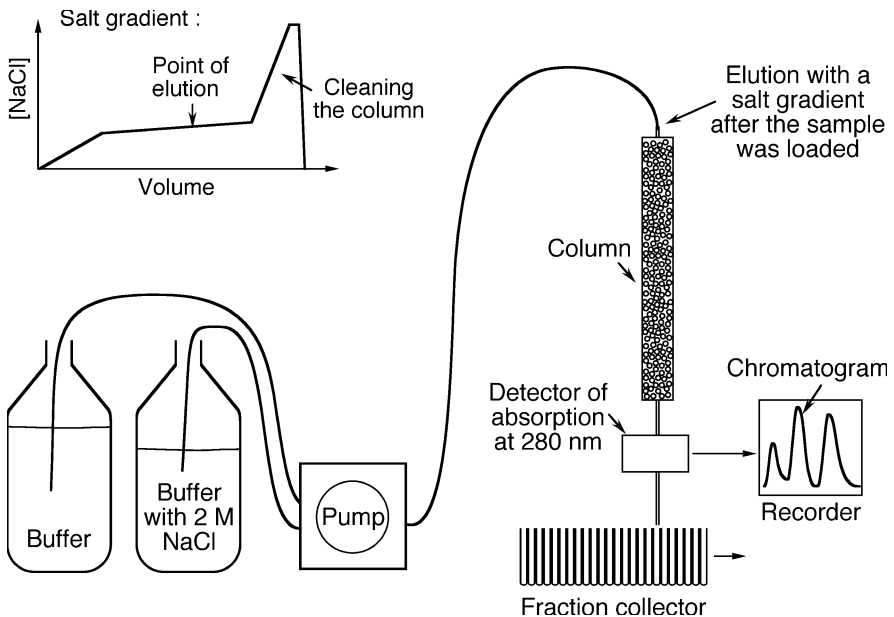


**Fig. 2.6** Typical setup for chromatographic purification of proteins with ion exchange FPLC. The pump mixes the salt gradient for sample elution after the sample was loaded, e.g., with a syringe

single ion exchange chromatographic step. However, in case of comparably low expression levels and substantial sample contamination, ion exchange chromatography alone may not be sufficient. Subsequent gel filtration chromatography (Sect. 2.2) can significantly further improve the protein purity.

## 2.2 Gel filtration chromatography

This type of chromatography is a variant of size exclusion chromatography (molecular exclusion chromatography), and is also known as gel permeation chromatography. It lacks an attractive interaction between the stationary phase

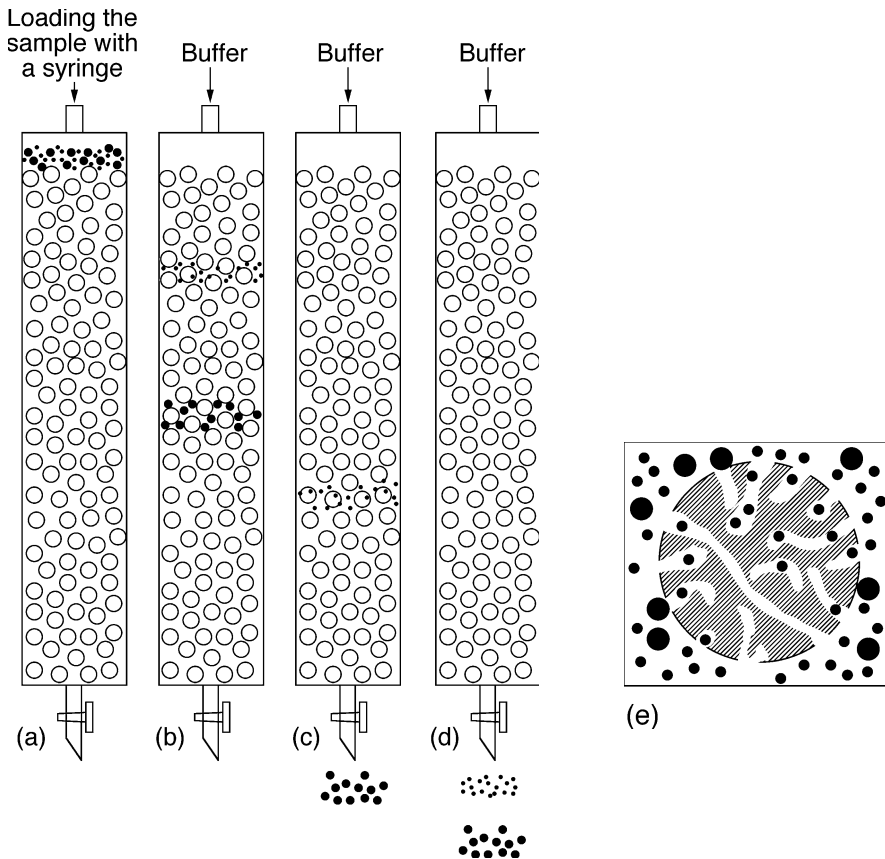


**Fig. 2.7** Gel filtration chromatography. When the sample passes through the porous gel, small sample molecules can enter the pores, causing them to flow slower through the column. Large molecules which cannot enter the pores, pass through the column at a faster rate than the smaller ones. Correct pore sizes and solvents are crucial for a good separation



(gel) and solute. The sample solution passes through the porous gel separating the molecules according to their size. The smallest molecules enter the bead pores, resulting in a relatively long flow path and long retention. Large molecules cannot enter the pores and have to flow around them, resulting in a relatively short flow path (Figs. 2.7–2.10).

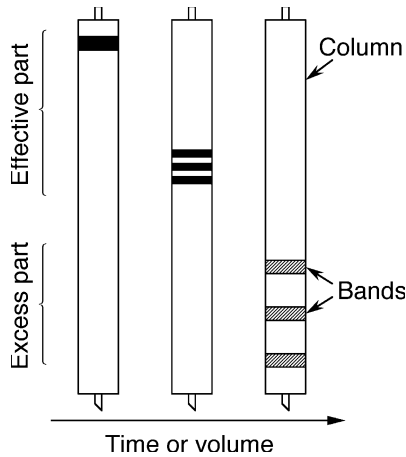


**Fig. 2.8** Band broadening in a column with too long a geometry. The so-called effective part of the column is sufficient for separation. Excessively long columns do not improve purity, but just cause dilution of the sample by band broadening

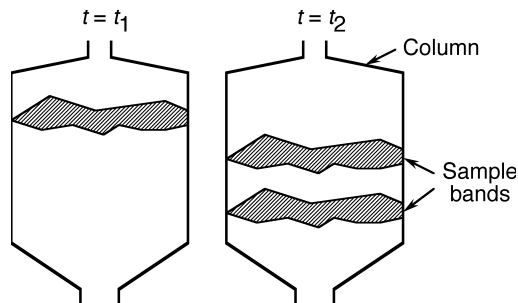


**Fig. 2.9** Band broadening in a column with too large a diameter. Despite the column length is about right to separate the two bands, significant sample dilution and possibly contamination occurs due to inhomogeneous loading of the column

Gel filtration chromatography is also an auxiliary method for assessing the molecular weight of biomolecules (Fig. 2.11). Although there are more precise methods, e.g., mass spectrometry (see Chap. 3), gel filtration chromatography is important for the measurement of monomer-multimer equilibria at about  $\mu\text{M}$ -concentrations of biomolecules.

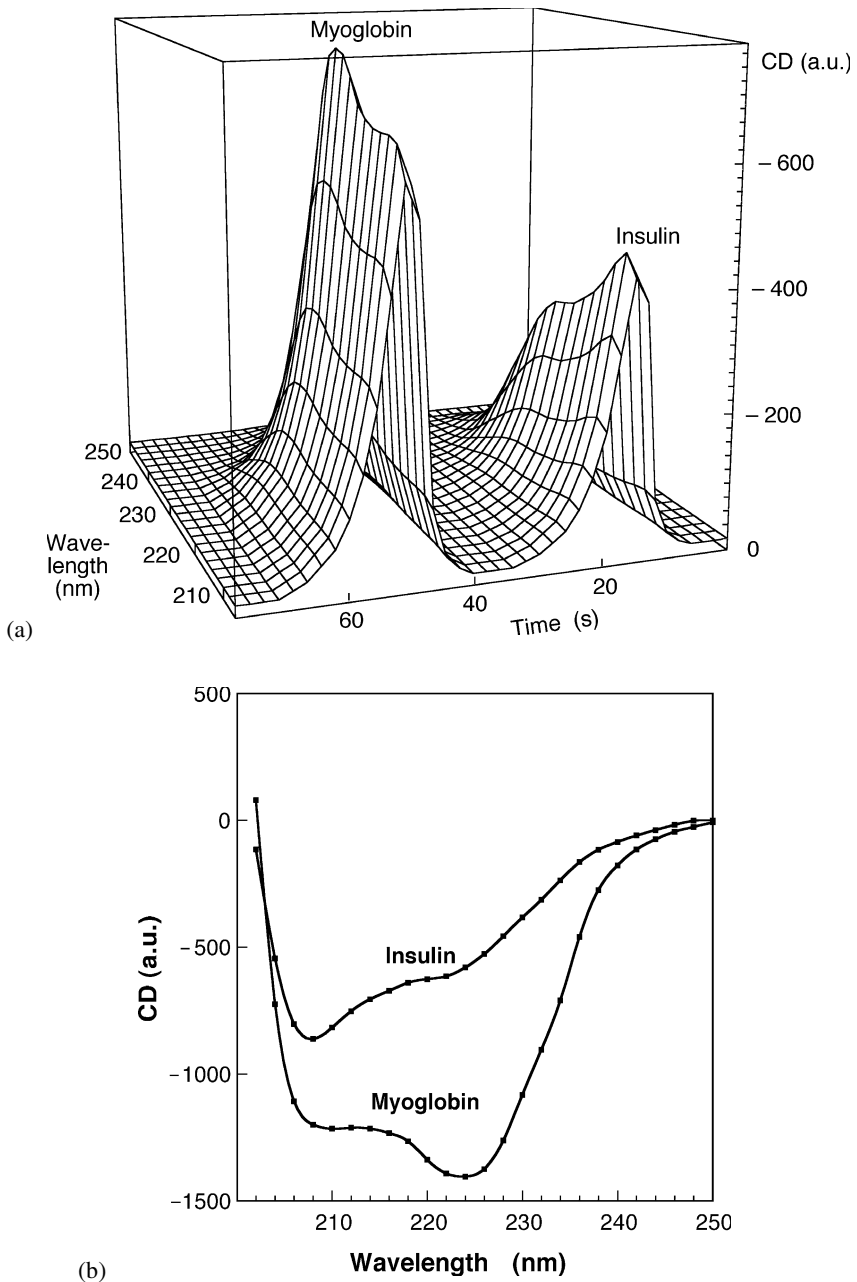


**Fig. 2.10** (a) Chromatogram of the separation of a mixture of myoglobin and insulin with multichannel circular dichroism (CD) detection. The multiplex advantage of the multichannel detection prevents distortion of the shape of the spectra (see Nölting, 2005). (b) CD spectra of myoglobin and insulin for comparison

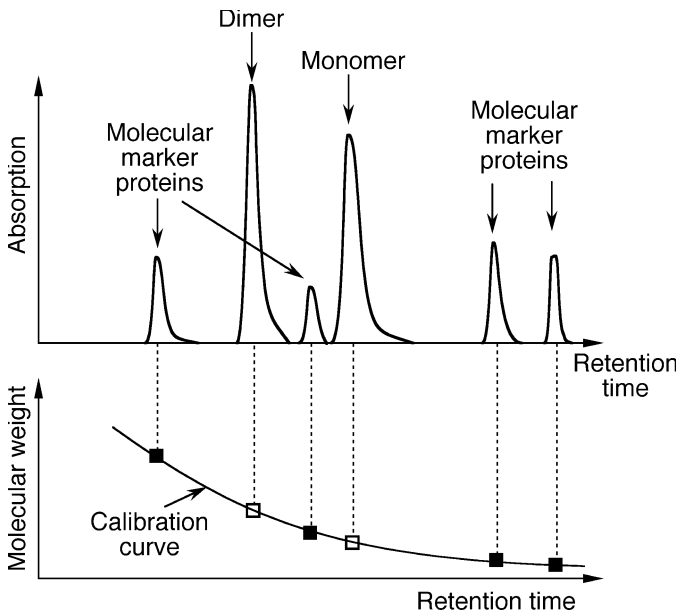


**Fig. 2.11** Molecules of known molecular weight enable an estimate of the molecular weight of the unknown molecule. In this case, two peaks of the investigated molecule indicate a monomer-dimer equilibrium

## 2.3 Affinity chromatography

Affinity chromatography is a method enabling purification of biomolecules and other macromolecules with respect to individual structure or function. It utilizes the highly specific binding of the macromolecule to a second molecule which is attached to the stationary phase. The principle of operation is as follows: (a) the sample is injected into the column; (b) buffer is rinsed through the column, so that sample molecules with no affinity to the stationary phase are eluted from the column, but sample molecules with a high affinity for the stationary phase are retained in the column; (c) the retained sample molecules are eluted from the column by buffer with a high salt concentration or a different pH or a different solvent composition (Fig. 2.12). The preparation of the protein can be performed by using a number of protein tags. The tags should not cause artificial interactions and should not alter the conformation of the tagged protein. Very common are poly-histidine tags that are attached to the protein by genetic engineering (Fig. 2.13). The tag typically consists of 8–12 histidine residues. It binds to nickel compounds at the surface of the chromatography beads. Fig. 2.14 illustrates a somewhat different variant of affinity chromatography in which misfolded proteins are continuously refolded by chaperones and eluted with buffer.

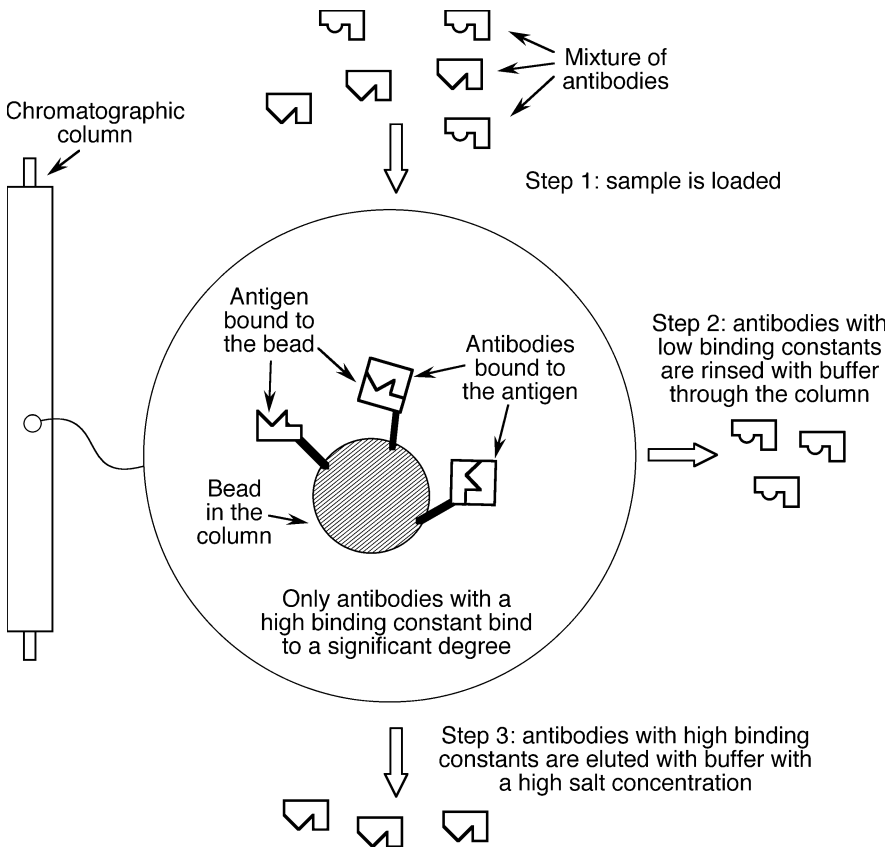


**Fig. 2.12** Purification of antibodies with affinity chromatography: The antigen is chemically bound to the beads of the column and the mixture of antibodies is rinsed through the column. Antibodies with high binding constants bind to the antigen and are eluted later with a buffer with a high salt concentration

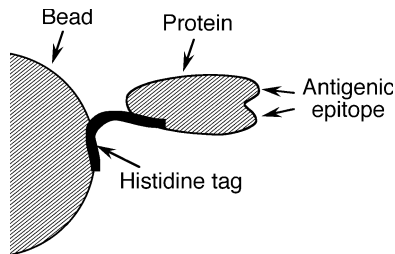


**Fig. 2.13** Attachment of a protein to a bead of an affinity column with a histidine tag. About 10 histidine residues were attached to the protein by genetic engineering, e.g., by polymerase chain reaction (PCR) mutagenesis (see, e.g., Nölting, 2005). The histidine residues strongly bind to the bead made from a nickel chelate resin

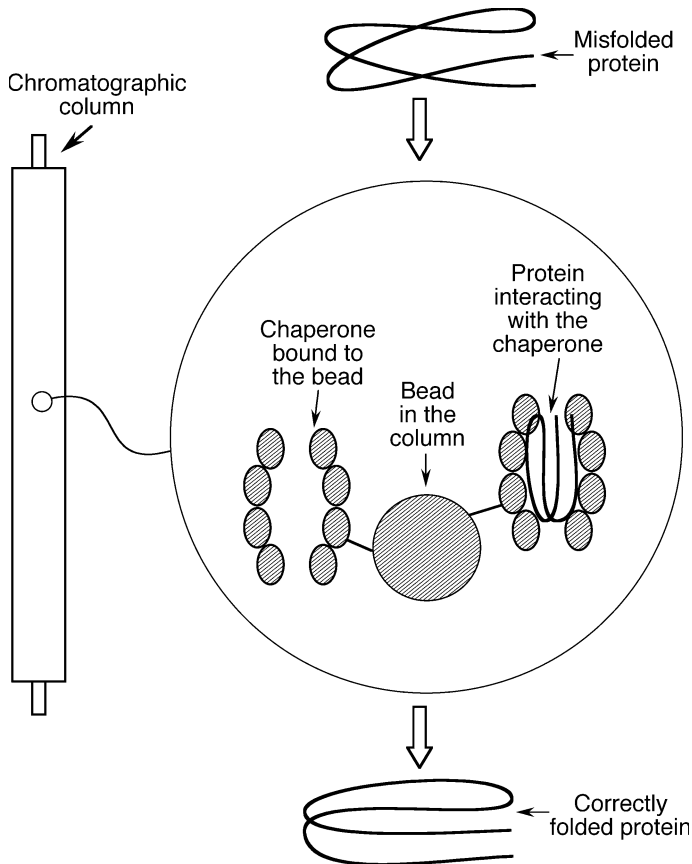


**Fig. 2.14** Refolding of expensive, poorly folding proteins: Folding chaperones, also known as chaperonins, are attached to the beads and the unfolded or misfolded protein is rinsed through the column. The chaperone interacts with the sample protein and catalyses its folding into the correct conformation

## 2.4 Counter-current chromatography and ultrafiltration

A relatively old method of chromatography is the Craig counter-current distribution apparatus (Fig. 2.15). Nowadays it serves for the large-scale purification of some chemicals for which other chromatographic methods are too expensive. As in other types of counter-current chromatography, both stationary and mobile phase are liquids and separation is based on sample partition between the two liquids. It may, e.g., function as follows (Fig. 2.15): (a) A certain biochemical has a higher solubility in phase A than impurities of the biochemical, but has a lower solubility in phase B than the impurities. (b) Phase B with a high concentration

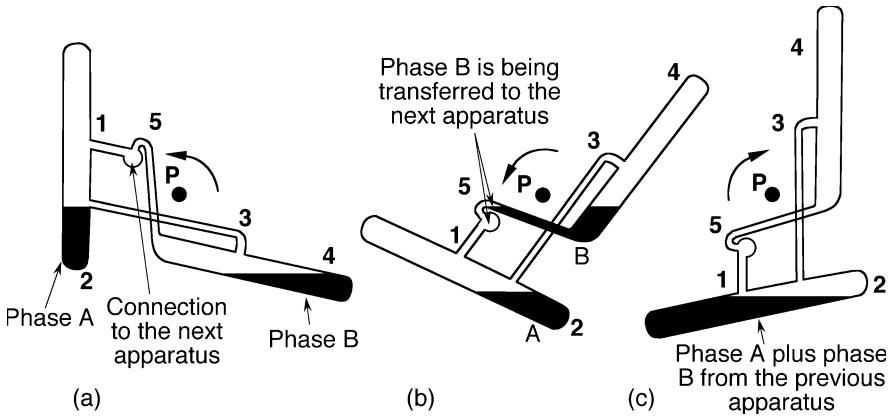


**Fig. 2.15** Craig counter-current distribution apparatus: both stationary and mobile phases are liquids. Sample separation is based on its partition between the two liquid phases (see text)

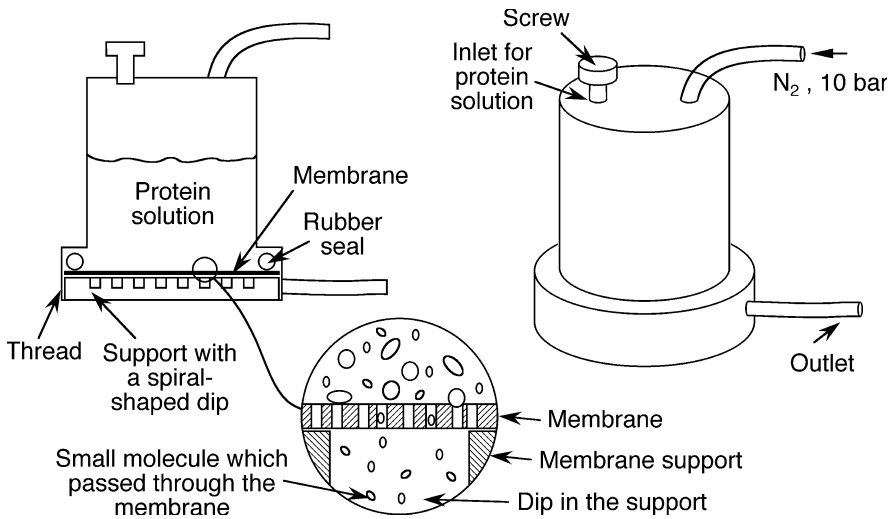


**Fig. 2.16** Ultrafiltration device (supplied, e.g., by Amicon Inc., Beverly, MA). Pressurized nitrogen from a nitrogen flask presses the protein solution against the membrane. Small molecules pass the membrane and are collectable at the outlet. Large molecules stay in the ultrafiltration vessel

of impurities is transferred to the next apparatus and fresh phase B is transferred from the previous apparatus to the shown apparatus. (c) Phases A and B are mixed and separated again, and the process continues with step (a). During suc-

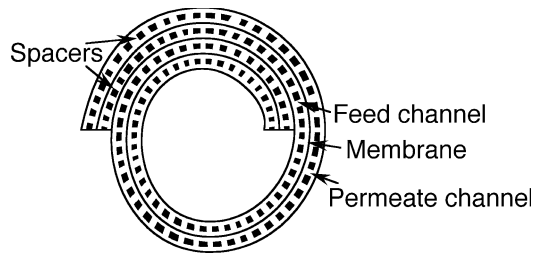


**Fig. 2.17** Side view of a spiral cartridge concentrator (e.g., Millipore Corporation, Bedford, MA). Pressure is applied by centrifuging the concentrator. Similarly to the pervious ultrafiltration device (Fig. 2.16), small molecules pass the membrane and large molecules are retained

cessive cycles, different chemicals move through a chain of counter-current distribution apparatuses with different speeds, and are collected, e.g., at the end of the chain.

Strictly speaking, ultrafiltration (Figs. 2.16 and 2.17) is not a chromatographic method. However, it should be mentioned here since it is an extremely useful tool of sample preparation prior to chromatography and can sometimes even substitute chromatography. It is applicable for (a) protein purification, (b) buffer exchange, and (c) concentrating protein solutions. Purification of a protein with a particular molecular weight,  $M_w$ , requires two steps: (a) First, one runs the ultrafiltration apparatus with a membrane with a cut-off higher than  $M_w$  and collects the solution leaving the vessel. (b) Then, one runs the apparatus with a membrane with a cut-off lower than  $M_w$  and collects the solution remaining in the vessel.

### 3 Mass spectrometry

Mass spectrometry is an incredibly important analytical technique for the identification of molecules by way of measuring their mass-to-charge ratios,  $m/z$ , in the ionized state. It is particularly useful for the detection and analysis of traces of macromolecules down to less than 1 pg ( $10^{-12}$  g). The general design of a mass spectrometer comprises sample injector, sample ionizer, mass analyzer and ion detector (Fig. 3.1). First the sample is injected into the ionizer which ionizes sample molecules. Then sample ions are analyzed and detected. To prevent collisions with gas molecules, sample ionizer, mass analyzer and ion detector are generally operated in vacuum.



**Fig. 3.1** General design of a mass spectrometer

The ion separation power of mass spectrometers is described by the resolution,  $R$ , defined as:

$$R = \frac{m}{\Delta m} , \tag{3.1}$$

where  $m$  and  $\Delta m$  are the ion mass and mass difference between two resolvable peaks in the mass spectrum, respectively.  $R$  typically ranges between 100 and 500,000.

#### 3.1 Principles of operation and types of spectrometers

According to their mass analyzer designs, there are five important types of mass spectrometers (MS): (a) magnetic and/or electric sector MS (Figs. 3.2 and 3.3), (b) quadrupole MS (Fig. 3.4), (c) ion trap MS (Fig. 3.5), (d) time-of-flight MS (Figs. 3.6–3.9), and (e) Fourier transform MS (Fig. 3.10). Time-of-flight mass spectrometers (TOFs) often are less expensive than other types of mass spectrometers and have, compared to quadrupole MS and many sector MS, the advantage of recording the masses of all ions injected into the analyzer without scanning, contributing to a high sensitivity. TOFs usually have a smaller mass range and resolving power than Fourier transform mass spectrometers (FTMS).



### 3.1.1 Sector mass spectrometer

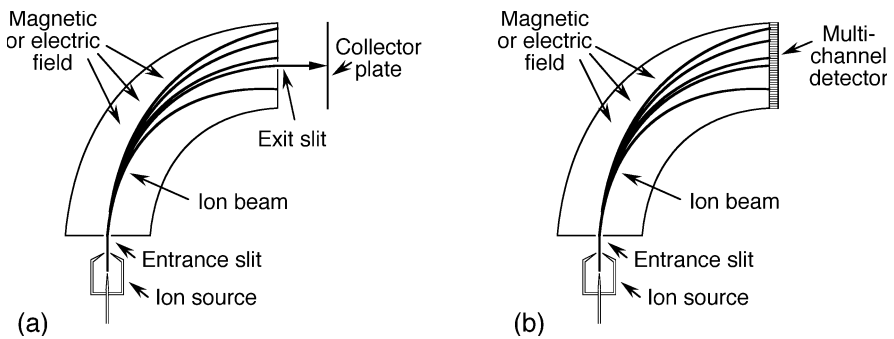


**Fig. 3.2** Single magnetic or electric sector mass spectrometer with a single channel (a) and multichannel (b) detector, respectively. Ions leaving the ion source are accelerated and passed through the sector in which the electric or magnetic field is applied perpendicular to the direction of the ion movement. The field bends the ion flight path and causes ions with different  $m/z$  to travel on different paths. In scanning mass analyzers (a) the electric or magnetic field strength is varied and only one mass detected at a time. In non-scanning mass analyzers (b) all masses are recorded simultaneously within a limited mass range with the help of a multichannel detector

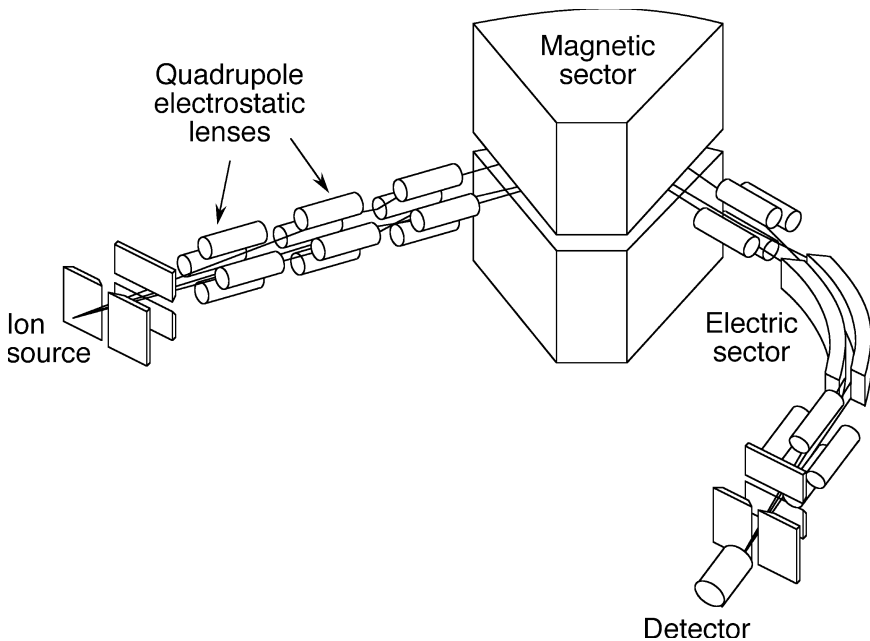


**Fig. 3.3** Advanced virtual image ion optics with high transmission in a benchtop single-sector mass spectrometer (GCmateII from JEOL Ltd., Tokyo; Matsuda et al., 1974; Matsuda, 1976, 1981)

### 3.1.2 Quadrupole mass spectrometer

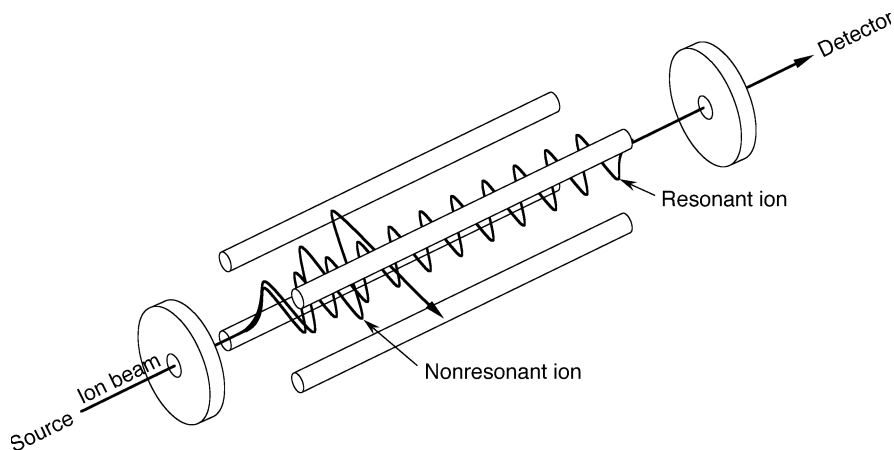


**Fig. 3.4** Quadrupole mass spectrometer. The ion beam is accelerated to a high velocity by an electric field and passed through the quadrupole mass analyzer comprising four metal rods. DC and AC potentials are applied to the quadrupole rods in such a way that only ions with one mass-to-charge ratio ( $m/z$ ) can pass through the analyzer at a time. To scan different  $m/z$ , DC and AC potentials are varied

### 3.1.3 Ion trap mass spectrometer

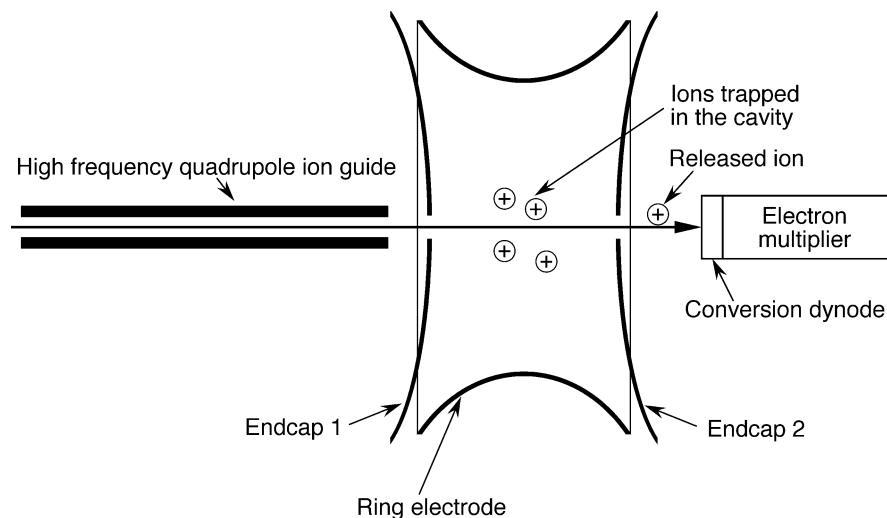


**Fig. 3.5** Ion trap mass analyzer. With the help of different radio frequency signals applied to the ring electrode and the endcaps, all ions are trapped in the cavity and then sequentially ejected according to their  $m/z$ .

### 3.1.4 Time-of-flight mass spectrometer

In time-of-flight mass spectrometers, a uniform starting time of ions is caused, e.g., by a pulse of an ionizing laser (Fig. 3.6) or a voltage pulse to an electric shutter (Fig. 3.7). After passing through the accelerating potential difference,  $V$ , the kinetic energy,  $E$ , of an ion with the charge,  $z$ , mass,  $m$ , and velocity,  $v$ , is:

$$E = zV = \frac{mv^2}{2} \quad (3.2)$$

For a length,  $l_{\text{TOF}}$ , the time of flight,  $t$ , is:

$$t = l_{\text{TOF}} \sqrt{\frac{m}{2zV}} \quad (3.3)$$

For example, for  $l_{\text{TOF}} = 0.1$  m,  $z = e = 1.602 \times 10^{-19}$  C,  $m = 10$  kDa =  $10 \text{ kg} / 6.0221 \times 10^{23}$ , and  $V = 100$  V we obtain  $t = 72 \mu\text{s}$ . A mass resolution of 1 Da requires in this example a time resolution of 3.6 ns. Unfortunately, not all ions start to move at the same time and not all ions have the same velocity. The differ-

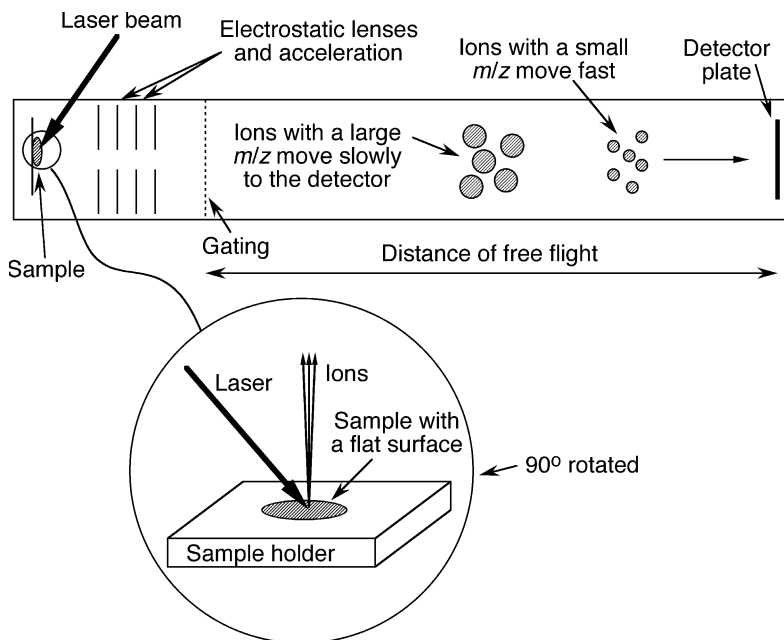


**Fig. 3.6** Linear time-of-flight mass spectrometer (TOF) with matrix-assisted laser desorption ionization (MALDI). The linear configuration of TOFs represents the simplest implementation of the time-of-flight technique. The typical mass range lies between 0 and 100 kDa, and the typical mass resolution  $m/\Delta m$  is 300–2000

ences in velocity are called chromatic aberration. Due to the chromatic aberration and the differences in the starting time, the requirements for a very high resolution are hard to meet in the simple design of a linear TOF (Fig. 3.6). In reflectron TOFs (Figs. 3.7–3.9), the ion optics reverses the flight direction of the ions and reduces chromatic aberration.

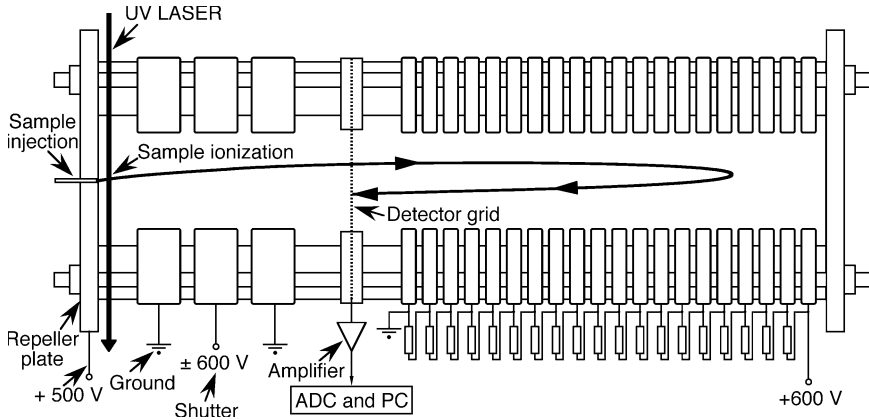


**Fig. 3.7** A simple reflectron time-of-flight mass spectrometer (e.g., Bryden, 1995). The reflector enhances mass-spectrometric resolution: it increases the time of flight and can focus ions. Here a voltage pulse at the shutter electrode causes a uniform starting time of the ions

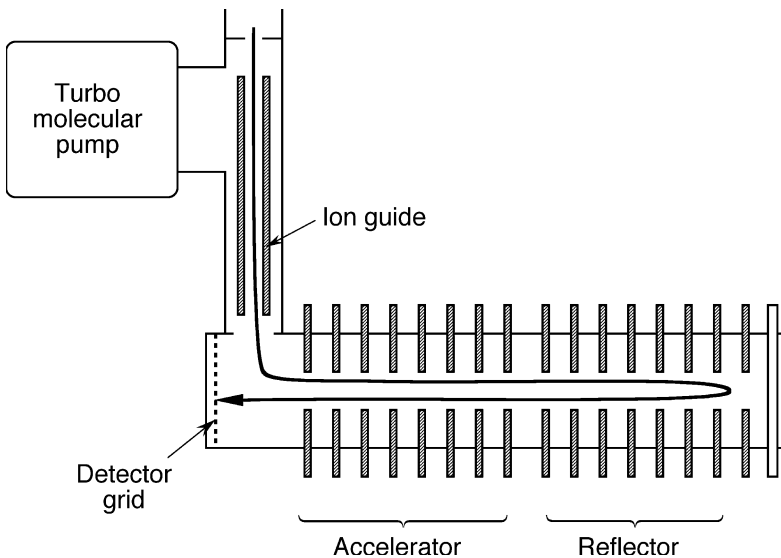


**Fig. 3.8** A reflectron time-of-flight mass spectrometer with orthogonal ion inlet (e.g., BioTOF II from Bruker Daltonik, Bremen, Germany)

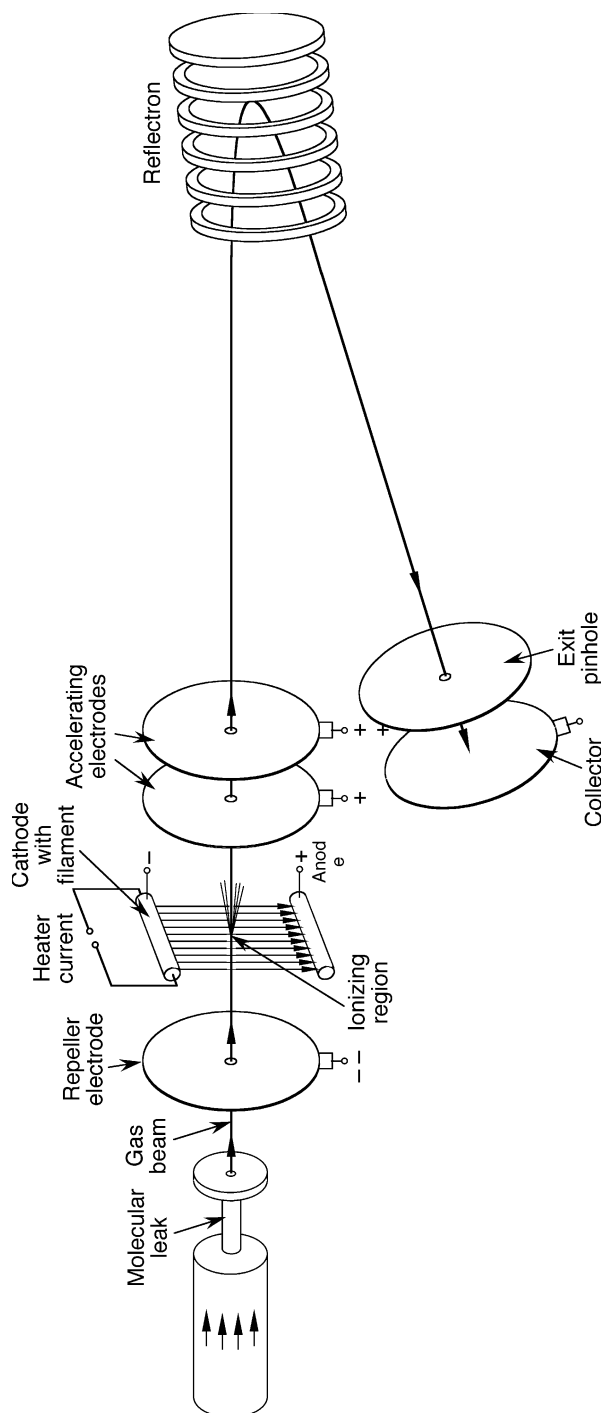


**Fig. 3.9** A high-resolution reflectron time-of-flight mass spectrometer. For further details see, e.g., IonSpec Corp., Irvine, CA; JEOL USA, Inc., Peabody, MA; Micromass and Waters Corporation, Milford, MA; Thermo Finnigan, San Jose, CA; Varian Instruments, Walnut Creek, CA

## 3.1.5 Fourier transform mass spectrometer

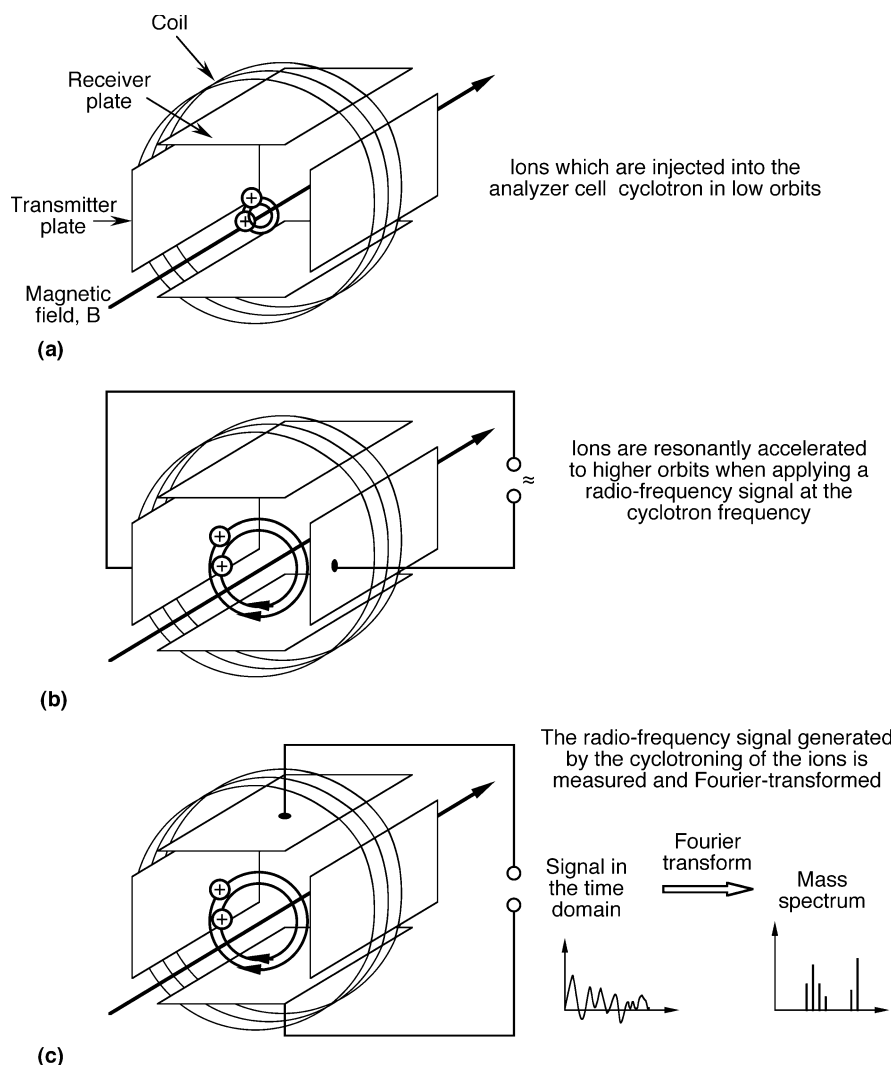


**Fig. 3.10** Principle of operation of a Fourier transform mass spectrometer (FTMS), also called “ion cyclotron resonance mass spectrometer” (see, e.g., IonSpec Corp., Lake Forest, CA; Bruker Daltonik, Bremen, Germany). **(a)** Ions are injected into the analyzer cell of the spectrometer. The magnetic field forces the thermal ions on orbits with small radii that depend on their mass-to-charge ratio. **(b)** An applied radio frequency pulse resonantly moves the ions to higher orbits. **(c)** The radio-frequency signal generated by the cyclotron of the ions is measured and Fourier-transformed. For the method of Fourier transform see also Sect. 4.1.1. The striking characteristic of FTMS is the high resolution,  $R$ , typically in excess of 100,000

### 3.1.6 Ionization, ion transport and ion detection

Common methods of ionization are electrospray (Fig. 3.11), MALDI (Fig. 3.6), electron bombardment, ion bombardment, and chemical ionization. Ions are mainly guided by electrostatic lenses and quadrupole or octopole ion guides (Fig. 3.12). With the exception of FTMS, the ion signals emerging from the mass analyzer of the MS are commonly detected with an electron multiplier (Fig. 3.13). In FTMS the cyclotroning ions are indirectly detected by measuring and Fourier-transforming the voltage signal they induce into receiver electrodes.

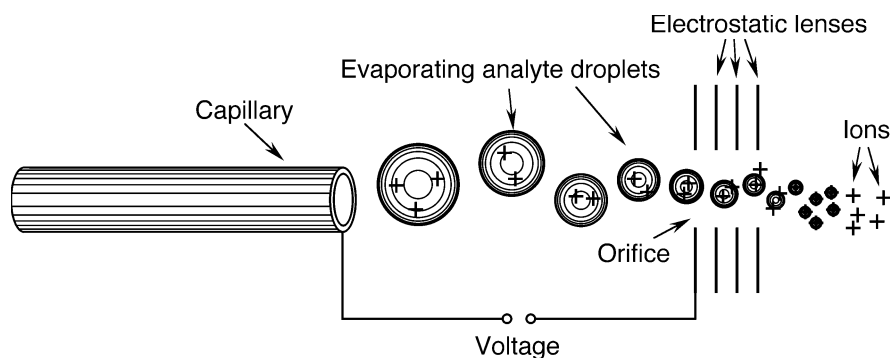


**Fig. 3.11** Electrospray ionization method. Analyte solutions delivered by liquid chromatography or a syringe pump are sprayed through the narrow, heated capillary leading into the mass spectrometer. A voltage of typically 200 V – 5 kV is applied between capillary and orifice in front of the electrostatic lenses. Ions form in vacuum by evaporation of the analyte solution of charged droplets

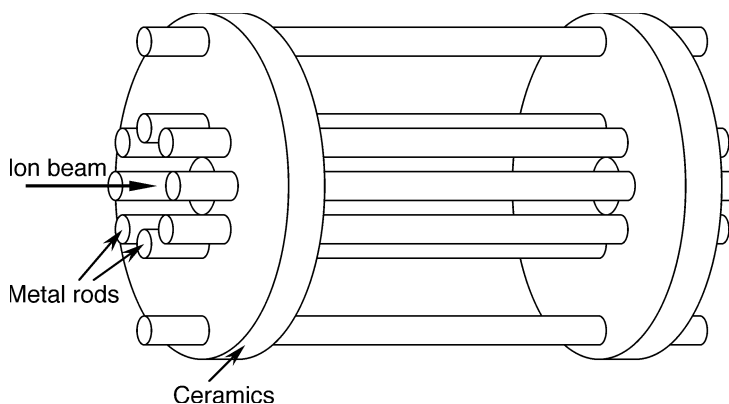


**Fig. 3.12** High frequency octopole ion guide for the injection of ions into an ion trap MS. Compared with a quadrupole ion guide, it enables a higher precision of guidance

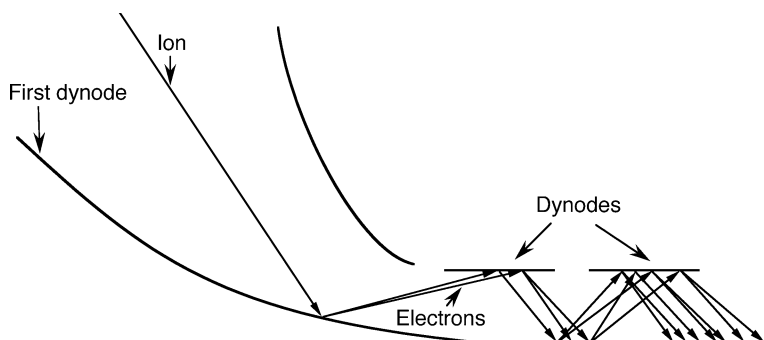


**Fig. 3.13** Electron multiplier for a MS. The first dynode converts the ion current into an electron current. Further dynodes amplify the electrons by a total factor of typically  $10^3$ – $10^8$ , largely dependent on the electron accelerating voltage between the dynodes, the number of dynodes, and the dynode composition. The last dynode is connected with an ammeter (not shown)

### 3.1.7 Ion fragmentation

Significant enlargement of the information content of spectra is achieved by fragmenting the sample, e.g., in a collision chamber (Fig. 3.14) or a helium-containing cavity of an ion trap mass analyzer (Fig. 3.5; see also Sect. 3.2).

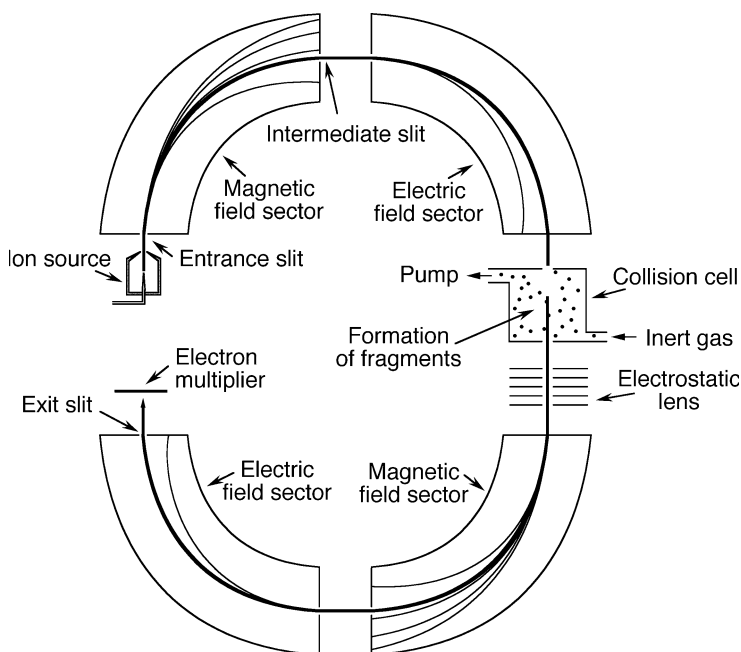


**Fig. 3.14** High resolution sector MS with a collision chamber



### 3.1.8 Combination with chromatographic methods

For the study of highly complex systems, such as complete cells, MS is often combined with chromatographic methods, such as HPLC (high pressure liquid chromatography; Fig. 3.15), FPLC (fast performance liquid chromatography) and gas chromatography (GC; Figs. 3.16 and 3.17). The two types of connectors between chromatography and MS shown in Figs. 3.15 and 3.18 are both applicable for HPLC and FPLC. Two-dimensional spectra are obtained through

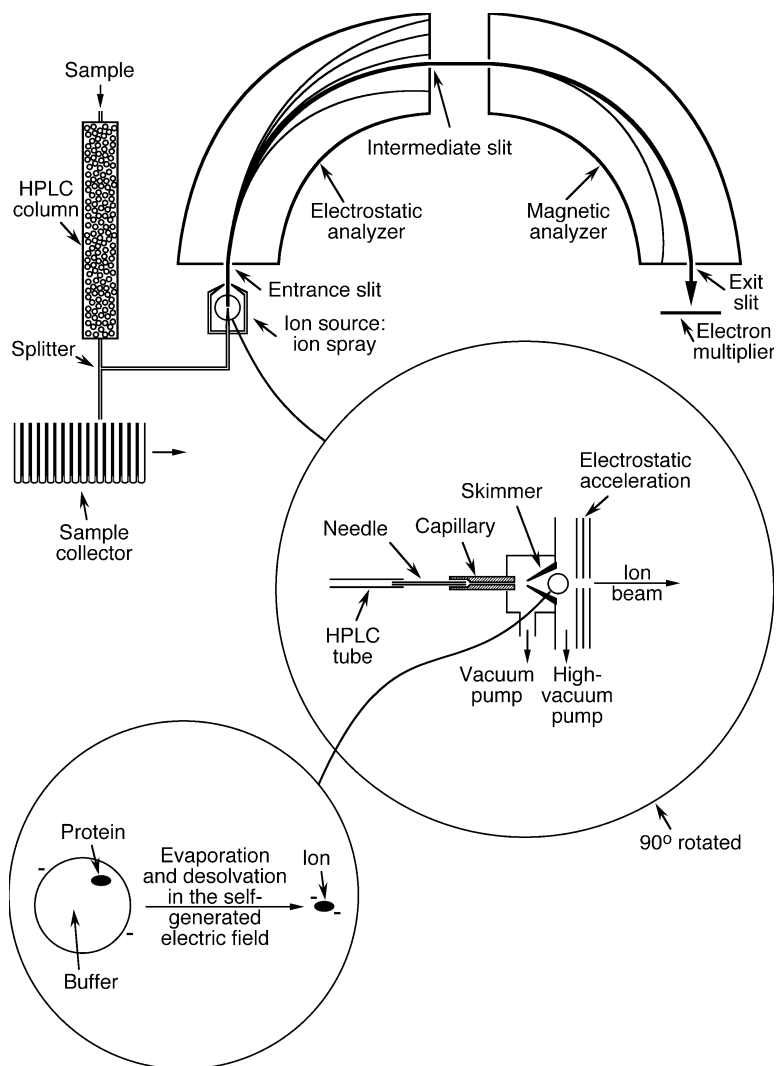


**Fig. 3.15** Double sector MS in combination with HPLC

combination of mass spectrometry with chromatographic methods (e.g., Fig. 3.17). The resolution in two dimensions greatly enhances the analyzability of complex mixtures with a large number of components. For example, ion exchange chromatography on a crude cell extract with a resolution of 100 combined with mass spectrometry with a resolution of 10,000 can result in a total resolution of almost 1,000,000 for small and medium-sized soluble cellular proteins for which both methods are often largely independent from each other.

Buffer interference which is occasionally observed in MS can usually be prevented by increasing the sample concentration, decreasing the buffer concentration, or changing the buffer (Fig. 3.19).

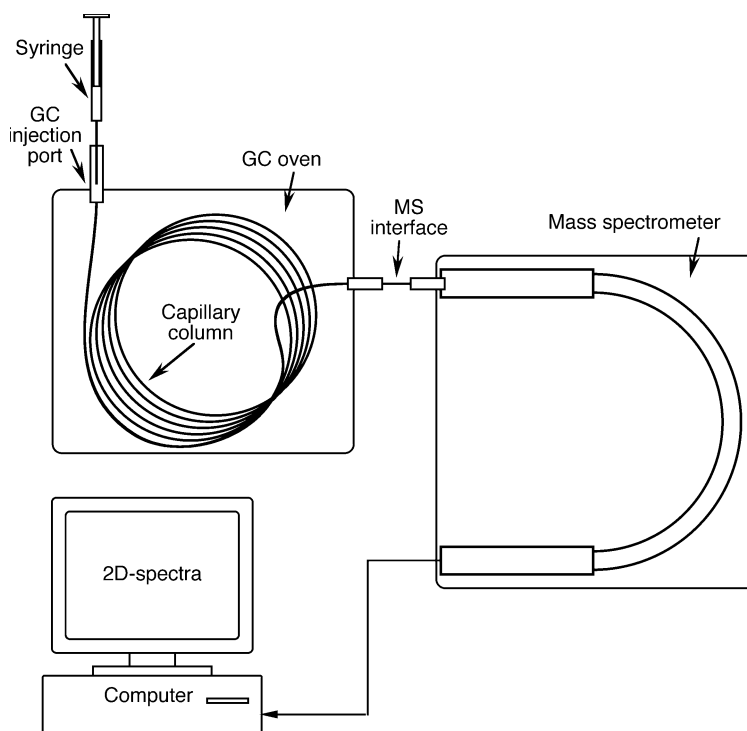


**Fig. 3.16** GC/MS. The combination of mass spectrometry with gas chromatography can greatly enhance the resolution of complex samples

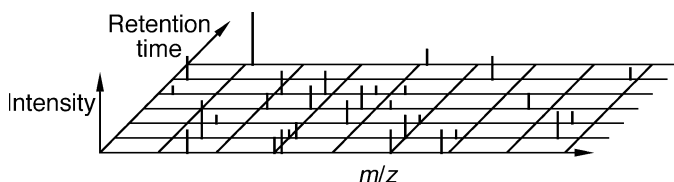


**Fig. 3.17** Example of a two-dimensional GC/MS spectrum

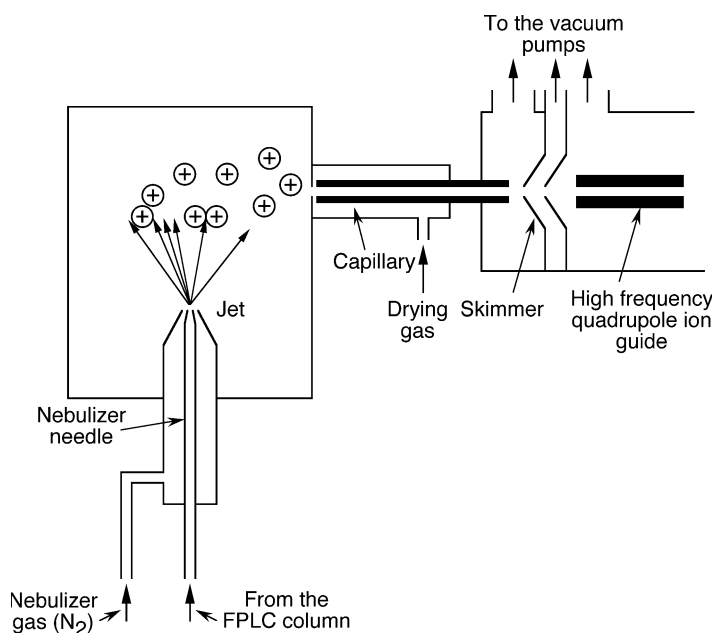


**Fig. 3.18** FPLC/MS connector. In several stages the solvent is removed from the analyte solution by application of dry nitrogen and vacuum. The quadrupole ion guide leads the ions to the mass analyzer of the mass spectrometer

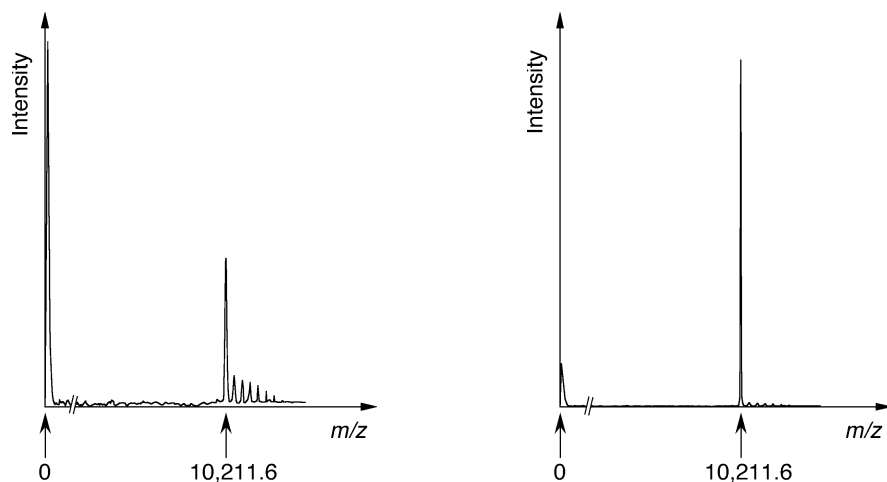


**Fig. 3.19** Mass spectrogram of barstar, the 89-residue inhibitor of the ribonuclease barnase (Nölting et al., 1995, 1997a). *Left:* a number of side-peaks indicate the binding of buffer ions to the highly charged protein. *Right:* a measurement with a lower buffer concentration and higher protein concentration at a pH closer to the pI of the protein yields a cleaner mass spectrogram

### 3.2 Biophysical applications

A considerable interest in the fast point detection of toxic and non-toxic biological materials, such as certain bacterial strains, viruses, and proteins led to the development of portable mass-spectrometric biological detectors (e.g., Figs. 3.20–3.27;

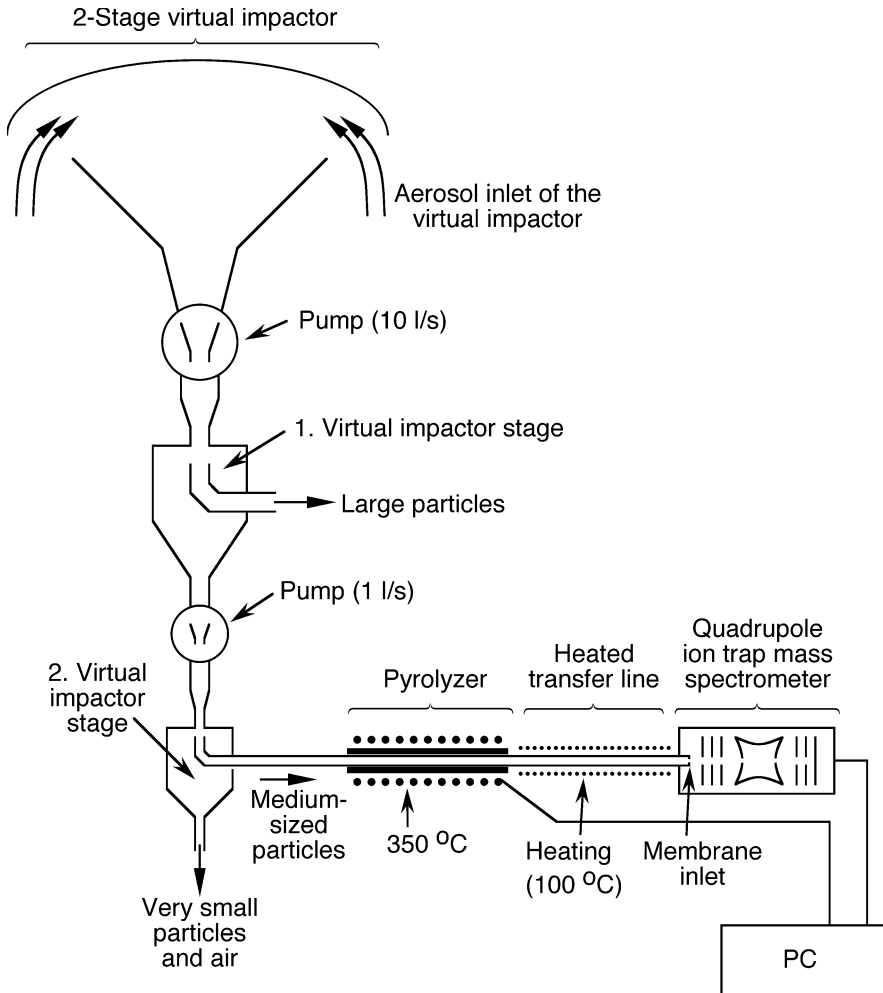


**Fig. 3.20** Mass-spectrometric detector of biological agents, comprising a virtual impactor, a pyrolyzer, and a mass spectrometer: The two-stage virtual impactor selects particles of a certain size range, e.g., 1–10  $\mu\text{m}$  (see also Fig. 3.21). These particles are then decomposed by pyrolysis (see Fig. 3.22) and analyzed by an ion trap mass spectrometer (see Figs. 3.24–3.27). For a similar design see the CBMS (chemical-biological mass spectrometer) from Bruker Daltonik, Bremen, Germany

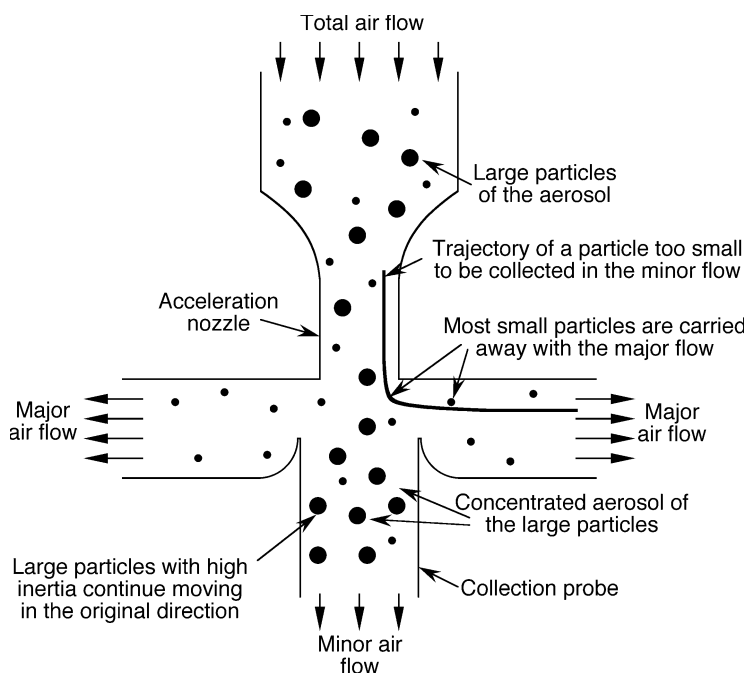


**Fig. 3.21** Principle of operation of a single-stage virtual impactor. The device splits the total flow of the aerosol into the minor and the major flow. Because the direction of the major air flow is perpendicular to the original direction of air flow, only particles with sizes smaller than the cut-off size can enter the major flow. In contrast, all large particles with a large inertia remain in almost the original direction of flow and join the minor flow containing also some of the small particles (Marple and Chein, 1980; Marple et al., 1998)

Williams et al., 2002). The sensitivity of some of these detectors is better than 1 biological agent particle per liter of air at a detection time of less than 3 minutes.

Further important biophysical applications of MS are the detection of mutations in DNA and DNA sequencing (e.g., Köster, 2001a, 2001b; Hung et al., 2002; Fig. 3.28), detection of mutations and post-translational modifications of recombinant proteins (e.g., Lee et al., 2002a; Sect. 9.1.2 in Nölting, 2005; Fig. 3.29), diagnosis of diseases (e.g., Anderson et al., 2002), protein identification (e.g., Aitken and Learmonth, 2002; and Chap. 9), protein purity control (e.g., Stephenson et al., 2002), peptide sequencing (e.g., Shimonishi et al., 1981; Katakuse et al., 1982; Chen et al., 2002a; Nemeth-Cawley and Rouse, 2002; Shevchenko et al., 2002; Stoeva et al., 2002; Figs. 3.30 and 3.31), proteome analysis (e.g., Giffin et al., 2001; Nyman, 2001; Kersten et al., 2002; Lim et al., 2002; and Chap. 9), protein folding investigations (e.g., Birolo et al., 2002; Canet et al., 2002), protein conformational studies (e.g., Favier et al., 2002; Grandori et al., 2002), protein-protein interaction comparisons (e.g., Powell et al., 2002; Zal et al., 2002), and the search for extraterrestrial life (e.g., Fig. 3.32; Schwartz et al., 1995).

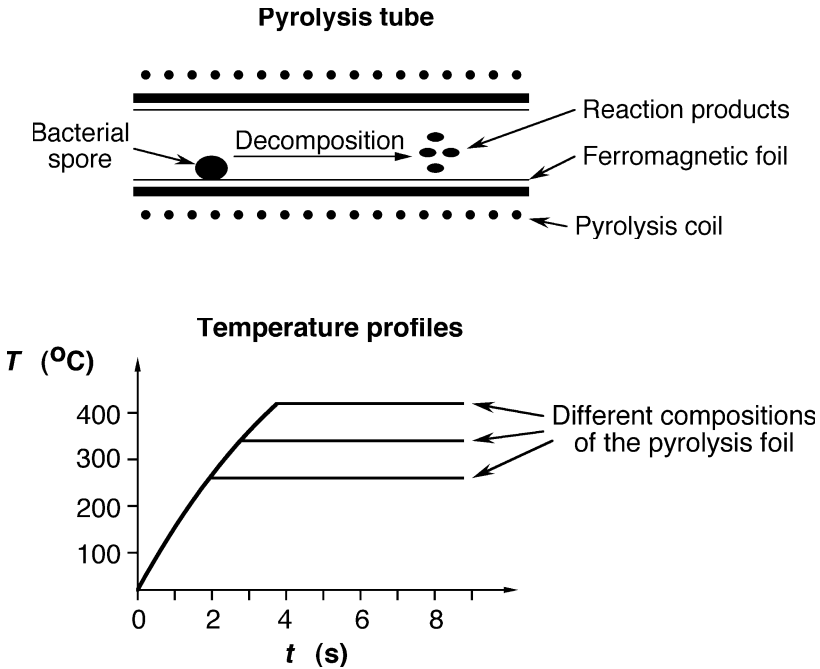


**Fig. 3.22** Principle of operation of pyrolysis: The pyrolysis tube is loaded sequentially and a radio-frequency current passed through the pyrolysis coil. The current rapidly heats the ferromagnetic foil up to the Curie point where the foil reversibly ceases to exhibit ferromagnetic properties and further heating stops. Suitable ferromagnetic materials are, e.g., iron-nickel alloys. Pyrolysates generated in vacuum are then transferred to the mass spectrometer. The pyrolysis mass spectrometry (PyMS) method (Aries et al., 1986; Berkeley et al., 1990; Goodacre, 1994; Freeman et al., 1995; Goodacre and Kell, 1996) is particularly useful for the detection and analysis of biological agents

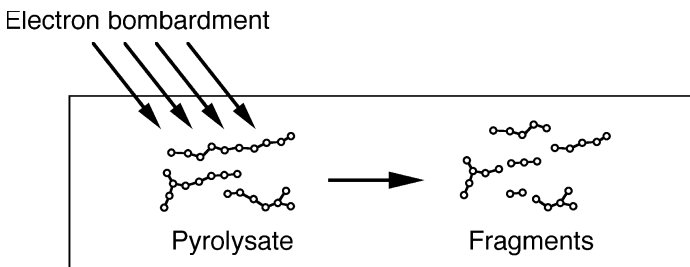


**Fig. 3.23** Fragmentation of the pyrolysate by electron bombardment, typically in the energy region around 25 eV, further increases the information content concerning the nature of the biological agent under investigation (see, e.g., Ikarashi et al., 1991)

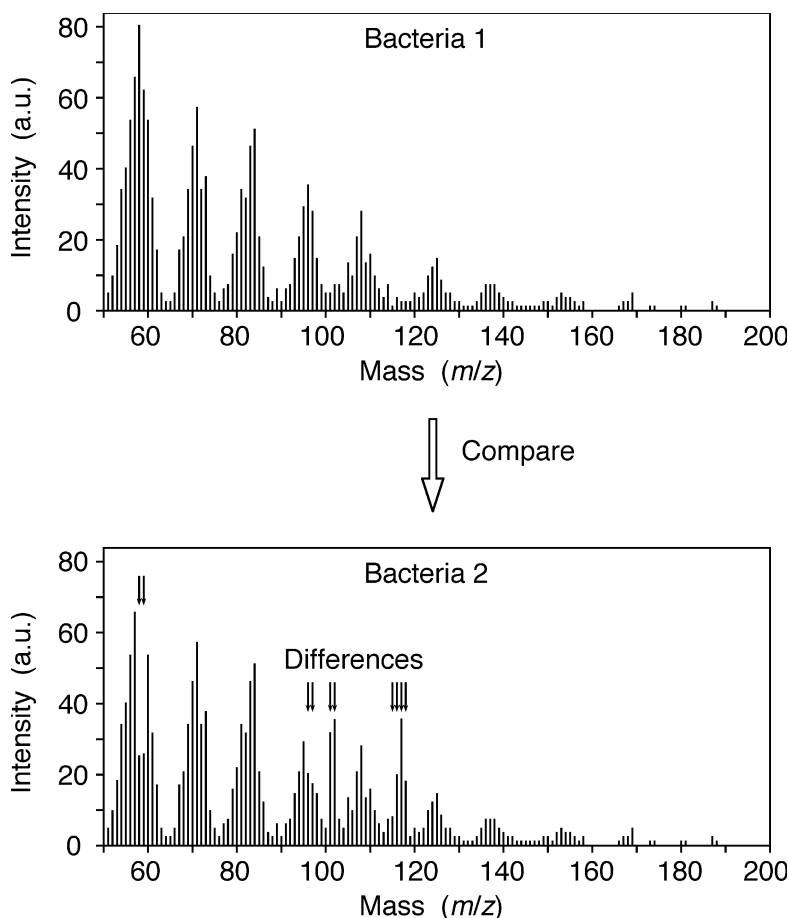


**Fig. 3.24** Detection of biological contamination and differentiation between different biological agents by comparison of the mass spectra of the pyrolysate with  $m/z$  in the range 50–200 (see, e.g., Goodacre, 1994; Goodacre and Kell, 1996)

Especially for the analysis of highly complex biological systems, such as bacterial spores, the combination pyrolysis-MS (PyMS) is extraordinarily useful. In this method the sample is partially decomposed in its components prior to mass-spectrometric analysis. The mass spectra of pyrolyzed biological systems may contain more than 100 lines, enabling a very sensitive differentiation of different samples. PyMS is used for the detection of bacteria, bacterial spores and viruses and the differentiation between different species of bacteria and viruses (Freeman et al., 1990, 1997; Snyder et al., 1990, 2001; Sisson et al., 1991; Sultana et al., 1995; Goodfellow et al., 1997; Helyer et al., 1997; Leaves et al., 1997; Magee et al., 1997; Timmins and Goodacre, 1997; Taylor et al., 1998; Barshick et al., 1999;

Goodacre et al., 2000; Tripathi et al., 2001), for the analysis of forensic samples and the personal identification of humans (Ishizawa and Misawa, 1990; Kintz et al., 1995; Armitage et al., 2001; Sato et al., 2001), and for biotechnological applications (Goodacre and Kell, 1996). PyMS spectra may be analyzed by using neuronal networks (Fig. 3.26; Goodacre et al., 1996, 1998a, 1998b; Nilsson et al., 1996; Kenyon et al., 1997). Ion trap mass spectrometers are particularly suitable for the pyrolysis-MS identification of biological agents since they can directly measure multiple fragmentation (Fig. 3.27).

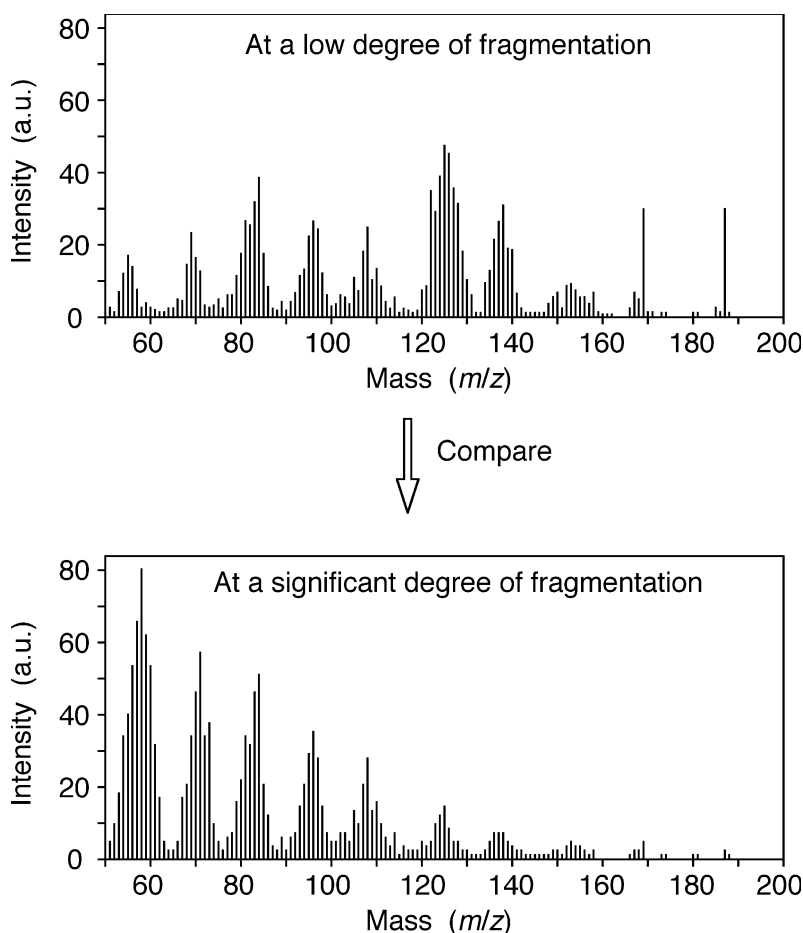


**Fig. 3.25** Detection of biological contamination and differentiation between different biological agents by comparison the mass spectra of the pyrolysate with  $m/z$  in the range 50–200 at different degrees of fragmentation. The fragmentation is achieved, e.g., by collision with helium atoms in the cavity of an ion trap MS (see also Fig. 3.27)



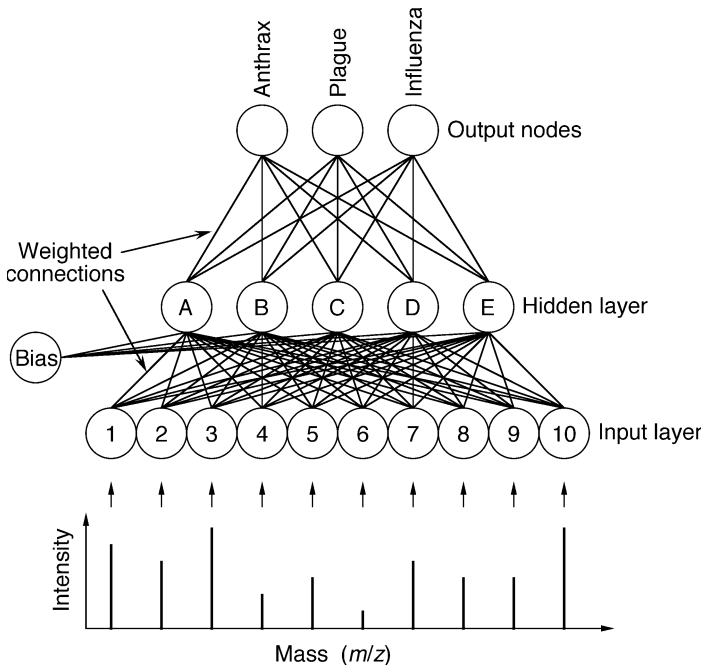


**Fig. 3.26** Example of a neuronal network for the analysis of PyMS spectra (Kenyon et al., 1997; Goodacre et al., 1998a, 1998b). In this simplified example the network consists of only 10 input, 5 hidden, 3 output nodes, a bias, and weighted connections. The actual number of nodes in the PyMS input layer is usually equal to 150 (one for each  $m/z$  from 51 to 200). The hidden layer may actually contain 8–20 nodes. Preferentially the weights of the connections and the bias are set by supervised learning using the hazardous substances to be detected or simulants of these hazardous substances

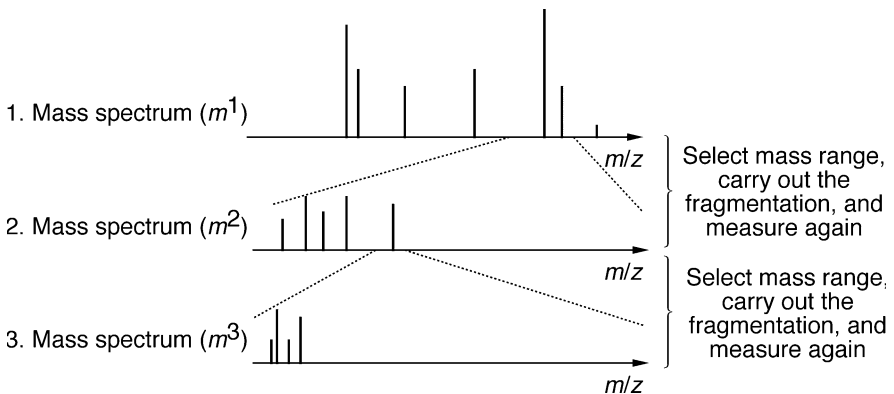


**Fig. 3.27** Example of mass spectrometry with multiple fragmentation ( $m^3$ ) in an ion trap mass spectrometer

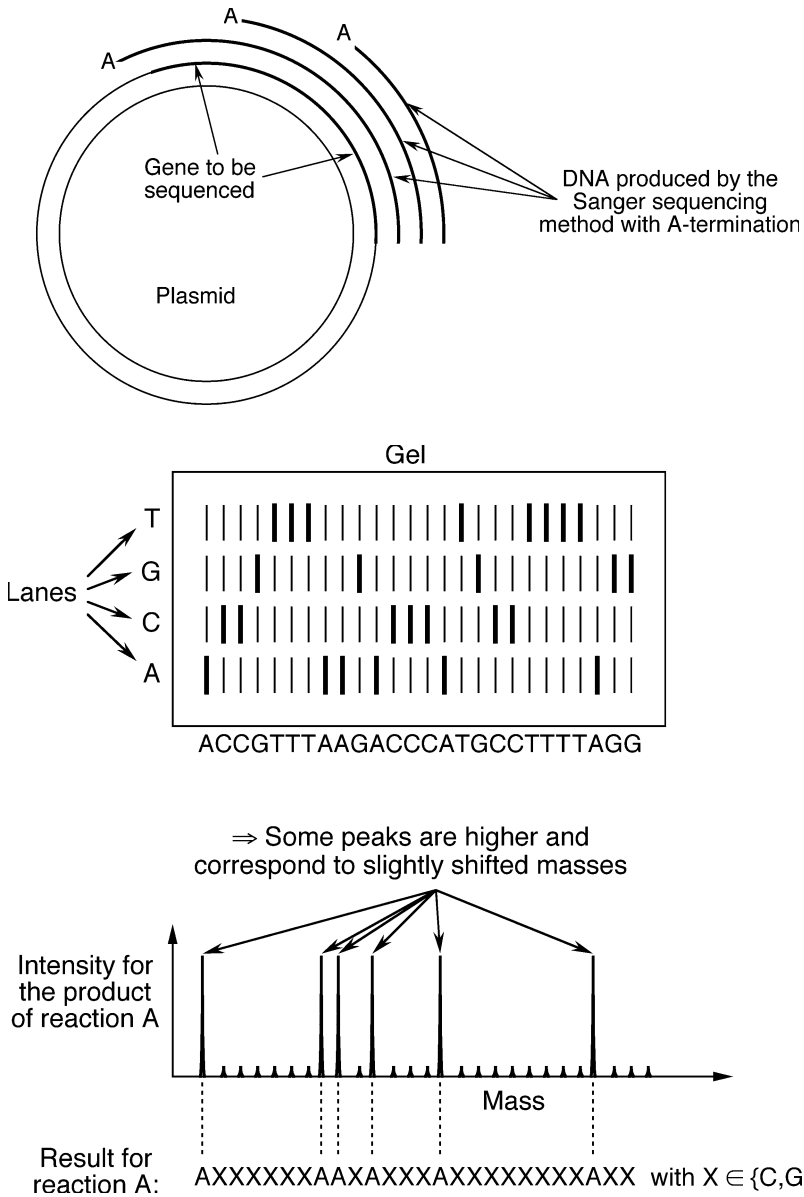


**Fig. 3.28** DNA sequencing with the Sanger dideoxynucleotide termination method (Sanger et al., 1977; Sanger, 1988) and mass-spectrometric detection. *Top*: amplification of the template DNA with termination (only one of the four reactions is shown). *Middle*: for comparison to the mass-spectrometric method: conventional analysis of the reaction products with polyacrylamide gel electrophoresis. *Bottom*: analysis of the products of reaction A by mass spectrometry: the pattern of mass peaks shows the positions of adenine (A) in the sequence

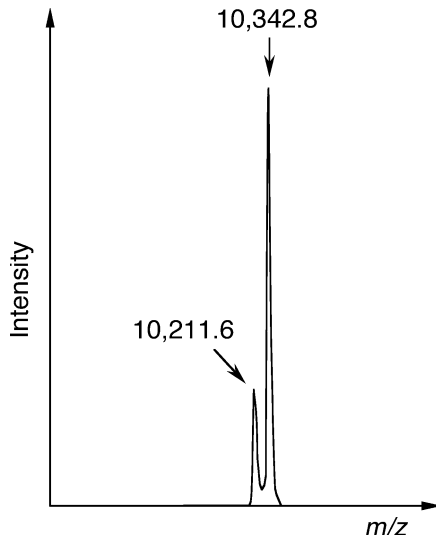


**Fig. 3.29** Mass spectrogram of the 10,212-Da protein barstar. This protein preparation contains a fraction with a molecular weight 131 Da higher than expected. This is due to an N-terminal methionine which is not properly cleaved after protein synthesis

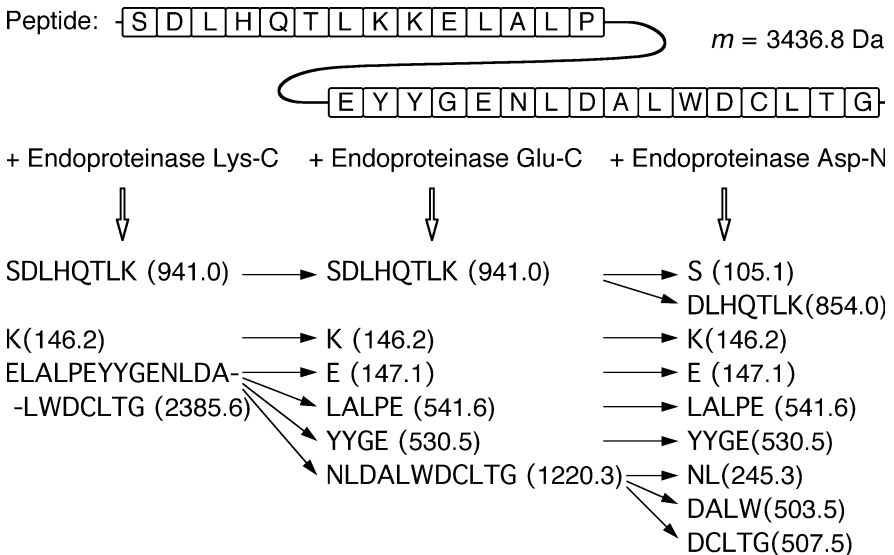


**Fig. 3.30** Sequencing of the peptide SDLHQLTKKELALPEYYGENLDALWDCLTG by proteolytic digestion and mass spectrometry. This peptide corresponds to the helix<sub>1</sub>-helix<sub>2</sub> peptide of the protein barstar (Nölting et al., 1997a). In this example with only three proteases, only some parts of the peptide sequence can unambiguously be identified

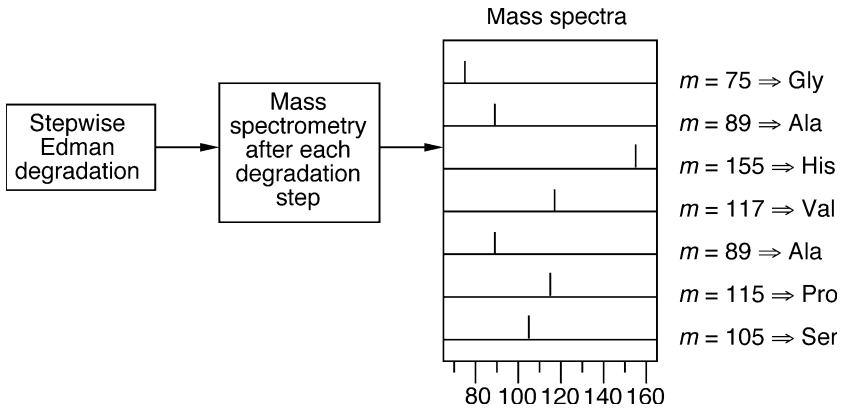


**Fig. 3.31** Peptide sequencing using Edman degradation and mass spectrometry (Shimomishi et al., 1981; Katakuse et al., 1982): reaction products of sequential degradation are mass-spectrometrically identified

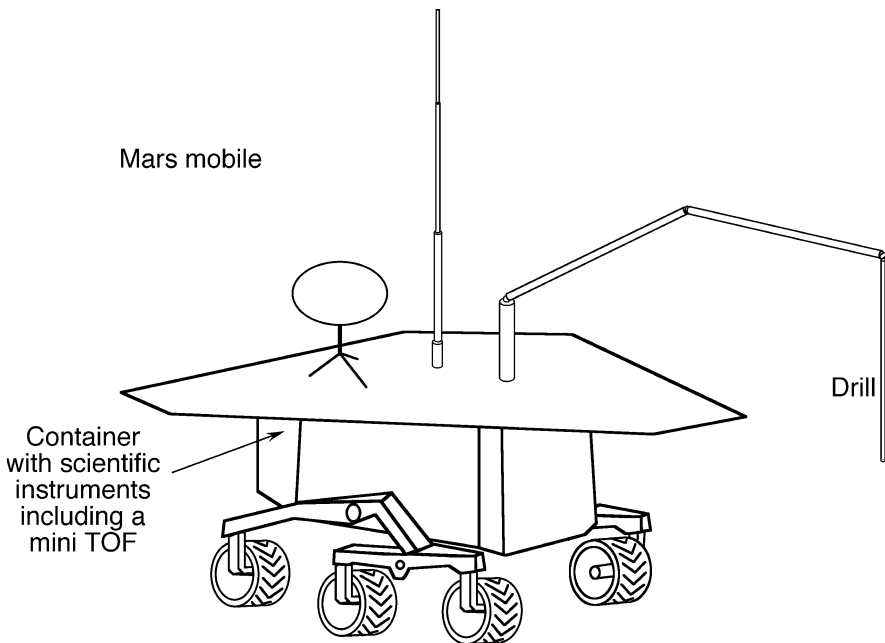


**Fig. 3.32** NASA plans to send rovers outfitted with MS to Mars. This sketch illustrates a mobile with mini-TOF searching for extraterrestrial life. Already now mass-spectrometry is utilized to search for extraterrestrial bacteria in meteors

## 4 X-ray structural analysis

### 4.1 Fourier transform and X-ray crystallography

X-ray crystallography is the method with the highest currently available resolution power for structures of large macromolecules and macromolecular complexes. Since the technique of Fourier transform is central to this method, we first deal with some essential aspects of this technique:

#### 4.1.1 Fourier transform

Mathematically the Fourier transform and inverse Fourier transform convert between two domains (spaces), e.g., the domain  $\mathbf{r}$  (e.g., space or time) and the domain  $\mathbf{k}$  (e.g., momentum or frequency):

$$\text{Fourier transform:} \quad F(\mathbf{k}) = (2\pi)^{-0.5} \int_{-\infty}^{\infty} f(\mathbf{r}) e^{-2\pi i \mathbf{r} \cdot \mathbf{k}} d\mathbf{r} \quad (4.1)$$

$$\text{Inverse Fourier transform:} \quad f(\mathbf{r}) = (2\pi)^{-0.5} \int_{-\infty}^{\infty} F(\mathbf{k}) e^{2\pi i \mathbf{r} \cdot \mathbf{k}} d\mathbf{k} \quad (4.2)$$

Fig. 4.1 illustrates a one-dimensional Fourier transform: (b) Represents the decomposition of the signal from (a). This decomposition was calculated from the Fourier transform (c). The inverse transform of (c) yields back exactly (a). (d) Is the inverse Fourier transform of the signal of (c) with all phases set to zero instead of using the correct phases. The comparison of (d) with (a) illustrates the importance of the phases in Fourier transform: in order to be able to correctly obtain back the original signal by inverse Fourier transform, both the amplitudes and the phases have to be known.

Three examples in Figs. 4.2–4.4 demonstrate the method of two-dimensional Fourier transform: Fig. 4.2b represents the Fourier transform of the hexagonal arrangement of peaks of Fig. 4.2a. In Fig. 4.3a some of Fourier components with low amplitudes are set to zero, and yet the inverse Fourier transform (Fig. 4.3b) shows that essentially all information is still preserved. Fourier transforming a noisy object, then substituting certain low-amplitude parts of the Fourier transform by zeros, and then inverse-transforming the modified Fourier transform, is an efficient method for noise reduction. Figs. 4.4a and 4.4b show the result when using only a small slice of the Fourier transform for the calculation of the inverse

Fourier transform: significant distortions are observed along the coordinate for which too few Fourier components were utilized for reconstruction.

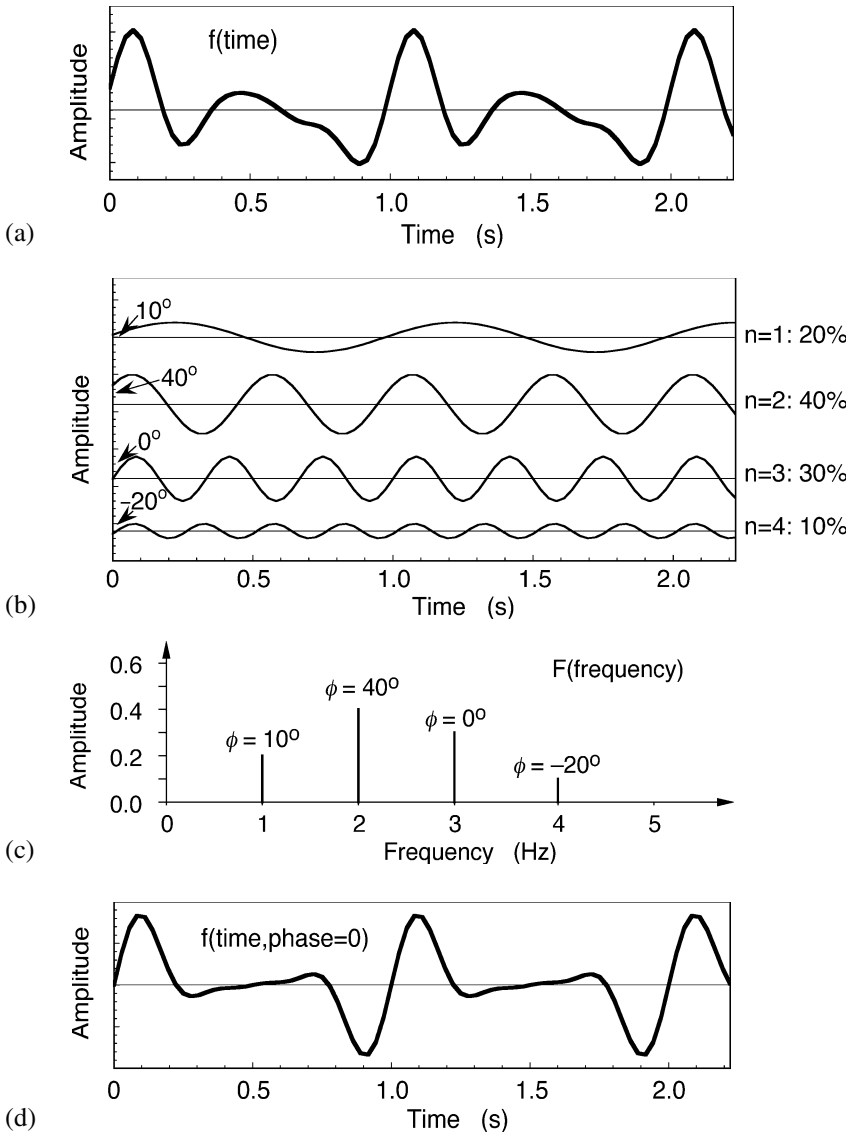


**Fig. 4.1** Example for the effect of the loss of phase information on the inverse Fourier transform: With the correct phases, the four frequency components (b) add to the sum shown in (a). However, when adding the four components with the wrong phase 0, we obtain the wrong sum (d). (c) Represents the Fourier transform of (a). In (a), (b), (c) only a fraction of the function is shown; the complete function is periodical in  $(-\infty, \infty)$

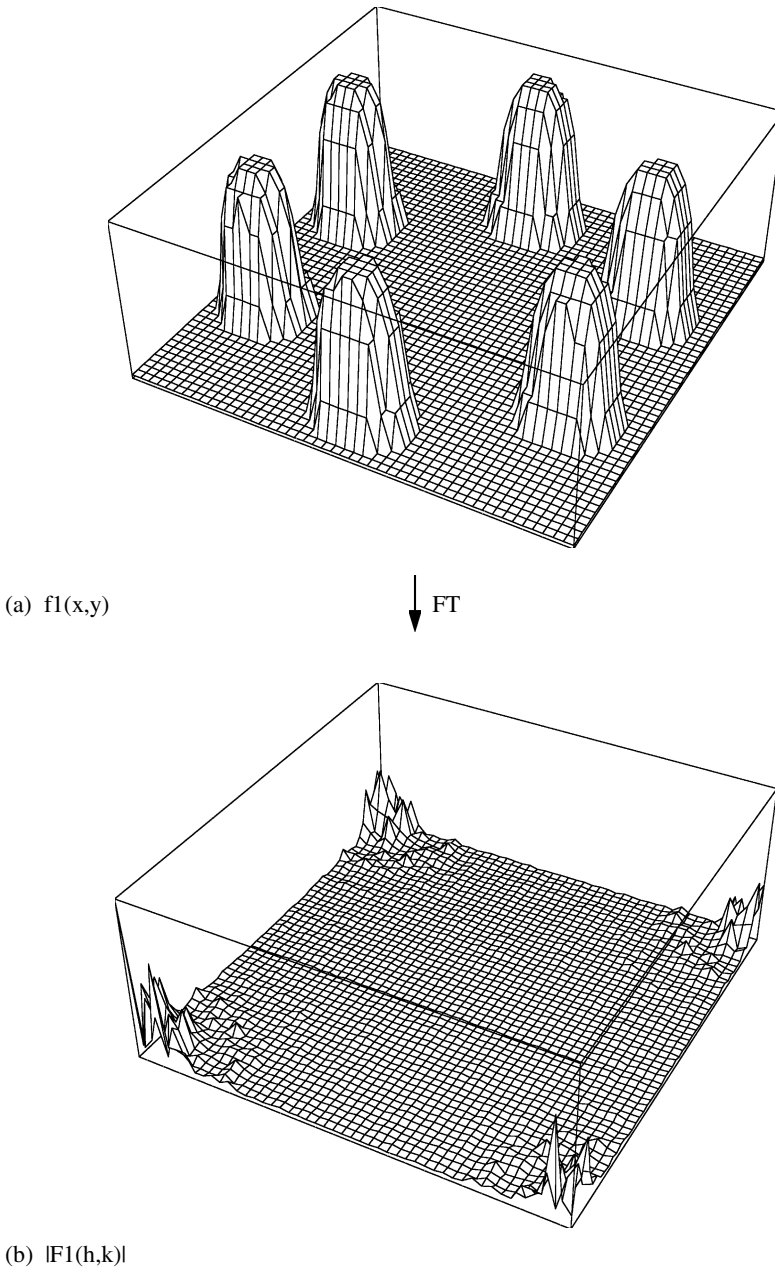


**Fig. 4.2** Example of a two-dimensional Fourier transform: **(b)** is the Fourier transform of **(a)**. Only the absolute of the function is drawn in **(b)**. However we must keep in mind that the complete function contains an amplitude and phase for each coordinate point (compare with Fig. 4.1)

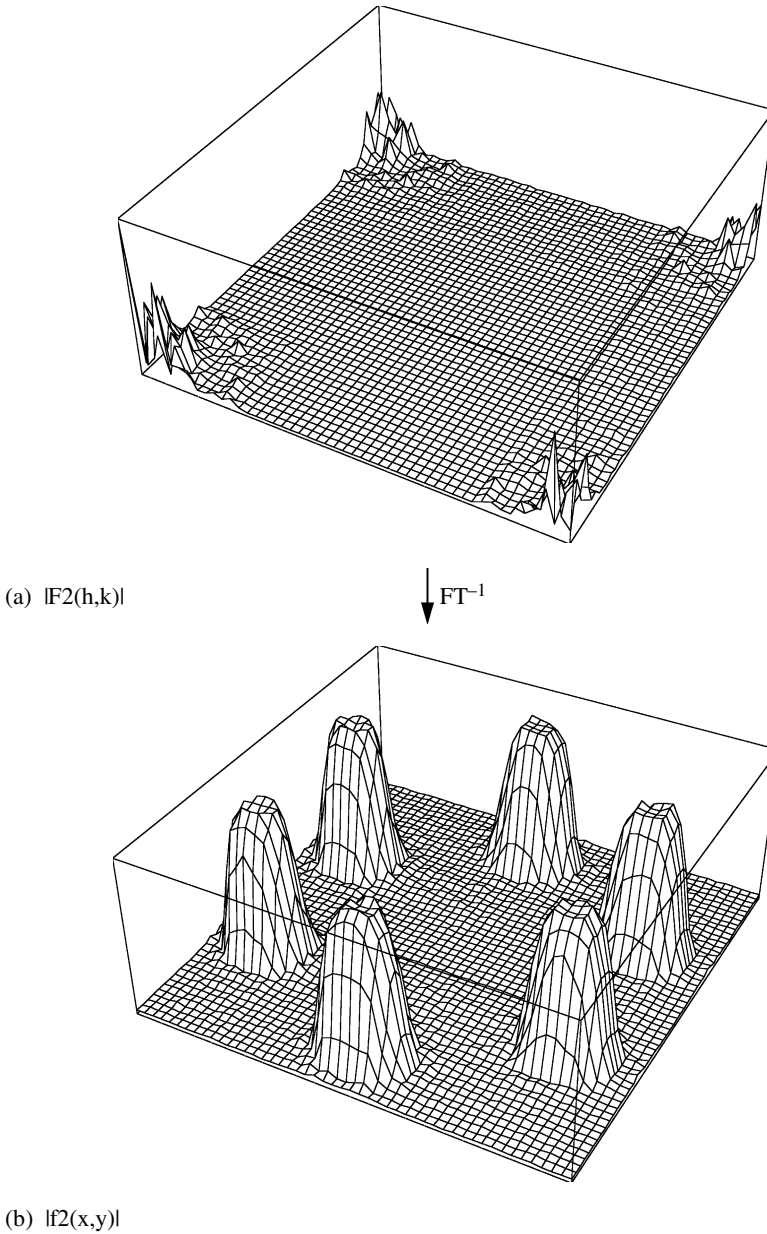


**Fig. 4.3** Example of a two-dimensional Fourier transform: In the corners, **(a)** is identical to Fig. 4.2b, but has the components with low amplitude in the middle of the coordinate space set to zero. **(b)** is the inverse Fourier transform of **(a)**. **(b)** is found to be almost identical to Fig. 4.2a showing that the deleted low-amplitude components did not contain much information. Note that in this figure only the absolutes of the functions are drawn



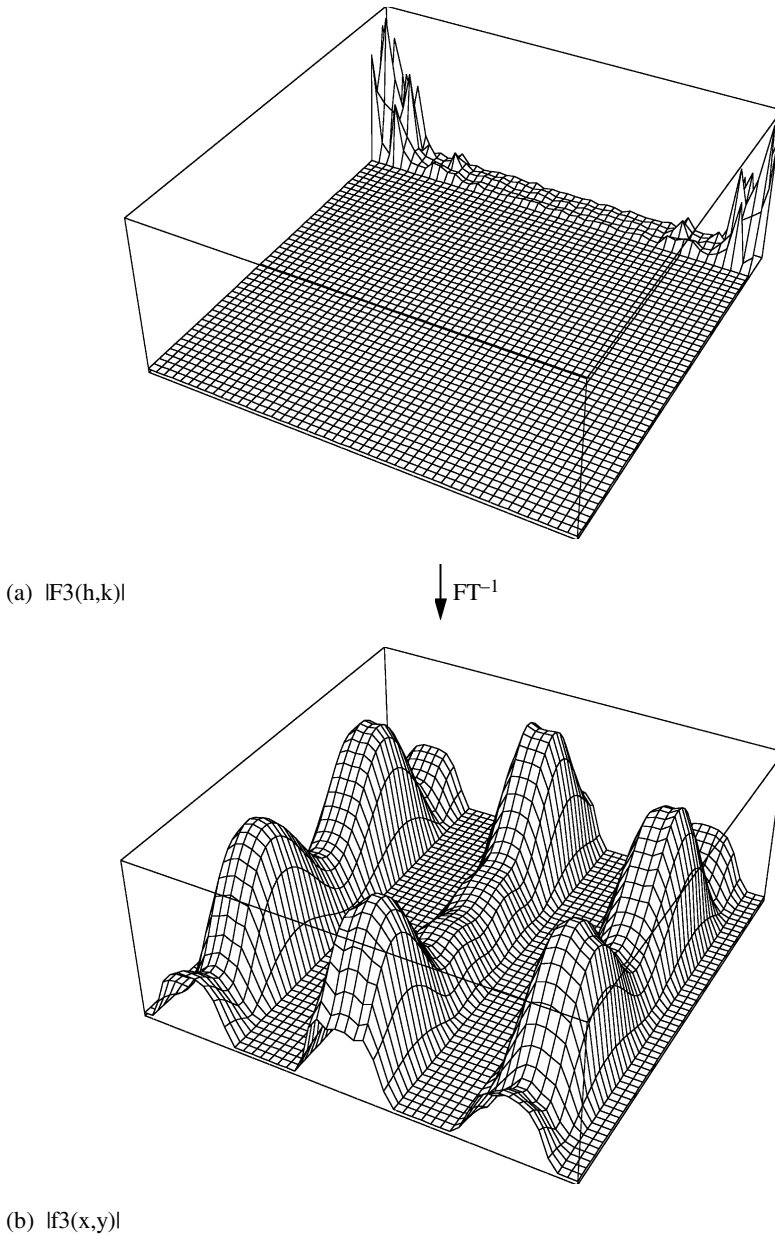


**Fig. 4.4** Example of a two-dimensional Fourier transform: **(a)** Is a thin slice of the function in Fig. 4.2b plus a thick slice with all components set to zero. **(b)** Represents the inverse Fourier transform of **(a)**: some features of the function in Fig. 4.2a are still preserved in **(b)**, but much information is lost. Note that in this figure only the absolutes of the functions are drawn

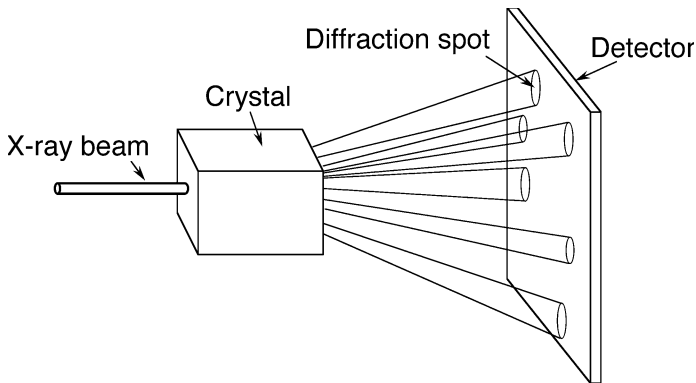


**Fig. 4.5** Example of a diffraction experiment on a crystal. The X-ray diffraction pattern of the crystal is recorded with an area detector. The pattern consists of a large number of discrete spots

Why is the Fourier transform so important for X-ray crystallography? This is because the diffraction pattern of a crystal (Fig. 4.5) or any other physical object is the Fourier transform of its structure (see also later Fig. 4.10).

To understand why the diffraction pattern of a physical object is its Fourier transform let us consider the diffraction of a wave by a single object (Fig. 4.6) and two point-sized objects separated by  $\mathbf{r}$  (Fig. 4.7): the scattering vector,  $\mathbf{S}$ , is defined as  $\mathbf{S} = \mathbf{s}/\lambda - \mathbf{s}_0/\lambda$ , where  $\mathbf{s}$ ,  $\mathbf{s}_0$ , and  $\lambda$ , are the vector of the incident wave, vector of the diffracted wave, and wavelength, respectively (Fig. 4.6). Then the phase difference in units of wavelengths between the two waves in Fig. 4.7 is given by:  $\mathbf{r}\mathbf{s}/\lambda - \mathbf{r}\mathbf{s}_0/\lambda = \mathbf{r}\mathbf{S}$ . Constructive interference of the two waves occurs in case of  $\mathbf{r}\mathbf{S} = 0, \pm 1, \pm 2, \dots$ ; destructive interference, i.e., extinction, is observed at  $\mathbf{r}\mathbf{S} = \pm 1/2, \pm 3/2, \dots$ . The diffraction pattern,  $F(\mathbf{S})$  of the two points is then given by  $F(\mathbf{S}) = e^{-2\pi i \mathbf{r}\mathbf{S}}$ , with  $i$  being the imaginary number defined as  $i \equiv \sqrt{-1}$ .

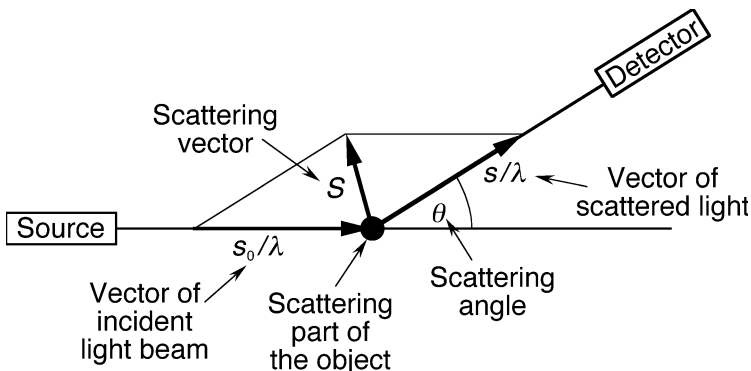


**Fig. 4.6** Diffraction of a wave by a single part of an object

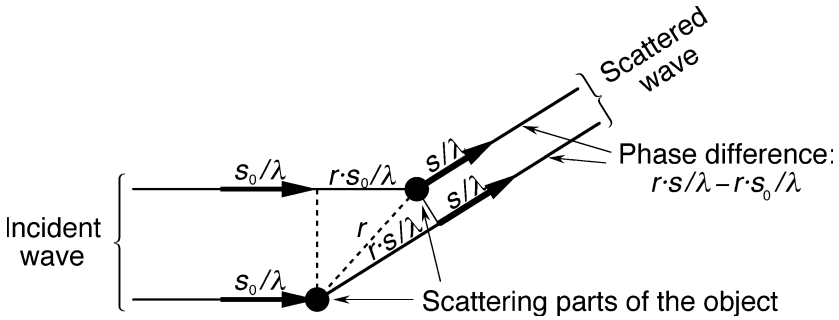


**Fig. 4.7** Diffraction of a wave by two objects of equal scattering power

For a the diffraction,  $F(S)$ , of a macroscopic object consisting of many diffracting points with varying diffraction power,  $\rho(r)$ , we have to integrate all scattered waves:

$$F(S) = \int_{-\infty}^{\infty} \rho(r) e^{-2\pi i r S} dr \tag{4.3}$$

This equation has the form of a Fourier transform (compare with Eq. 4.1). Hence the electron density and structure of a protein can be obtained from the inverse Fourier transform of its diffraction image.

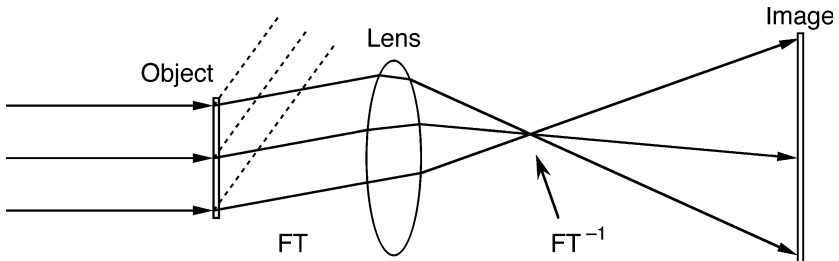


**Fig. 4.8** A lens projecting the image of an object onto a screen performs an inverse Fourier transform of the diffraction pattern of the object

In microscopes the inverse Fourier transform is performed by lenses (Fig. 4.8). Unfortunately, currently there is no X-ray microscope with sufficient resolution and sensitivity. X-ray mirrors do not provide sufficient resolution, and because of radiation damage, we would not obtain a satisfactory resolution for a single protein molecule anyway. That is why we have to record the diffraction pattern of a protein crystal and to calculate the inverse Fourier transform of the diffraction pattern with a computer. Unfortunately, when recording the diffraction pattern of an object with the help of a camera, all phase information is lost. With other

words, we do not record the complete Fourier transform, but only a fraction of it. The consequences of this serious problem were illustrated in Fig. 4.1. Thus, additionally to the recording of the diffraction pattern, one needs a special technique to recover the phase information. The currently most important method to recover phase information in protein crystallography on new structures is the technique of heavy atom replacement (see Sect. 4.1.2.4).

A specifics of the diffraction of macroscopic crystals is that not a continuous diffraction pattern is obtained, but discrete spots. To understand this behavior, consider the structure of a crystal (Fig. 4.9):

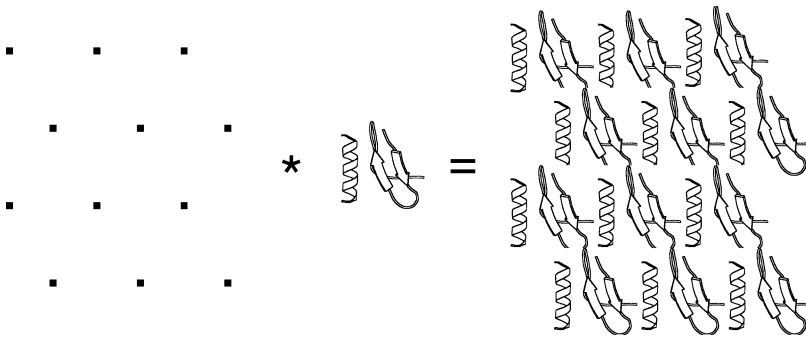


**Fig. 4.9** Mathematically a protein crystal can be described as the convolution of the crystal lattice with the unit cell (one or a few protein molecules)

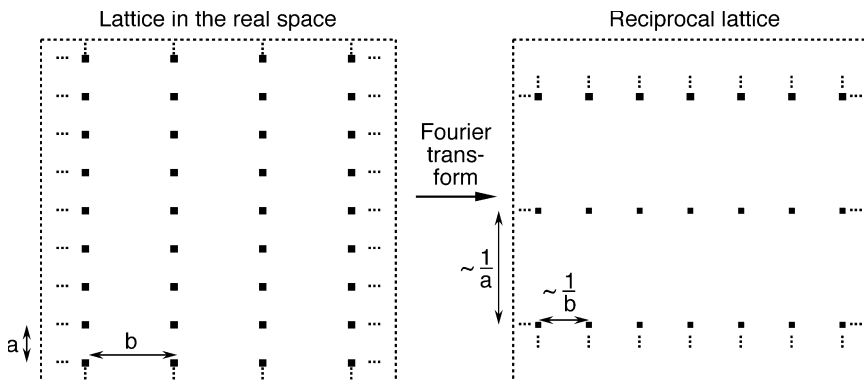


**Fig. 4.10** The Fourier transform of the crystal lattice is the so-called reciprocal lattice. It determines the maximum number and positions of the observed diffraction spots

The protein crystal can be described as the convolution of the crystal lattice with the unit cell (Fig. 4.9): crystal = lattice \* unit cell. The unit cell is the smallest unit from which the crystal can be generated by translations alone. It

usually contains one or several protein molecules. According to the convolution theorem, the Fourier transform, FT, of two convoluted functions  $f_1(\mathbf{r})$  and  $f_2(\mathbf{r})$  is the product of their Fourier transforms:

$$\text{FT}(f_1(\mathbf{r}) * f_2(\mathbf{r})) = \text{FT}(f_1(\mathbf{r})) \cdot \text{FT}(f_2(\mathbf{r})) \quad (4.4)$$

Thus, the diffraction pattern of a protein crystal is the Fourier transform of the unit cell times the Fourier transform of the crystal lattice. The latter is called reciprocal lattice (Fig. 4.10). Since the reciprocal lattice is zero outside its lattice points, the crystal diffraction pattern corresponds to the Fourier transform of the unit cell sampled at the points of the reciprocal lattice.

A second way to explain the occurrence of discrete spots in the diffraction pattern of macroscopic crystals, and to evaluate the information from the intensity of these spots, is to think of the diffraction as a reflection on the X-ray at the lattice planes of the crystal (Fig. 4.11). These lattice planes are described by the Miller indices (Fig. 4.12).

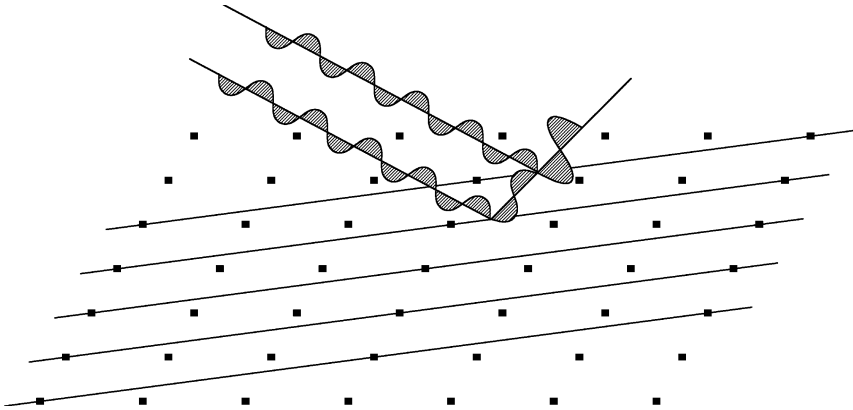


**Fig. 4.11** Reflection of X-rays at the lattice planes of a crystal. Diffraction is viewed as reflection of the X-ray on the lattice planes

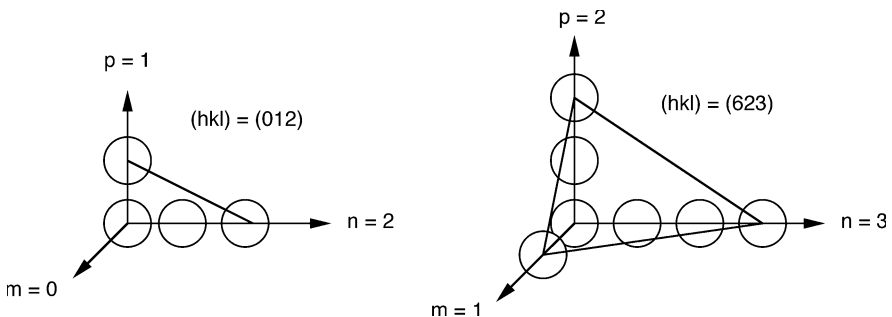


**Fig. 4.12** Example for the nomenclature of Miller indices,  $hkl$ . Miller indices are defined as the smallest integer multiple of the reciprocal axis sections in which  $1/0$  is set to 0

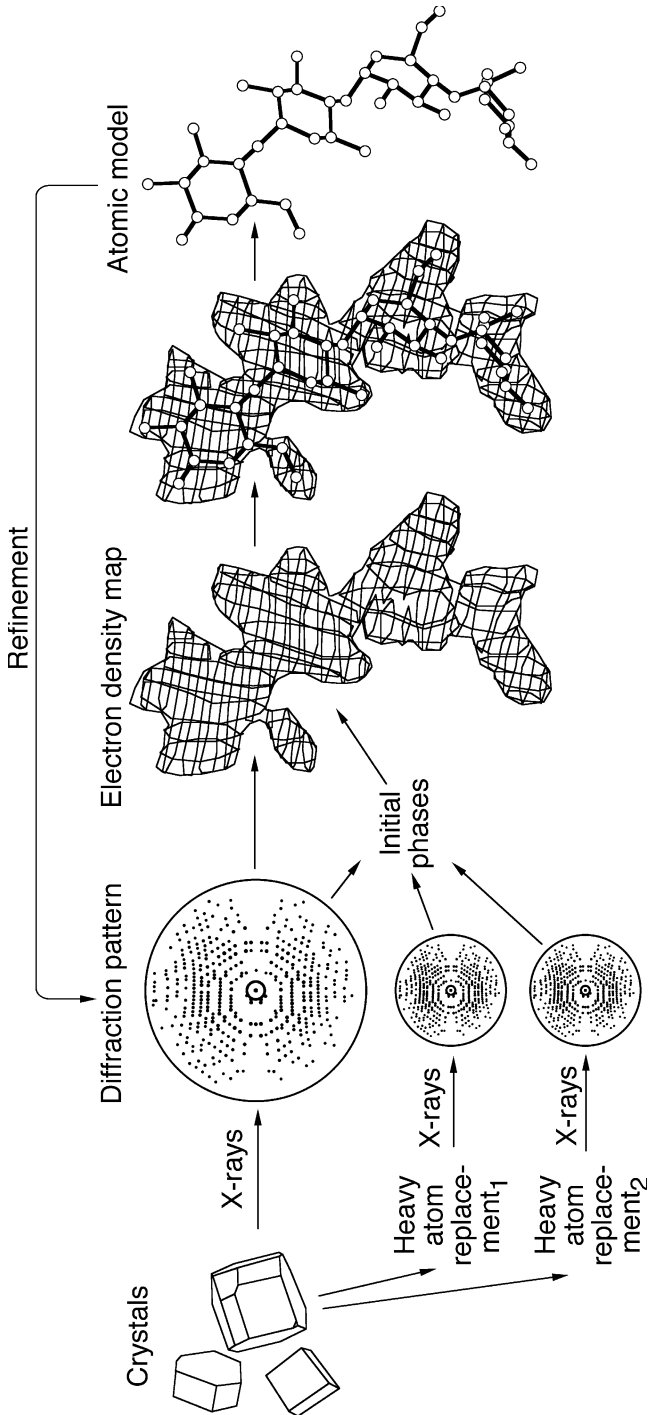


**Fig. 4.13** Overview of X-ray crystallographic analysis of proteins: From the measured diffraction pattern of suitable native and, if necessary, heavy atom replaced crystals, an initial electron density and atomic model is calculated. The initial model is refined, e.g., by modifying it till its calculated diffraction pattern matches the measured pattern.

## 4.1.2 Protein X-ray crystallography

### 4.1.2.1 Overview

In 1934 Bernal and Crowfoot discovered that pepsin crystals give a well-resolved X-ray diffraction pattern (Bernal and Crowfoot, 1934; Bernal, 1939). It took three decades and the development of computers to obtain the first 3-D structures of proteins (Kendrew et al., 1960; Perutz et al., 1960). Many thousands of native protein structures have been solved since then. Examples are found in Figs. 1.6–1.8. A few structure determinations were even made under artificial conditions, e.g., in organic co-solvents (Schmitke et al., 1997, 1998).

### 4.1.2.2 Production of suitable crystals

For X-ray diffraction we must have a single crystal of suitable geometry and size (Fig. 4.13 on the previous page and Figs. 4.14–4.16). Commercial crystal screening kits, containing the most prominent buffers for protein crystallization, may be obtained, e.g., from JenaBioScience (Jena, Germany). Important parameters for coarse-screening and fine-adjustment are protein concentration, salt types and concentrations, pH, type and concentration of surfactants and other additions, temperature, and speed of crystallization.

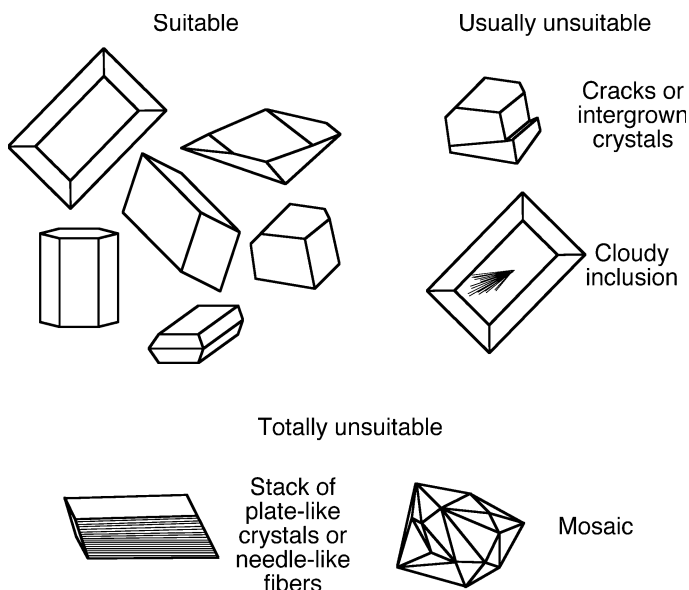


**Fig. 4.14** Suitable protein and virus crystals are transparent and do not have inhomogeneities of color or refractive index. Crystals with cracks, intergrown crystals and crystals with cloudy inclusions are generally unsuitable for X-ray crystallography. Totally unsuitable are stacks of plate-like crystals or needle-like fibers and mosaics

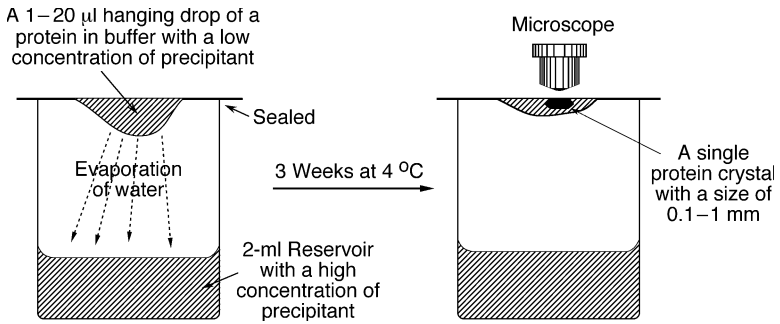


**Fig. 4.15** Hanging drop method. The solvent of a small drop of protein or virus solution attached to a cover slide slowly evaporates partially. At the right conditions, a single crystal of suitable size grows

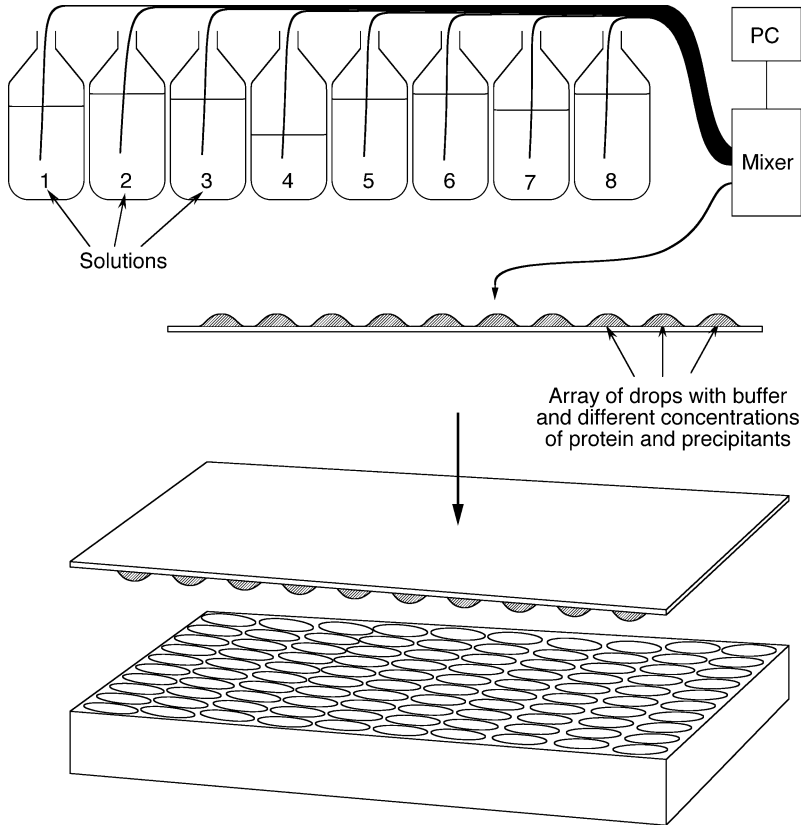


**Fig. 4.16** Crystallization robot for hanging drop crystallization. The computer-controlled mixer draws different solutions from reservoir bottles, mixes them with various ratios, and places the mixtures on a glass plate



One generally starts with a protein concentration of about 2–50 mg ml<sup>-1</sup>. Usually, the protein or virus must not contain a significant amount of contaminants, such as other proteins or viruses, protein or virus fragments, unfolded or misfolded protein, particulate matter, chemical additions unnecessary for stability or solubility. In most cases compact proteins that do not contain floppy ends, such as histidine tags or native unstructured peptides, crystallize better. Suitable crystals have sizes of a few 0.1 mm.

#### 4.1.2.3 Acquisition of the diffraction pattern

For the acquisition of the crystal diffraction pattern (Figs. 4.17–4.19), multi wire area detectors or CCD area detectors (Fig. 4.20) are commonly used. With the example of a linear CCD, Fig. 4.21 illustrates the basic principle of operation of CCDs.

The most common X-ray sources for protein and virus crystallographic analysis are rotating anode generators (Fig. 4.22) with typically 5–25 kW electrical power and synchrotrons (Figs. 4.23 and 4.24). Synchrotrons are comparably expensive, but have a higher brightness enabling shorter measuring times. Reduction of the exposition time often results in a better quality of the diffraction pattern since decomposition of the crystal due to radiation damage is reduced.

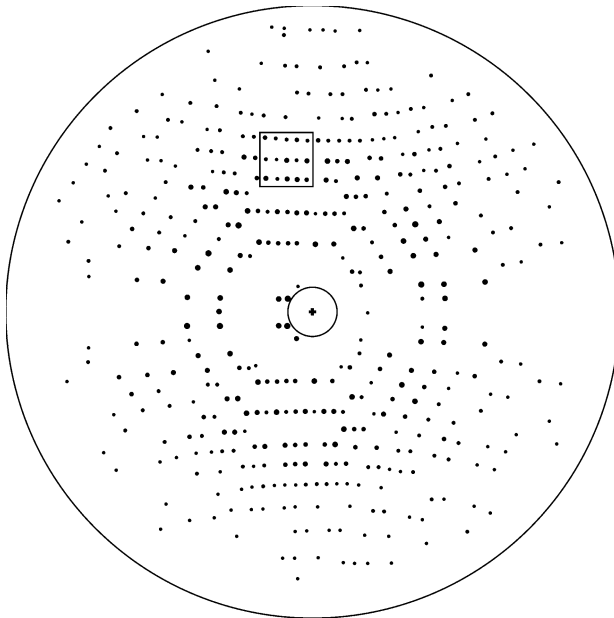


**Fig. 4.17** X-ray diffraction pattern of a protein crystal (Norledge et al., 1996). The highlighted section is referred to in Fig. 4.26

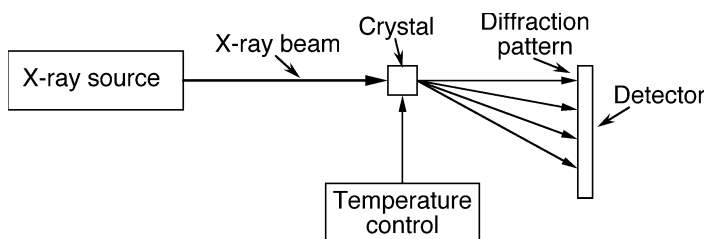


**Fig. 4.18** General setup for the acquisition of the diffraction pattern

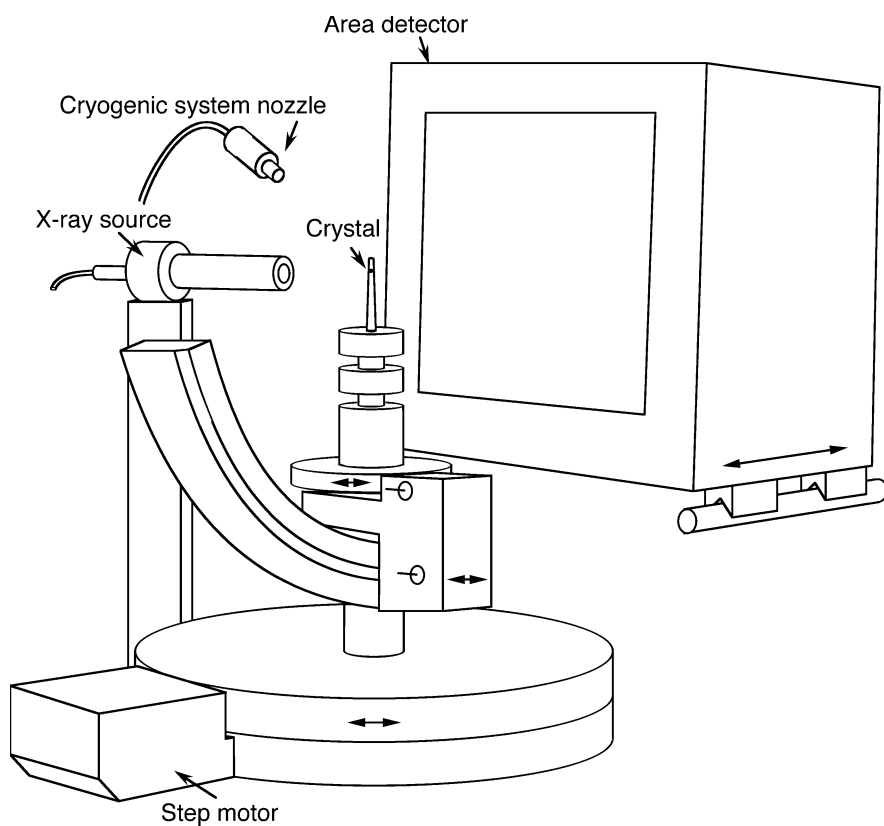


**Fig. 4.19** Setup for acquiring the diffraction pattern with an area detector (see, e.g., area detectors from Rigaku, The Woodlands, TX). The crystal is cooled with nitrogen from the cryogenic system nozzle. Cooling the crystal reduces radiation damage, but somewhat changes the intermolecular distances. Diffraction of the X-rays from the X-ray source by the crystal are recorded with the area detector with typically  $2048 \times 2048$  or  $4096 \times 4096$  pixels (see next figure)

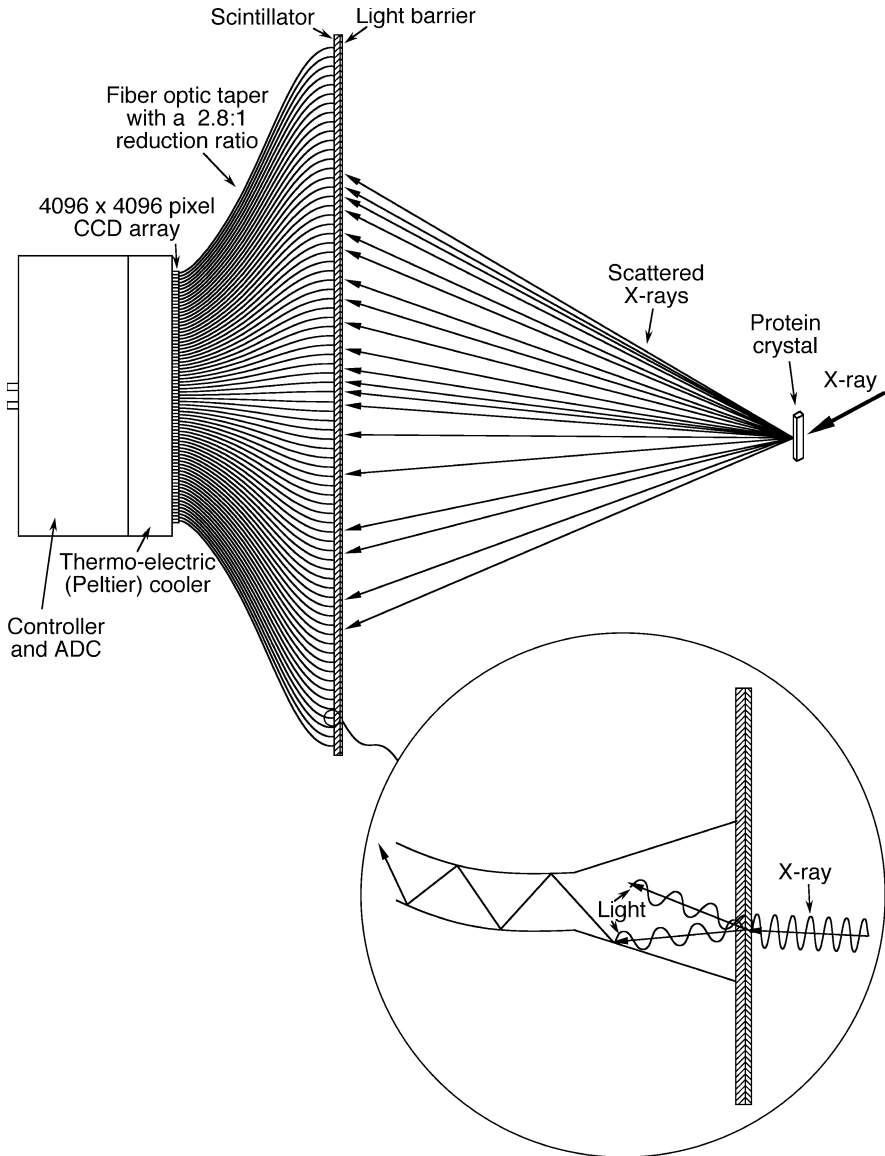


**Fig. 4.20** A CCD area detector used for recording of X-ray diffraction patterns. For reduction of the dark current, this CCD is operated at  $-40\text{ }^{\circ}\text{C}$ , allowing it to detect single photons. The fiber optic taper serves also for blockage of X-rays and thereby prevention of radiation damage to the sensitive CCD array. At a pixel size of  $20\text{ }\mu\text{m} \times 20\text{ }\mu\text{m}$ , the full well capacity is typically several 100,000 electrons per pixel, enabling the necessary high dynamic range

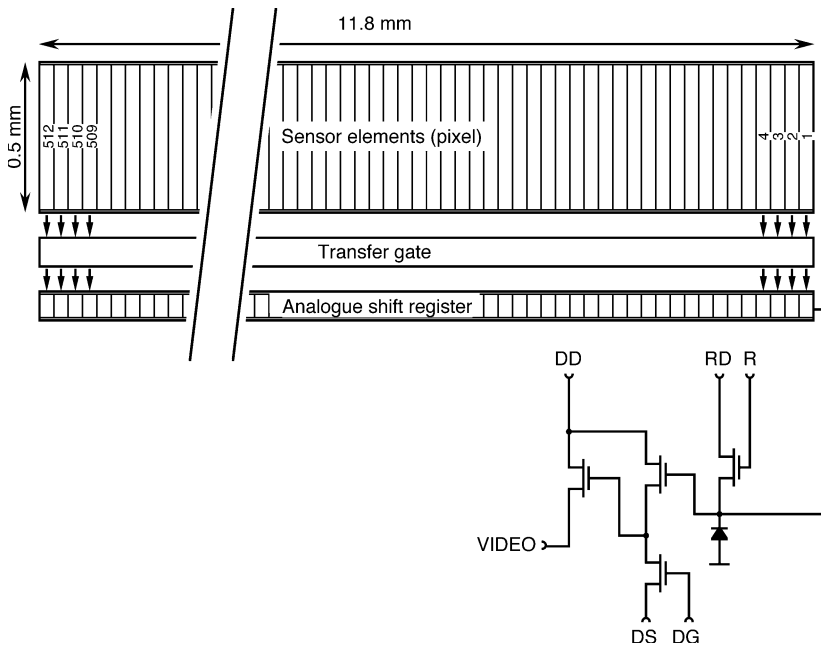


**Fig. 4.21** Linear charge coupled device (CCD). The sensor elements generate electrons by absorption of photons and store the electrons in potential wells. After a certain period of time, the collected electrons are transferred to the analogue shift register and read out. The symbols are: DD, drain of the output amplifier; DS, source of the output amplifier; DG, gate of the output amplifier; RD, drain of the reset transistor; R, clock gate of the reset transistor (Nölting, 1991)

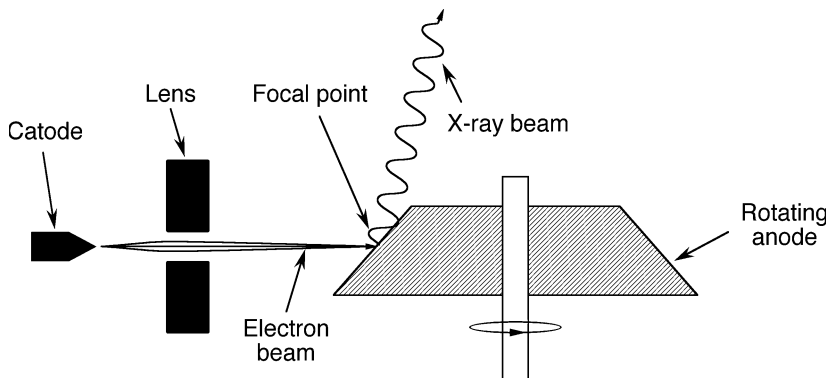


**Fig. 4.22** Rotating anode generator. An electron beam is focussed onto the rotating anode. It knocks out electrons from the inner electron shells of the anode metal. Reoccupation of the vacant shells by electrons from higher level shells involves the emission of X-ray radiation. The interaction of the electron beam with the anode metal generates also a large amount of heat which is quickly dissipated by rotating the anode below the spot of incidence of electrons

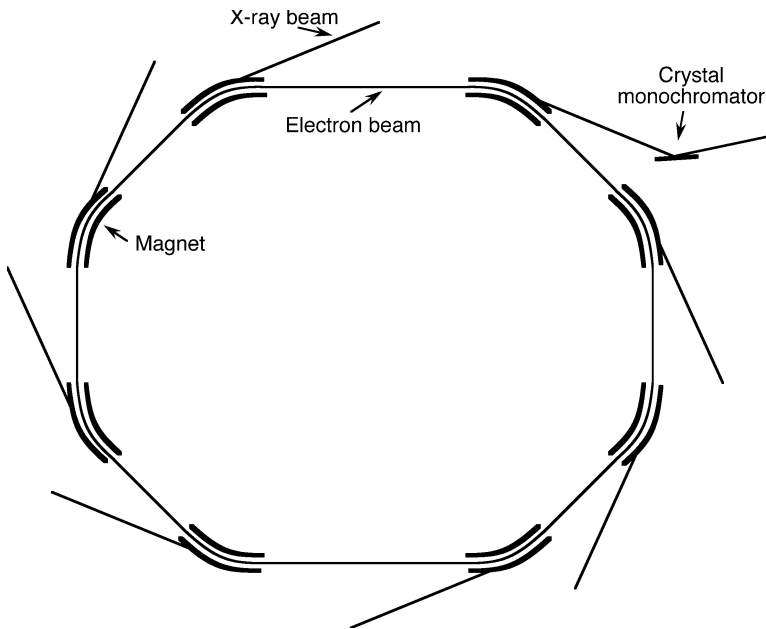


**Fig. 4.23** Design of a synchrotron. Ions or electrons are accelerated to a speed close to the speed of light and forced on a curved trajectory. A broad spectrum of radiation is produced along the curved sections of the beam. For protein crystallography, a certain wavelength, e.g., 1 Å, is selected by a monochromator

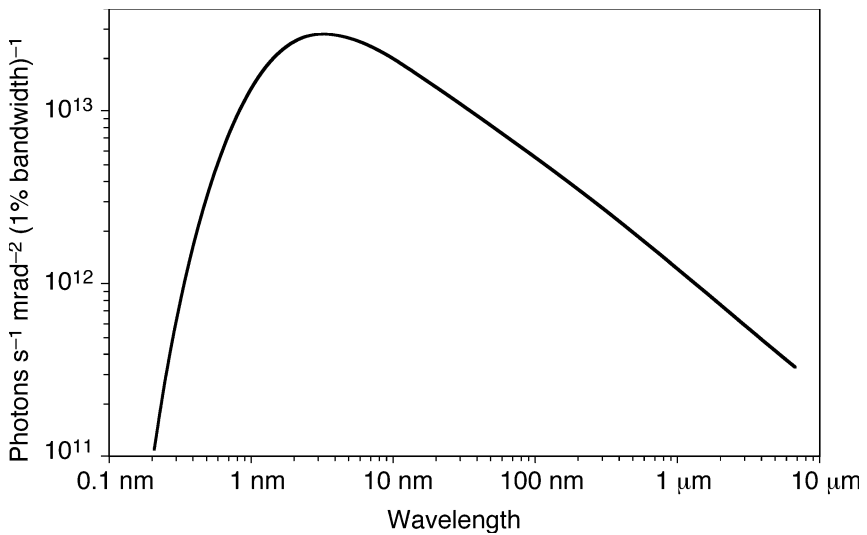


**Fig. 4.24** Emission of the Berlin Electron Synchrotron Storage Ring (BESSY I)

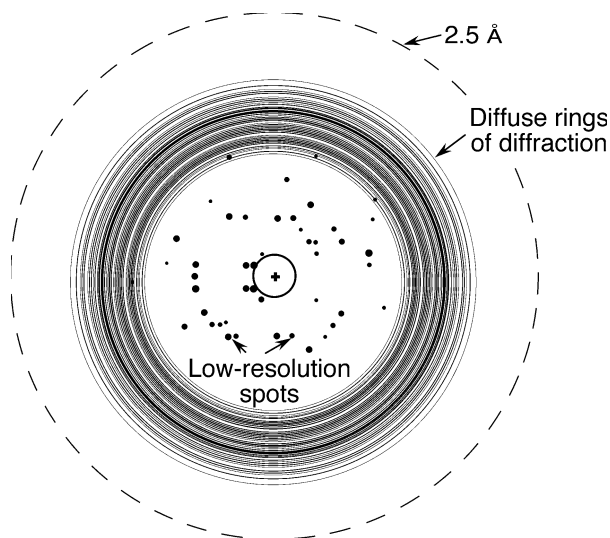


**Fig. 4.25** Diffraction pattern of a poorly scattering crystal: only a few spots near the center are observed, any high resolution information is absent. The dashed circle indicates the area corresponding to a resolution of 2.5 Å. If diffraction spots would be visible up to this circle, the resolution of the obtained structure would be 2.5 Å. One can see that the resolution is much lower in this example

Already superficial inspection of the diffraction pattern provides a lot of information about the quality of the crystals: since the information about fine details of the protein structure is found at large diffraction angles, the absence of spots far outside the center of the diffraction pattern shows that only a low resolution will be obtained (Fig. 4.25).

#### **4.1.2.4 Determination of the phases: heavy atom replacement**

As mentioned earlier, after measurement of the diffraction pattern, determination of the phase information is required. If we do not have information from molecules with a similar structure, or anomalously scattering atoms in the molecule, the method of choice may be the heavy atom replacement: the diffraction pattern of the original (native) crystal is compared with crystals that contain a single or a few heavy atoms at fixed positions. Those crystals can be prepared, e.g., by diffusing a solution of a heavy atom salt into the protein crystal.

Fig. 4.26 depicts sections of the diffraction pattern of the native protein crystal and heavy atom derivatized crystal, respectively. The diffraction spots labeled with “++” are significantly increased in intensity for the heavy atom derivative. This shows that they belong to phases with a large magnitude. How can we make this conclusion? See Fig. 4.27 which, in the upper part, shows the intensity of an interferogram of two waves as function of phase: when we introduce a small shift

to one of the waves (lower part), a large increase of intensity of the interferogram is found for large positive phases. Essentially no change of intensity occurs at phases around zero. Thus, analogously we can conclude that diffraction spots which increase in intensity only slightly between native crystal and heavy atom derivative belong to phases around zero or  $\pi$ . So, by comparing the intensities of the spots between native crystal and the heavy atom derivative we can estimate the phases of the individual diffraction spots. With only one heavy atom derivative, an uncertainty of two possibilities remains for each spot, but this can easily be removed with a further, different heavy atom derivative of the protein crystal.

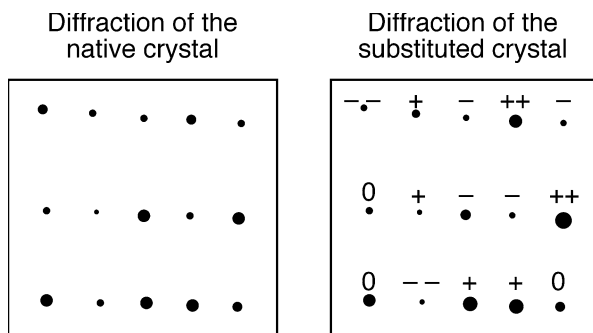


**Fig. 4.26** Section of the diffraction pattern of a protein crystal. *Left:* “native” crystal. *Right:* heavy atom derivative

Another way of showing the importance and meaning of phases in crystallography is illustrated in Fig. 4.28: Atoms with different phases and relative positions may cause a diffraction spot at the same position. Thus, without information from heavy atom replacement, or from diffraction patterns of proteins with similar structure or other information, we cannot deduce the protein structure from the diffraction pattern. Theoretically one could also try out all possible phases and see if it leads to a meaningful structure, but currently for macromolecules the computational effort would be much too high.

It should be noted that the problem of loss of phase information occurs only in the common methods of recording the crystal diffraction, such as with a photographic film or a semiconductor detector. The use of lenses or mirrors to produce an image like in an microscope would prevent this loss of information (see p.65). Unfortunately, currently we cannot build a lens which is sufficiently suitable for focussing X-rays of less than a few Å wavelength: the surface of a conventional lens would not be smooth enough and the bulk of the lens would act like a non-regular grating. Further, it is also very difficult to build highly precise X-ray mirrors (Figs. 4.29 and 4.30). X-ray mirror microscopes using soft radiation currently reach only a few 10 nm resolution. More importantly, the radiation damage would prevent atomic resolution of a single protein molecule or virus.

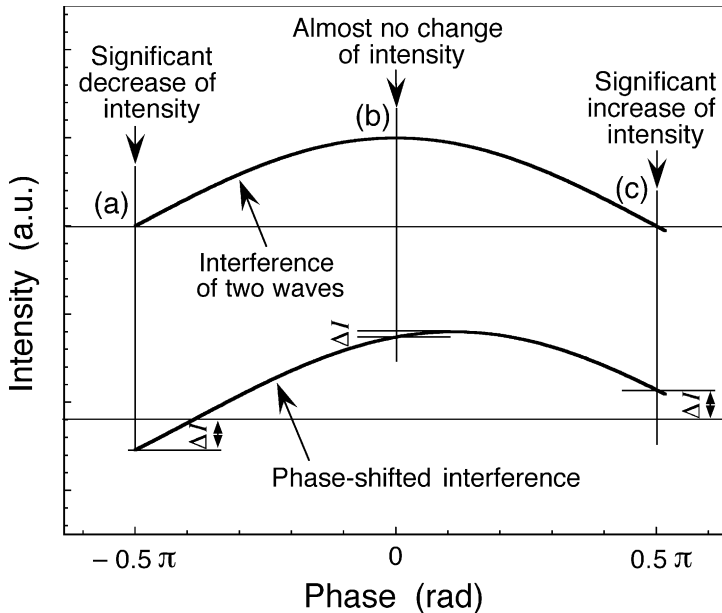


**Fig. 4.27** Interferogram of two waves: within the phase interval  $[-\pi/2, \pi/2]$ , a small phase shift causes a large negative amplitude change,  $\Delta I$ , for large negative phases (**a**), and a large positive amplitude change for large positive phases (**c**), but almost no amplitude change for zero phases (**b**). Thus, e.g., from a large amplitude increase of a diffraction spot upon application of a small phase shift by an additional heavy atom, we can conclude that the phase of the spot has a large magnitude. Analogously one can estimate the phases from the observation of various intensity changes of diffraction spots upon derivatization of the crystal with a heavy atom. For the complete phase interval,  $(-\pi, \pi]$ , there are still two phases for each amplitude change (not shown). This uncertainty is removed by using data from a second heavy atom derivative

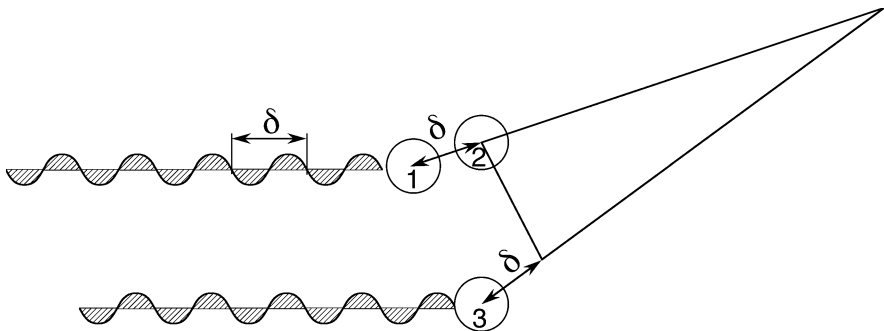


**Fig. 4.28** Different phases and relative positions may cause a diffraction spot at the same position: the atom pairs (1,2) and (2,3) with completely different relative locations cause positive interference at the same position



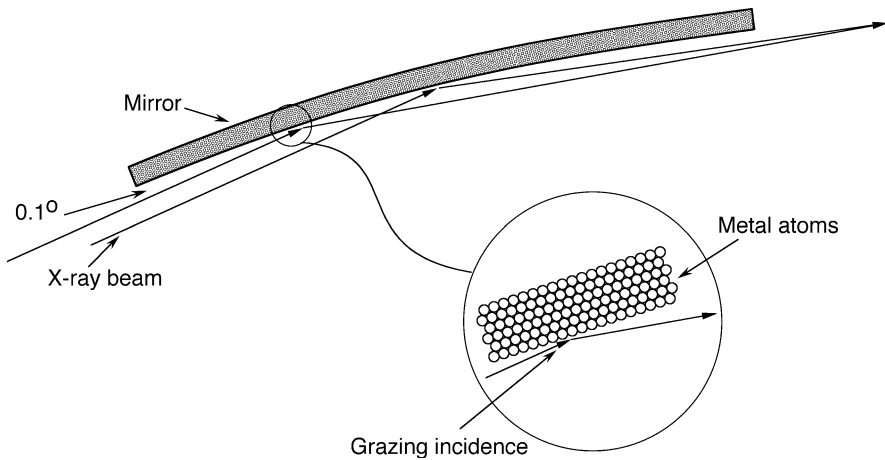


**Fig. 4.29** Common X-ray mirrors are only suitable for low angles of incidence

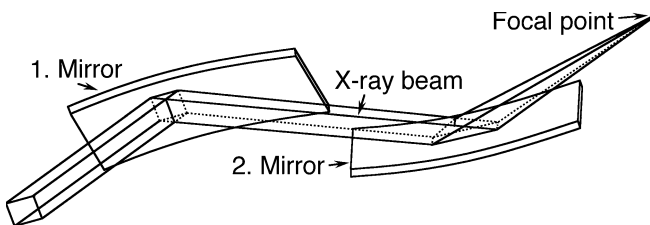
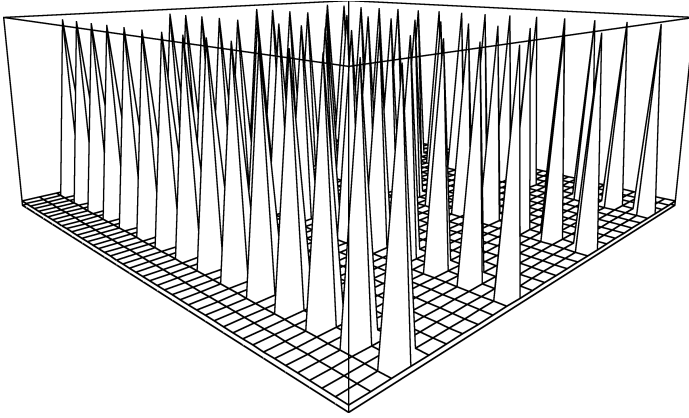


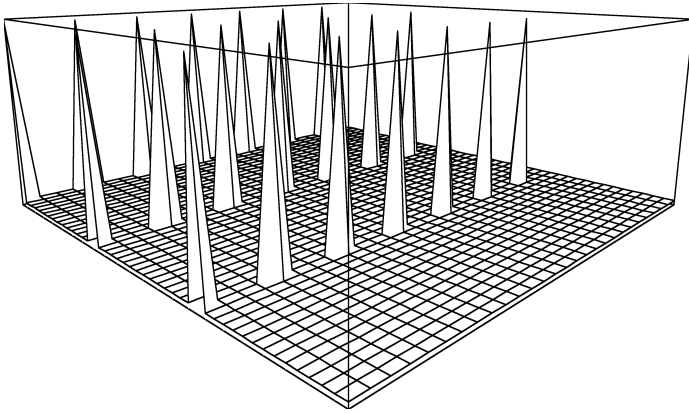
**Fig. 4.30** A pair of X-ray mirrors with grazing incidence focuses an X-ray beam to a spot

The mathematics behind the method of heavy atom replacement is exemplary illustrated in Figs. 4.31–4.34. Fig. 4.31a represents an array of atoms. Fig. 4.31b is the absolute of the Fourier transform of this array. From the imaginary and real parts (Fig. 4.32) of this Fourier transform, the phase was calculated (Fig. 4.33). Fig. 4.34a represents the same array as above, but with one additional heavy atom causing a small change of the Fourier transform. The difference of the absolutes of Fourier transforms between native array and heavy atom derivatized array is shown in Fig. 4.34b. Comparing this difference of the absolutes of Fourier transforms with the absolutes of the phases of the native array (Fig. 4.33b), we find a connection between phases (Fig. 4.33b) and amplitude differences (Fig. 4.34b). This connection allows the magnitude of the phase angles to be determined. As mentioned, the remaining ambiguity of sign is removed by including the data from a second isomorphous heavy atom derivative.



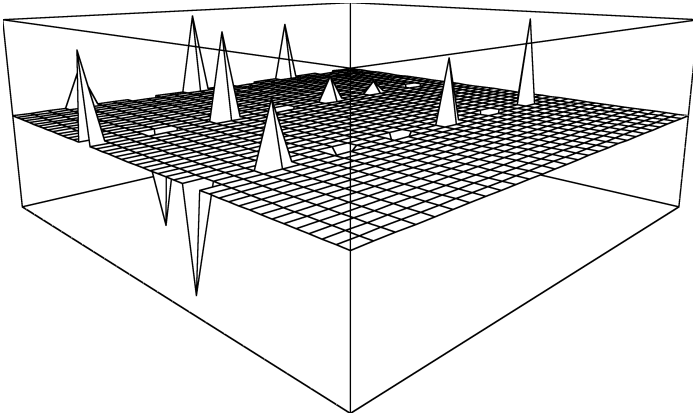
(a)  $f(x,y)$

↓ FT

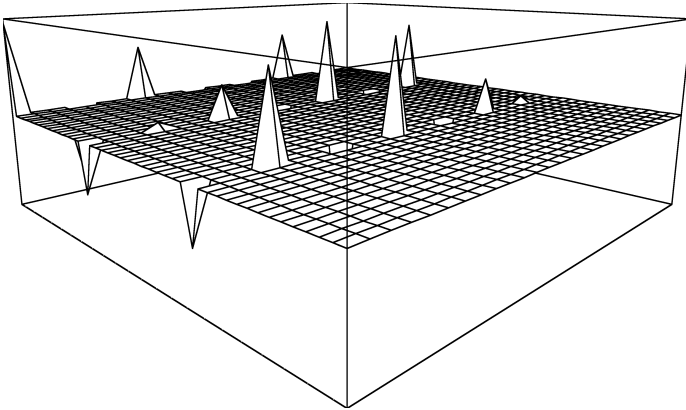


(b)  $|F(h,k)|$

**Fig. 4.31** (a) Representation of an array of atoms. (b) Absolute of the Fourier transform of (a)

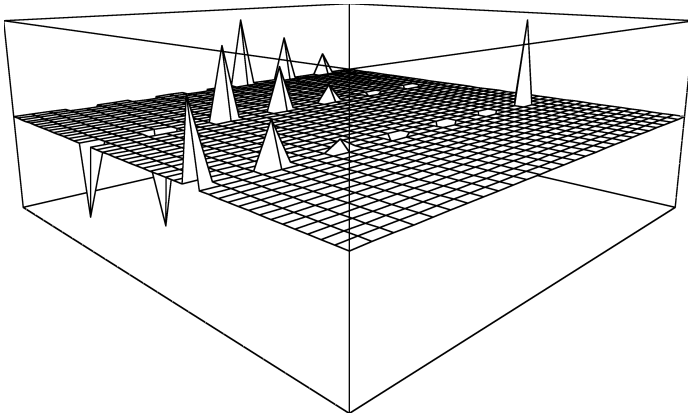


(a)  $\text{Im}(F_1(h,k))$

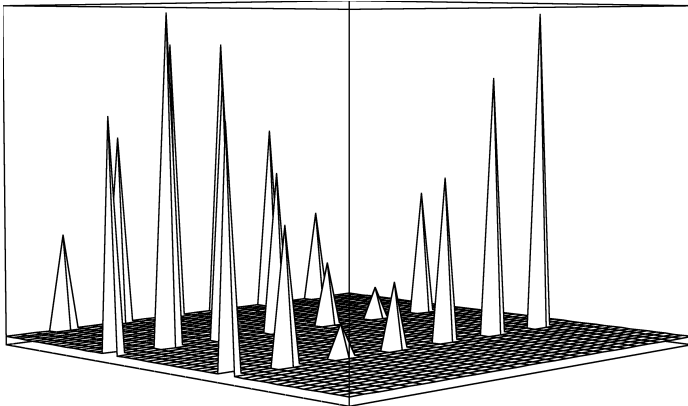


(b)  $\text{Re}(F_1(h,k))$

**Fig. 4.32** (a) Imaginary part of the Fourier transform of the array of Fig. 4.31a. (b) Real part of the Fourier transform of the array of Fig. 4.31a

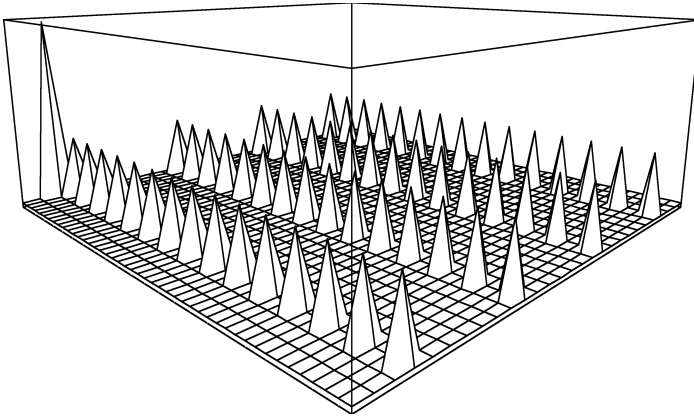
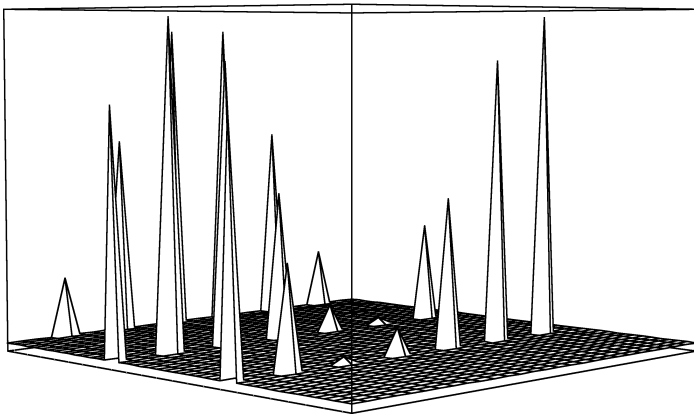


(a)  $\text{Phase}(F1(h,k))$



(b)  $|\text{Phase}(F1(h,k))|$

**Fig. 4.33** Phase (a) and absolute of the phase (b) of the Fourier transform of the array of Fig. 4.31a, calculated from imaginary and real parts of the Fourier transform

(a)  $f_2(x,y)$ (b)  $|F_1(h,k)| - |F_2(h,k)|$ 

**Fig. 4.34** (a) Representation of the array from Fig. 4.31 with an additional heavy atom. (b) Difference of the absolutes of the Fourier transforms of native array (Fig. 4.31a) and heavy atom replaced array (Fig. 4.34a). When we compare Figs. 4.33b and 4.34b, we can see a connection between phases and amplitude differences. Note that  $|F| = ((\text{Im}(F))^2 + (\text{Re}(F))^2)^{0.5}$ ;  $\text{phase}(F) = \arctan(\text{Im}(F)/\text{Re}(F))$ , where "Im" and "Re" stand for imaginary and real parts, respectively

#### 4.1.2.5 Calculation of the electron density and refinement

Software for the calculation of the initial electron density from the diffraction data and the refinement of structures is being rapidly developed by several academic institutions and often supplied for free. It may be found on the internet, e.g., by searching with the keywords "protein crystallography software".

### 4.1.2.6 Cryocrystallography and time-resolved crystallography

Short-living conformational intermediates in the microsecond and nanosecond time scale have been resolved by time-resolved crystallography (Srajer et al., 1996; Genick et al., 1997; Fig. 4.35) and cryocrystallography (Schlichting et al., 2000; Petsko and Ringe, 2000; Wilmot and Pearson, 2002; Fig. 4.36). Time-

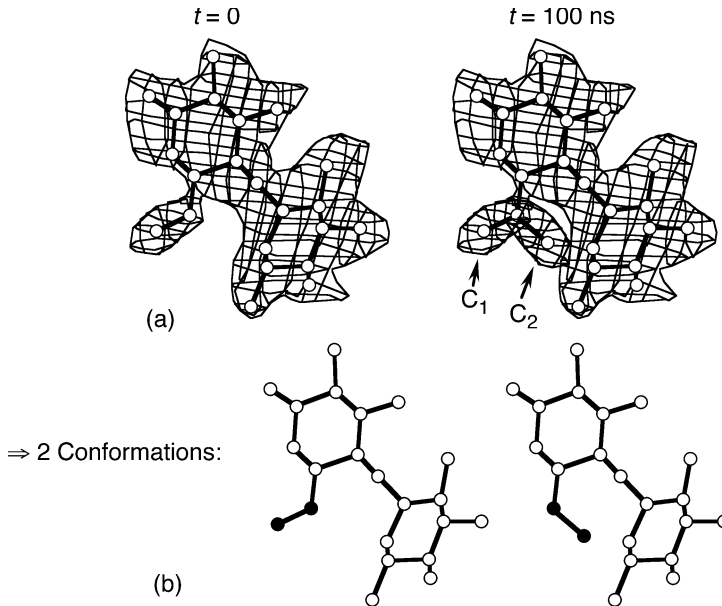


**Fig. 4.35** Example for time-resolved crystallography. 100 ns after initiation of a conformational change, the electron density indicates the occurrence of two conformations,  $C_1$  and  $C_2$

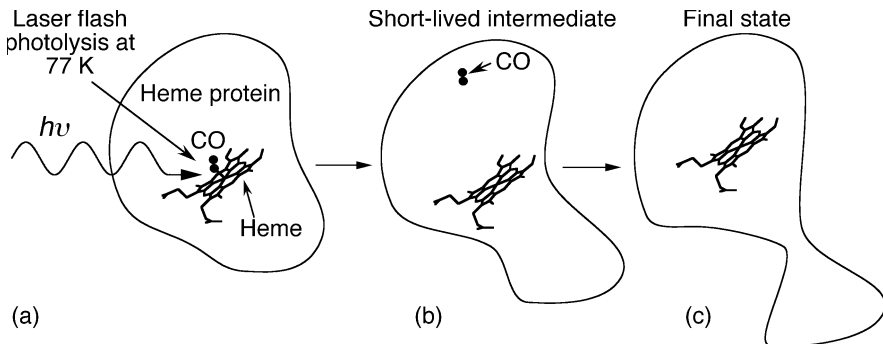


**Fig. 4.36** Example for cryocrystallography. The CO is flashed off the heme group of the heme protein. This initiates a conformational transition which is detected, e.g., at  $-196^\circ\text{C}$

resolved crystallography interprets time-dependent electron density maps and can offer detailed structural information on short-lived intermediates under near-physiological conditions. In cryocrystallography, reactions are induced and measured at a low temperature. At the very low temperatures of flash photolysis and acquisition of the diffraction pattern in the experiment shown in Fig. 4.36, the reaction kinetics of the conformational changes is slowed down by many orders of magnitude. This enables to determine the coordinates of structural intermediates that would normally be too short-lived to be resolved by X-ray crystallography.

## 4.2 X-ray scattering

### 4.2.1 Small angle X-ray scattering (SAXS)

Small angle X-ray scattering serves for the elucidation of microstructural information in amorphous materials on length scales ranging from a few Å to a few  $\mu\text{m}$  (Figs. 4.37 and 4.38). Fig. 4.39 is an illustration of the setup for SAXS. Significant effort is undertaken to enable the measurement at very small angles. Since there is an about reciprocal relationship between distance separation of scattering points ( $\Delta x$ ) and the scattering angle ( $\theta$ ), this measurement is essential to obtain sufficient information in the relatively large length scale compared with the wavelength ( $\lambda$ ) of the X-rays ( $\Delta x \approx 0.5\lambda \sin^{-1}(\theta/2)$ ). For details on X-ray optics see also the previous section.

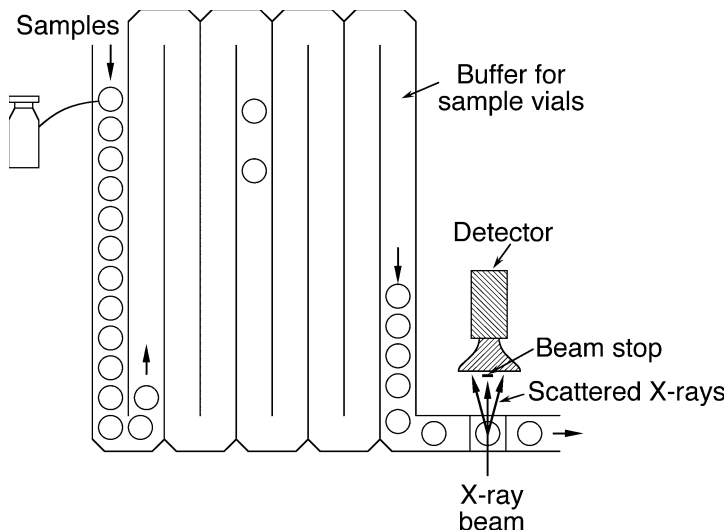


**Fig. 4.37** Automatic SAXS and wide angle X-ray scattering analysis of biological samples. A large number of vials is automatically sampled and production faults immediately are detected and responded to

SAXS measurements revealed that

- (a) an unliganded aspartate transcarbamoylase adopts a T-quaternary structure (Fetler et al., 2002),
- (b) the axial period of collagen fibrils is  $65.0 \pm 0.1$  nm in healthy human breast regions, and 0.3 nm larger in cancer-invaded regions (Fernandez et al., 2002),
- (c) flax cellulose microfibrils probably have a cross section of  $10 \times 50 \text{ \AA}^2$  (Astley and Donald, 2001),
- (d) microfibrils with an axial repeating period of approximately 8 nm are present in the major ampullate silk from the spider *Nephila* (Miller et al., 1999; Riekel and Vollrath, 2001), and
- (e) the ATPase domain of SecA has dimensions of approximately  $13.5 \text{ nm} \times 9.0 \text{ nm} \times 6.5 \text{ nm}$  (Dempsey et al., 2002).

SAXS revealed information regarding the conformational diversity and size distribution of unfolded protein molecules (Kamatari et al., 1999; Panick et al., 1999a; Garcia et al., 2001; Choy et al., 2002), and was used in a large number of protein-folding and peptide-folding studies to obtain information about size changes (e.g., Chen et al., 1998; Panick et al., 1998, 1999b; Arai and Hirai, 1999; Segel et al., 1999; Kojima et al., 2000; Russell et al., 2000; Aitio et al., 2001; Canady et al., 2001; Katou et al., 2001; Muroga, 2001; Tcherkasskaya and Uversky, 2001). SAXS is one of the very few methods which can directly monitor structural changes of small virus particles (Sano et al., 1999; Perez et al., 2000).

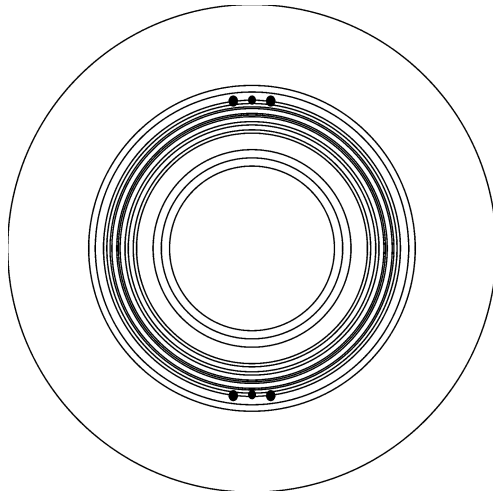


**Fig. 4.38** Diffraction pattern of a cell suspension. SAXS can serve to obtain a “fingerprint” of a biological specimen which helps to identify unknown biological samples



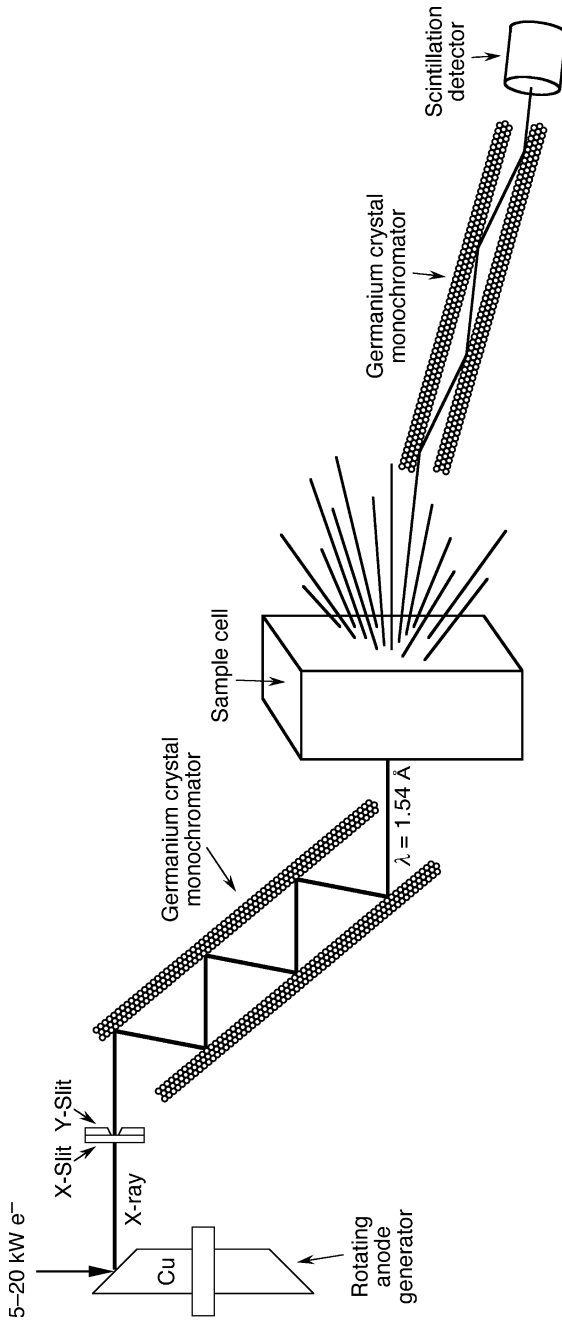


**Fig. 4.39** Setup for small angle X-ray scattering (SAXS). The X-ray beam from a rotating anode generator is passed through a crystal monochromator that selects a wavelength. The monochromatic X-ray beam is passed through the sample cell, and scattered X-rays at very small angles are passed through a second crystal monochromator and then detected with a scintillation detector. For many applications, this set-up may be simplified, e.g., by choosing fewer reflections in the monochromators which yields a higher intensity of X-rays

Distance constraints derived from SAXS measurements can be used to filter candidate protein structures for the purpose of protein structure prediction (Zheng and Doniach, 2002). In some cases even low resolution solution structures of proteins were obtained solely from SAXS data (Chacon et al., 1998; Shilton et al., 1998; Bada et al., 2000; Maruyama et al., 2001; Scott et al., 2002) or SAXS data combined with neutron scattering data (Egea et al., 2001). SAXS can reveal the structure of bones (Rinnerthaler et al., 1999) and structural changes in bones due to diseases (Grabner et al., 2001). The method was used to obtain information about conformational changes of bacterial cell wall enzymes upon binding to a substrate (Schönbrunn et al., 1998), and structural changes in artificial biological membranes (Riske et al., 2001). SAXS results on human dentin, which is a complex composite of collagen fibers and carbonate-rich apatite mineral phase, are consistent with nucleation and growth of an apatite phase within periodic gaps in the collagen fibers (Kinney et al., 2001).

#### 4.2.2 X-ray backscattering

The property of X-rays to penetrate materials is used in many biophysical applications, ranging from for the purpose of determination of the molecular weight of

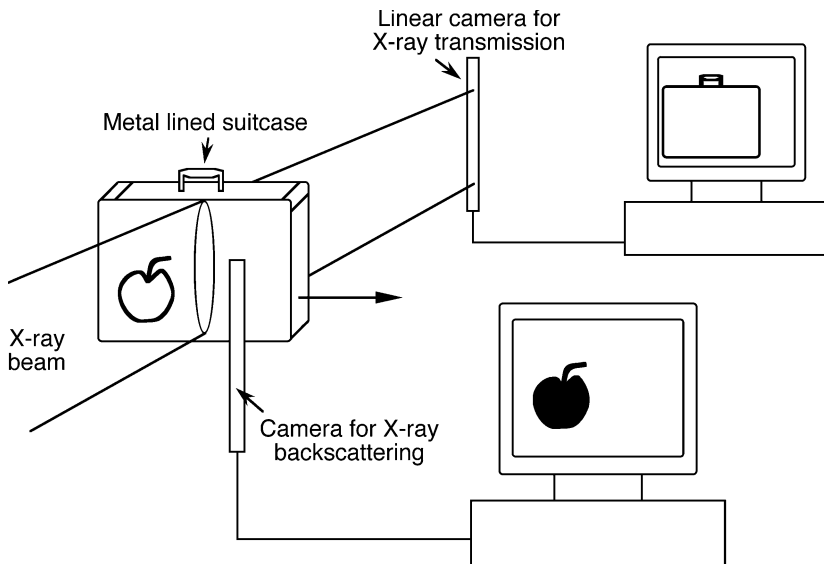


**Fig. 4.40** Detection of biological and other organic material behind a metal layer with X-ray backscattering: since the absorption of biological material is much smaller than that of metal, the biological material is difficult to detect in single-wavelength X-ray absorption measurements. X-ray backscattering provides much better contrast in this application. However, the quantum efficiency of X-ray scattering is low and thus relatively large exposures and sensitive cameras must be used

proteins to X-ray backscattering for the purpose of detection of organic material hidden in metal containers (see, e.g., Fig. 4.40).

A problem of detection of organic material, such as illicit drugs and explosives, by X-ray absorption is their low absorption coefficient compared with metals and the possibility to camouflage the material, e.g., by embedding it in other organic material, such as flour or sugar. X-ray backscattering offers a good contrast for the detection of such powdery material (Fig. 4.40). The main disadvantage is the low backscattering coefficient compared with transmission coefficient of most organic samples. Thus, a significantly higher exposure compared with X-ray transmission is usually required.

## 5 Protein infrared spectroscopy

Infrared spectroscopy is based on the infrared absorption of molecules and is, compared with crystallography, a relatively simple and inexpensive tool for the global characterization of molecular conformations and conformational changes of proteins and other biomolecules. Depending on the measurement technique, scanning infrared (IR) spectrometers, Fourier transform infrared (FTIR) spectrometers, and single wavelength infrared apparatuses are distinguished (see Sect. 5.1). Typically the most interesting spectral region for biomolecules is  $\nu = 400 - 4000 \text{ cm}^{-1}$ , where the wavenumber,  $\nu$ , is defined as  $\nu \equiv 1/\text{wavelength}$ . Infrared activity requires a change of dipole moment upon excitation (Fig. 5.1). For proteins the amide chromophore absorption in the region of  $1500 \text{ cm}^{-1} - 1700 \text{ cm}^{-1}$  ( $\approx 6 \mu\text{m}$  wavelength) is particularly important for the assessment of secondary structure content and structural changes. Regarding the resolution of protein secondary structure, the information content of IR and FTIR spectroscopy is comparable with that of circular dichroism (see, e.g., Nölting et al., 1997b; Nölting, 2005), and regarding the resolution of features of the tertiary structure of proteins, IR and FTIR are often inferior, and yet IR is much easier to apply on a fast time scale and for remote sensing (see, e.g., LIDAR in Sect. 5.1.3).

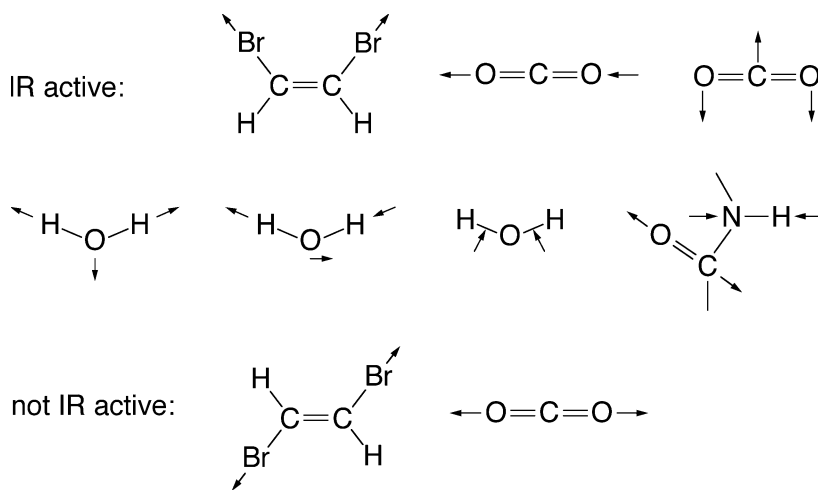


**Fig. 5.1** Example of infra-red active and non-active vibrations. Note that infra-red activity requires a change of dipole moment

## 5.1 Spectrometers and devices

### 5.1.1 Scanning infrared spectrometers

Early IR spectrometers (Fig. 5.2) were constructed similarly to scanning UV/VIS absorption spectrometers. The emission of the source, e.g., a thermal source operated at 1000 °C, is passed through a monochromator selecting a single wavelength. The monochromatic beam is split into two beams – one having the sample in the path. A shutter passes through only one of the two beams at a time. Both beams are alternately detected by an IR detector, e.g., a pyroelectric detector, and compared with each other. The optical density of the sample is calculated from the logarithm of the intensity quotient. The use of light modulation is quite indispensable since the problem of background radiation is much more severe than in UV/VIS spectrometers. Spectra are recorded by scanning the wavelength region of interest. This scanning principle of operation is still widely used in IR spectrometers with time resolutions in the femtosecond to nanosecond region, where infrared lasers serve as IR source (see Nölting, 2005).

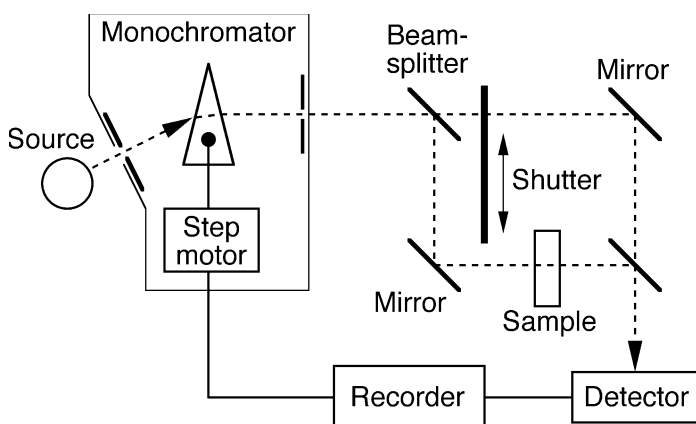


**Fig. 5.2** Example of a scanning infrared (IR) spectrometer. The monochromator separates the radiation of the IR source into its different wavelengths and selects one wavelength at a time. A beam splitter separates the monochromatic beam into sample beam and reference beam. The absorption coefficient, according to the chemical and structural properties of the sample molecules, is calculated using the detected intensity quotient between both beams, the pathlength, and the sample concentration

### 5.1.2 Fourier transform infrared (FTIR) spectrometers

FTIR spectrometers (Figs. 5.3–5.7) use the technique of Michelson interferometry and have the advantage of using a larger part of the emission of the IR source during the measurement of a spectrum, compared with scanning IR spectrometers

that are based on monochromators which select only one wavelength at a time. The better usage of radiation improves the inherent signal-to-noise ratio, especially for strongly absorbing samples for which the measurement may be photon shot noise limited. Also the spectral resolution of FTIR spectrometers, which is limited by the path length of the moving mirror, is often better than that of scanning IR spectrometers.

In FTIR spectrometers (Fig. 5.3) the beam of radiation from the IR source is focused on a beam splitter constructed such that half the beam is transmitted to a moving mirror and the other half is reflected to a fixed mirror. Both the moving mirror and the fixed mirror reflect the beam back to the beam splitter which reflects the half of both beams to the detector where they interfere according to their phase difference. The light intensity variation with optical path difference, called interferogram, is the Fourier transform of the incident light spectrum (light intensity as a function of the wavenumber). Absorption spectra are obtained by measuring interferograms with a sample and with an empty sample cell in the beam and inverse Fourier transforming the interferograms into spectra (Figs. 5.4–5.6).

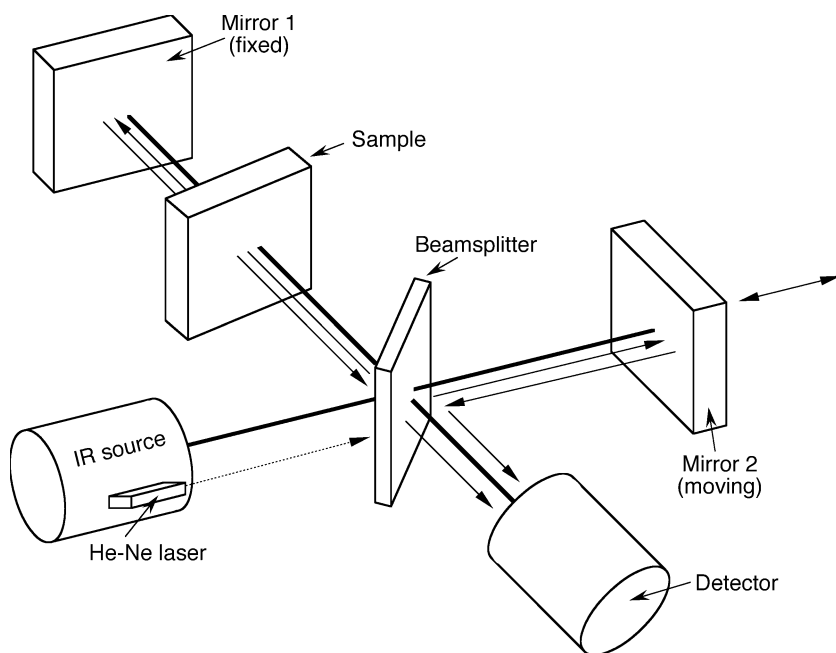


**Fig. 5.3** Typical design of FTIR spectrometers. The lamp, e.g., a thermal source, emits a beam of infrared radiation. A Michelson interferometer, consisting of a beamsplitter, a fixed mirror and a moving mirror, splits the beam into two beams and generates an interference of them. The sample inserted in one of the beam paths changes the interference. Interferograms with and without sample are recorded and the absorption of the sample is calculated by inverse Fourier transform (see Fig. 5.6)

Fig. 5.4 shows three examples of interference of the two monochromatic light beams of the interferometer resulting in different intensities of the interferogram. Eq. 5.1 describes the intensity of the interferogram,  $I_{\text{interferogram}}$ , for the interference of two polychromatic beams of equal intensity in the FTIR spectrometer:

$$I_{\text{interferogram}}(\delta) = \text{const} \times \int_0^{\infty} I_{\text{beam}}(\nu) \cos(2\pi\delta\nu) d\nu, \quad (5.1)$$

where  $\delta$  is the phase difference of the two beams,  $\text{const}$  a constant,  $I_{\text{beam}}$  the intensity of the beams, and  $\nu$  the wavenumber. From the interferogram, the intensity of the beams can be calculated by inverse Fourier transform:

$$I_{\text{beam}}(\nu) = \text{const} \times \int_{-\infty}^{+\infty} I_{\text{interferogram}}(\delta) \cos(2\pi\delta\nu) d\delta \quad (5.2)$$

Analogously, the intensity of the beam with the sample in the path is calculated from the corresponding interferogram. The absorption is given by the logarithm of the intensity quotient of blank to sample.

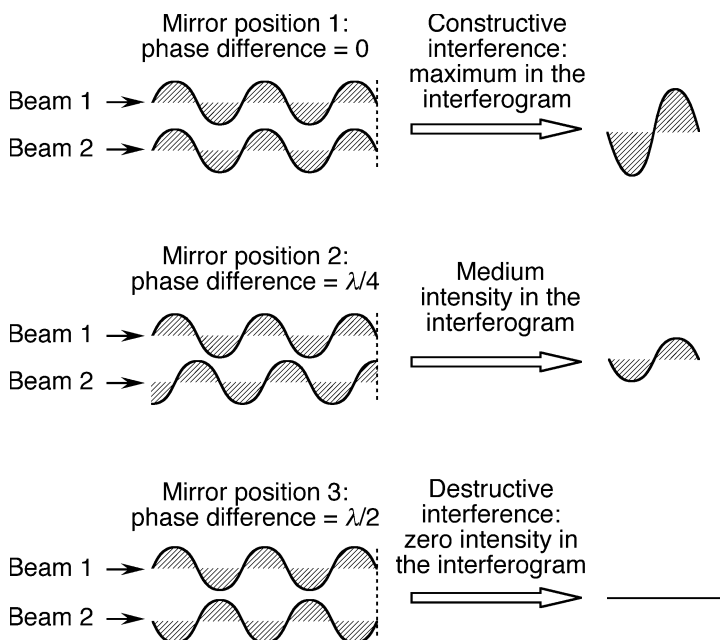


**Fig. 5.4** Interference of two monochromatic light waves with equal intensity. *Top:* both beams have the same phase; their interference yields the maximum of the interferogram, i.e., the sum of both intensities. *Middle:* at a phase difference of  $\lambda/4$ , the intensity of the interferogram equals the intensity of the interfering beams. *Bottom:* at a phase difference of  $\lambda/2$ , both beams extinguish each other

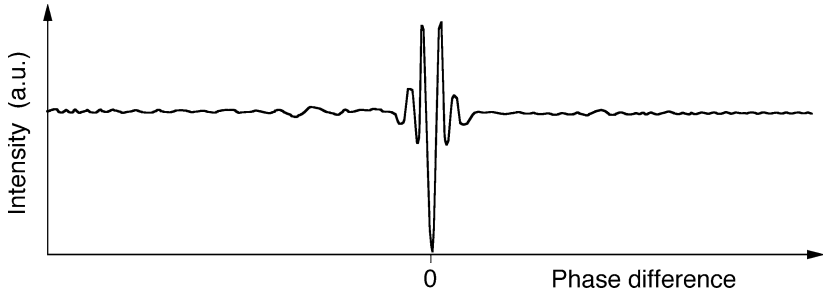


**Fig. 5.5** Example of an interferogram of two polychromatic light beams

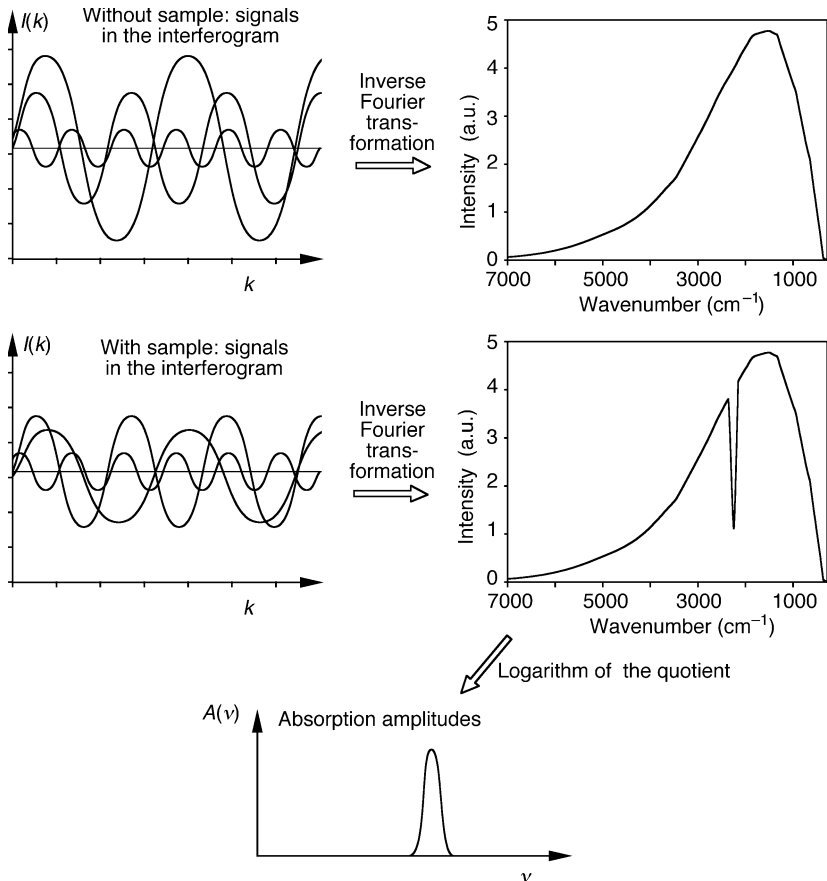


**Fig. 5.6** Principle of operation of a FTIR spectrometer. IR intensities at the detector are recorded both for the sample cell filled with solvent and for the sample cell filled with sample. Inverse Fourier transformation of the two interferograms yields the IR intensities. The IR absorption spectrum is calculated using the logarithm of the intensity quotient



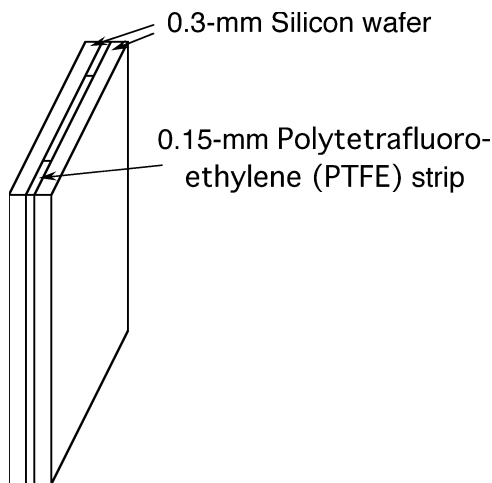


**Fig. 5.7** Sample cell for FTIR experiments. The transparent walls of the cell are made from silicon wafers supplied by a manufacturer of electronic chips

A very suitable material for the manufacture of sample cells, sample holders, and windows is silicon (Fig. 5.7). Polished silicon wafers of 0.5 – 1 mm thickness are sufficiently transparent from 400 to 4000  $\text{cm}^{-1}$  (25 – 2.5  $\mu\text{m}$  wavelength) (Jiang et al., 1996). Only the fragility and the high refractive index of this material might be problematical in some experimental set-ups. Used infrared sources are often thermal sources operated at about 1000  $^{\circ}\text{C}$ . Beam splitters made from a thin germanium film evaporated on a potassium bromide (KBr) or cesium iodide (CsI) slide are transparent down to about 400  $\text{cm}^{-1}$  (25  $\mu\text{m}$  wavelength) and 200  $\text{cm}^{-1}$  (50  $\mu\text{m}$  wavelength), respectively. Liquid nitrogen cooled mercury cadmium telluride (MCT) detectors and deuterated triglycine sulfate (DTGS) pyroelectric detectors are frequently applied for infrared detection. For an excellent introduction into the instrumentation of FTIR spectroscopy see Perkins, 1986.

### 5.1.3 LIDAR, optical coherence tomography, attenuated total reflection and IR microscopes

IR spectroscopy is exquisitely suitable for remote sensing of clouds of biological agents (Fig. 5.8). The IR LIDAR set-up consists of a pulsed IR laser and an IR detector which senses the backscattered light from the laser. Since the light travels extremely fast, the detector senses the return echo before the next pulse is sent. The time it takes for the laser pulse to travel down and back is a measure of the distance. Mobile commercial LIDAR systems quite often employ an integrated global positioning system (GPS) to determine the own position.

Equipped, e.g., with an optical modulator which rapidly changes the direction of the beam, and mounted on top of a roof, the IR LIDAR can scan the 360°-environment at distances of 0 to several 10 km. This method has importance, for example, for early warning systems of smog in large cities and for three-dimensional analysis of forest structure and terrain (Fig. 5.9). Remote sensing of changes in forest structure utilizes the information of time and intensity of multiple reflections from leaves and branches. Effects of environmental pollutants and pests are quickly detectable in vast areas and economic damage is largely reducible.

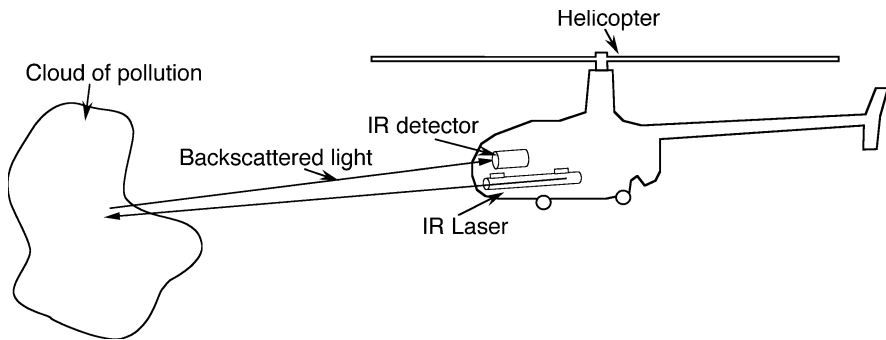


**Fig. 5.8** Remote sensing of environmental changes, e.g., a cloud of biological material, with an IR LIDAR (light detection and ranging; measurement of light backscatter)

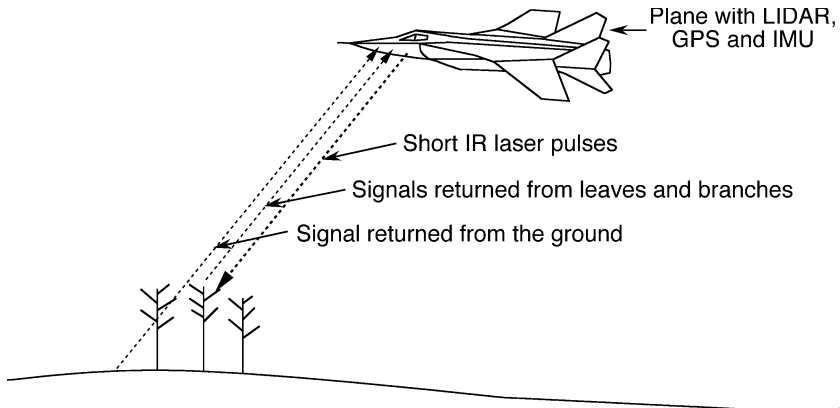


**Fig. 5.9** Remote survey of forest structure and terrain with IR LIDAR technology. The plane is equipped with a GPS and an inertial measurement unit (IMU). The latter contains several gyroscopes and an accelerometer and can determine the position and angle of tilt with some accuracy during periods of failure of the GPS

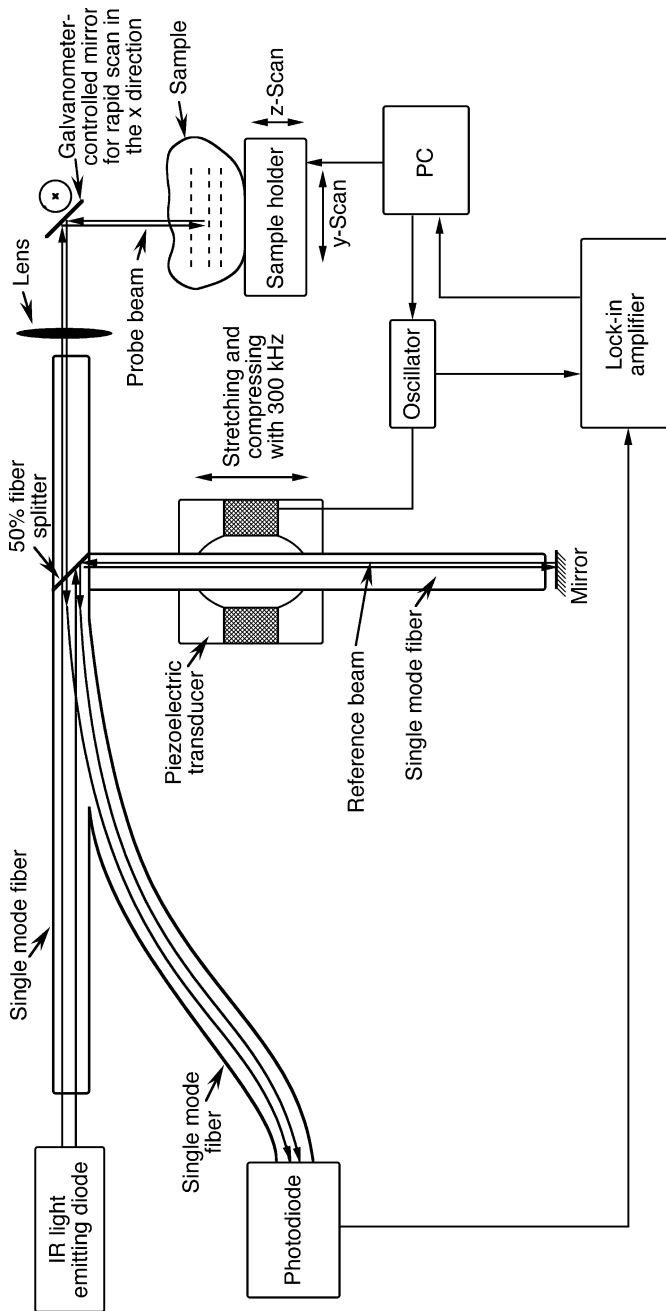


**Fig. 5.10** Optical coherence tomography (OCT). The IR light from a light emitting diode is split into reference and probe beams. Light of the probe beam reflected from the sample is interfered with light of the reference beam, and the interference is detected by the photodiode. The pathlength of the reference beam is modulated by stretching an optical fiber with a piezoelectric transducer. Light from the sample which has traveled the same distance as the reference beam interferes constructively. Its signal is extracted from the interference intensity by a lock-in amplifier (Duncan et al., 1998)

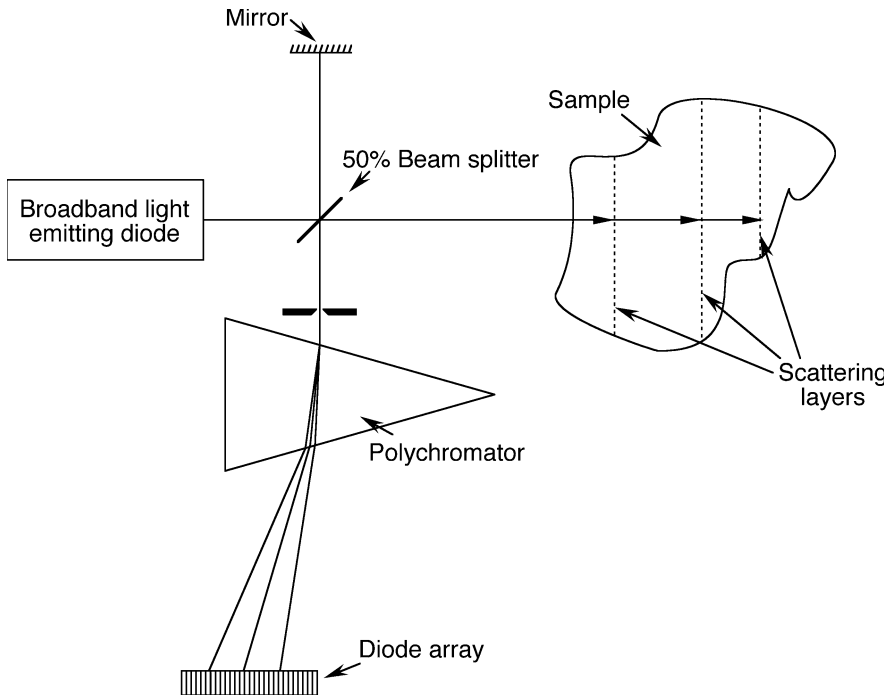


**Fig. 5.11** Spectral domain optical coherence tomography (SDOCT) (Andretzky et al., 1998; Häusler and Lindner, 1998). Polychromatic backscattered light from different depths interferes with polychromatic light of a reference beam. The interference of the beams is analyzed with a polychromator and a multichannel detector. From the spectral changes due to interference, information about the depth of the scattering layer is obtained

Another important variant of IR spectroscopy on biological samples is optical coherence tomography (OCT). OCT (Figs. 5.10 and 5.11) utilizes echoes of infrared light waves backscattered off the internal microstructures within biological objects to obtain images on a  $\mu\text{m}$  scale. In the design of Fig. 5.10, IR radiation backscattered from the sample is interfered with a reference beam. Light from a scattering layer in the sample with a certain depth has the same phase as the reference beam and thus interferes constructively, i.e., produces a high interference intensity. Light from slightly deeper or shallower scattering layers cause a lower interference intensity. By modulating the phase of the reference beam and detecting the interference intensity with a lock-in amplifier, the signals from layers with different depths are extracted from the interference intensity (Duncan et al., 1998). Fig. 5.11 depicts a second design variant of optical coherence tomography (Andretzky et al., 1998; Häusler and Lindner, 1998). Here the information on depth is gained by analyzing the spectrum of the backscattered light.

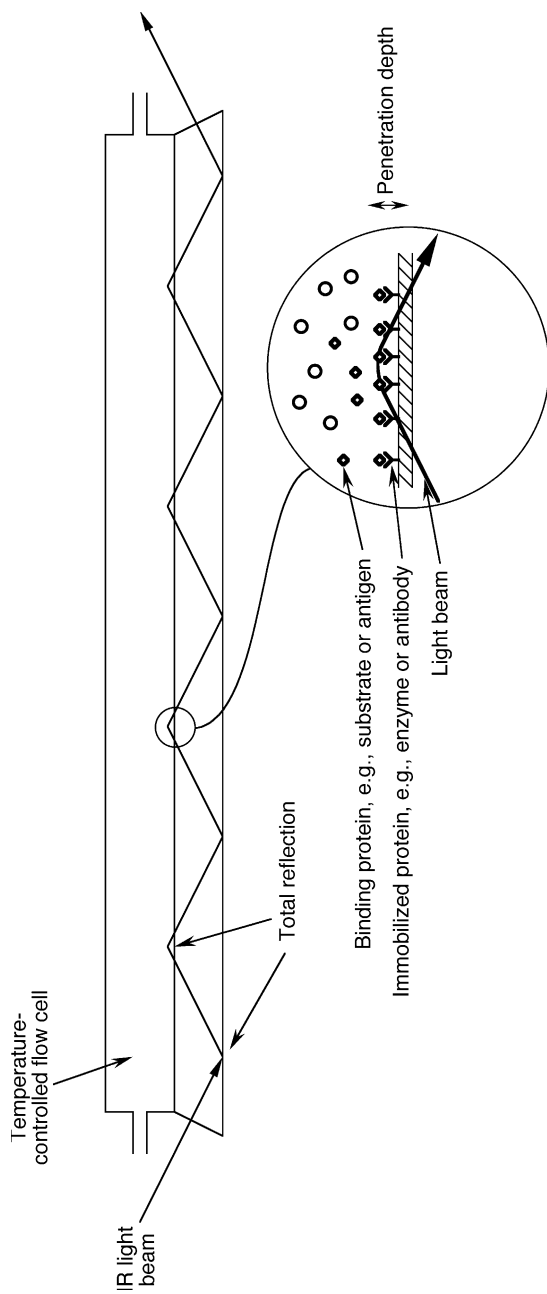


**Fig. 5.12** Flow cell for attenuated total reflection (ATR) infrared spectroscopy (Fringeli et al., 1998; Feughelman et al., 2002; Snabe and Petersen, 2002). The internally total-reflected light slightly leaves the waveguide and so can probe the sample molecules on the outside of the waveguide. The part of the light wave which leaves the waveguide at the total reflection points is called evanescent wave. Only very little sample is needed. Using a large number of reflections can lead to a more than 100-fold amplification of the measured signal

The next IR spectroscopic technique to be mentioned is attenuated total reflection (ATR) infrared spectroscopy (see, e.g., Fringeli et al., 1998; Ding et al., 2002; Feughelman et al., 2002; Snabe and Petersen, 2002; Figs. 5.12 and 5.13). Here the coefficient of internal total reflection of an IR beam in a waveguide is changed by a sample deposited on the surface of the waveguide. An advantage of ATR on thin layered samples is the dramatic increase of the effective optical path-length and sensitivity through multiple reflections compared with conventional transmission spectroscopy on such a sample.

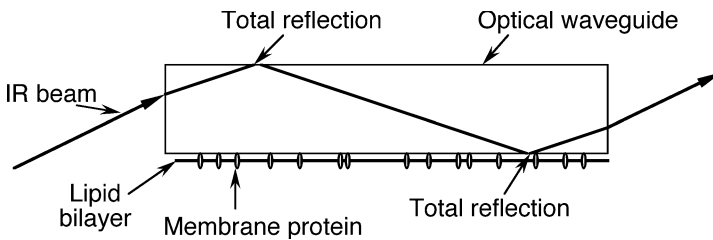


**Fig. 5.13** Attenuated total reflection (ATR) infrared spectroscopy on membrane proteins (see, e.g., Ding et al., 2002)

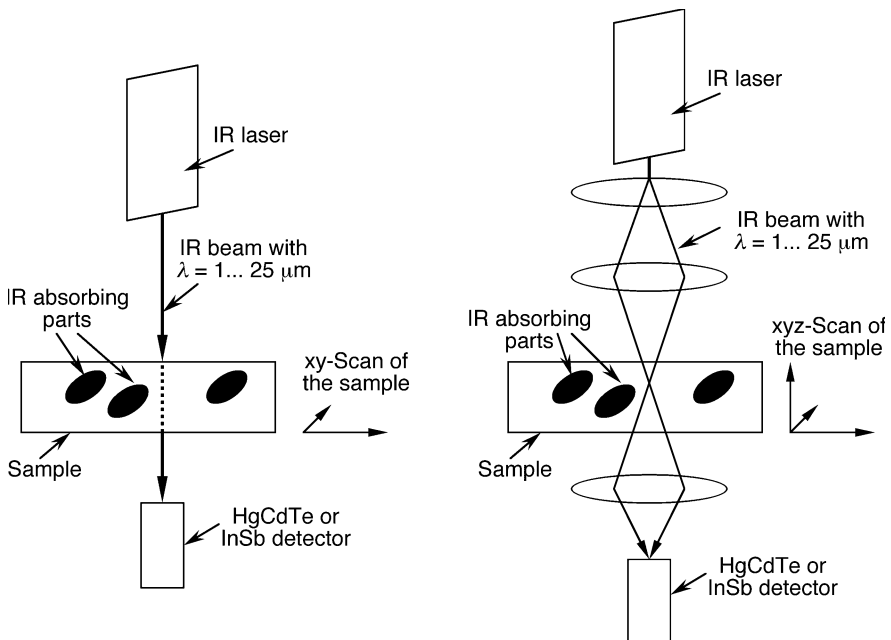


**Fig. 5.14** Scanning IR microscope. The focussed beam from an IR laser is passed through the sample and detected. *Left*: simple microscope with planar resolution, especially suitable for thin layer samples. *Right*: microscope with three-dimensional resolution: for acquisition of the image, the sample is moved in xyz-directions

Because of the significantly lower scattering of IR light relative to light of shorter wavelength, IR microscopes (Fig. 5.14) enable the inspection of most strongly scattering samples. Computer aided image processing allows two- or three-dimensional resolution. More complicated microscopes may utilize step-scan interferometry for photoacoustic depth profiling, monochromators for spectral analysis and polarizers/analyzers for linear dichroism (LD) analysis.

## 5.2 Applications

One of the biophysical main applications of FTIR is the characterization of the structure and conformational changes of proteins (Barrera et al., 2002; Butler et

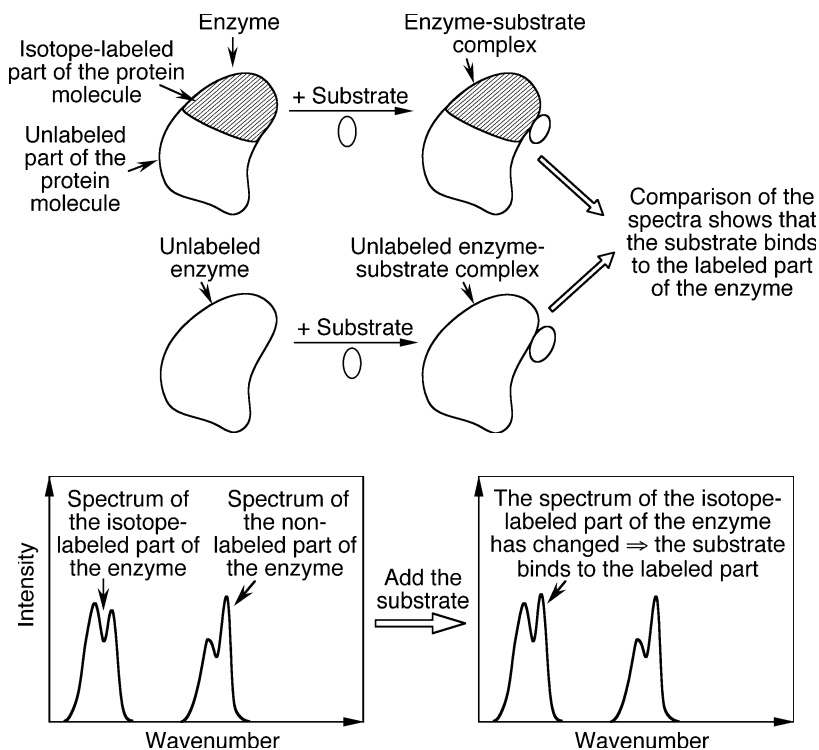


**Fig. 5.15** Isotope-edited FTIR spectroscopy (see, e.g., Li et al., 2002; Barth, 2002). Since the spectrum of the isotope-labeled part of the protein molecule is significantly shifted, it can be distinguished from the spectrum of the non-labeled part. A change of the protein IR spectrum upon binding of the substrate to the protein shows which part of the molecule the substrate binds to. In this example, the magnitude of a peak in the spectrum of the isotope-labeled part of the protein has changed upon binding of the substrate. This shows that the substrate binds to the labeled part of the enzyme

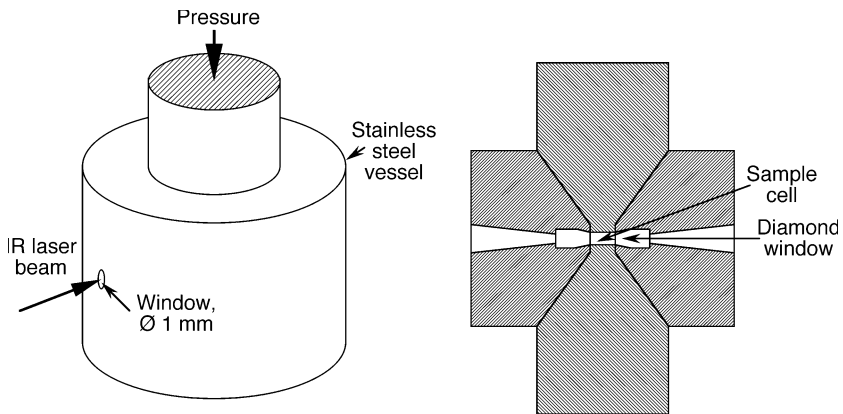


**Fig. 5.16** Apparatus to monitor protein unfolding under high pressure with IR. Since the volume of unfolded protein is less than that of folded protein, high pressure favors transition to the unfolded state

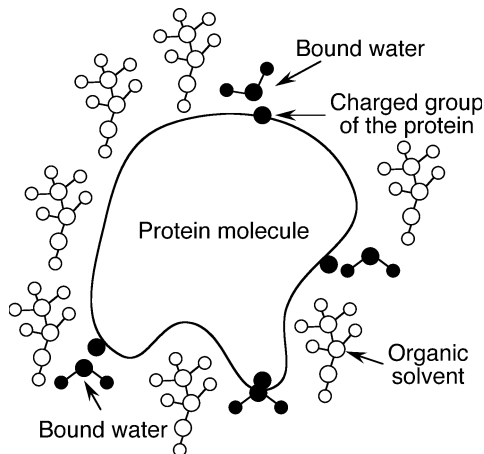


**Fig. 5.17** Protein molecule in organic solvent: only a few strongly bound water molecules remain attached to the protein molecule

al., 2002; Castellanos et al., 2002; Dong et al., 2002; Hilario et al., 2002; Moritz et al., 2002; Mui et al., 2002; Noinville et al., 2002), of peptides (Bianco et al., 2002; Gordon et al., 2002; Huang et al., 2002; Torres et al., 2002), and of DNA (Lindqvist and Graslund, 2001; Malins et al., 2002). In some cases, interactions were resolved at the level of individual amino acid residues (Kandori et al., 2002; Mezzetti et al., 2002; Zhang et al., 2002a).

Isotope-edited FTIR is particularly useful for the structural characterization of specific macromolecular regions (Fig. 5.15): e.g., the three phosphate stretching



vibrations of the phosphate calcium ATPase complex were detected at a background of 50,000 protein vibrations in an isotope exchange experiment (Barth, 2002).

Time-resolved step-scan FTIR spectroscopy enables the monitoring of conformational changes of proteins in the microsecond time scale (Bailey et al., 2002).

FTIR spectroscopy allowed to map out the nucleotide binding site of calcium ATPase (Liu and Barth, 2002). IR and FTIR spectroscopy are two of the only few methods suitable to monitor conformational changes of proteins under high pressure (Fig. 5.16; Dzwolak et al., 2002). FTIR spectroscopy on bacteriorhodopsin revealed a pre-melting conformational transition at 80 °C (Heyes et al., 2002). FTIR is also suitable to investigate the structure and hydration shell of protein molecules in organic solvents (Fig. 5.17; Costantino et al., 1995). Further, IR and FTIR spectroscopy was used for the characterization of irradiated starches (Kizil et al., 2002), and the determination of dihedral angles of tripeptides (Schweitzer-Stenner, 2002). Molecular changes of preclinical scrapie can be detected by IR spectroscopy (Kneipp et al., 2002). FTIR spectroscopy can serve as an optical nose for predicting odor sensation (van Kempen et al., 2002) and for chemical analysis of drinks (Coimbra et al., 2002; Duarte et al., 2002).

FTIR microscopy at a spatial resolution of 18  $\mu\text{m}$  resolved single cells (Lasch et al., 2002). IR spectroscopy is also a tool for discrimination between different strains or types of cells (Gaigneaux et al., 2002).

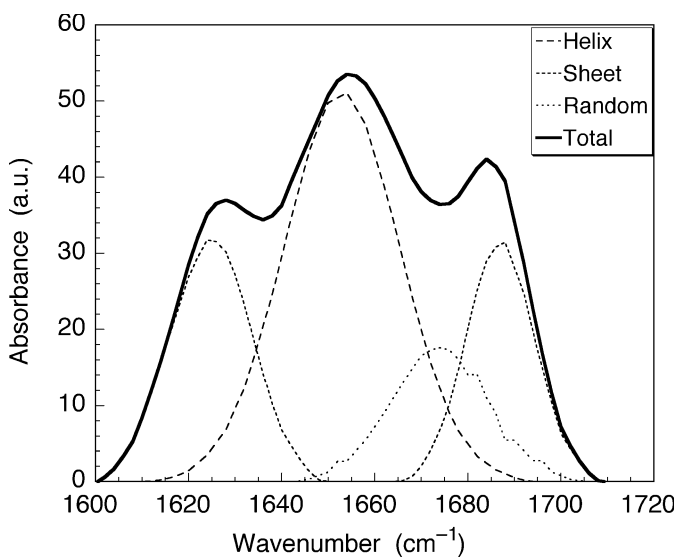


**Fig. 5.18** Decomposition of a FTIR spectrum into three components corresponding to helical structure, sheets and non-regular structure, respectively. Percentages of structure content and structural changes, e.g., due to protein denaturation, are quantifiable

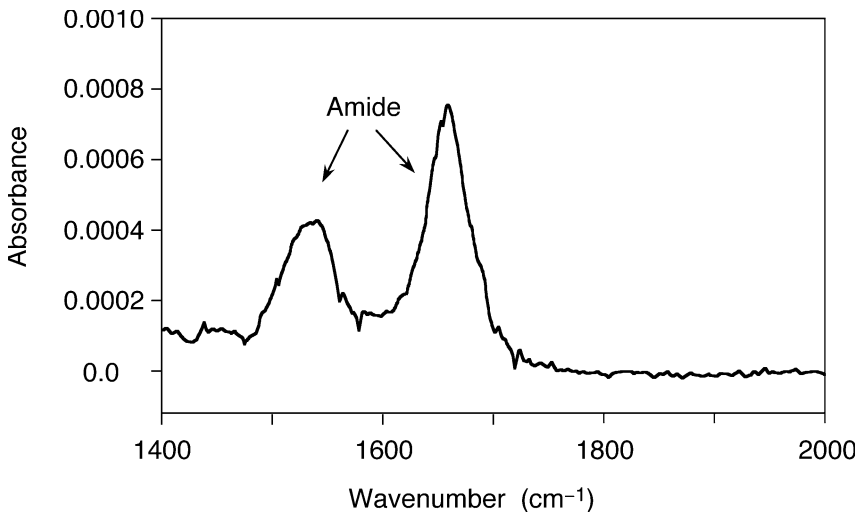


**Fig. 5.19** FTIR spectrum of a single molecular monolayer of A126C sperm whale myoglobin (Jiang et al., 1996). The peaks around  $1660\text{ cm}^{-1}$  and  $1530\text{ cm}^{-1}$  correspond to the amide I and amide II bands, respectively. The spectrum was acquired with a BioRad FTIR spectrophotometer equipped with a TGS detector

Fig. 5.18 shows an example for the decomposition of a FTIR spectrum of a protein into the components corresponding to helical, sheet-like and random coil-like (non-regular) structures, respectively. Such decompositions can be calculated, e.g., by fitting a linear combination of the base spectra for the secondary structure components to the measured spectrum.

Fig. 5.19 illustrates the amazing sensitivity of FTIR spectroscopy. The sample was only two monolayers of a protein. Since at very low sample absorbances it is quite difficult to avoid the sharp lines of water-vapor absorption, these measurements were taken in a nitrogen-filled chamber at two different, very low concentrations of water, and later the water spectrum was subtracted. With this procedure, average artifact and noise levels were reduced to less than 0.00003 absorbance units.

# 6 Electron microscopy

## 6.1 Transmission electron microscope (TEM)

Transmission electron microscopy utilizes the wave properties of moving electrons to generate highly resolved images of specimens.

### 6.1.1 General design

In 1986 the Nobel prize in physics was awarded by one half to Ernst Ruska for his fundamental work in electron optics, and for the design of the first electron microscope (EM), and by one half to Gerd Binnig and Heinrich Rohrer for their design of the scanning tunneling microscope (see Chap. 7). In some aspects, the

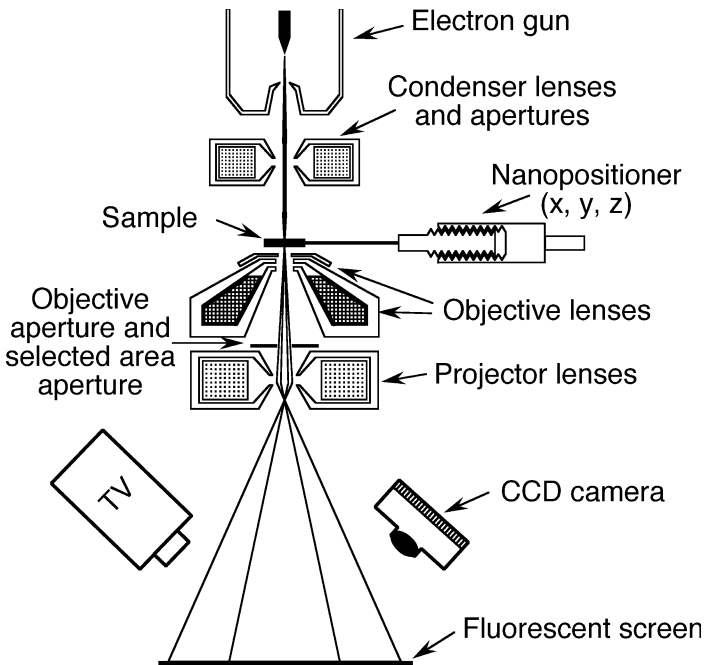


**Fig. 6.1** Transmission electron microscope (see text on pp. 107 and 109)

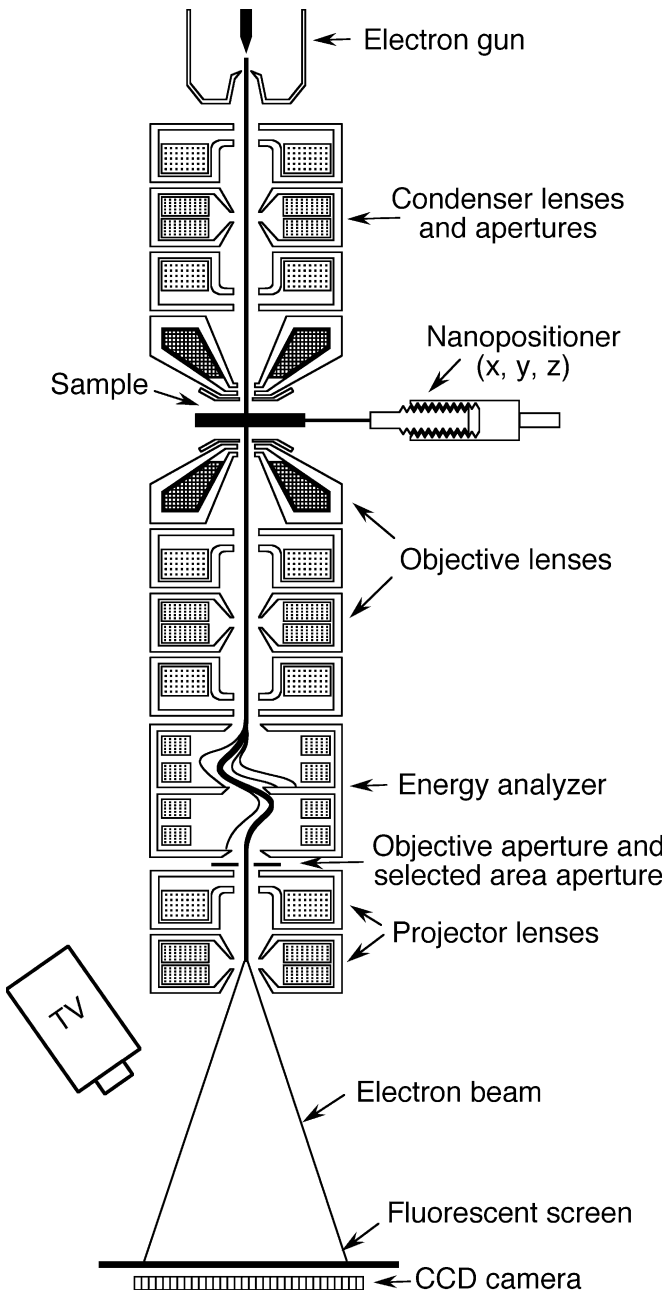


**Fig. 6.2** A more complicated design of a transmission electron microscope with an analyzer which can remove inelastically scattered electrons (see, e.g., LEO Elektronenmikroskopie GmbH, Oberkochen, Germany)

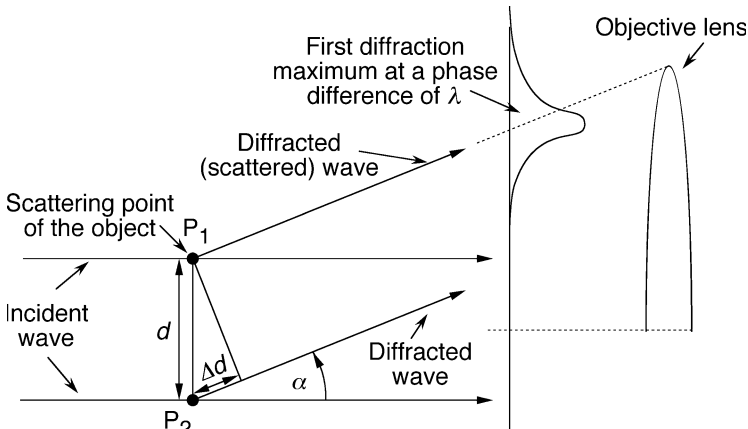


**Fig. 6.3** In order to resolve the two points  $P_1$  and  $P_2$  of an object, the objective lens has to catch the first diffraction maximum of the two points. It appears in the direction where the diffracted (scattered) waves from the two diffracting (scattering) points have a phase difference,  $\Delta d$ , of one wavelength. Eq. (6.1) was derived from this condition. A typical objective lens has a bore of 2 mm and a focal length of about 1–2 mm

operation of a transmission electron microscope (TEM) is comparable with that of a slide projector (Figs. 6.1 and 6.2): Electrons from the electron gun pass through condenser lenses that focus the electrons onto the sample. The electron beam shines through the specimen. Objective lenses and projector lenses magnify the transmitted beam and project it onto the fluorescent viewing screen. Impact of electrons excites the screen and produces a visible magnified image of the sample. This image is recorded with various detectors, such as a CCD camera.

### 6.1.2 Resolution

Electron microscopes enable significantly greater magnification and greater depth of focus than conventional optical microscopes. High-resolution TEMs permit spatial resolutions around 0.1 nm (1 Å) at acceleration voltages of 50–600 kV. Because of the wave nature of the electrons, the resolution limit,  $d$ , is given by the diffraction theory of coherent imaging:

$$d = \frac{\lambda}{n \sin(\alpha)}, \quad (6.1)$$

where  $\lambda$ ,  $n$ , and  $\alpha$  are the vacuum wavelength, index of refraction of the medium ( $=1$  in TEMs), and aperture half angle of the objective lens, respectively (Fig. 6.3). The de Broglie relation provides the wavelength,  $\lambda$ , of the electrons:

$$\lambda = \frac{h}{mv}, \quad (6.2)$$

where  $h = 6.6261 \times 10^{-34}$  J s,  $m$ , and  $v$ , are the Planck constant, electron mass, and electron velocity, respectively. For the relativistically high velocities of the electron beam we have to use Einstein's equations:

$$m = \frac{m_e}{\sqrt{1 - \frac{v^2}{c^2}}}, \quad E = mc^2, \quad (6.3)$$

and obtain:

$$\lambda = \frac{hc}{\sqrt{2E_0\Delta E + (\Delta E)^2}} = \frac{hce^{-1}}{\sqrt{2m_0c^2e^{-1}V + V^2}} \approx \frac{1.24 \text{ nm kV}}{\sqrt{(1022 \text{ kV}) \cdot V + V^2}}, \quad (6.4)$$

where  $e = 1.6022 \times 10^{-19}$  C is the elementary charge,  $m_e = 9.1094 \times 10^{-31}$  kg the electron rest mass,  $c = 2.99792 \times 10^8$  m s<sup>-1</sup> the speed of light in vacuum,  $E = E_0 + \Delta E$ ,  $E_0 = m_e c^2$ ,  $\Delta E = V \cdot e$  the kinetic energy of the electrons, and  $V$  is the applied acceleration voltage, typically 200 V – 200 kV. For a voltage of, e.g., 100 kV we find  $\lambda = 0.0037$  nm. In contrast to most light microscopes, TEMs have small objective lens apertures of typically  $\alpha = 1\text{--}2^\circ$ , and thus according to Eq. 6.1 the limit of spatial resolution is 0.1–0.2 nm in this example.

### 6.1.3 Electron sources

Thermionic electron guns (Fig. 6.4) and cold field emission guns (Fig. 6.5) are

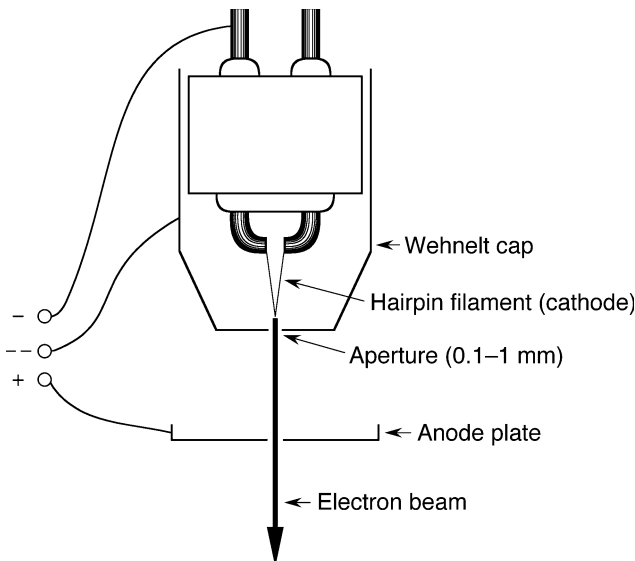


**Fig. 6.4** Thermionic electron gun (e.g., Structure Probe, Inc., West Chester, PA)

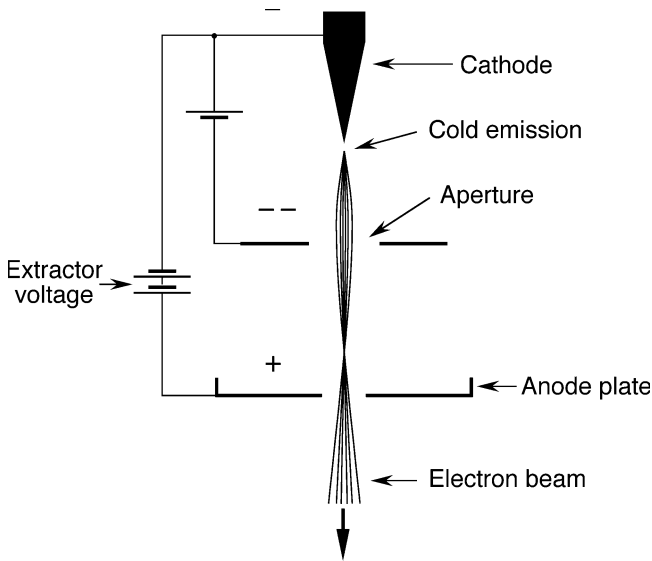


**Fig. 6.5** Cold field emission gun focusable with an electrostatic lens comprised of two apertures with different electrostatic potentials

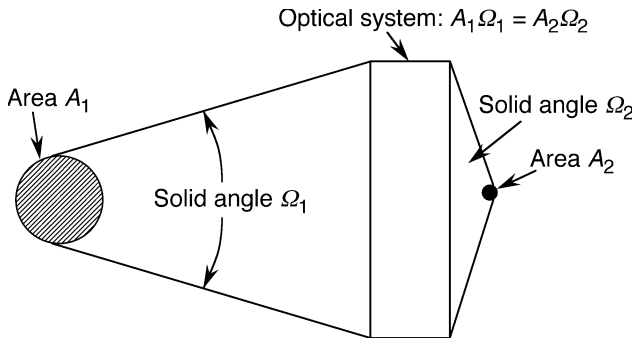


**Fig. 6.6** In the production of an image of an object by an optical system, the product of area,  $A$ , and aperture solid angle,  $\Omega$ , remains about constant

common electron sources. A considerable concern is the brightness and size of electron sources. Fig. 6.6 illustrates why this is important: For a light beam passing through an optical system, the product of area and aperture solid angle of radiation remains constant. Thus, a large source can be focussed on a small spot only by using a large aperture angle of the optical system. Considering the limited aperture angles of electron lenses, a source of small size and high brightness is required to obtain a sufficiently bright picture of the sample.

### 6.1.4 TEM grids

TEM grids (Fig. 6.7) should not get charged during measurement which would distort the electron path. Usually they are made from conductive chemically inert non-gassing materials suitable for high vacuum, such as platinum and platinum-iridium alloys.

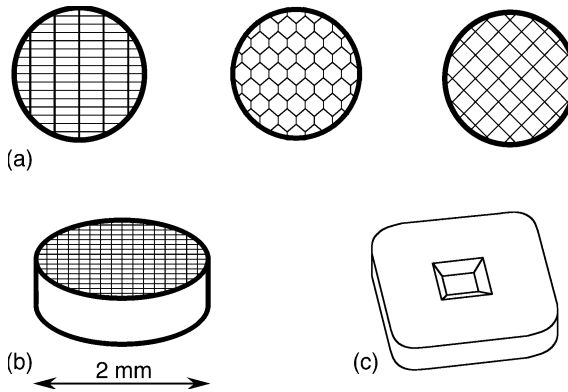


**Fig. 6.7** TEM grids. (a), (b) Some common patterns of TEM grids made from a variety of materials, e.g., platinum, silver, tungsten, molybdenum, stainless steel, or titanium. Among these materials, platinum is the chemically most inert, but expensive. (c) Silicon nitride “grid” with a single window (from SPI Supplies, West Chester, PA)

### 6.1.5 Electron lenses

There are magnetic (Figs. 6.8 and 6.9), electrostatic (Fig. 6.5) and compound lenses (Figs. 6.10 and 6.11). Electron lenses have some similar characteristics like optical lenses, such as focal length, spherical aberration, and chromatic aberration.

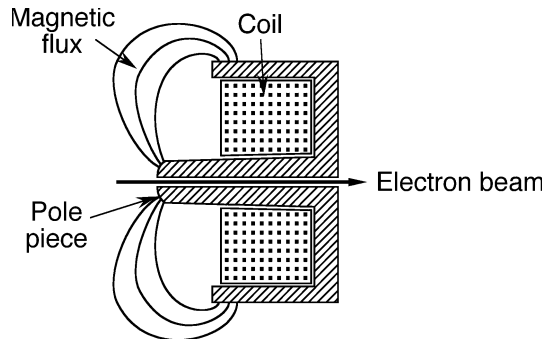


**Fig. 6.8** Ernst Ruska's pohlschuh lens: the circular electromagnet is capable of projecting a precisely circular magnetic field in the region of the electron beam



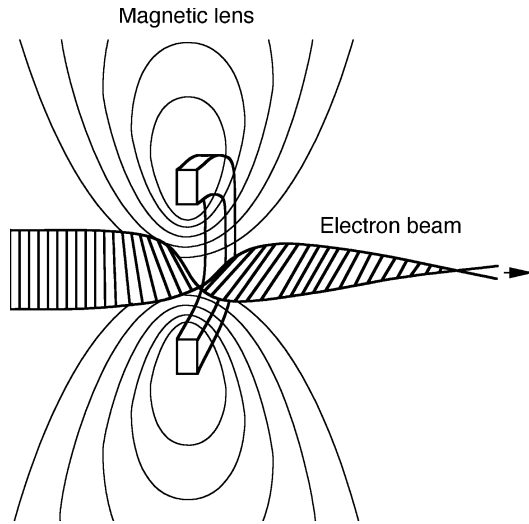


**Fig. 6.9** Function of a magnetic electron lens (pohlschuh lens). One of Ernst Ruska's major achievements was the development of electron lenses

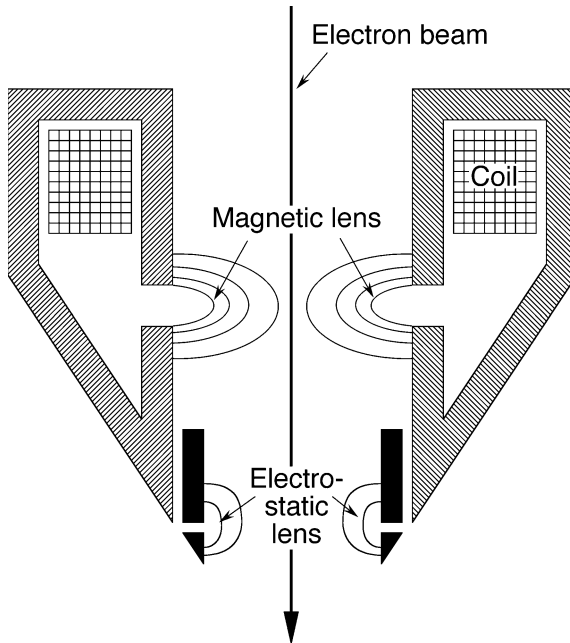


**Fig. 6.10** Compound lens made from magnetic and electrostatic lenses: the magnetic field forces the electrons on spiral-shaped trajectories; the electric field further decreases the diameter of the electron beam. Additional coils may serve for the correction of spherical aberration (not shown)

One important difference of electron optics compared with photon optics is the mutual charge interaction of electrons in the beam. That is why electron optics is often designed for beam paths with few if any intermediate crossovers.

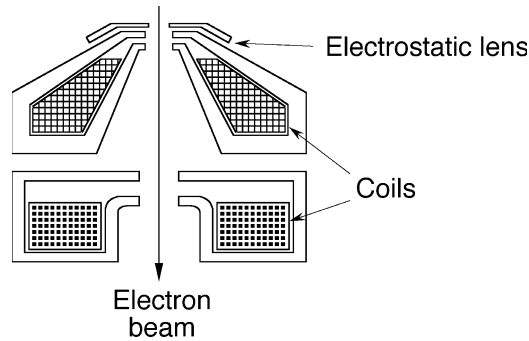


**Fig. 6.11** Compound lens made from magnetic and electrostatic lenses

In the beam booster technique (LEO Elektronenmikroskopie GmbH, Oberkochen, Germany; Fig. 6.12) a high energy beam is generated, passed through the condenser column of the microscope, and then decelerated and passed through the sample. The high energy electrons are less affected by stray magnetic and electric fields. Also the propagation of the electrons in the column is independent from the selected electron probe energy.

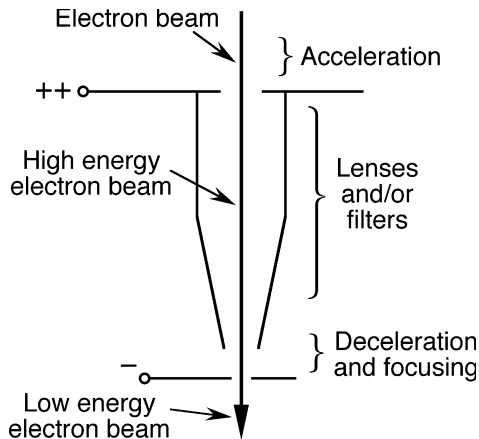


**Fig. 6.12** Beam booster (LEO Elektronenmikroskopie GmbH, Oberkochen, Germany). The electrons are accelerated to a high energy, passed through condenser lenses and filters, and then decelerated prior to interacting with the sample. This technique largely protects the electron beam against stray magnetic fields in the column of the microscope

### 6.1.6 Electron-sample interactions and electron spectroscopy

There are different sources of chromatic aberration: (a) inelastic scattering of the electrons by the sample changes their energy (Fig. 6.13), and (b) the electrons leave the electron source with slightly different energies. The dispersion of electron energy is measured with energy filters (Fig. 6.14). Similar dispersive elements serve for the reduction of chromatic aberration, i.e., the selection of monochromatic electrons (Figs. 6.14 and 6.15)

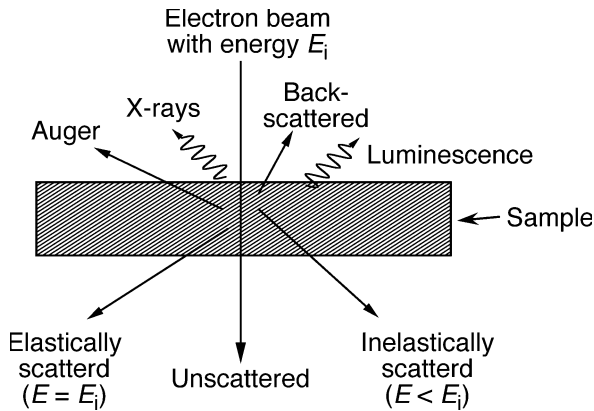


**Fig. 6.13** Interaction of the electron beam with the sample. Inelastically scattered electrons have changed both direction and energy and may generate a diffuse contrast-reducing background image unless these electrons are eliminated by energy filtering (see Fig. 6.15). Elastically scattered electrons interfere with another and with unscattered electrons to produce a phase contrast image

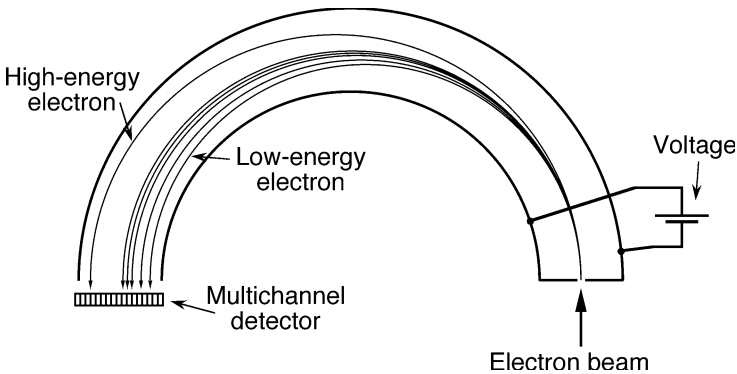


**Fig. 6.14** Determination of electron energies. The voltage applied between the two hemispherical electrodes disperses the electrons with respect to their velocity. In order to record a full spectrum for a large range of electron energies, the applied voltage is swept

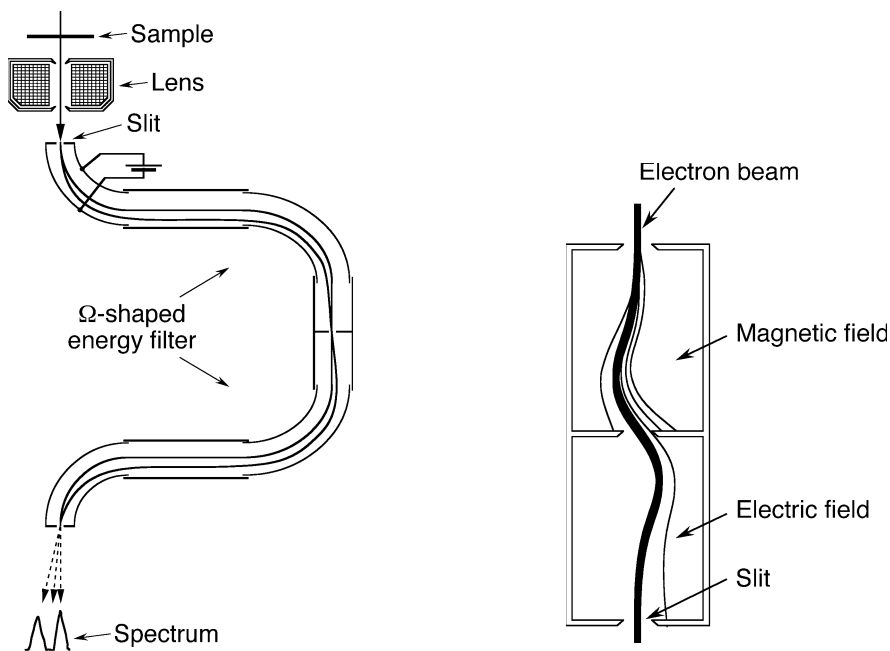


**Fig. 6.15** Two types of dispersive elements for energy filtering of the electron beam to eliminate inelastically scattered electrons, removing the diffuse background and thereby enhancing contrast, or to perform a chemical analysis of the sample. *Left:*  $\Omega$ -filter. *Right:* filter using magnetic and electric fields

Phase differences due to differences in the optical pathlength and electron scattering contribute to the contrast (Fig. 6.16). Often it is quite difficult to generate sufficient sample contrast at very high resolutions. A common method to visualize very small biological structures, such as single protein molecules, is negative staining: the sample is embedded in a stain with strong electron-optical properties (Fig. 6.17). Important innovations towards better contrast were the introduction of a technique for enhanced resolution (Haider et al., 1998) and the nanofabrication of solid-state Fresnel lenses for electron optics (Ito et al., 1998).

For biological samples a further important reason for the limitation of the resolution of TEMs is radiation damage, i.e., the destruction of the sample by inelastically scattered electrons. Since a certain number of electrons is necessary to obtain an image, this limit depends on the ratio of inelastically to elastically scattered electrons. Practically the resolution of frozen protein molecules is restricted by this reason to worse than about 5 Å. Negatively staining (Fig. 6.17) may provide some improvement, nevertheless atomic resolution of proteins is still beyond reach. It was suggested the theoretical possibility of a neutron microscope, for which the ratio of elastically to inelastically scattered particles may much better for isotope-exchanged proteins (Henderson, 1996). Another theoretic-

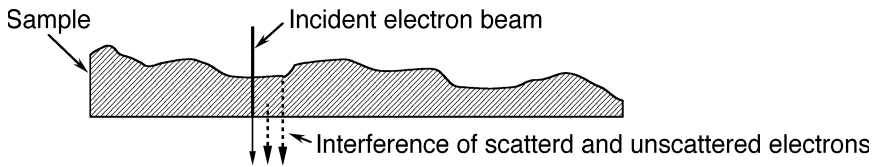


**Fig. 6.16** Generation of amplitude contrast. The electron beam is weakened at different points to a different degree by scattering and interference: elastically scattered electrons, i.e., those which have changed direction but not energy, interfere with each other and with unscattered electrons to produce a phase contrast image

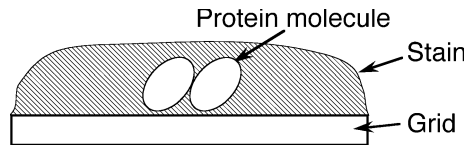


**Fig. 6.17** Edge-on view of a negatively stained sample: the TEM senses volumes of lower density in the stain

cal possibility to overcome the problem of the decay of the structure of sample during the measurement might be the use of ultrashort electron flashes on deeply frozen samples: if the duration of the flash is shorter than the time of mechanical movement of the protein molecule, its chemical decomposition would affect the obtained micrograph to a lesser degree.

### 6.1.7 Examples of biophysical applications

Fig. 6.18 demonstrates the resolution power of TEM for large protein complexes (Roseman et al., 1996; White et al., 1997; Ranson et al., 1998; Rye et al., 1999; Saibil, 2000a). Clearly differences between two conformations of GroEL/GroES are resolved. The TEM structure is consistent with the crystal structure.

Electron microscopy resolved the structure of the bacteriophage  $\Phi 29$  packaging motor (Simpson et al., 2000) and visualized the filamentous phage pIV multimer (Linderoth et al., 1997). Electron microscopy contributed to the understanding of conformational changes connected with the opening of an ion channel through a membrane (Saibil, 2000b), and with connexin trafficking (Gaietta et al., 2002).

In groundbreaking experiments Terry G. Frey and coworkers succeeded in the 3D-visualization of cell organelles using electron tomography. In this method the three-dimensional structure is calculated from a series of electron micrographs of samples tilted over a range of angles (Dierksen et al., 1992; Perkins et al., 1997a, 1997b; Frey and Mannella, 2000).

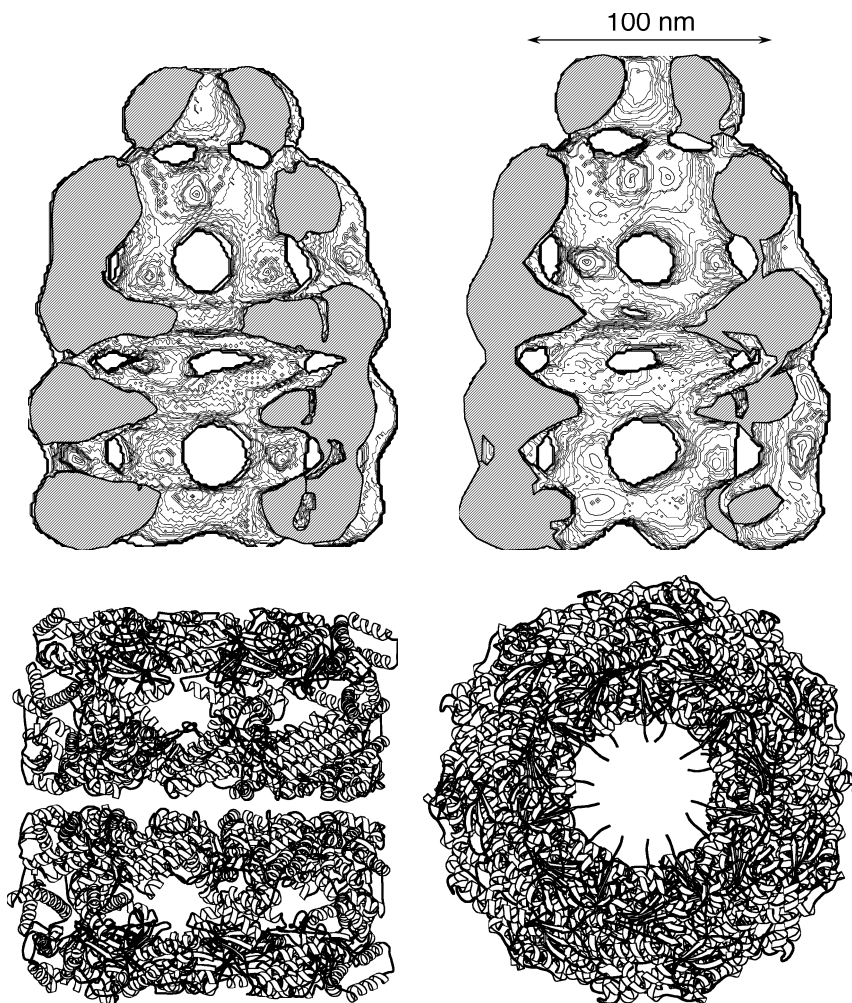


**Fig. 6.18** *Top*: electron micrograph of two conformations of GroEL/GroES at 30 Å resolution (Roseman et al., 1996; White et al., 1997; Ranson et al., 1998; Rye et al., 1999; Saibil, 2000a). *Bottom*: the X-ray crystal structure of GroEL at 2.4 Å resolution for comparison (Braig et al., 1994; Boisvert et al., 1996). The latter figure part was generated using MOLSCRIPT (Kraulis, 1991)

## 6.2 Scanning transmission electron microscope (STEM)

In contrast to TEMs, scanning transmission electron microscopes use an electron beam with only a few Å or nm diameter to scan the sample area (Fig. 6.19). The resolution is generally limited by the diameter of the electron beam at the location of the sample and radiation damage.

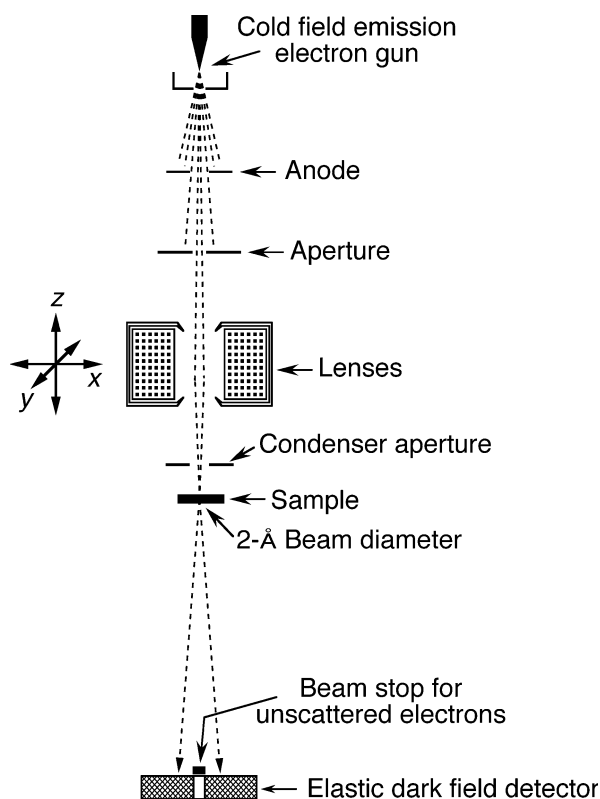


**Fig. 6.19** Scheme of a scanning transmission electron microscope: The objective lens focuses the electron beam onto a small sample section. Scattered electrons are detected with the elastic dark field detector. The STEM image is generated by moving the focussed beam over the specimen

Although the STEM was pioneered already in the thirties of last century, mainly by adding scan coils to a TEM (von Ardenne, 1940), significant developments have taken place in the last years: electron optics has been significantly improved and the resolution increased by several orders of magnitude. Nowadays high resolution STEMs offer unprecedented capability for the characterization of biomolecules, allowing structure to be determined with up to sub-nm resolution.

Similarly to TEMs, the STEM can employ various energy filtering techniques for chemical analysis and improvement of resolution, e.g., by removing unscattered electrons in inelastic dark field imaging (Fig. 6.20). Many STEM have both capabilities, elastic dark field imaging (Fig. 6.19) and inelastic dark field imaging (Fig. 6.20). A third mode is bright field detection where electrons are collected through a small aperture placed on the optical axis and an energy

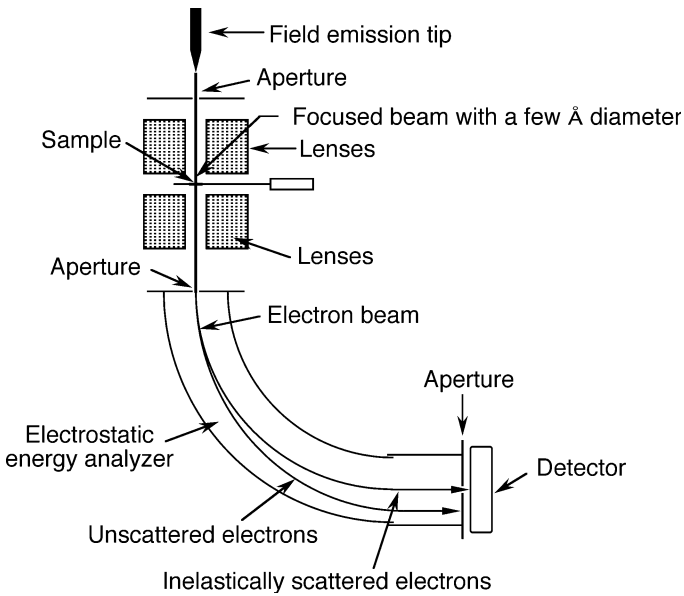


**Fig. 6.20** Example of a scanning transmission electron microscope with an energy filter: inelastically scattered electrons, i.e., those which have changed both energy and direction upon interaction with the specimen, are collected yielding the inelastic dark field image. Electrons with different energies are separable by their trajectories with different curvatures in the electric field applied perpendicular to the flight direction

filter removes those electrons that have lost energy, i.e., low-angle elastically scattered and unscattered electrons are collected to produce the image.



# 7 Scanning probe microscopy

Scanning probe microscopes generate a highly-resolved image of the specimen by scanning it with a small mechanical, electrical, optical, thermal, or other probe.

## 7.1 Atomic force microscope (AFM)

The AFM was invented by Gerd Binnig, Christoph Gerber, and Calvin F. Quate in the mid-eighties (Binnig et al., 1986), and is one type of the so-called scanning

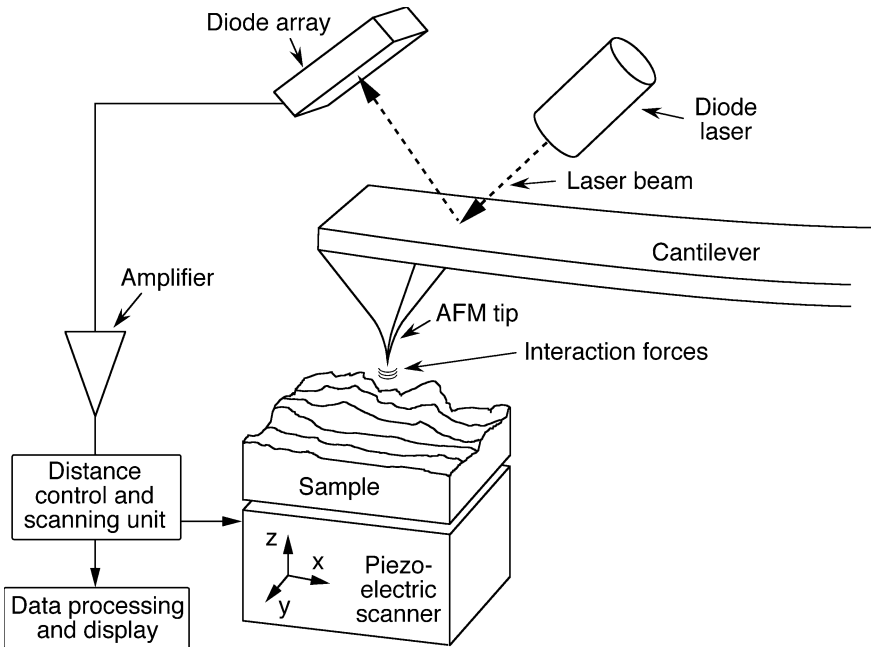


**Fig. 7.1** Principle of operation of an atomic force microscope. A very sharp tip attached to a tiny cantilever probes the sample surface. An optical system comprised of diode laser and detector, e.g., a diode array or a position-sensitive diode, senses the bending of the cantilever and thereby the distance-dependent tip-sample interaction force. For scanning the surface, the sample is moved by the piezoelectric scanner (Binnig et al., 1986)

probe microscopes (SPMs) which also include scanning tunneling microscope (STM; Sect. 7.2; Binnig et al., 1982a, 1982b, 1983; Binnig and Rohrer, 1987), scanning near-field optical microscope (SNOM; Sect. 7.3), scanning thermal microscope (SThM; Sect. 7.4), and the scanning ion conductance microscope (SICM; Sect. 7.4). The AFM is used in both industrial and fundamental research to obtain atomic-scale images of metal surfaces and nanometer-scale images of the three-dimensional profile of the surface of biological specimens. It is a very useful tool for determining the size and conformation of single molecules and aggregates adsorbed on solid surfaces. The AFM scans the sample with a tiny tip mounted on a small cantilever (Fig. 7.1). It measures the small force of interaction between tip and sample surface by sensing the reflection changes of a laser upon cantilever movement caused by interaction with the sample. An image of the sample surface relief is recorded using piezoelectric translation stages that move the sample beneath the tip, or the tip over the sample surface, and are accurate to a few Å.

Note the similarity of the AFM (Fig. 7.1) to the stylus profilometer (Fig. 7.2) and to the STM (Fig. 7.19). Actually, the idea of AFM is based on the design of stylus profilometers, but the AFM can reveal the sample relief with subnanometer resolution.

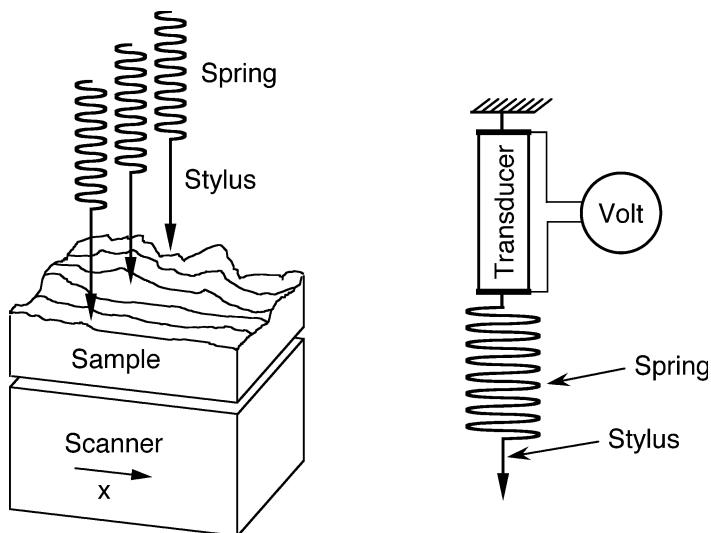


**Fig. 7.2** Stylus profilometer for comparison with the AFM. A set of styli probes the sample which is drawn below the set of styli. The small motions of the styli are transformed into an electrical signal by linear, variable transducers. Step heights of down to a few 10 nm are resolvable

The force of tip-sample interaction (Fig. 7.3) has a magnitude of typically only a few pN – nN. That is why the cantilever must have a small mass, and the

weight-bearing parts of the AFM (Figs. 7.4 and 7.5) have to be rigid and equipped with a good vibrational damping. Three support posts in the design of Fig. 7.4 reduce wobbling. The xyz-translation stages for coarse adjustment of the piezoelectric scanner with the sample on top are engineered for little wobbling as well. The whole AFM is placed on a rubber support preventing transmission of high frequency vibrations from the laboratory (not shown). A low force of interaction is crucial for high resolution force microscopy on soft biological specimens. Low spring constants of the cantilever may facilitate this purpose at the expense of resolution, but the most common way of gentle measurement is to reduce the intensity and duration of contact by oscillating the cantilever, as will be explained later (Fig. 7.13).

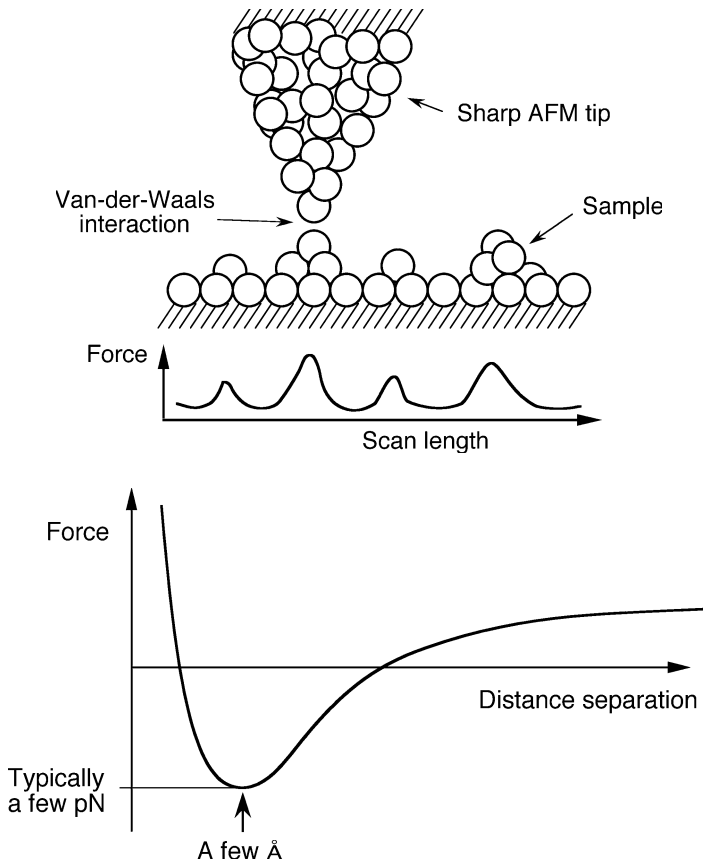


**Fig. 7.3** When a small tip approaches a surface, it experiences the van-der-Waals force which is attractive at a distance of a few Å, but repulsive at very short distances (see, e.g., Chap. 3 in Nölting, 2005). Additional Coulomb forces may play a role when the AFM tip was charged

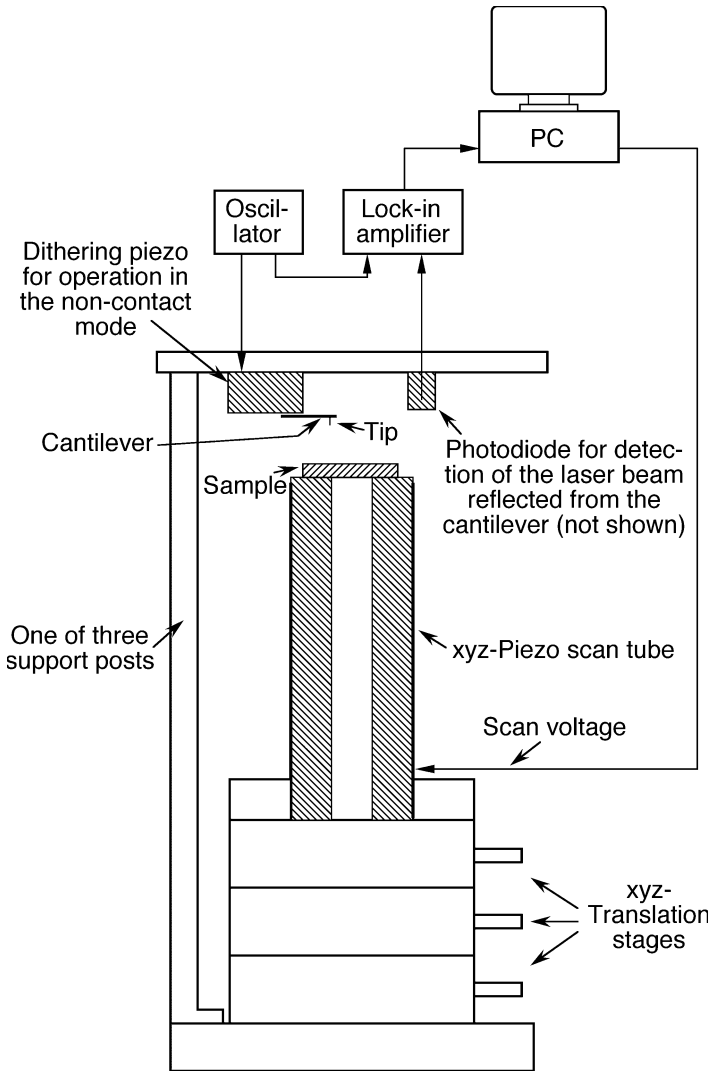


**Fig. 7.4** Design of an AFM. The sample spot of interest is positioned near the tip by coarse xyz-translation stages. The piezoelectric scanner (see also Fig. 7.5) then heightens the sample position further till the tip starts to interact with the sample. It allows motion control of the tip with subnanometer precision. A photodiode detects the reflection changes of a laser beam from the cantilever upon approach of tip to sample. In this example, the cantilever is mounted to a dithering piezo element which excites oscillations of the cantilever. The lock-in amplifier detects changes of these oscillations due to tip-sample interactions. The sample surface is scanned by sample movement in horizontal direction by the piezoelectric scanner. The scanner also adjusts the relative height of the cantilever during scanning to avoid crashes of the tip with the sample surface. Such crashes can damage the tip and then cause artifacts (see Fig. 7.6)

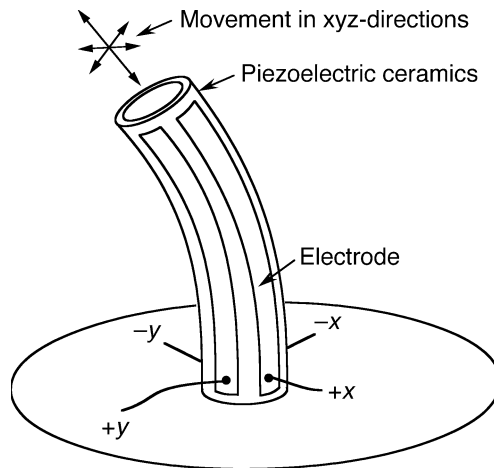


**Fig. 7.5** Principle of operation of the xyz-piezoelectric scanner, a ceramic positioning device which changes its size in response to a change in applied voltage. A voltage change at the x- or y- electrodes causes bending in the horizontal plane; contraction and expansion are generated by simultaneous application of x- and y-voltage

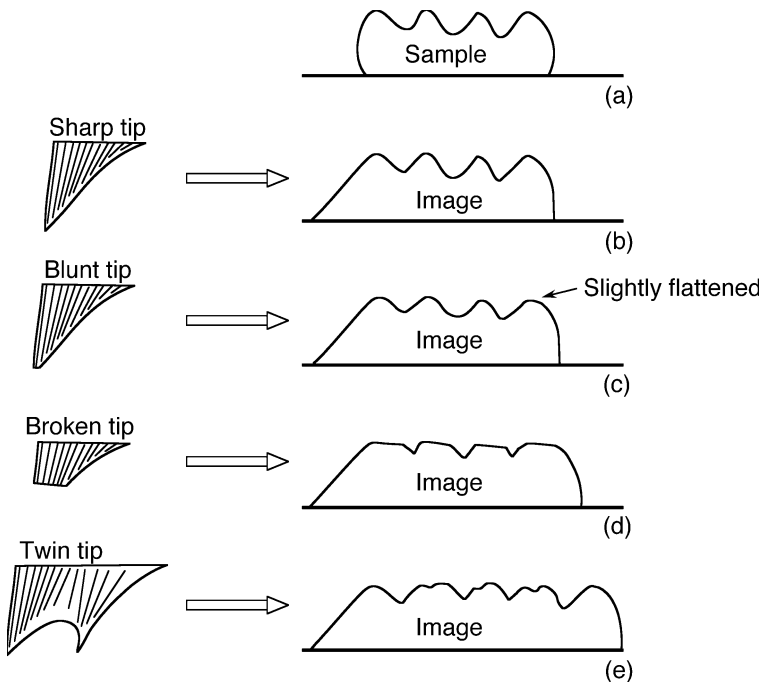


**Fig. 7.6** Artifacts caused by different shapes of the AFM tip. Blunt tips and broken tips give rise to an seemingly flattened sample relief which may be difficult to recognize as an artifact

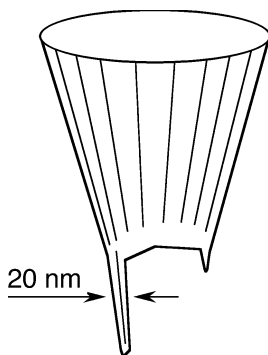


**Fig. 7.7** Tungsten tip, made by sharpening a tungsten wire by dragging it over a plate coated with alumina. This self-made tip may also be used for STMs (see Sect. 7.2)

Obviously a robust and sharp single tip is essential for this method. Typical apex radii of commercial tips are  $\approx 10\text{--}20$  nm. Fig. 7.6 depicts common types of artifacts observed when using worn out tips, broken tips, or probes with more than one tip.

One can make tips themselves by grinding a tungsten wire on a sheet covered with alumina (Fig. 7.7). These tips are also suitable for STM (Sect. 7.2), but the tip shape is not very reproducible and tungsten is not very hard.

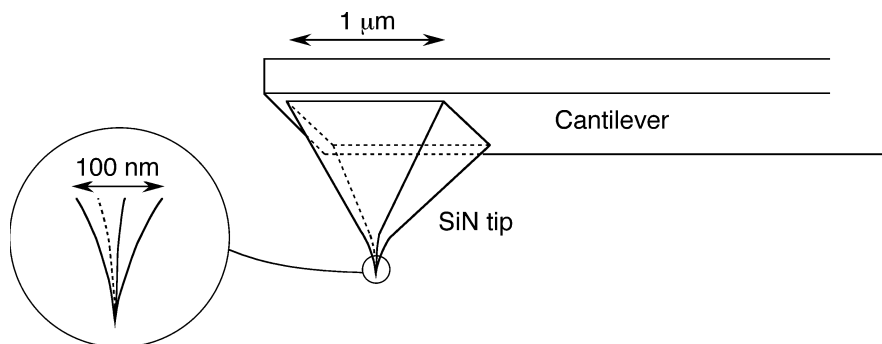


**Fig. 7.8** Sharpened pyramidal silicon nitride tip. SiN is extremely hard, and tips can be engineered with radii of only a few nm

Silicon nitride tips are the currently available tips with highest robustness (Fig. 7.8). Sharper tips with quite reproducible shape are made from silicon which is relatively fragile, however (Fig. 7.9a). Even sharper tips for application on samples with particularly deep structures are manufactured by attaching a high

density carbon fiber to a silicon tip (Fig. 7.9b). Sharp cantilevers for the examination of very rough surfaces (Fig. 7.10) and cantilevers with trigonal design for the purpose of high resistance against torsion (Fig. 7.11) are supplied, e.g., by Olympus Optical Co. (Tokyo).

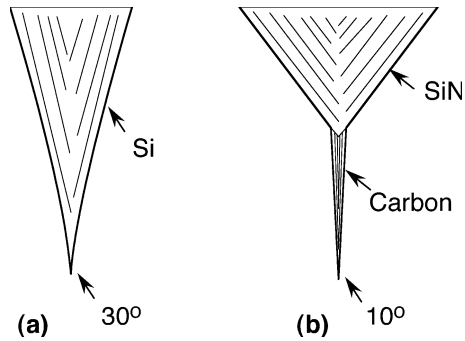


**Fig. 7.9** (a) AFM tip made from silicon. (b) Silicon tip with a high density carbon fiber attached to it

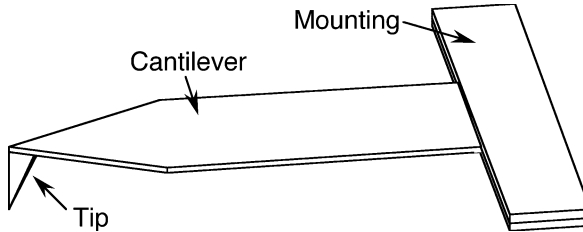


**Fig. 7.10** Sharp cantilever geometry for very rough samples (e.g., Olympus Optical Co., Tokyo)

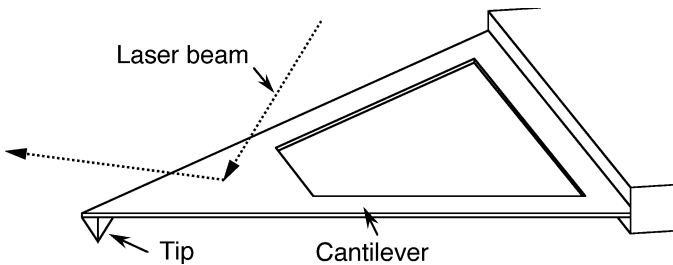


**Fig. 7.11** A trigonal design of the cantilever (e.g., Olympus Optical Co., Tokyo) causes a better stability against torsion, compared with rod-shaped cantilevers

The life of the AFM tip decreases very rapidly with applied force (Fig. 7.12). High aspect-ratio tips made from silicon or carbon fiber are generally less durable than low aspect-ratio tips made from silicon nitride.

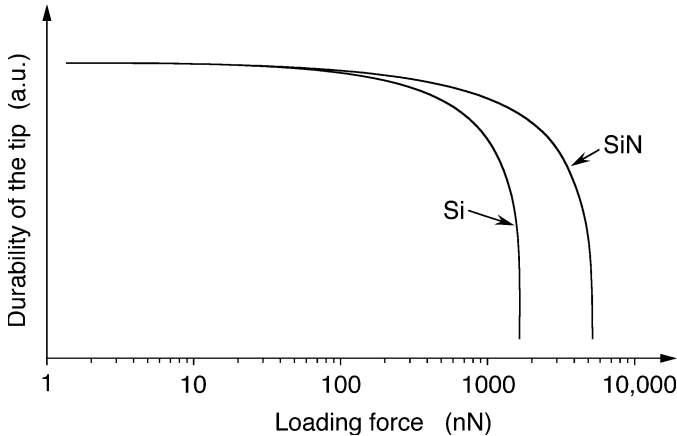


**Fig. 7.12** Example for the wear of two AFM tips due to surface load

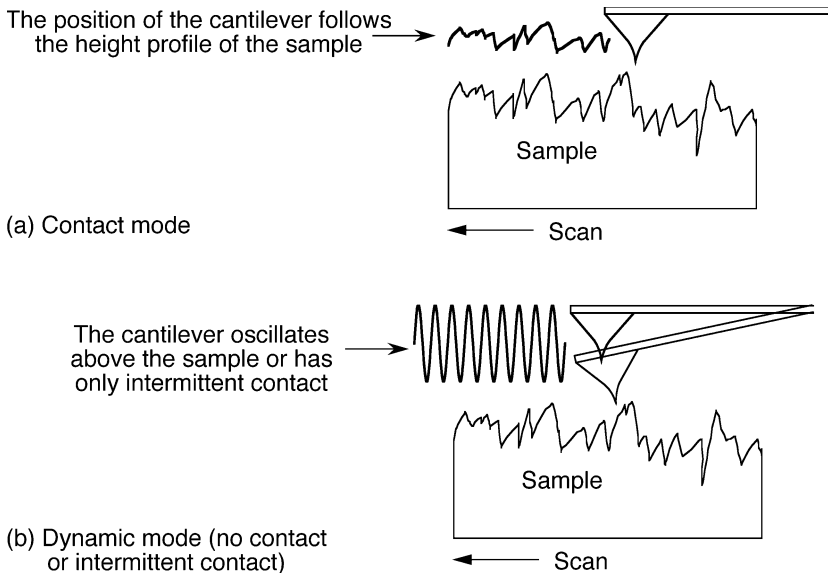


**Fig. 7.13** (a) Contact mode: the cantilever follows the height profile of the sample. (b) Dynamic mode: the cantilever has only intermittent contact or oscillates above the sample. In the latter mode, oscillations are excited by a piezo crystal and the forces between tip and sample are very small. This mode permits truly atomic resolution (Giessibl, 2000)



There are two common modes of operation of AFMs (Fig. 7.13): the contact mode and the dynamic force mode. In the contact mode, the probe tip is in continuous contact with the sample surface. The force the cantilever exerts on the substrate in contact mode may perturb the surface of soft biological materials. In the gentler dynamic mode, the probe tip only oscillates up and down as it is scanned over the sample surface. Two sub-modes may be distinguished for the dynamic force mode, the non-contact sub-mode in which the distance between tip apex and sample surface is always larger than the van-der-Waals distance, and the tapping sub-mode in which the tip has intermittent contact.

As pointed out, a high degree of protection against external high-frequency vibrations is obviously crucial for the operation scanning probe microscopes with atomic resolution. Fig. 7.14 shows a further solution to this problem. Here the AFM is made from very thick and short plates of steel and the AFM is placed on three rubber balls that do not transmit fast vibrations. Another technique of efficient vibrational damping is to hang the AFM on a rubber string (Fig. 7.15).

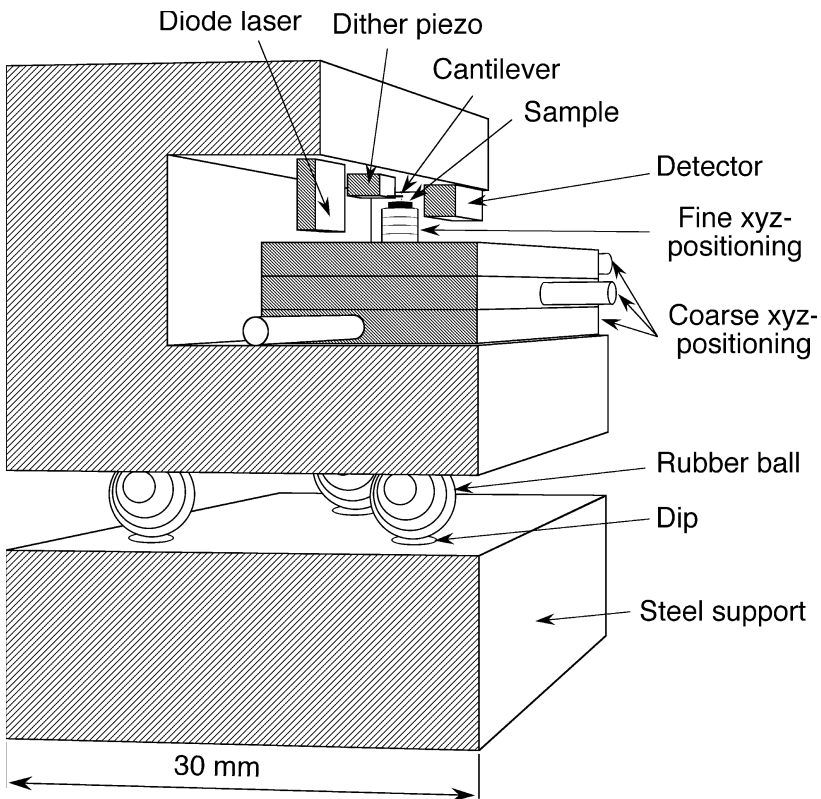


**Fig. 7.14** Robust design of an AFM with atomic resolution. The vibrational damping is attained by a very rigid construction and an elastic support in form of three rubber balls

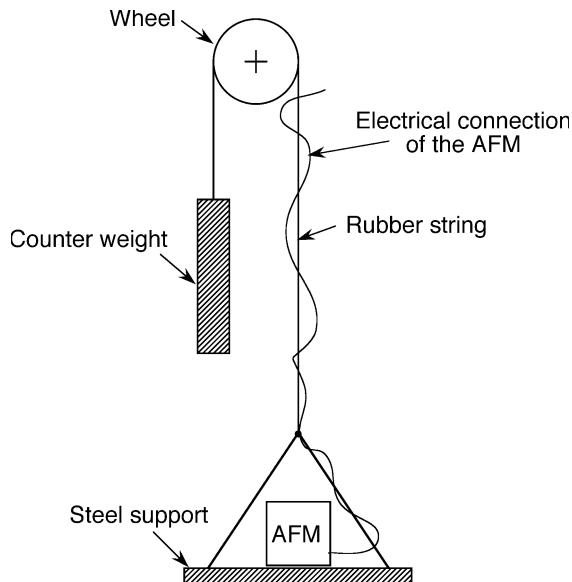


**Fig. 7.15** “Hanging AFM”: vibrational isolation of an AFM by hanging it on a rubber string

Important biological applications of AFMs were the direct observation of the structure of DNA (Lindsay et al., 1989) and the monitoring of actin filament dynamics in living cells (Henderson et al., 1992). The direct visualization of a DNA glycosylase searching for damage shows that the glycosylase interrogates DNA at undamaged sites by introducing drastic kinks (Chen et al., 2002b). Intramolecular triplex DNA formation results in a kink in the double helix path (Tiner et al., 2001). A sharp DNA bend is induced by binding of integration host factor (IHF) to the region between the upstream regulatory sequence and the promoter sequence (Seong et al., 2002). Single DNA molecule force spectroscopy can discriminate between different interaction modes of small drug molecules with DNA by measuring the mechanical properties of DNA and their modulation upon binding of small drug molecules (Krautbauer et al., 2002) and dye molecules (Kaji et al., 2001). A decrease of the ionic strength from 50 mM to 1 mM resulted in a change of the number of nodes (crossings of double helical segments) of a supercoiled 3000-bp piece of DNA from a 15 to one or two nodes (Cherny and Jovin, 2001). High resolution fluorescence imaging of  $\lambda$ -phage DNA molecules, intercalated with the dye YOYO-1, by a SNOM/AFM (SNOM, scanning near-field optical microscope; see Sect. 7.3) resolved the distribution of the dye (Kim et al., 2001).

AFM proved to be a very useful tool for the study of proteins, yielding some unique insights into structure and physical properties:  $\beta$ -Lactoglobulin forms fine-stranded aggregates at pH 2 with the diameter of strands being ca. 4 nm (Ikeda and

Morris, 2002). AFM technology was used to map out the electrostatic potential of the transmembrane channel OmpF porin (Fig. 7.16; Philippssen et al., 2002). AFMs gave crucial topological information of blood cell adhesion on different sensor materials (Hildebrand et al., 2001). Ac-GWWL(AL)nWWA-Etn peptides induce the formation of extremely ordered domains in some biologically relevant membranes (Rinia et al., 2002). The heads of bacteriophage  $\Phi$ KZ and T4 have different compressibilities (Matsko et al., 2001). Atomic force microscopy resolved fusion pores in the apical plasma membrane in live pancreatic cells (Cho et al., 2002) and visualized the growth of Alzheimer's  $\beta$ -amyloid-like fibrils (Goldsbury et al., 2001). Cardiac muscle and skeletal muscle exhibit different viscous and elastic properties as determined by atomic force microscopy. Cardiac cells are stiffer (elastic modulus =  $100 \pm 11$  kPa) than skeletal muscle cells (elastic modulus =  $25 \pm 4$  kPa; see Mathur et al., 2001). Atomic force microscopy allowed to visualize the structure of biomolecules, e.g., the native chaperone complex from *Sulfolobus solfataricus*, in solution under physiological conditions providing a nanometer resolution topographic image of the sample (Valle et al., 2001). It is also an excellent technique to study the initial events of mutual cell adhesion (Razatos, 2001). An AFM image of a monomolecular film of bovine serum albumin shows individual monomers and dimers (Fig. 7.17; Gunning et al., 1996; Morris et al., 1999).

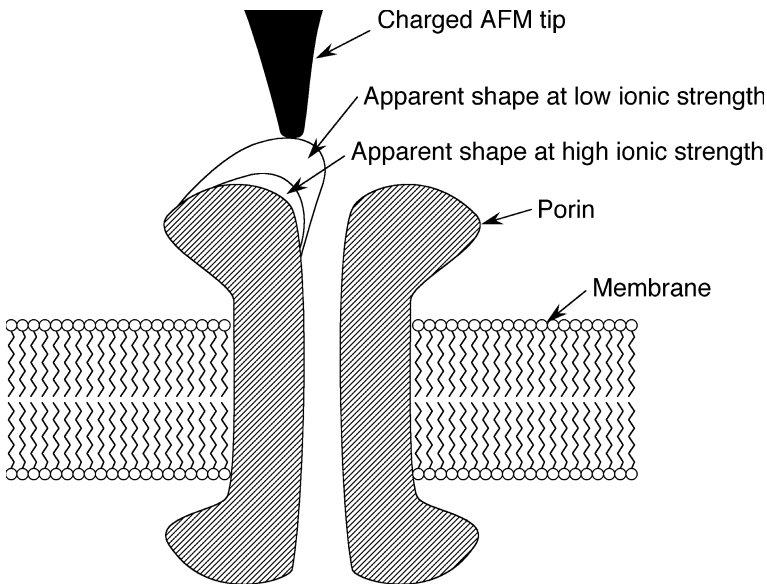


**Fig. 7.16** Imaging the electrostatic potential of the transmembrane channel OmpF porin (Philippssen et al., 2002). Different apparent shapes of the porin are observed at different ionic strengths. These differences reflect changes of the electrostatic potential which is experienced by the charged tip of the AFM

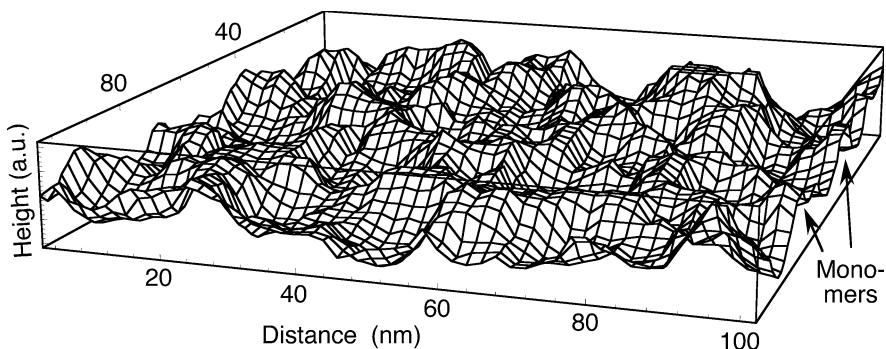


**Fig. 7.17** AFM image of a monomolecular film of the protein bovine serum albumin (BSA,  $M_{w, \text{monomer}} = 66$  kDa) adsorbed at an oil/water interface (Gunning et al., 1996; Morris et al., 1999). Individual monomers and dimers of BSA can be seen

AFMs are also very useful for the manipulation of macromolecules: proteins may physisorb to the AFM tip and can then be lifted and manipulated (Fig. 7.18). The sensitivity of the AFM cantilever, to forces in the pN range, was exploited to measure folding-unfolding forces within single protein molecules and breakaway forces between different biomolecules (Jiao et al., 2001; Allison et al., 2002). Atomic force microscopy has yielded tantalizing insights into the dynamics of protein self-assembly and the mechanisms of protein unfolding (Furuike et al., 2001; Yip, 2001). For further, similar applications of AFM technology see Chap. 8.

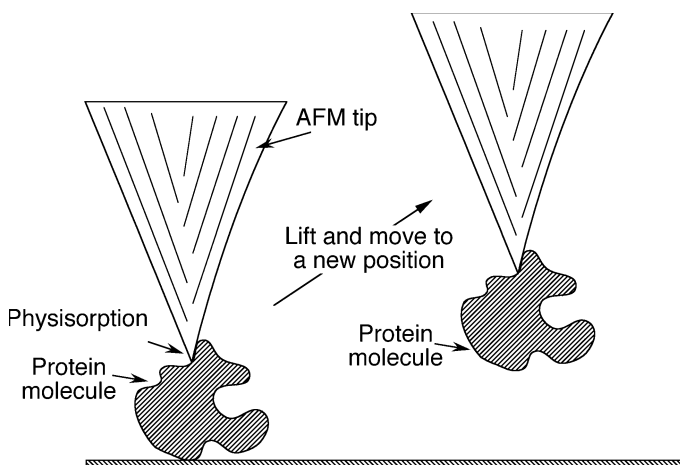


**Fig. 7.18** Manipulation of a protein molecule with an AFM: The tip is lowered till it touches the macromolecule. Due to the attractive action of the van-der-Waals interaction, the macromolecule sticks to the tip and can be lifted and moved to a different place

## 7.2 Scanning tunneling microscope (STM)

In 1986 Gerd Binnig and Heinrich Rohrer were awarded the Nobel Prize for Physics for the groundbreaking invention of the STM. It was the first member of the family of scanning probe microscopes (SPM) that can characterize surface morphology with atomic resolution. In contrast to the AFM, its principle of operation (Fig. 7.19) requires electrically conductive samples. A sharp tip located on a flexible cantilever is used to probe the distance between the tip and sample surface, as judged by the tunneling current (Fig. 7.20). Since the tunneling current also depends on the chemical nature of sample and tip, the STM also serves for characterization of electronic properties of solid samples.

Significant complications on the way towards higher resolution of proteins are the undesired excitation of the soft biological material by the high current of STMs, typically pA–nA, and the distribution of conductivity within the sample distorting the image (Fig. 7.21). Low currents and stable attachment of the sample to the support are required for high resolution images of biological macromolecules.

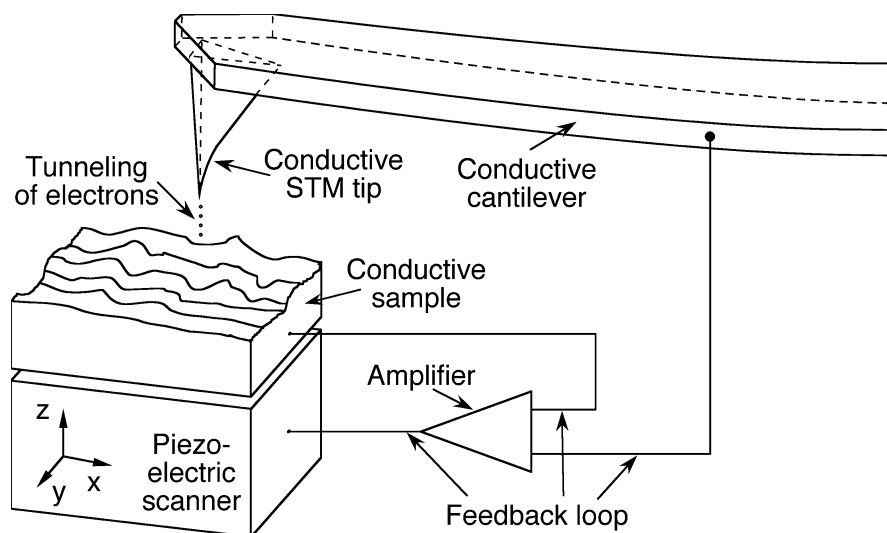


**Fig. 7.19** Principle of operation of STMs. A finely sharpened electrically conductive tip is first positioned within about 1 nm of the sample by mechanical translation stages (not shown) and the piezoelectric scanner. At this small separation, electrons tunnel through the gap between tip and sample (Fig. 7.20). The tunneling current depends on the applied bias voltage between tip and sample, the distance, the tip shape, and the chemical compositions of sample and tip. The feedback loop ensures constant height or constant current. Tunneling current and feedback voltage are a measure of surface morphology and composition (Binnig et al., 1982a, 1982b, 1983; Binnig and Rohrer, 1987)

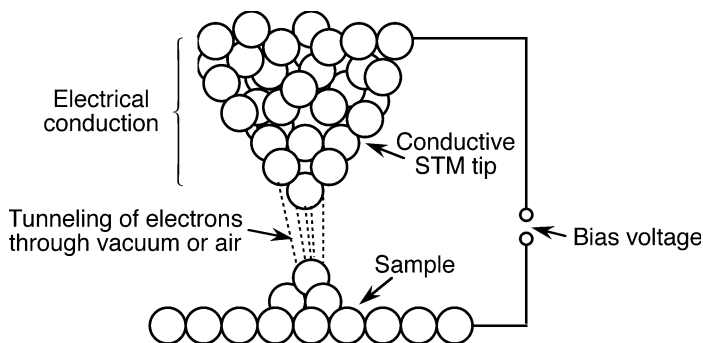


**Fig. 7.20** When the distance between conductive tip and conductive sample is lowered to a few Å, electrons can traverse the gap with some transmission probability. The STM measures not purely distance like the AFM, but the local density of electronic states

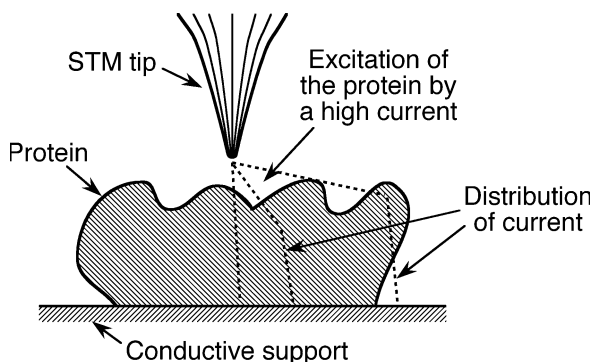


**Fig. 7.21** Different possible current paths in STM measurements of extended biological structures lower the resolution and complicate the interpretation of data

Similar as in atomic force microscopy, the quality of the tip is crucial for a high resolution (Figs. 7.7–7.11, 7.22). Commonly tips are micromachined and/or electrochemically etched and have apex radii of 5–100 nm.

STM images of a 1:1 mixture of K344C cytochrome P450<sub>cam</sub> / putidaredoxin adsorbed on gold (111) showed a regular array of pairs of the two proteins (Djuricic et al., 2002). I21C/E25C plastocyanin essentially maintains its native redox properties upon immobilization onto a gold substrate as shown by the full potentiostatic control of the electron transfer reaction during STM imaging (Andolfi et al., 2002). Scanning tunneling microscopy demonstrated that the otherwise nearly linear mammalian metallothionein-2 molecule bends by about 20 degrees at its central hinge region between the domains in the presence of ATP (Maret et al., 2002). Electrochemical scanning tunneling microscopy on thiol-derivatized DNA immobilized on a gold (111) single crystal surface showed

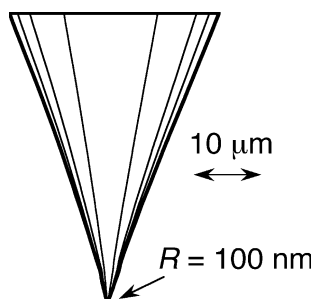


**Fig. 7.22** An etched tungsten tip for STM (see also Figs. 7.7–7.11)

potential-dependent orientation changes of the DNA in the potential range from 200 to 600 mV (Zhang et al., 2002b). A STM study of morphology and electron transport features in cytochrome c offers evidence for sequential discrete electron-tunneling effects (Khomutov et al., 2002). Tunneling in proteins adsorbed onto a conductive substrate may depend on the applied potential (Facci et al., 2001). The resistance of a single octanedithiol molecule is 900 M $\Omega$  (Cui et al., 2001). The ability to site-specifically introduce cysteine residues and to engineer tags, such as histidine tags and biotin-acceptor peptides, allow the creation of ordered immobilized protein structures that can be characterized both electrochemically and topographically by using scanning probe microscopy and cyclic voltammetry (Gilardi et al., 2001).

## 7.3 Scanning nearfield optical microscope (SNOM)

### 7.3.1 Overcoming the classical limits of optics

SNOMs (Figs. 7.23–7.25), also known as NSOMs, utilize a light source with a diameter smaller than the wavelength of the light (Synge, 1928; Ash and Nicholls, 1972; Pohl et al., 1984; Betzig et al., 1986, 1991, 1992; Toledo-Crow et al., 1992; Williamson et al., 1998; Egawa et al., 1999; Heimel et al., 2001). By means of this technological innovation they achieve a resolution which may be well beyond the resolution limit,  $d$ , of classical Abbe-Fourier optics (see also Sect. 6.1.2):

$$d = \frac{\lambda}{n \sin(\alpha)}, \quad (7.1)$$

where  $\lambda$ ,  $n$ , and  $\alpha$  are the vacuum wavelength, refractive index of the medium between sample and objective lens, and half angle of aperture, respectively. For visible light with  $\lambda=500$  nm,  $n=1.6$ , and  $\alpha$  near  $90^\circ$ , we obtain a resolution limit of classical optics of about 300 nm. Using UV light and image processing can

yield improvement beyond this, but it is clear from Eq. 7.1, that classical optics can hardly penetrate the 100-nm resolution barrier. SNOMs have been the first optical microscopes that significantly overcame the limit of Eq. 7.1.

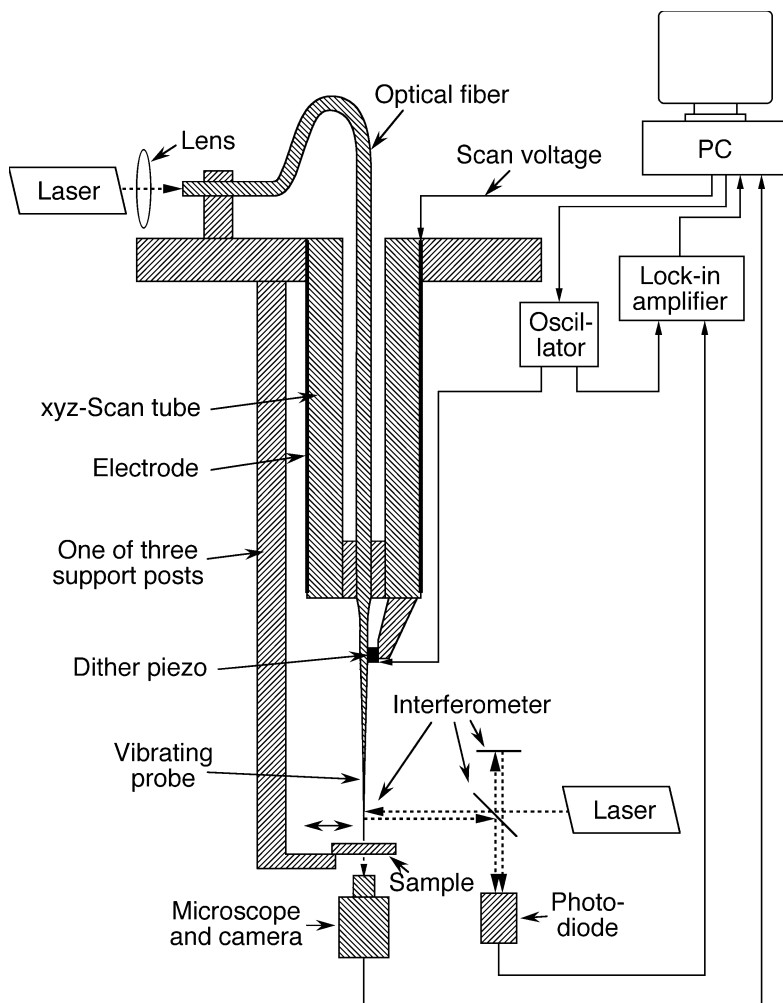


**Fig. 7.23** A design of a SNOM. An optical probe emits light from points above the 2D sample. The subwavelength probe tip takes advantage of the physical effect of optical tunneling. In this SNOM it is made using a metal coated tapered glass fiber: a first taper for the probe was manufactured by melt-drawing, and a second taper at the very end of the probe was etched. The damping of the horizontally vibrating SNOM probe caused by shear forces is taken as a measure for the distance from the sample. A shear force feedback loop which involves an interferometric measurement of the horizontal position of the probe tip keeps it at constant height (Betzig et al., 1992). Near-field optical properties of the sample surface are mapped out by scanning each point within a certain area



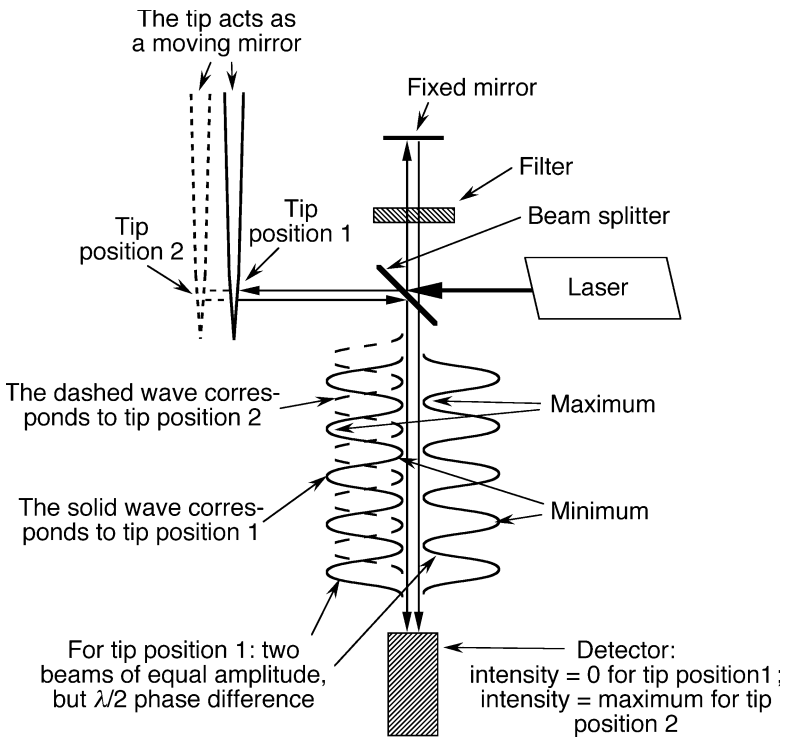


**Fig. 7.24** Design of an interferometer used for the detection of shear force of the SNOM tip. The principle of operation is based on the extinction of light at the position of the detector due to the interference of the two incident light beams of equal amplitude when the probe tip (movable mirror) is in position 1. A small perturbation of the position of the tip causes a small deviation from  $\lambda/2$  of the phase shift of the two beams incident on the detector which leads to a non-negligible detector signal. The light filter in the fixed path ensures an equal amplitudes of the two interfering beams

Generally the working principle of SNOMs is as follows (Figs. 7.23–7.25): The subwavelength light source is positioned a few  $\mu\text{m}$  above the specimen surface with the help of mechanical coarse translation stages and a piezoelectric fine translation device, e.g., a piezoelectric scan tube. Transmission is measured below the specimen. An image of the specimen surface is obtained by moving the light source (or the sample in some designs) with the help of the piezoelectric fine translation device in horizontal direction. To avoid crashes with the sample, in many SNOMs the light source is oscillated over the specimen surface and damping of oscillations due to source-sample interactions detected. The piezoelectric fine translation device somewhat lifts the subwavelength light source (or lowers the sample) when damping increases. Near-field optical excitation of the sample can be seen as a dipole-dipole energy transfer (Sekatskii and Dietler, 1999).

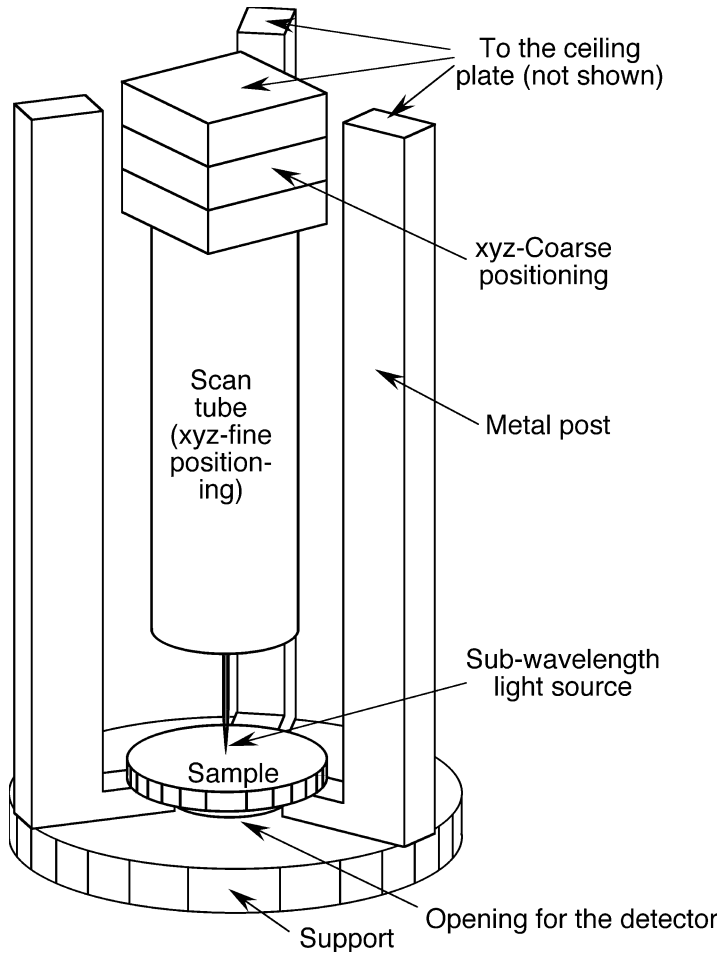


**Fig. 7.25** A design of a SNOM with a xyz-coarse positioning and a xyz-fine positioning

There is virtually no resolution limit of SNOMs as long as one can manufacture light sources of sufficient small size (see next section) and detect very small intensity differences of light passing through thin sample layers.

### 7.3.2 Design of the subwavelength aperture

The most common methods to manufacture subwavelength apertures are (a) adiabatic pulling of an optical fiber during heating (Betzig et al., 1991; Williamson and Miles, 1996; Figs. 7.26a and 7.27), (b) etching (Muramatsu et al., 1999), in particular tube etching (Turner, 1983; Stöckle et al., 1999a; Figs. 7.26b

and 7.28), and (c) microfabrication (Schurmann et al., 2000; Mitsuoka et al., 2001), e.g., by ion beam milling (e.g., Veerman et al., 1998).

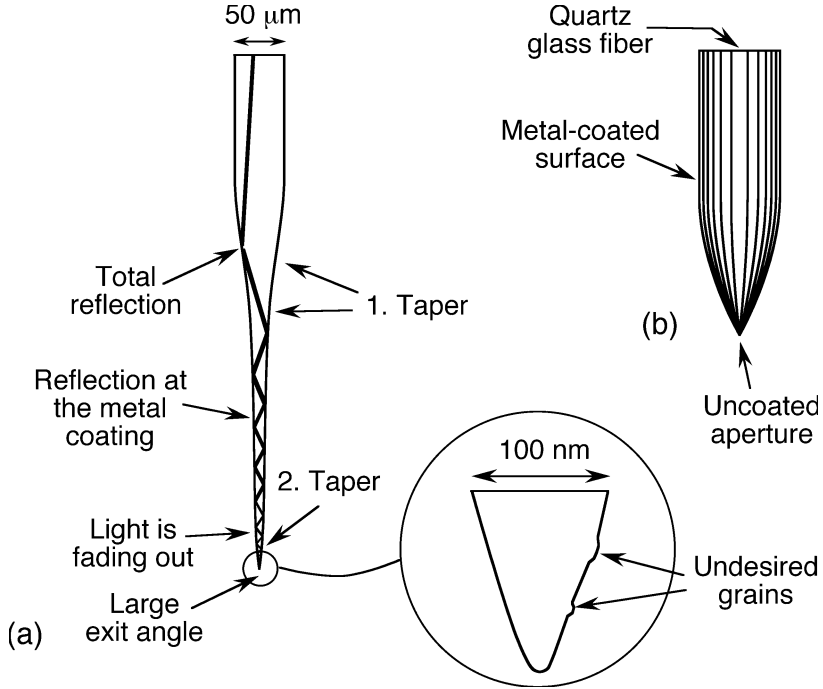


**Fig. 7.26** (a) Melt-drawn probe: in the upper part of the probe, the light is reflected from the walls by total internal reflection (TIR). TIR is the phenomenon involving the reflection of all the incident light off a boundary when both (i) the light is traveling in the more optically dense medium and approaching the less optically dense medium and (ii) the angle of incidence is greater than the so-called critical angle. (b) Etched probe. A desirable high brightness is obtained by a large cone angle. An optical aperture is formed by rotational evaporation of the etched fiber with an opaque metal, e.g., aluminum

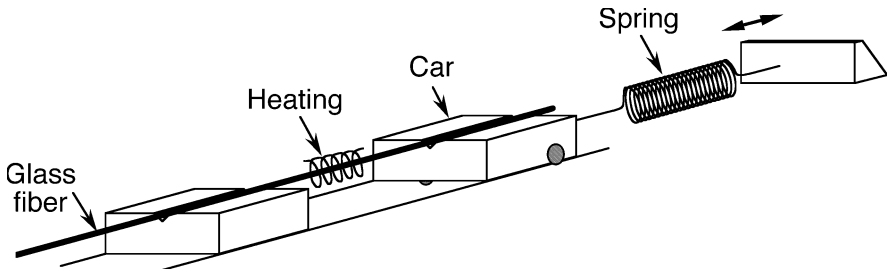


**Fig. 7.27** Fabrication of a probe by adiabatic pulling of an optical fiber during heating (melt-drawing; see, e.g., Williamson and Miles, 1996)

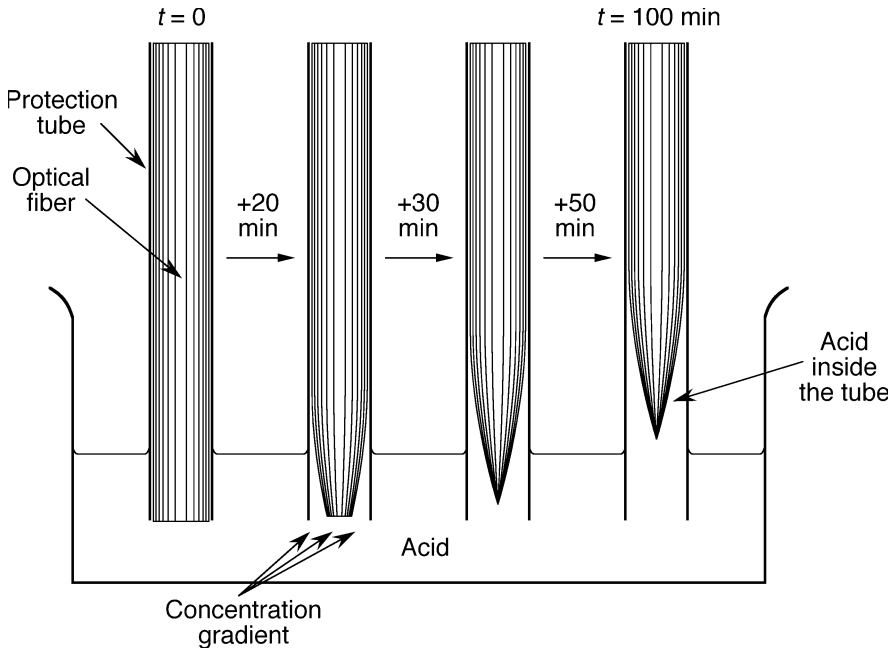


**Fig. 7.28** Tube-etching of a quartz glass fiber with hydrofluoric acid (Turner, 1983; Stöckle et al., 1999a, 1999b): the tip forms due to concentration gradients of acid and dissolved fiber. The tube serves also for suppression of convection of the acid. These tube-etched tips are inexpensive and have large cone angles permitting high light throughputs

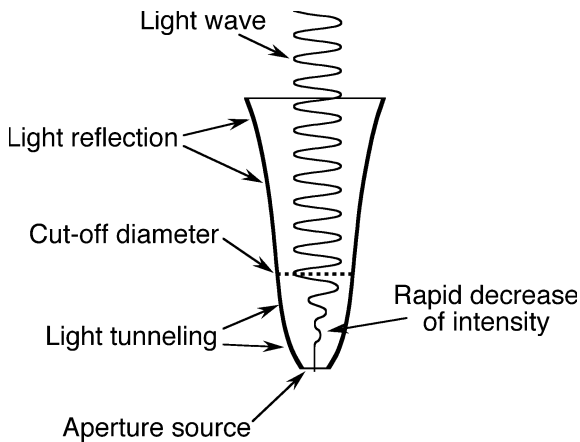


**Fig. 7.29** Propagation of a light wave in a SNOM probe tip. Up to the cut-off diameter (about equal to the wavelength), the light travels with only little attenuation. Beyond this critical diameter, the light intensity very rapidly falls off

Usually the aforementioned probe tips are coated with a metal. Since the light transmission of the tip dramatically depends on the distance from the cut-off region to the aperture (Fig. 7.29), the optical throughput of etched tips with cone angles around  $30^\circ$  is, in general, 2–3 orders of magnitude better than that of heat-pulled fiber probes. Even brighter sources can be microfabricated (Fig. 7.30).

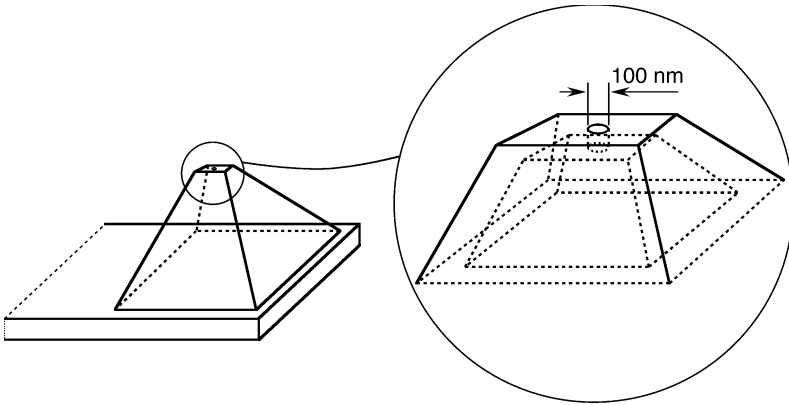


**Fig. 7.30** SNOM tip made from silicon nitride. It was manufactured by using photolithography, potassium hydroxide etching, and electron beam nanolithography (Zhou et al., 1998, 1999)

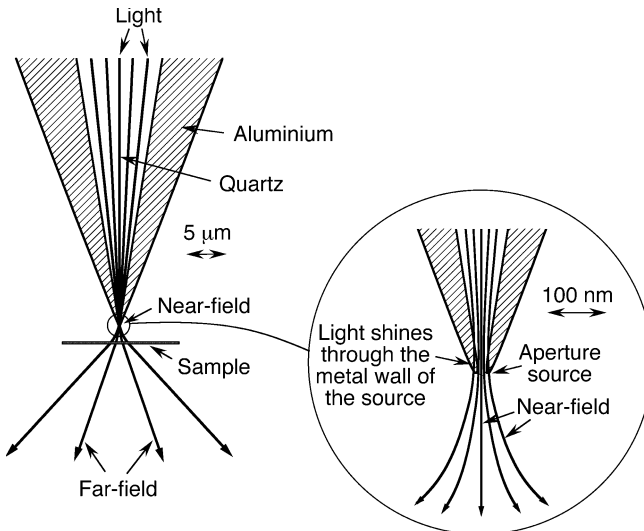


**Fig. 7.31** Optical far-field and near-field in the vicinity of a small optical tip for a SNOM. Since the light can transmit through thin layers of metal, the diameter of the light beam in this design cannot be less than a few 10 nm

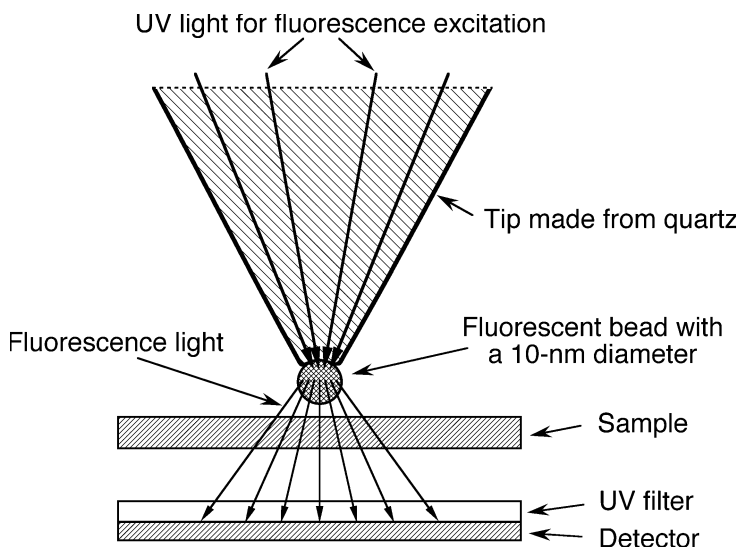


**Fig. 7.32** A 10-nm sized light source for SNOMs made from fluorescent material. UV light excites fluorescence of the 10-nm sized bead at the end of the probe. The transmission of the fluorescence light through the sample is sensed by a detector which is covered with an UV-absorbent layer. Antioxidants may be added to the fluorescent material to enhance stability and life. The resolution for thin-layered samples enabled by this type of light sources depends on the size of the fluorescent bead and the detectability of small absorbance differences of the fluorescent light

In the aforementioned methods of source fabrication, a limitation for the source size is the transmission of light through thin layers of metal (Fig. 7.31). Sources of 10 nm diameter could hardly be made just by machining an opening in a metal plate or in an optical fiber since light would significantly shine through the walls of the opening. Smaller light sources involve the excitation of small fluorescent particles (Fig. 7.32).

### 7.3.3 Examples of SNOM applications

An important applicability is seen in cell biology, microbiology (Meixner and Knepe, 1998), and proteomics (Gao et al., 2001). SNOM imaging visualized domains of photosystem II core complex bound to lipid monolayers (Trudel et al., 2001). Topographic, friction, fluorescence, and surface potential distributions for a Langmuier-Blodgett film can simultaneously be observed using a SNOM-AFM with a thin step-etched optical fiber probe (Horiuchi et al., 1999). Fig. 7.33 demonstrates a 50-nm resolution.

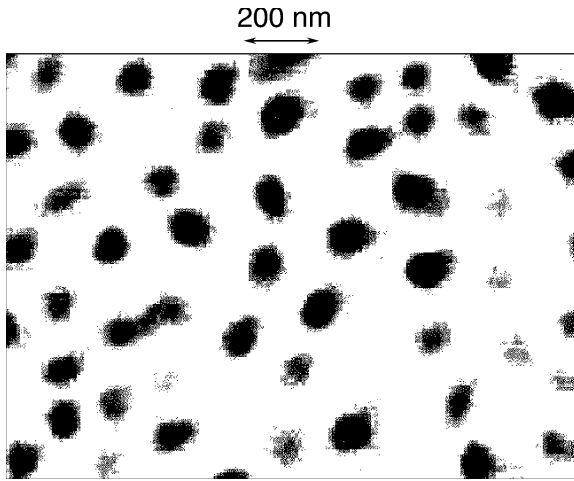


**Fig. 7.33** Absorption of latex beads with approximately 100 nm diameter taken with a SNOM at a resolution of about 50 nm (OMICRON, Tausnusstein, Germany)

## 7.4 Scanning ion conductance microscope, scanning thermal microscope and further scanning probe microscopes

Important scanning probe microscopes are also the magnetic force microscope, scanning Hall probe microscope (Chang et al., 1992a, 1992b), friction force microscope (Fig. 7.34; Howald et al., 1995), scanning ion conductance micro-

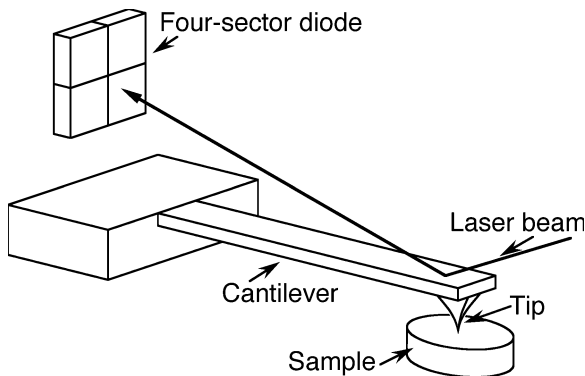


**Fig. 7.34** Example of a friction force microscope: the detector has sectors in both vertical and horizontal direction so that the torsion of the cantilever can be estimated and a frictional (lateral) force be calculated (see, e.g., Howald et al., 1995)

scope (Fig. 7.35; Hansma et al., 1989; Korchev et al., 1997, 2000a, 2000b; Stachelberger, 2001; Bruckbauer et al., 2002a), and scanning thermal microscope (Fig. 7.36; Mills et al., 1998, 1999). There are two common types of thermal probes for scanning thermal microscopes: thermocouples and thermal resistors. The thermocouple probe in Fig. 7.36 involves two dissimilar metal wires which bisect over the top of a blunt silicon nitride pyramid (Mills et al., 1998). A potential biophysical application is the elucidation of local heating effects in biological tissue due to cell metabolism.

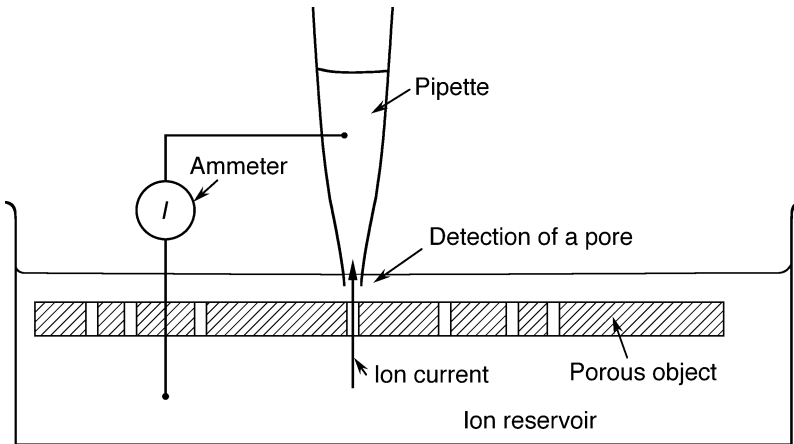


**Fig. 7.35** Detection of membrane pores by a scanning ion conductance microscope. The probe is a nanopipette filled with electrolyte solution. The current between pipette and ion reservoir starts increasing when the pipette tip approaches a pore. The technique permits 100-nm resolution characterization of distribution and sizes of pores

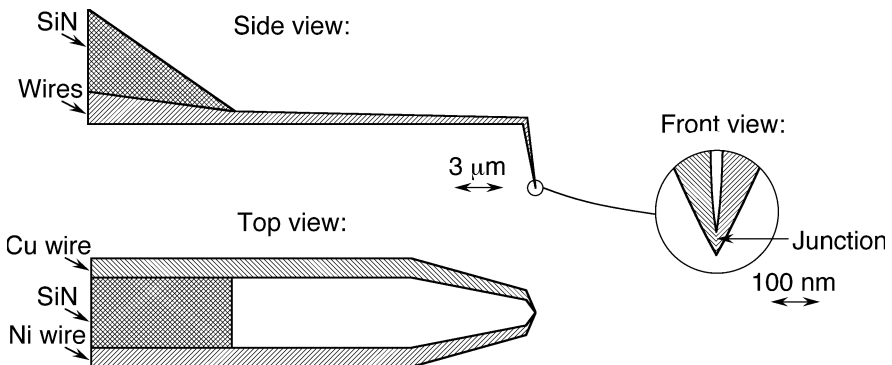


**Fig. 7.36** Design of the tip of a scanning thermal microscope (Mills et al., 1998, 1999). A submicrometer-sized Cu/Ni thermocouple at the end of the cantilever detects the thermal microenvironment



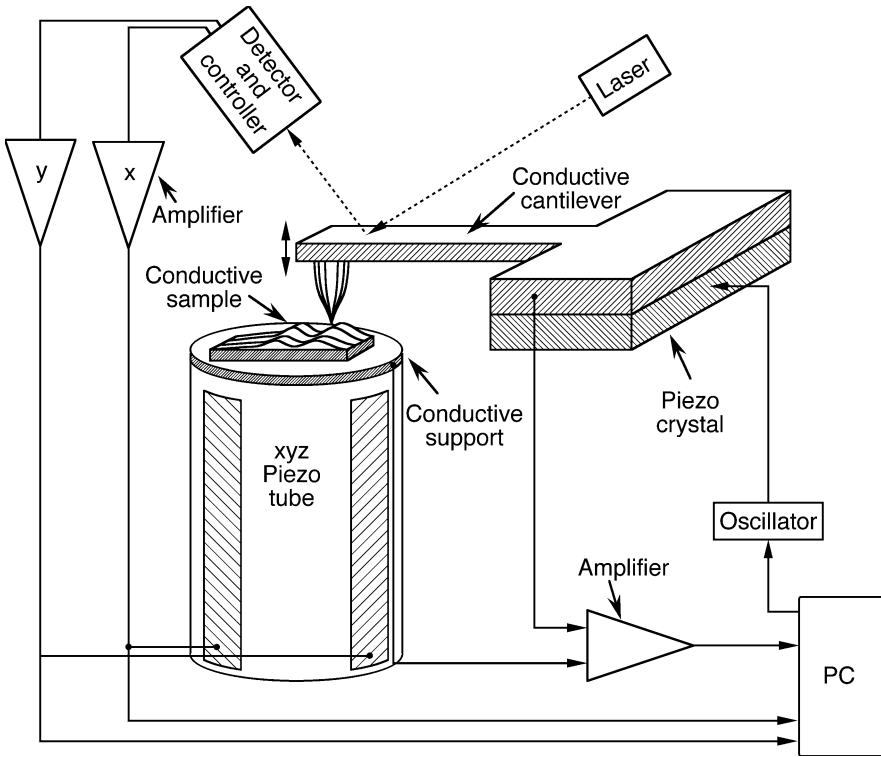


**Fig. 7.37** STM with simultaneous AFM capability: AFM and STM sense different physical properties. The combined information provides greater insight into the chemical nature of the sample and its physico-chemical properties

The STM with simultaneous AFM capability (Fig. 7.37) provides simultaneously information about surface relief and chemical composition of the specimen.

## 8 Biophysical nanotechnology

### 8.1 Force measurements in single protein molecules

Atomic force microscope (AFM)-related techniques can induce and monitor the unfolding of single protein molecules. Experiments on the protein titin, which is a main component of skeletal muscles (Figs. 8.1–8.3), revealed that the force for unfolding of its individual domains with cross sections of less than  $5 \text{ nm}^2$  is of the order of 100–300 pN and dependent on the pulling speed (Rief et al., 1997; Gaub and Fernandez, 1998; Carrion-Vasquez et al., 1999). A similar investigation on bacteriorhodopsin showed that its helices are anchored to the bacterial membrane with 100–200 pN (Fig. 8.4; Oesterhelt et al., 2000). Similarly, single-molecule force spectroscopy on spider dragline silk protein molecules revealed that the molecule unfolds through a number of rupture events, indicating a modular structure within single silk protein molecules (Oroudjev et al., 2002). The minimal unfolding module size of 14 nm indicates that the modules are composed of 38 amino acid residues (Oroudjev et al., 2002). Adhesion between two adjacent cell surfaces of the eukaryote *Dictyostelium discoideum* involves discrete interactions characterized by an unbinding force of about 23 pN. This force probably originates from interactions of individual “contact site A” (csA) glycoprotein molecules (Fig. 8.5; Benoit et al., 2000).

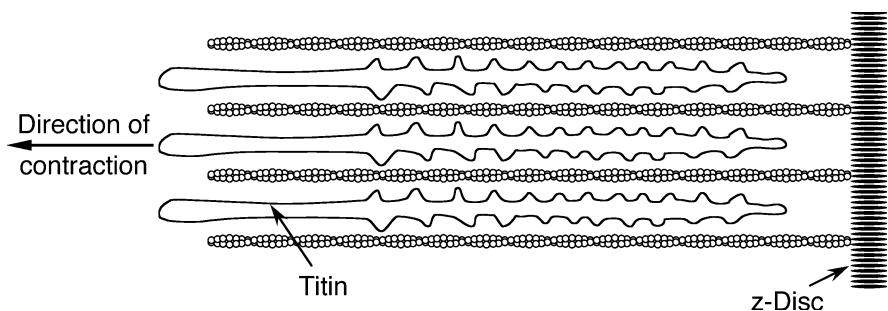


**Fig. 8.1** Molecular architecture of skeletal muscle fibers. AFM-related techniques contributed to the understanding of the role of individual titin molecules in such fibers: some skeletal muscle proteins can withstand drags of  $600 \text{ kp cm}^{-2}$  (see Figs. 8.2 and 8.3; Rief et al., 1997; Gaub and Fernandez, 1998; Carrion-Vasquez et al., 1999)

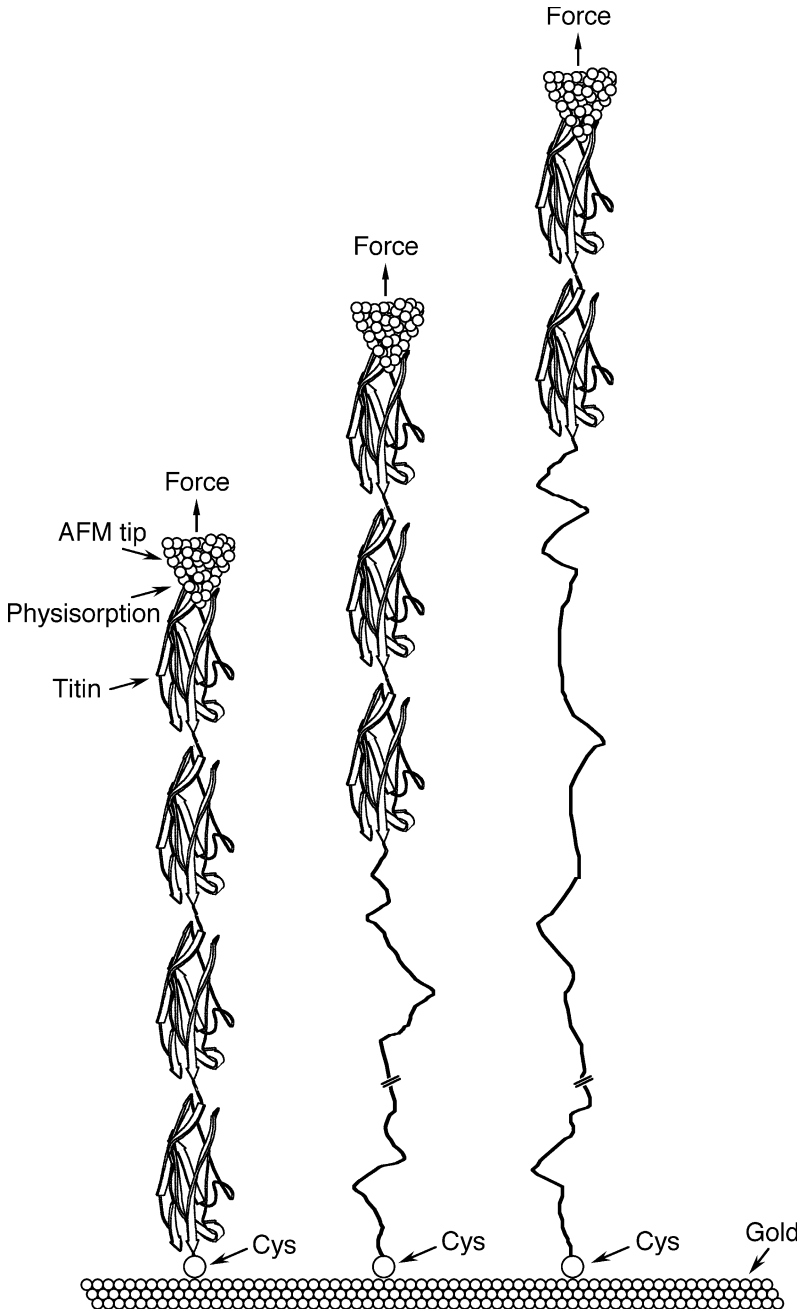


**Fig. 8.2** Unfolding of a titin fragment with the help of an AFM (Gaub and Fernandez, 1998; Carrion-Vasquez et al., 1999). The unfolding force for the protein, anchored with a cysteine (Cys) to a gold surface, ranged from about 100 to 300 pN (see Fig. 8.3)

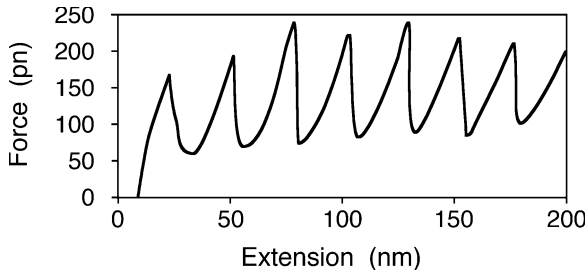


**Fig. 8.3** Sketch of a force-distance curve for the unfolding of a titin fragment with the help of an AFM (see Fig. 8.2). The saw tooth-shaped force-extension curve reflects the unfolding of individual titin domains according to an all-or-non mechanism (Gaub and Fernandez, 1998; Carrion-Vasquez et al., 1999)

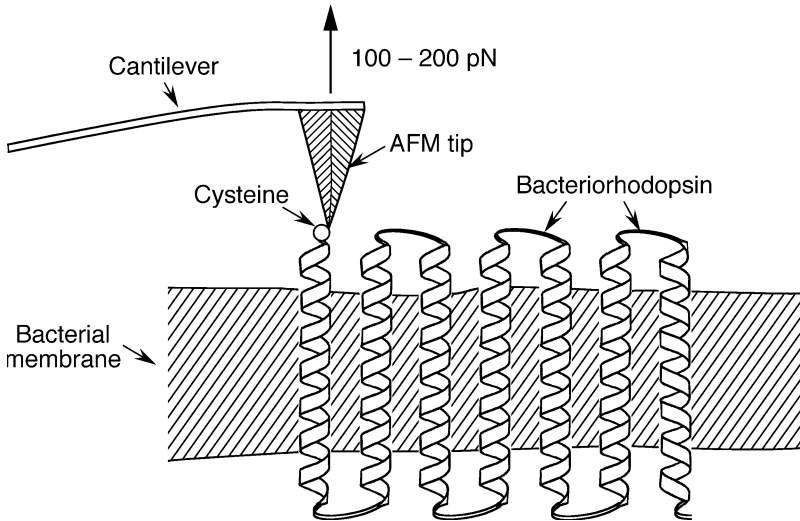


**Fig. 8.4** Unfolding of individual bacteriorhodopsins. A force of 100–200 pN is required to remove a bacteriorhodopsin helix from the bacterial membrane (Oesterhelt et al., 2000)

Recoverin, a calcium-myristoyl switch protein, binds to a phospholipid bilayer in the presence of  $\text{Ca}^{2+}$  with an adhesion force of  $48 \pm 5$  pN (Desmeules et al., 2002). Single molecules of *holo*-calmodulin (i.e., the calcium-loaded form) require a significantly larger force of unfolding by an AFM tip than single molecules of the *apo*-form (Hertadi and Ikai, 2002). Single molecules of the giant filamentous protein titin exhibit mechanical fatigue when exposed to repeated stretch and release cycles (Kellermayer et al., 2001). For further AFM studies on single protein molecules see also Sects. 7.1, 8.2, and 8.3.

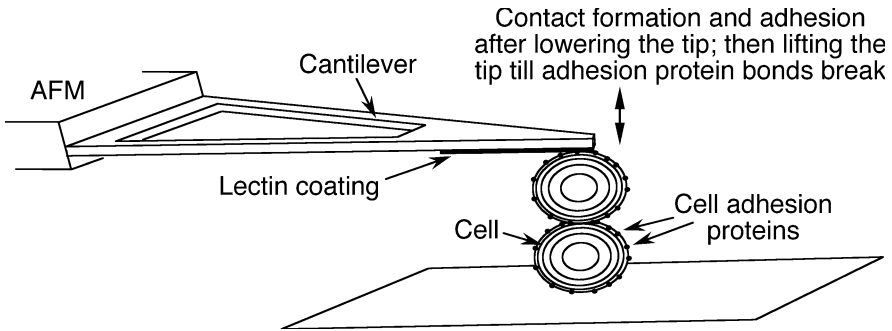


**Fig. 8.5** Measurement of discrete interactions in cell adhesion (Benoit et al., 2000)

## 8.2 Force measurements in a single polymerase-DNA complex

DNA polymerases catalyze DNA replication. The replication reaction requires single-stranded DNA (ssDNA) as a template. In the course of the reaction, a complementary strand of ssDNA is synthesized to the original ssDNA. Already during the polymerization reaction, both strands coil around each other, leading to a shortening of the end-to-end distance of the DNA. Exerting strain on the DNA strand during polymerization can stop and even revert the extension reaction

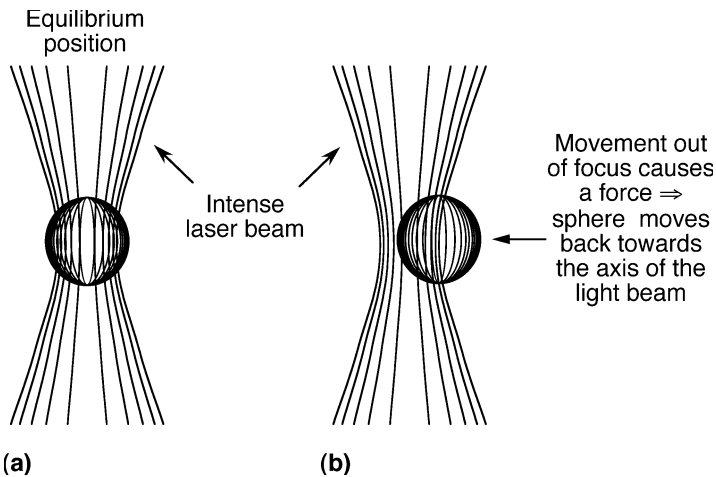


**Fig. 8.6** Optical tweezers for the measurement of the effect of template tension on T7 polymerase activity (Fig. 8.7; Smith et al., 1996; Wuite et al., 2000). Regarding the method of optical tweezers see also the groundbreaking studies of single-molecule mechanics by Florin et al. (Florin et al., 1997; Jeney et al., 2001; Pralle and Florin, 2002) and Smith et al. (Bustamante et al., 2000; Liphardt et al., 2001; Smith et al., 2001)

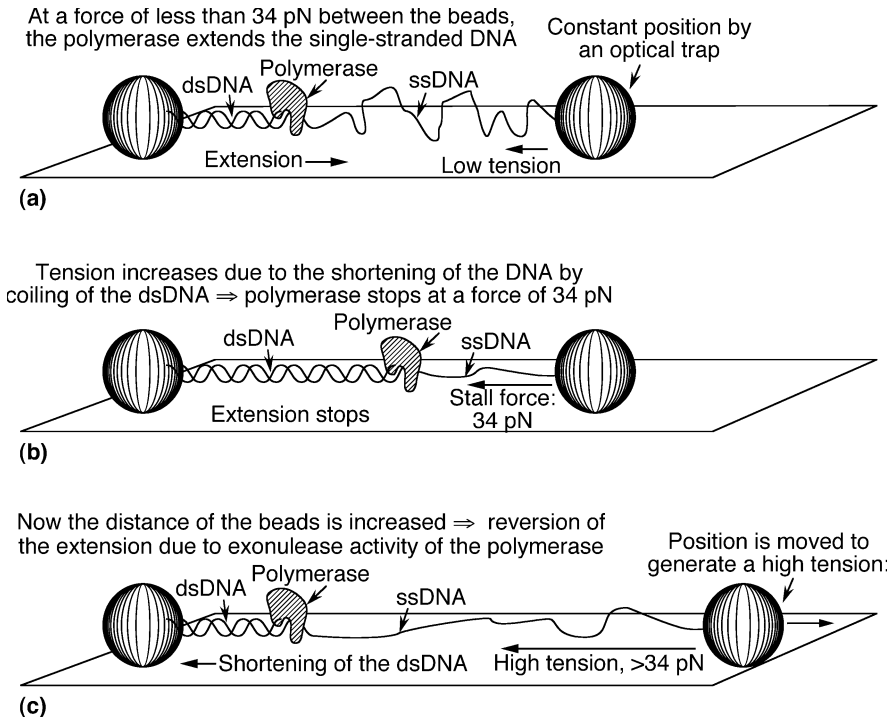
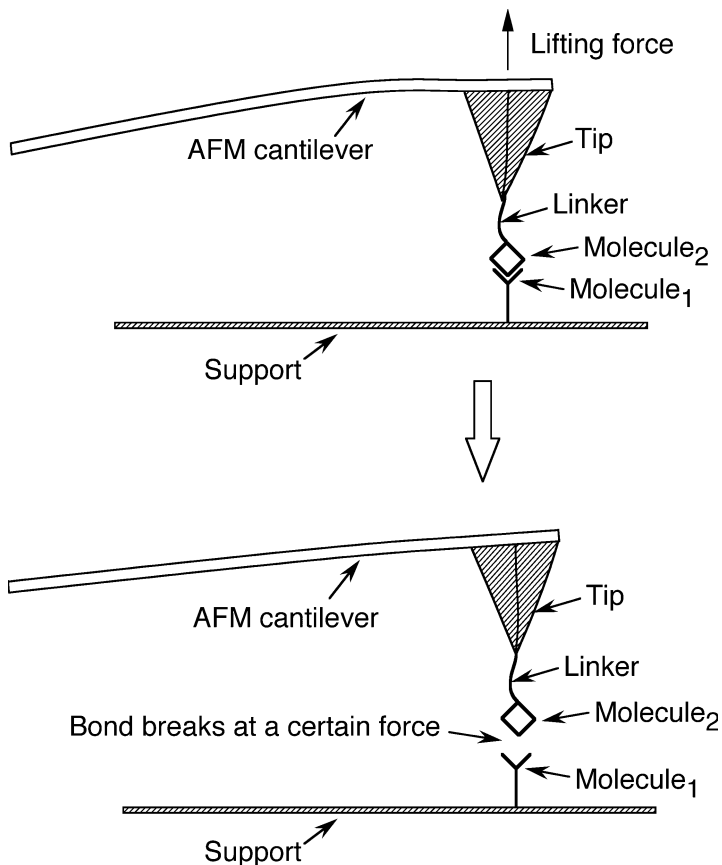


**Fig. 8.7** Measurement of the effect of template tension on T7 polymerase activity (Smith et al., 1996; Wuite et al., 2000): the polymerase which catalyses DNA replication can work against a maximum force of about 34 pN. Exonuclease activity increases about 100-fold above 40 pN template tension.

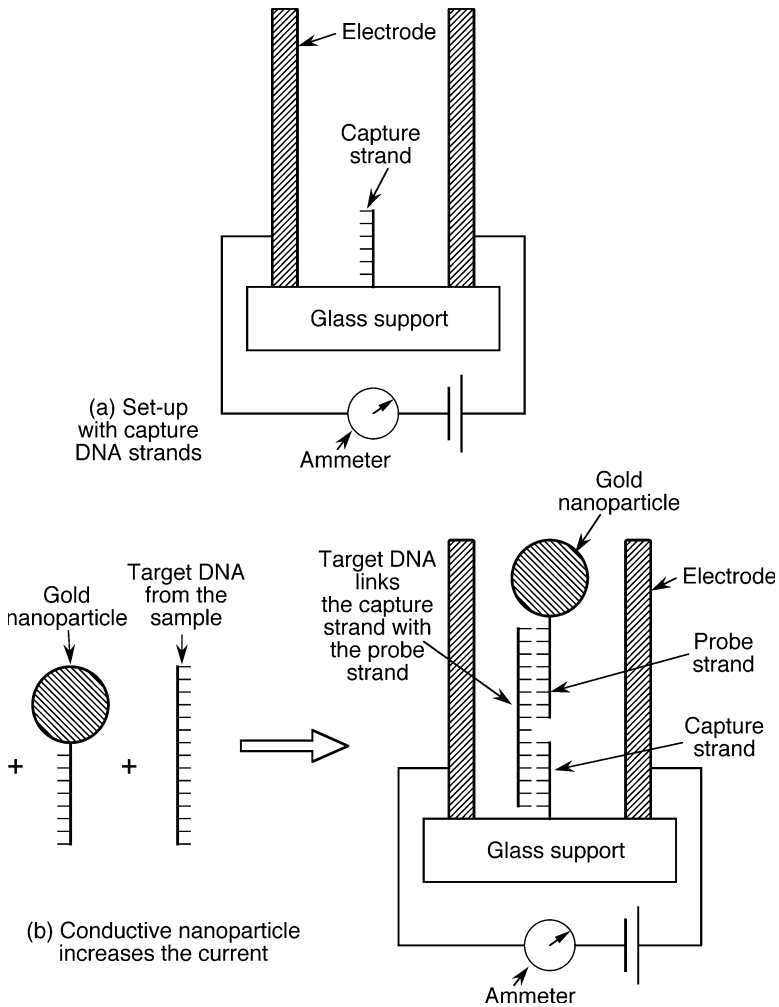
(Figs. 8.6 and 8.7; Smith et al., 1996; Wuite et al., 2000). For the measurement of the small forces in the single DNA-protein complex, an optical trap was used: a small bead with DNA attached to it is held into position and moved by an intense laser beam. The main mechanism of the action of such optical tweezers is commonly as follows: The bending of light rays through the refractive sphere is connected with a change of momentum of the light which exerts a force back on the sphere. When the sphere is out of focus of the light beam, these light deflection forces pull the sphere back into focus. Another mechanism is as follows: When an isotropically scattering bead moves out of focus, the momentum of the photons scattered in the direction of the movement increases due to the Doppler effect which decelerates the bead. The larger the light intensity the larger is the deceleration of the movement. Thus, the Brownian motion out of focus is energetically unfavorable relative to the motion into focus. Choosing a wavelength just below an absorption maximum of the bead increases the trapping force since then movement causes increased absorption due to the Doppler-shift of the wavelength and thus an additional momentum slowing down the bead.

### 8.3 Molecular recognition

AFM-related techniques allow the direct measurement of individual intermolecular interactions (Figs. 8.8–8.11; Florin et al., 1994; Dammer et al., 1995, 1996; Merkel et al., 1999; Strunz et al., 1999; De Paris et al., 2000; Fritz et al., 2000; Schwesinger et al., 2000; Zocchi, 2001; Pechtel et al., 2002; see also Sect. 7.1). Virtually any intermolecular interaction forces, e.g., of antibody-antigen interactions, are measurable with the technique illustrated in Fig. 8.8.



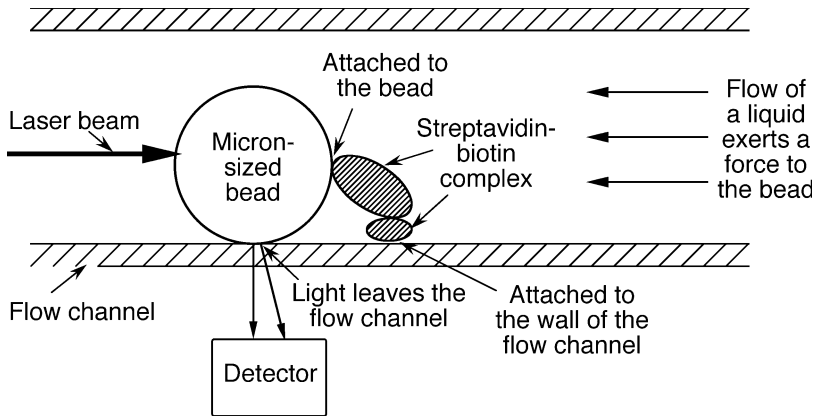
**Fig. 8.8** Direct measurement of intermolecular interactions by an AFM-related technique. One of the interacting molecules is immobilized on the surface of the support, the other is connected to the AFM tip by a linker. The tip is approached to the surface so that a specific interaction can take place. Retracting the cantilever ruptures the biophysical interaction. The strength of the interaction is determined from the retract force distance curves (De Paris et al., 2000; Schwesinger et al., 2000; see also Sect. 7.1)



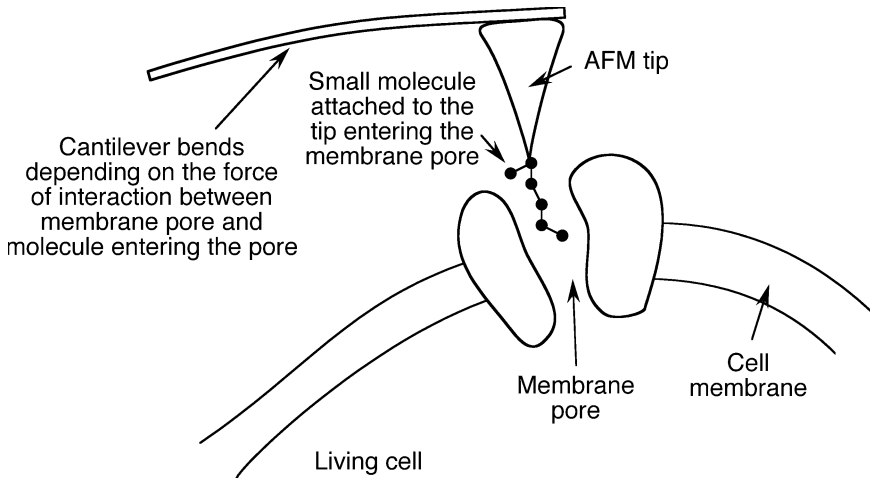
**Fig. 8.9** Sensor of biological agents using recognition between single DNA molecules (Park et al., 2002; Service, 2002; see also Demers et al., 2002). (a) Two electrodes and single-stranded capture DNA strands are attached to a glass substrate. The capture DNA is complementary to one end of the target DNA of the agent. (b) Target DNA and probe strand DNA was added. The probe strand DNA has a gold nanoparticle attached and is complementary to the other end of the target DNA. When all three strands of DNA hybridize together, the gold nanoparticle gets held between the two electrodes. This is detected by an increase of current

Fig. 8.9 illustrates a new type of DNA sensor with potential application for detection of biological contaminants (Park et al., 2002; Service, 2002). It is based on the change of electrical conductivity when gold particles attached to DNA bind





**Fig. 8.10** Force measurement on single molecular contacts through evanescent wave microscopy (Zocchi, 2001). The motion of the bead attached to the wall of the flow channel through a single streptavidin-biotin complex is tracked by detecting the evanescent wave as a force is exerted through a flow. This technique allows the direct measurement of the bond rupture force of the molecular complex



**Fig. 8.11** Nanobiosensor using the cantilever of an AFM (Pereira, 2001). Entering or exiting of specific molecules, including medications, from living cells is observed in real-time and the force of interaction measured

to the targeted sample DNA immobilized between two electrodes. A problem of this detection method might be the difficulty to find pieces of DNA that are unique for the organism of interest. In particular, some genetically engineered bacteria and viruses might remain undetected.

## 8.4 Protein nanoarrays and protein engineering

Lee et al. (2002b) manufactured protein nanoarrays by means of dip-pen nanolithography (Figs. 8.12 and 8.13): A gold thin-film substrate was patterned, by using an AFM, with a protein-binding chemical linker in the form of dots or grids. Non-patterned surface was inactivated and then protein bound to the linker patterns. Another method for the manufacture of protein nanoarrays is to use germanium pyramids as a support (Fig. 8.14). Calvo et al. (2002) report on the molecular wiring efficiency of glucose oxidase in organized self-assembled nanostructures. Wired protein molecules may be important for future nanotechnological tools (Figs. 8.15 and 8.16). Also the design of non-native macromolecular assemblies, e.g., hexameric helical barrels (Ghirlanda et al., 2002) is an endeavor with implications for nanotechnology (Fig. 8.17). Finally, Fig. 8.18 displays the manufacture of ordered inorganic nanocrystals on top of an array of genetically engineered viruses (Lee et al., 2002c).

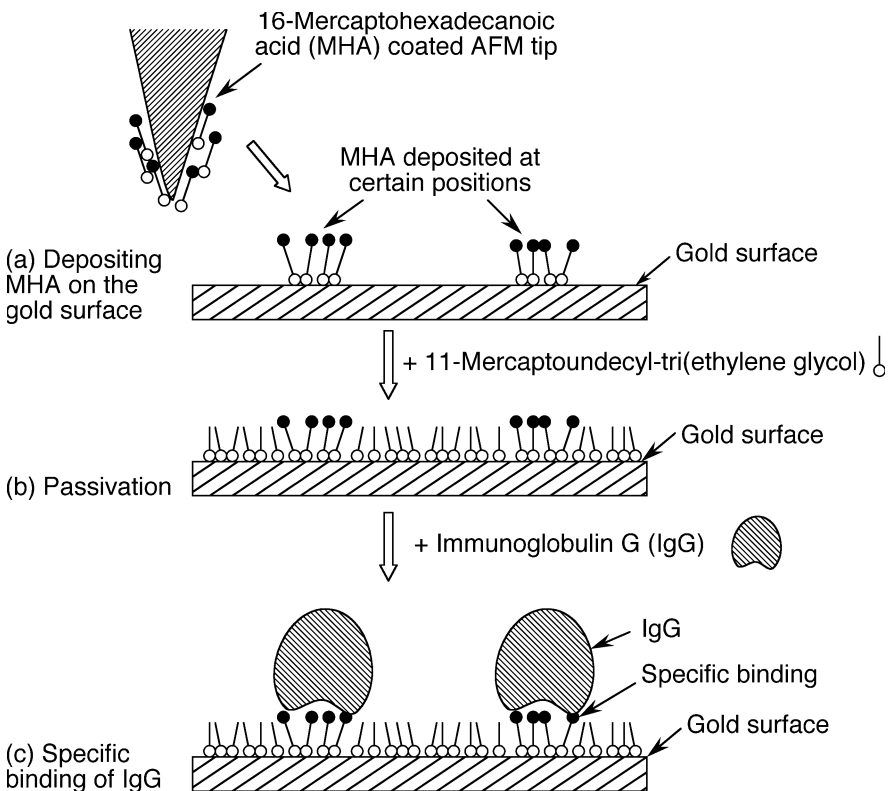


**Fig. 8.12** Manufacture of protein nanoarrays for the investigation of molecular interaction and other recognition processes (Lee et al., 2002b; see also Hodneland et al., 2002)

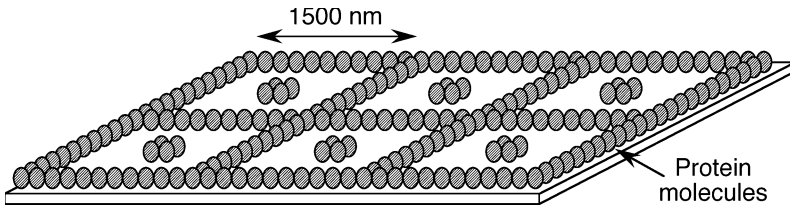


**Fig. 8.13** Example of an engineered protein nanoarray (Lee et al., 2002b). Protein arrays with 100- to 350-nm features were fabricated with dip-pen nanolithography (see Fig. 8.12)

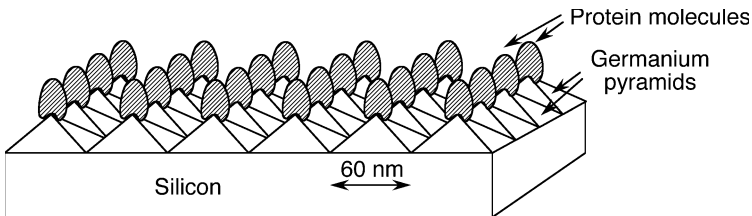


**Fig. 8.14** Protein nanoarray manufactured by self-assembly on nanometer-sized germanium pyramids (Riedel et al., 2001). Dynamic contact angle measurements with water droplets revealed that the germanium substrate is highly hydrophilic, and thus should be suitable for adsorption of hydrophilic proteins. Some protein inactivation was observed, however

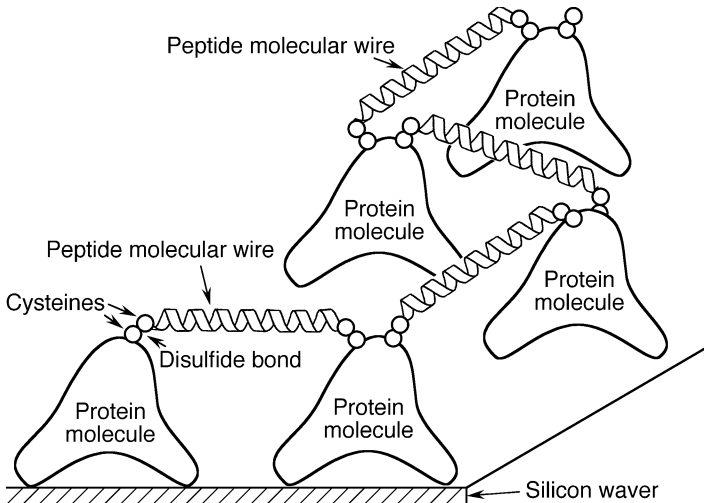


**Fig. 8.15** Wired protein molecules might be components in future nanobiotechnological devices (see, e.g., Service, 2001; Calvo et al., 2002; Seeman and Belcher, 2002). Suitable wires are made, e.g., from chemical compounds, peptides, or carbon nanotubes. Proteins may act in such bioelectronic structures, e.g., as redox relays (Calvo et al., 2002)

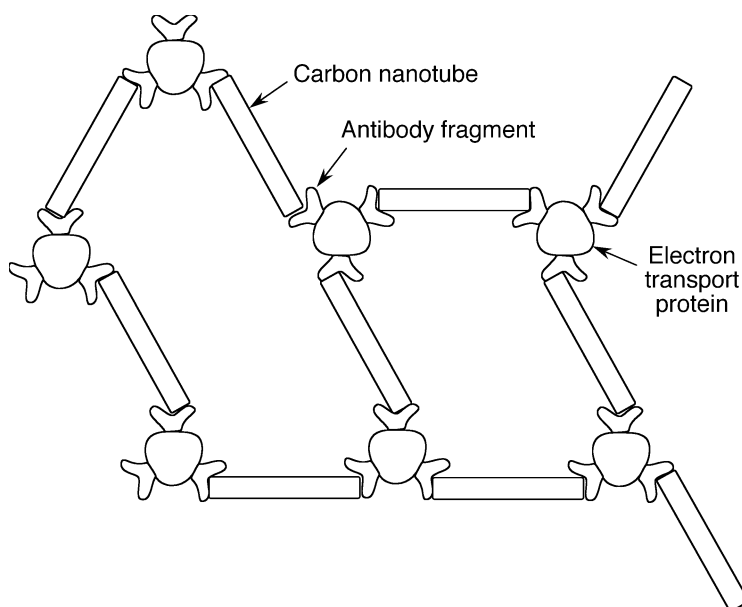


**Fig. 8.16** Network of single-walled carbon nanotubes and genetically engineered proteins in a future nanobiotechnological device. Carbon nanotubes display an exceptionally low resistance and are seen as especially useful for the production of bridging nanowires and other nanostructures (see, e.g., Fagas et al., 2002; Odom et al., 2002)

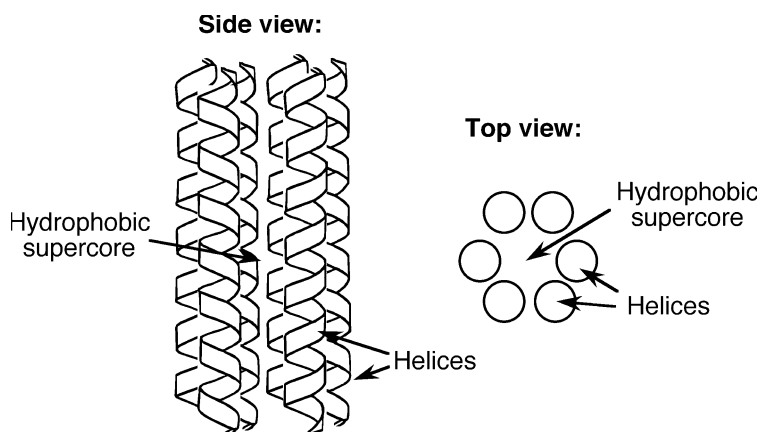


**Fig. 8.17** Engineered hexameric helical barrels (Ghirlanda et al., 2002). A dimeric three-helix bundle was designed from first principles. In order to probe the requirements for stabilizing the hexamer, Ghirlanda et al. systematically varied polarity and steric bulk of the residues in the supercore of the hexamer. Formation of the hexameric assembly was best stabilized by changing three polar residues per three-helix bundle to hydrophobic residues (two phenylalanines and one tryptophan)

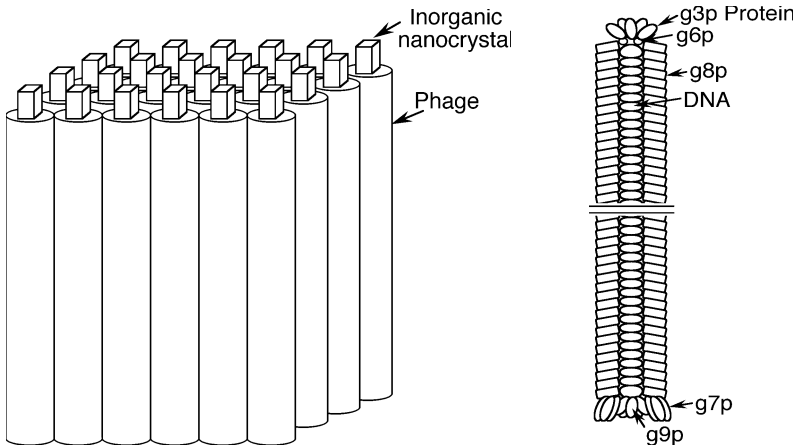


**Fig. 8.18** *Left:* ordering of inorganic nanocrystals using genetically engineered phages (Lee et al., 2002c). The bacteriophages form the basis of the self-ordering system. Genetic engineering enables the phages to specifically bind to nanocrystals. *Right:* structure of a phage

## 8.5 Study and manipulation of protein crystal growth

The fabrication of properly diffracting protein and virus crystals is often the main obstacle for the high resolution of proteins using X-ray methods (see Sect. 4.1).

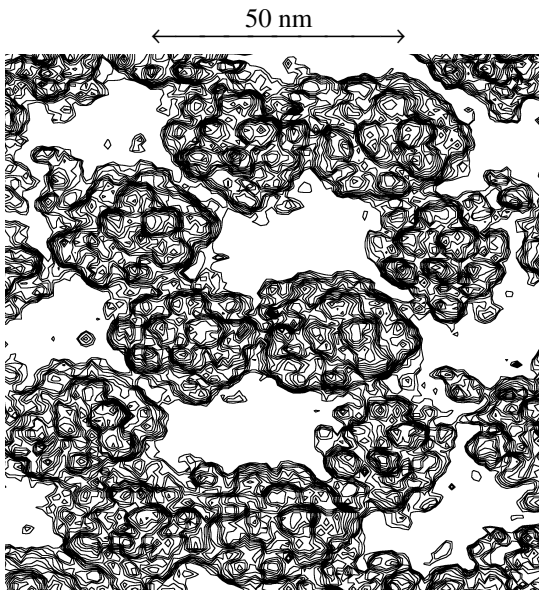


**Fig. 8.19** AFM image of the surface of a turnip yellow mosaic virus crystal (Malkin et al., 1995, 2002; Kuznetsov et al., 2000; McPherson et al., 2000, 2001). AFM investigation revealed the sources of crystal disorder and mechanisms of their formation

AFM is exquisitely useful for the study and manipulation of crystal growth (Fig. 8.19; Durbin and Carlson, 1992; Durbin et al., 1993; Malkin et al., 1995; McPherson et al., 2000; Mollica et al., 2001; Biscarini et al., 2002). Most protein and virus crystals grow, through a process of two-dimensional nucleation, by formation of new crystal layers (McPherson et al., 2000). Scratching the surface of a lysozyme crystal which was completely covered by an impurity stopping crystal growth resulted in resumption of crystal growth (McPherson et al., 2000).

## 8.6 Nanopipettes, molecular diodes, self-assembled nanotransistors, nanoparticle-mediated transfection and further biophysical nanotechnologies

Bone cells respond to stretching by an AFM tip with activation of stretch-activated ion channels (Charras and Horton, 2002). Dissecting bacterial surface layers with an AFM tip provided a better understanding of the high stability of this protective bacterial surface coat (Fig. 8.20; Scheuring et al., 2002). Micronized salbutamol particles stick to glass stronger than to polytetrafluoroethylene (Eve et al., 2002). For further nanobiotechnological innovations see Figs. 8.21–8.27 and Sect. 7.1.

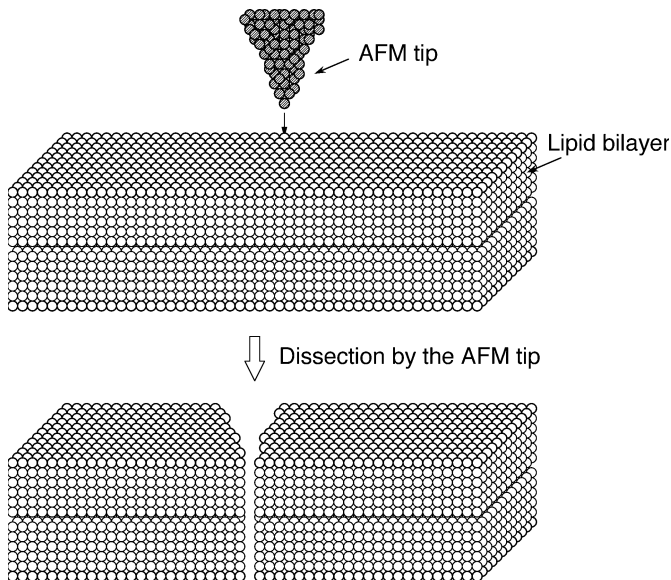


**Fig. 8.20** Unzipping a double layer of lipids adsorbed to mica (not shown), with an AFM tip (Scheuring et al., 2002). Using the AFM stylus as a nanodissector, native bacterial surface layers were separated and their mechanical and protective properties against hostile environments examined

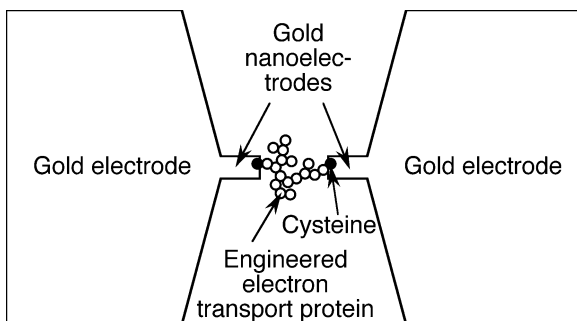


**Fig. 8.21** Conduction between nanoelectrodes through a single molecule (Reimers et al., 2002) or a few organic molecules forming a nanocrystal (Rinaldi et al., 2002). In some cases, rectifying behavior is observed, e.g., for deoxyguanosine nanocrystals (Rinaldi et al., 2002)

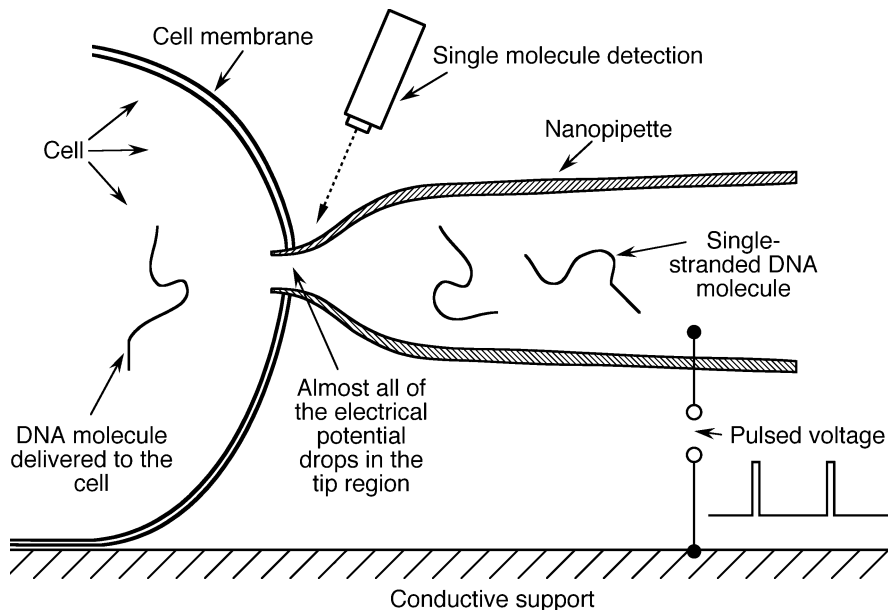


**Fig. 8.22** Programmable delivery of DNA through a nanopipette (Ying et al., 2002; Bruckbauer et al., 2002b). The conical geometry of the pipette causes most of the electrical potential drop to occur in the tip region. Pulsatile delivery of DNA molecules is achieved by controlling the applied voltage

The nanopipette in Fig. 8.22 was designed for controlled delivery of macromolecules into living cells (Ying et al., 2002). A voltage applied to the nanopipette moves the DNA molecules slowly towards the tip of the pipette. Since, because of the conical geometry of the nanopipette, most of the potential

drop occurs in the tip region, the DNA molecules are rapidly delivered to the cell once they have reached the tip region. In combination with single molecule detection, individual DNA molecules can be delivered to the living cell in a controlled manner.

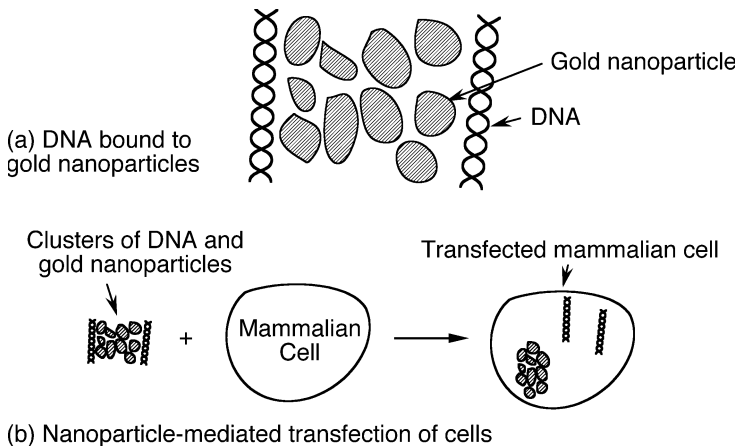


**Fig. 8.23** Gold nanoparticle-mediated transfection of cells (Sandhu et al., 2002). (a) Mixed monolayer protected gold cluster functionalized with quaternary ammonium chains binding to DNA. (b) Schematic of the transfection process

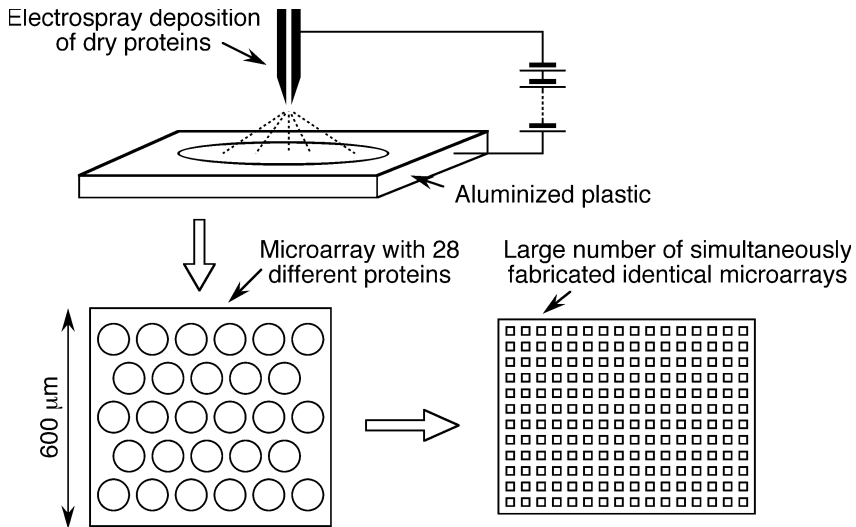


**Fig. 8.24** Electro spray deposition of dry proteins for the fabrication of microarrays and nanoarrays (Avseenko et al., 2001, 2002). These arrays can detect antibodies in plasma samples from mice immunized with the proteins used for the arrays



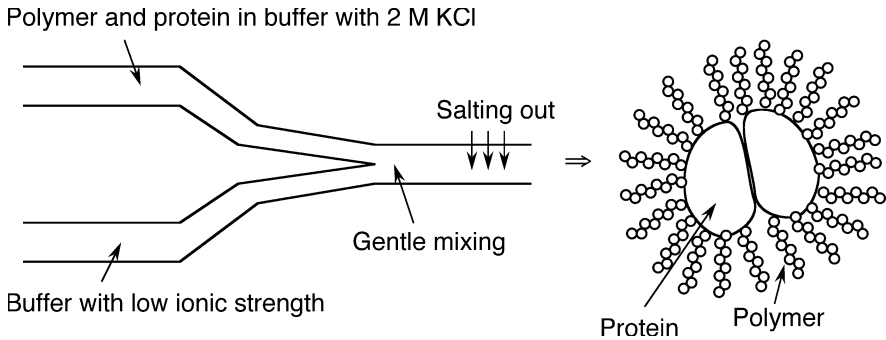


**Fig. 8.25** Continuous-flow preparation of 100-nm nanoparticles for drug delivery, protein delivery, and gene therapy (Prokop et al., 2001; Davda and Labhasetwar, 2002; Igartua et al., 2002; Konan et al., 2002; Haas and Lehr, 2002)

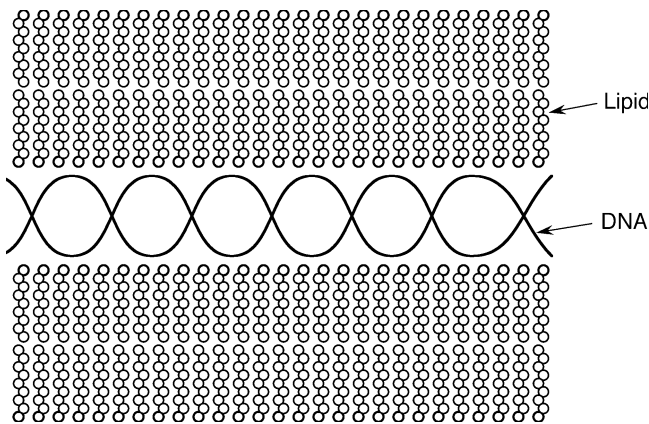


**Fig. 8.26** De-novo designed virus-mimicking particle for drug delivery, protein delivery, and gene therapy (Xu et al., 2002). In contrast to the protein envelope of most viruses, this particle has an envelope made from lipids

Fig. 8.25 illustrates a technique for the fast production of protein-polymer nanoparticles: A solution of polymer and protein is gently mixed with a salt solution. The salting-out effect causes the self-organization of nanoparticles that have different surface properties than the protein in the core (Prokop et al., 2001; Davda and Labhasetwar, 2002; Igartua et al., 2002; Konan et al., 2002; Haas and Lehr, 2002). In a similar way, also DNA can be camouflaged with lipids (Fig. 8.26; Xu et al., 2002). Some of these particles can cross the blood-brain barrier and are seen as promising candidates for future gene therapy and drug delivery.

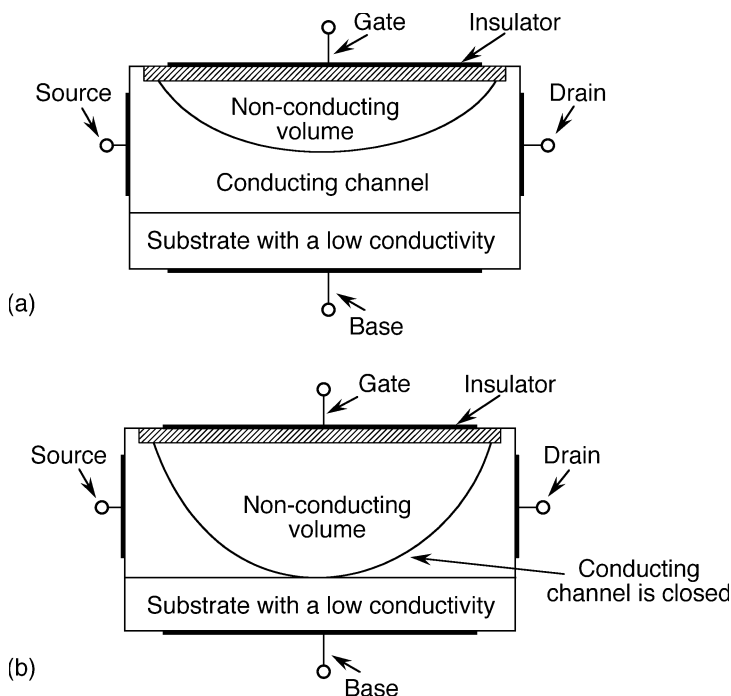


**Fig. 8.27** Self-assembled monolayer organic field-effect transistor (Collet and Vuillaume, 1998, Collet et al., 2000; Fujita et al., 2003). The figure depicts an example of the principle of operation of a field-effect transistor: The source-drain conductivity is controlled through the gate which is electrically insulated from the device itself: the width of a conducting channel between source and drain is varied by adjusting the voltage between gate and base. **(a)** Open channel between source and drain: current can flow between source and drain. **(b)** The source-drain channel is closed by application of a voltage between gate and base: now the source is isolated from the drain

A field effect transistor was manufactured by using self-assembly of organic molecules (Collet and Vuillaume, 1998, Collet et al., 2000). For an example of the principle of operation of field-effect transistors see Fig. 8.27.

## 9 Proteomics: high throughput protein functional analysis

Currently, there is a major effort, on a genome-wide scale, to map protein-drug interactions and to discover drug targets (Sect. 9.1), to map protein-protein interactions (Sect. 9.2), to discover chemical activity of proteins (Sect. 9.3), and to resolve protein structures (Sect. 9.5). This effort, called proteomics, provides significant knowledge of the biology of organisms far beyond the level of sequence information (see, e.g., Adam et al., 2002b; Burbaum and Tobal; Edwards et al., 2000, 2002; Christendat et al., 2000; Figeys, 2002a, 2002c; Gallardo et al., 2002; Hubbard, 2002; Kersten et al., 2002; Koshland and Hamadani, 2002; Lin and Cornish, 2002; Liu et al., 2002; Morrison et al., 2002; Natsume et al., 2002; Yarmush and Jayaraman). The system-wide study of proteins and as well non-proteinaceous interaction partners largely employs protein microarray technology (see, e.g., MacBeath, 2002; Gera et al., 2002; Kukar et al., 2002; Talapatra et al., 2002) and bioinformatic methods (see, e.g., Bork, 2002).

Proteomics-based approaches for the study of organ-specific regulatory and signaling cascades are seen as a key for a better understanding and therapeutical management of diseases (e.g., Jäger et al., 2002). Proteomics has provided new vaccine candidate antigens (Klade, 2002; Nilsson, 2002; Vytvytska et al., 2002). The identification of individual proteins abnormally expressed in tumors may have an important relevance for making diagnosis, prognosis, and treatment (e.g., Celis et al., 2002; Dwek and Rawlings, 2002; Jain, 2002; Michener et al. 2002; Zheng et al., 2003). Proteomics analysis of the neurodegeneration in the brain of transgenic mice discovered 34 proteins with significantly changed intensity (Tilleman et al., 2002). A proteomics approach was used to identify the translation products of squid optic lobe synaptosomes (Jimenez et al., 2002). A central nervous system (CNS) proteome database derived from human tissues is expected to significantly accelerate the development of more specific diagnostic and prognostic disease markers as well as new selective therapeutics for CNS disorders (Rohlf and Southan, 2002). Proteomics provides an extremely powerful tool for the study of variations in protein expression between different ages and for the understanding the changes that occur in individuals as they become older (Cobon et al., 2002).

Innovations towards higher throughput and cost cutting include mass spectrometry advances (Sects. 9.1 and 9.2), DNA microchips (Sect. 9.1), protein microchips (Sect. 9.2), genetic hybrid systems (Sect. 9.2), and lab-on-a-chip technology (Sect. 9.4).

## 9.1 Target discovery

Two-dimensional electrophoresis and mass spectrometry (Fig. 9.1) are widely used for the study of protein composition and protein changes in humans, animals, and plants. Important applications are (a) the identification of biomarkers specific for certain cell types, disease states, or aging processes, and (b) the study of protein composition changes as a response to drug treatment.

Also, high throughput microarray-based assays hold tremendous promise for the discovery of proteins connected with diseases (Fig. 9.2).

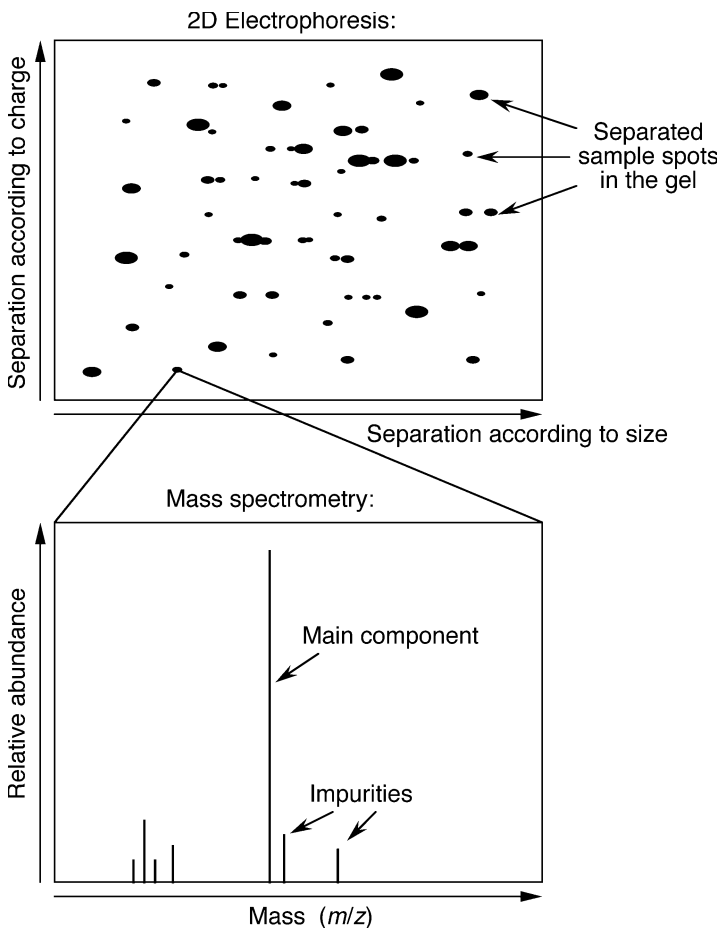


**Fig. 9.1** Discovery of proteins relevant to a certain disease by two-dimensional polyacrylamide gel electrophoresis and mass spectrometry (see, e.g., Edwards et al., 2000; Blomberg, 2002; Kersten et al., 2002; Man et al., 2002; Mo and Karger, 2002; Rohlff and Southan, 2002)

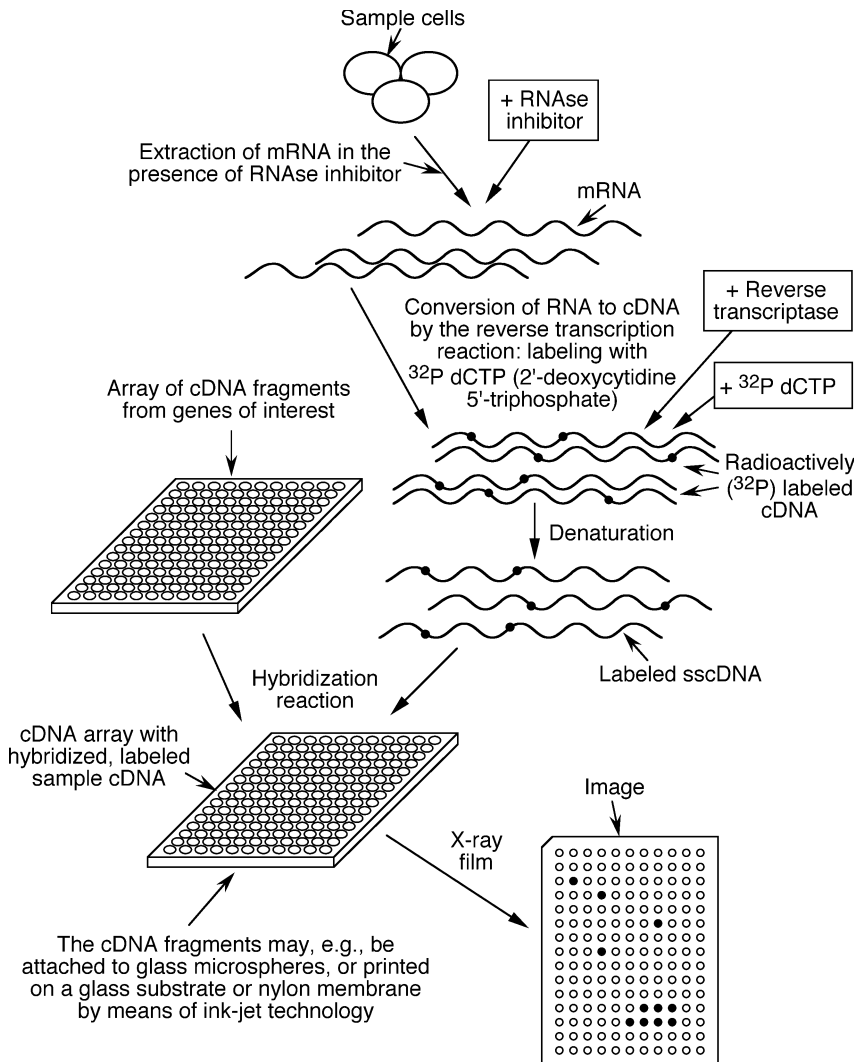


**Fig. 9.2** Discovery of proteins relevant to a certain disease, e.g., cancer markers, by detection of changes in the abundance of mRNA by means of cDNA (complementary DNA) microarray technology (supplied, e.g., by SuperArray, Inc., Bethesda, MD). cDNA chips with spot sizes of 10–500  $\mu\text{m}$  are commonly fabricated by high speed robotics or ink-jet printing on glass or nylon substrates. Every spot contains a different, 100–10,000 bases long, immobilized probe cDNA fragment which is complementary to targeted cDNA. The targeted, radioactively labeled cDNA is synthesized by reverse transcriptase from mRNA of the sample cells. Single stranded target cDNA is hybridized with complementary cDNA of the array and non-binding cDNA rinsed off with buffer. Detection of the pattern of radioactivity of the array then shows which mRNA was present in the sample cells, and thus which proteins were expressed

## 9.2 Interaction proteomics

Analysis of several 100,000 protein-protein interactions using microarray technology (Fig. 9.3) and the yeast two-hybrid system (Fig. 9.4) has led to dozens of

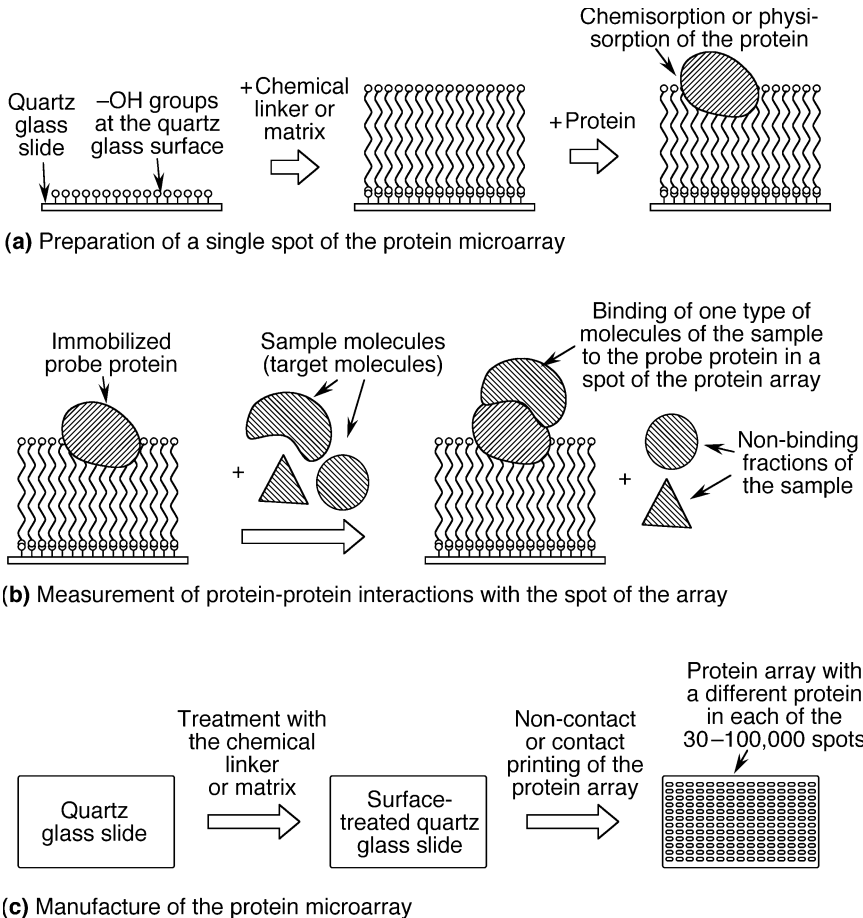


**Fig. 9.3** (a) Manufacture of a spot of a protein microarray for the assay of protein-protein interactions (see, e.g., Grayhack and Phizicky, 2001; MicroSurfaces, Inc., Minneapolis, MN). For a better maintenance of structural integrity, protein immobilization is carried out on a matrix or layer of a chemical linkers that provide a native-like environment for embedded proteins. (b) Sample protein molecules (target molecules) interact with a probe molecule of a spot of the array. Non-binding sample proteins are simply washed off with buffer. Sample molecules are radioactively or fluorescence labeled so that binding of target protein molecules with probe protein molecules can be detected. (c) Manufacture of an array with 30–100,000 individual probe proteins immobilized on a single slide by chemical treatment of the surface of a quartz glass slide and ink-jet or contact printing of the protein spots

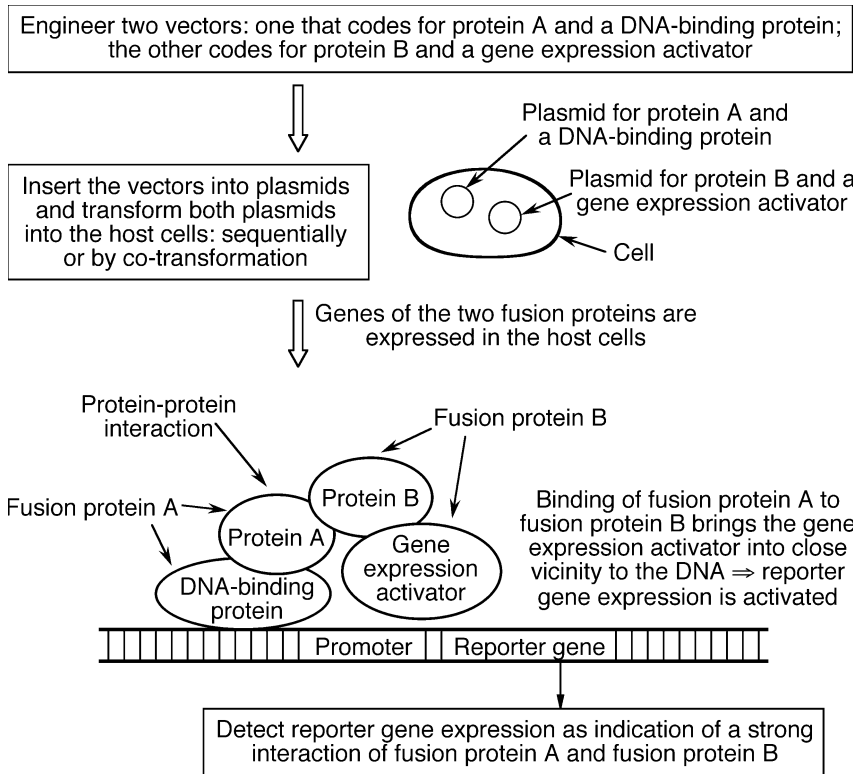


**Fig. 9.4** Discovery of protein-protein interactions by means of the yeast two-hybrid system (McCraith et al., 2000; Ito et al., 2002; Stagljar and Fields, 2002): Two vectors are constructed so that (i) one contains the code for a protein (protein A: e.g., a predicted open reading frame) followed by the code for a DNA-binding protein, and (ii) the other contains the code for another protein (protein B: e.g., another predicted open reading frame) followed by the code for a gene expression activator. Expression of both vectors in the cell yields a DNA-binding fusion protein and an expression-activating fusion protein. Attraction of both fusion proteins brings the expression activator into vicinity to the DNA. This leads to reporter gene activation. Diploids expressing the two-hybrid reporter gene in the host cells are then identified

novel findings of important intermolecular interaction (see, e.g., McCraith et al., 2000; Ito et al., 2002; Stagljar and Fields, 2002).

Figs. 9.5 and 9.6 present a mass-spectrometric method for the analysis of a large number of protein-protein and protein-drug interactions, respectively, without need of 2D-chromatography or electrophoresis. Possible ambiguities in the assignment of mass peaks may be resolved by the technique of ion fragmentation (see, e.g., Fig. 3.27). The discovery of new drug targets is highly important for developing new drugs (e.g., Pillutla et al., 2002; Whitelegge and le Coutre, 2002).

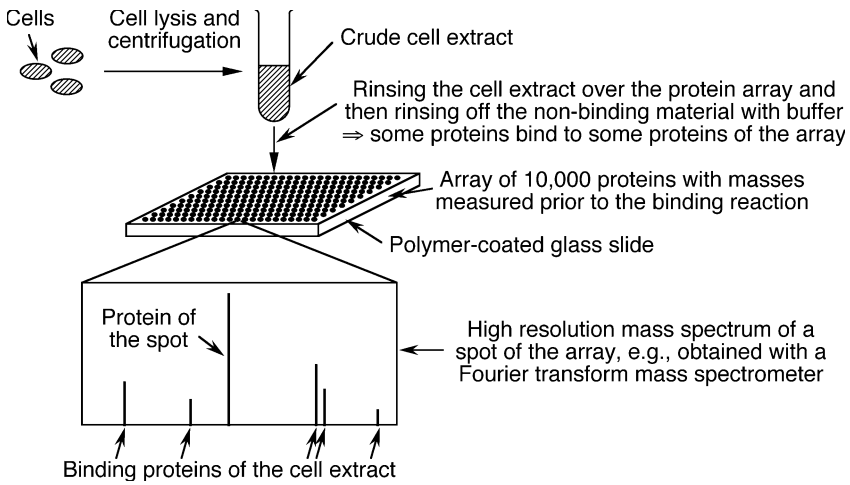


**Fig. 9.5** Analysis of millions of protein-protein interactions in one organism without 2D-chromatography or electrophoresis: Target proteins immobilized on the microarray interact simultaneously with all proteins expressed in a certain type of cells. After rinsing off the non-binding molecules, a high resolution mass spectrogram is recorded for each spot of the array. Each mass spectrogram shows a peak corresponding to the target protein and possibly further peaks corresponding to binding proteins. The binding proteins are then identified by their masses

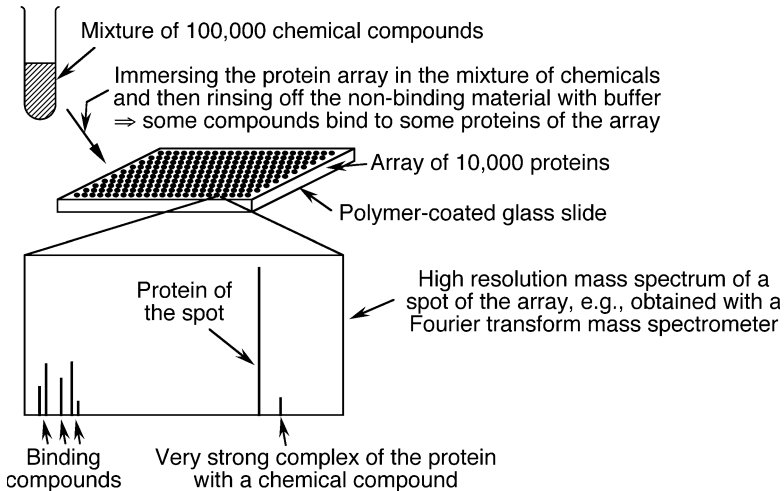


**Fig. 9.6** Large-scale analysis of interactions of chemical compounds with proteins without 2D-chromatography or electrophoresis: The protein array is dipped into the mixture of chemicals. After some time, non-binding chemicals are washed away with buffer. The spots are then mass-spectrometrically analyzed. Since the masses of the involved proteins and chemicals were previously measured, binding chemicals can easily be identified



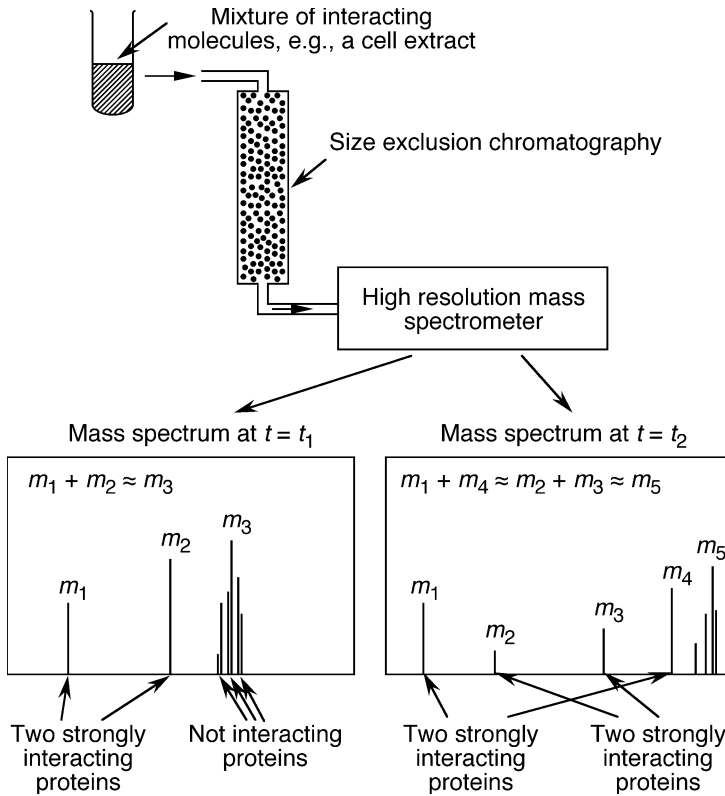


**Fig. 9.7** Direct determination of strong protein-protein interactions in a cell extract without need for the manufacture of arrays. First the mixture of monomeric proteins and protein-protein complexes is separated according to size by gel chromatography. Conditions for the chromatography are chosen in a way that strong complexes do not completely dissociate. Then mass spectrometry is performed for each chromatographic fraction which identifies the dimeric complexes and their two interacting macromolecules in the fraction: During ionization in the mass spectrometer, the complexes dissociate causing two peaks in the spectrum. These twin peaks are identified by their total mass which is roughly equal to the mass of the non-binding macromolecules. This method may analogously be applied to map out other strong macromolecular interactions

High resolution mass spectrometry even allows the simultaneous mapping-out of a large number of protein-protein and protein-drug interactions without use of microarrays (Fig. 9.7). A fast size exclusion chromatography separates the complicated mixture of interacting molecules into fractions. The parameters for chromatography were chosen such that strongly interacting molecule complexes remain together. Chromatographic fractions are then mass-spectrometrically analyzed. Strongly interacting dimers of molecules appear in the spectrogram as pairs with a total mass of about that of the monomers in the fraction.

### 9.3 Chemical proteomics

Chemical proteomics assigns molecular and cellular functions to thousands of identified or predicted gene products. Assaying activities of large pools of constructed strains with subsequent deconvolution of active pools is an efficient method to discover new functions of genes (see, e.g., Fig. 9.8; Martzen et al., 1999; Grayhack and Phizicky, 2001; Adam et al., 2002a; Phizicky et al., 2002).

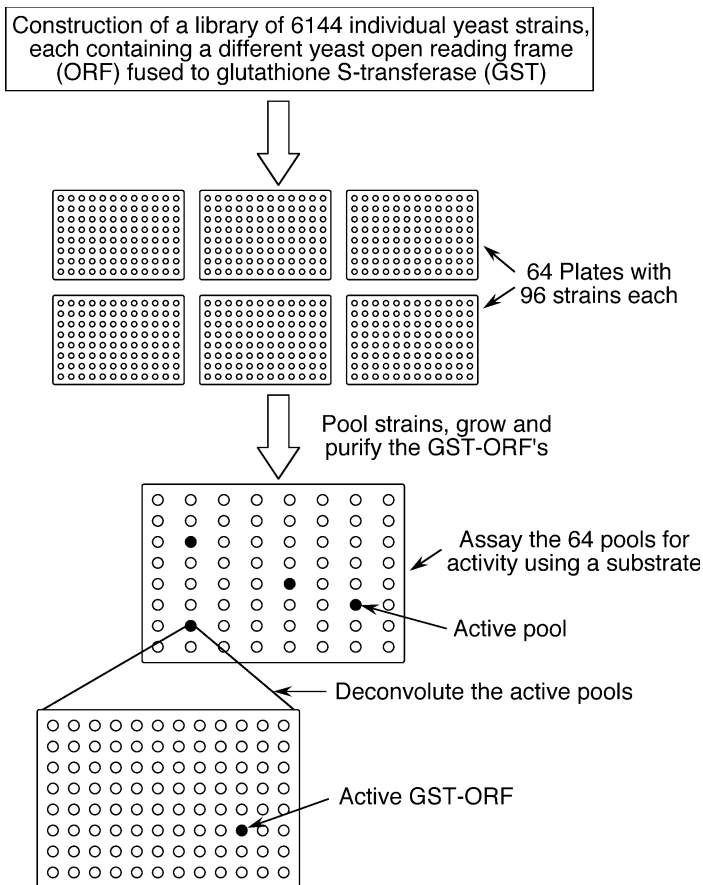


**Fig. 9.8** Example of chemical proteomics (Martzen et al., 1999; Grayhack and Phizicky, 2001; Phizicky et al., 2002). A library of 6144 yeast strains was constructed. Each strain expresses a unique yeast open reading frame (ORF) as a GST-ORF fusion (GST, glutathione S-transferase). Each 96 strains were pooled and biochemical activity of the pools was assayed. Active pools were deconvoluted using the library of strains to identify the GST-ORF responsible for activity. Several previously unknown biochemically active gene products were discovered

## 9.4 Lab-on-a-chip technology and mass-spectrometric array scanners

Protein and DNA microarrays are increasingly often processed with the lab-on-a-chip technology (Figs. 9.9 and 9.10): tiny channels etched into a glass slide, microswitches, micromixers, and other small devices act as small chemical factories.

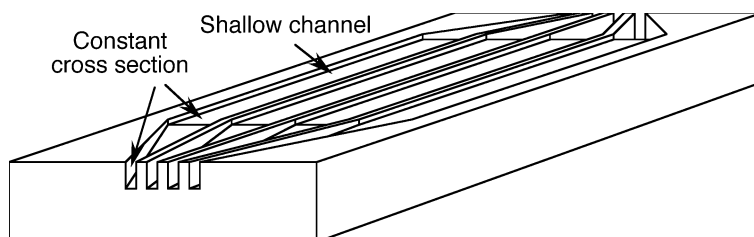


**Fig. 9.9** Simplified example for lab-on-a-chip technology (see, e.g., Swedberg et al., 1996; Swedberg and Brennen, 2001; Cheng et al., 2002; Figeys 2002b, Laurell and Marko-Varga, 2002). Tiny channels are microfabricated or etched into the support. The top is then sealed with another plate (not shown). A single chip may contain all the channels, switches and reservoirs necessary for complicated multi-stage chemical reactions

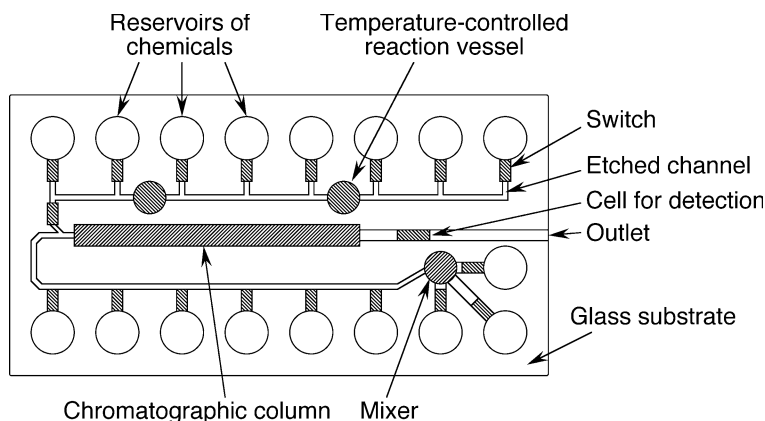


**Fig. 9.10** Example of lab-on-a-chip technology. Channels are etched into the glass support

Scanning of protein and DNA arrays with fluorescence detectors usually requires special labeling of the sample and may be prone to errors due to limitations of sensitivity and due to unspecific binding. More importantly, mixtures of signals can often not be resolved. Automatic mass-spectrometric

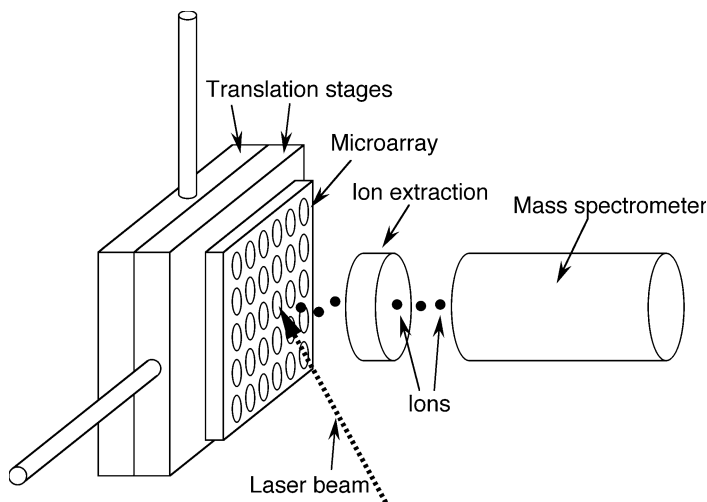


**Fig. 9.11** Mass-spectrometric array scanner for automatic mass-spectrometric measurement of protein and DNA microarrays. Step motor controlled translation stages rapidly move the microarray into position. A mass spectrum for each of the spots is automatically taken and analyzed. The scanner can be used, e.g., in the methods outlined in Figs. 9.5 and 9.6

detection of the molecules in the spots of the array can greatly enhance the information yield (Fig. 9.11).

## 9.5 Structural proteomics

Proteomics is driving a substantial effort towards large-scale protein structure prediction (see, e.g., Renfrey and Featherstone, 2002; Schmid, 2002) and determination. High resolution structure determination still relies on X-ray crystallography and NMR (nuclear magnetic resonance). Since both methods are expensive and time-consuming, further optimization of the methods is being in progress. NMR peaks can now automatically be assigned to the corresponding amino acid residues (Nilges et al., 1997; Heinemann et al., 2001). The Berlin Protein Structure Factory develops and applies large-scale NMR and crystallographic methods (Heinemann et al., 2000, 2001; Boettner et al., 2002).

On the other hand, structure computer simulation using simplifications of the conformational space of proteins is rapidly progressing (see Sect. 1.4), and so it can be hoped that comparably inexpensive computational methods will make an increasing contribution to structural proteomics in the near future.

# 10 Ion mobility spectrometry

## 10.1 General design of spectrometers

Ion mobility spectrometry was developed for the simple and cheap detection and characterization of organic compounds (Cohen and Karasek, 1970; Karasek, 1970; Caroll et al., 1971; Caroll, 1972; Cohen et al., 1972; Cohen and Crowe, 1973; Vora et al., 1987; St. Louis and Hill, 1990; Campbell et al., 1991; Burke, 1992; Eiceman and Karas, 1994; Taylor, 1996; Baumbach and Stach, 1998; Baumbach and Eiceman, 1999; Saurina and Hernandez-Cassou, 1999; Asbury and Hill, 2000; Purves et al., 2000; Wu et al., 2000; Beegle et al., 2001; Eiceman et al., 2001; Matz and Hill, 2001; Stone et al., 2001). The ion mobility spectrum reflects the ion mobilities which correlate well with the size-to-charge ratios of the sample compounds.

In the ion mobility spectrometer (IMS), (a) sample molecules in the vapor phase are ionized, (b) the charged sample molecules (ions) are accelerated by an electric field, and (c) their time of flight in the gaseous medium of the drift channel is measured and recorded (Figs. 10.1–10.6). These simple spectrometers can detect and analyze astonishing tiny traces of small and as well large molecules and clusters.

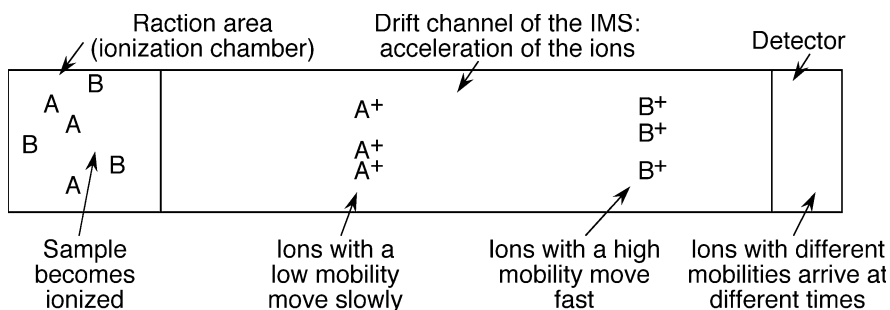


**Fig. 10.1** Principle of operation of ion mobility spectrometers: Molecular ions are generated and accumulated in the reaction area. A gating pulse transfers the molecular ions to the drift channel where said ions are accelerated by an electric field. Ions with different mobilities in the gaseous medium of the drift channel arrive at different times at the detector

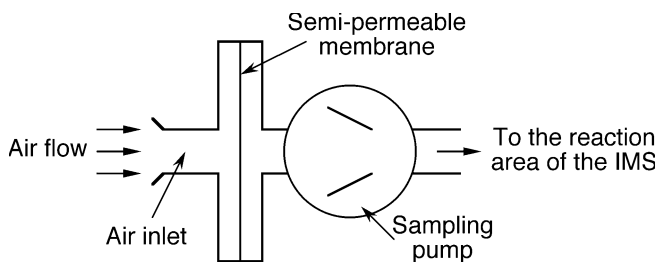


**Fig. 10.2** Design of a sample inlet for an IMS. The sampling pump draws air through the semi-permeable membrane which attenuates the influx of large dust particles and other interferences (see also Spangler, 1982). A suitable membrane is, e.g., a 5–50  $\mu\text{m}$  polytetrafluoroethylene (PTFE) foil or silicone rubber membrane (Spangler and Carrico, 1983; Kotiaho et al., 1995). For IMS for detection of biological agents, a metal grid instead of a membrane may be more appropriate because of its better transparency for high molecular-weight compounds

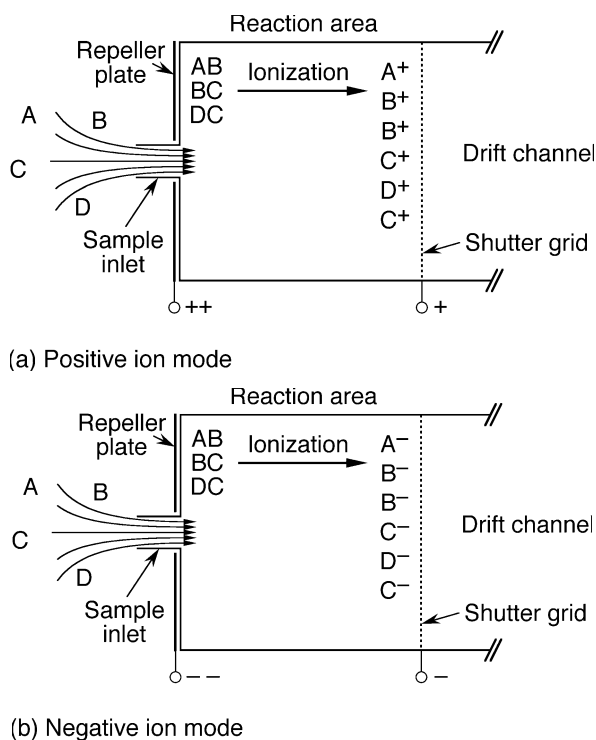


**Fig. 10.3** Reactions of the sample in the reaction area. Sample molecules are ionized, either directly by dissociation or indirectly by clustering with other ions. In the positive ion mode, positive ions are repelled from the repeller plate and accumulated in front of the shutter grid. In the negative ion mode, negative ions are analogously accumulated. Many IMS operate alternately in the positive and negative ion mode

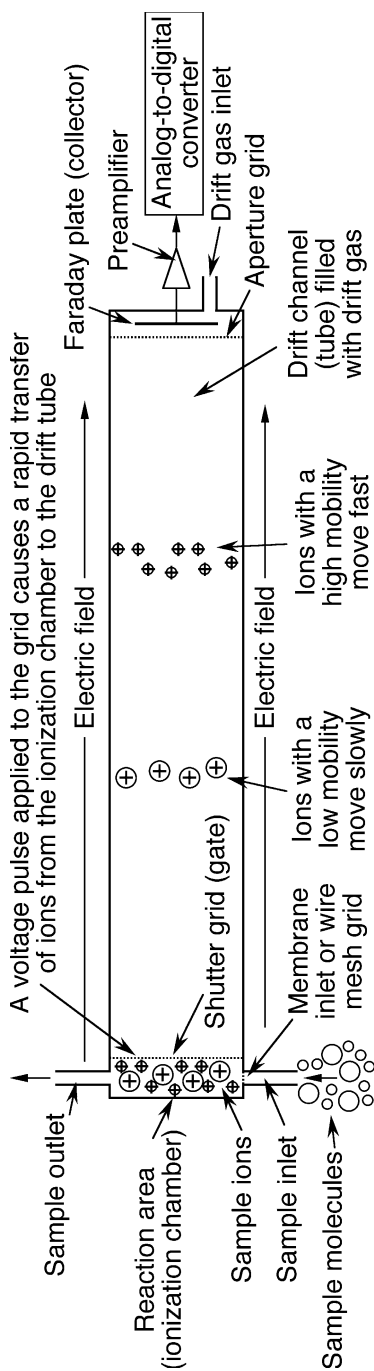


**Fig. 10.4** Principle of operation of an ion mobility spectrometer (IMS) (Cohen and Karasek, 1970; Karasek, 1970; Carroll et al., 1971; Keller, 1975; Eiceman and Karas, 1994). Sample molecules are injected into the reaction area (ionization chamber) and ionized. A thin membrane or a wire mesh grid separates reaction area and drift channel (drift tube, drift region). An electrical pulse applied to the shutter grid (gate, grid, gating grid) transfers the ions into the drift channel where the ions are further accelerated by the electric field which is generated by guard rings (see Figs. 10.5 and 10.6). The time of flight of the ions in the gaseous phase is measured with the help of a Faraday plate (collector plate, Faraday cup) or collector grid. The mobility of a gas phase ion is a measure of its collision cross section which in turn depends on its size and structure. Small ions with compact structures have smaller cross sections than large ions with open structures. Consequently, since different ions have different mobilities in the gas of the drift tube, they can result in distinct peaks in the ion mobility spectrum. A computer (not shown) determines the identity of the sample molecules by matching the spectra to reference signatures. In order to reduce the noise, the IMS is enclosed in a grounded copper foil (not shown). The collector is directly connected with a  $10^{10}$ -V/A preamplifier via a cable of only a few mm length. The feedback resistor of the preamplifier is selected for a low noise level. Since fluctuations of the electric field of the drift channel add noise to the signal of the Faraday plate, the voltage supply for the guard rings is highly stabilized. In contrast to mass spectrometers, this device needs no hot filaments with a limited lifetime, electron multipliers, energy-consuming vacuum pumps, or expensive vacuum tubes, and its sensitivity can be several orders of magnitude higher than that of a mass spectrometer. Drift times of macromolecules are usually milliseconds to seconds in 3–20 cm drift tubes with drift voltage gradients of about 100–1000 V/cm. For most IMS, a few seconds are required after each measurement to purge the drift channel

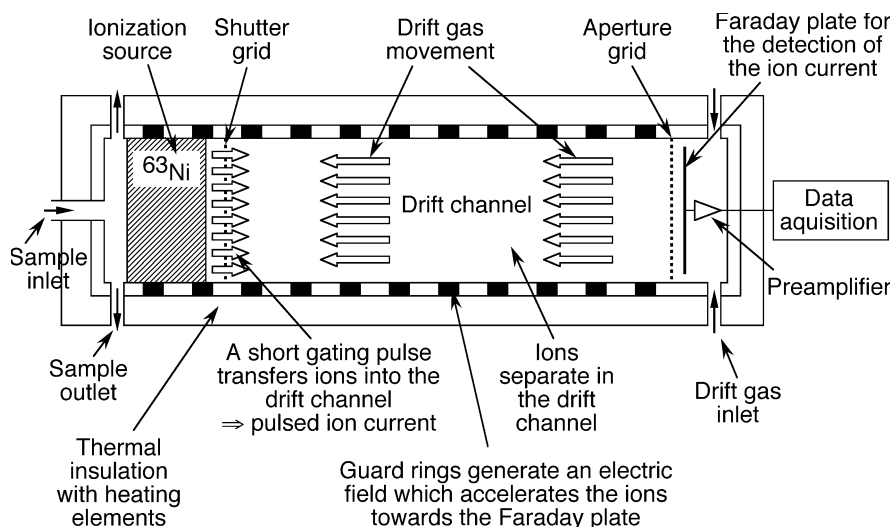


**Fig. 10.5** Design of an IMS (Cohen and Karasek, 1970; Karasek, 1970; Caroll et al., 1971; Eiceman and Karas, 1994; Matz and Schröder, 1996, 1997; IUT Institute for Environmental Technologies, Berlin, Germany; Bruker Daltonik, Bremen, Germany; Graseby Dynamics, London, U.K.; Barringer Instruments, Warren, NJ). The ionization source ionizes sample molecules. Guard rings generate an electric field which accelerates the sample ions towards the shutter grid where they accumulate. After a few seconds, a voltage pulse is applied to the shutter grid causing the release of the sample ions into the drift channel. Now the electric field can further move the sample ions towards the ion detector (Faraday plate). Different ions interact differently with the drift gas molecules in the drift channel. This causes the ions to spread out according to their different mobilities. The recorded ion mobility spectrum corresponds to differences in the time of flight of the sample ions. Typically, the drift channel has a length of a few cm, and the electric field strength in the drift channel is  $100\text{--}1000\text{ V cm}^{-1}$ . At this field strength and length, small organic compounds which have mobilities of a few  $\text{cm}^2\text{ V s}^{-1}$  need about 1–100 milliseconds to reach the detector. Biomacromolecules typically travel about 1–3 orders of magnitude slower. Drift channel and reaction area are enclosed in a thermal isolation with heating elements. The operating temperature for the detection of biological agents is typically  $100\text{--}150\text{ }^\circ\text{C}$

The IMS is comprised of (a) a thermally isolating housing, a source of ionization, reaction area, shutter grid, drift channel with guard rings, possibly an aperture grid, collector, (b) a source of clean gas or a gas filter, (c) a shutter controller, (d) a high voltage supply, (e) an electrometer, (f) temperature control instrumentation, (g) a computer-aided data collection and processing unit.

The major advantage of IMS is the extreme sensitivity (see Sect. 10.2). Another important advantage of IMS, which do not need vacuum parts, is the lower cost and lower energy consumption relative to most mass spectrometers. This makes it particularly suitable for large-scale field applications.



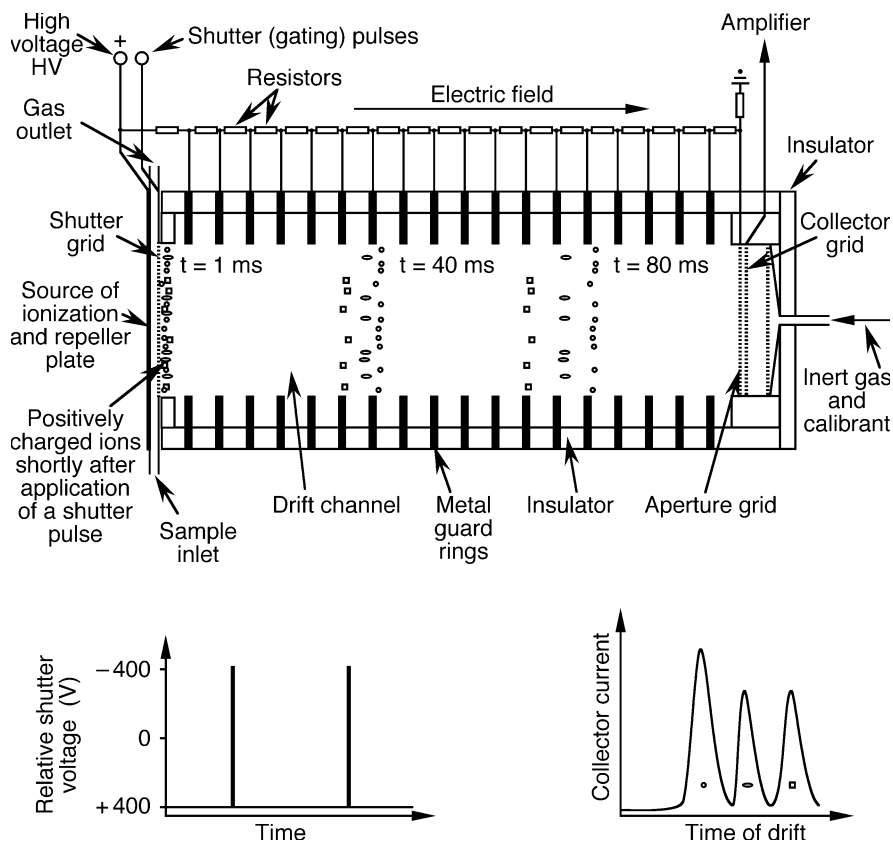


**Fig. 10.6** *Top*: design of an IMS containing 18 stacked copper guard rings that are separated by insulating ceramics spacers and connected by resistors. These resistors are selected for low noise. The voltage supply for the guard rings is stabilized to better than 0.1% rms. In order to ensure a homogenous electric field, the guard rings have sufficiently narrow separations. In this example the IMS is operated in the positive ion mode. *Bottom left*: example of the shutter voltage: Most of the time, a positive shutter voltage prevents positively charged ions from entering the drift channel. After a period of time during which positive ions accumulate in front of the shutter grid, a negative shutter voltage pulse is applied. Now positive ions can enter the drift channel where they are further accelerated. *Bottom right*: recorded spectrum

A suitable inert gas for the detection of many organic compounds is nitrogen, but clean air can also serve for this purpose. Cleaning the drift gas from water vapor and sample residues is frequently performed with molecular sieves (Fig. 10.7). These molecular sieves are made from zeolites which are certain aluminosilicates. Zeolites can adsorb water molecules and other small organic compounds. After a few weeks or month of use in an IMS, the zeolite is saturated. It can be reconstituted by heating it in an oven and be re-used.

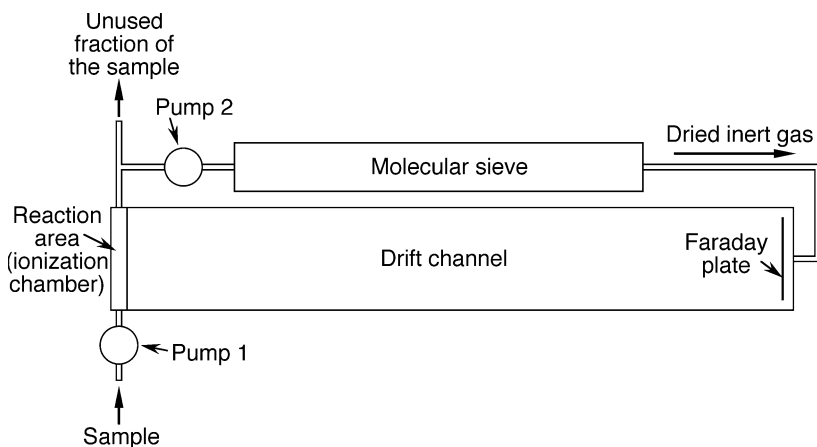


**Fig. 10.7** Drying the inert gas with a molecular sieve (Carnahan and Tarassov, 1998; Taylor and Turner, 1999). Suitable dimensions for a length of the drift channel of 5–20 cm, a diameter of the drift channel of 2–3 cm, and a height of the ionization chamber of 0.5–1 cm are: flow rate of pump 1: 5–50 ml min<sup>-1</sup>; flow rate of pump 2: 50–500 ml min<sup>-1</sup>

## 10.2 Resolution and sensitivity

The resolution,  $R$ , of an IMS is defined as

$$R = 0.5 \cdot t_d \tau^{-1}, \quad (10.1)$$

where  $t_d$  is the drift time of the peak,  $\tau$  and is its temporal width at half peak height (St. Louis and Hill, 1990).

Important factors affecting the resolution are: (a) initial ion pulse width and shape (shutter pulse width), (b) broadening by Coulomb repulsion between the ions in both the reaction region and drift channel, (c) ion-molecule and ion-ion reactions in the reaction region, (d) gate depletion, (e) ion-molecule reactions in the drift region, (f) spatial broadening by diffusion of the ion packet during the drift, (g) temperature and pressure inhomogeneities within the spectrometer, (h) capacitive coupling between aperture grid and collector, and (i) the response time of the preamplifier, amplifier, and analog-to-digital converter. Broadening by Coulomb repulsion is particularly severe in narrow designs of reaction region and drift channel.

$R$  strongly depends on the design of the spectrometer, but can theoretically exceed 1000 (Figs. 10.8–10.10). A high resolution requires a relatively bulky design with a drift channel of sufficient diameter and large length and a high drift voltage. Most commercial IMS have resolutions of only 20–150 since they are mainly optimized for low weight and portability.

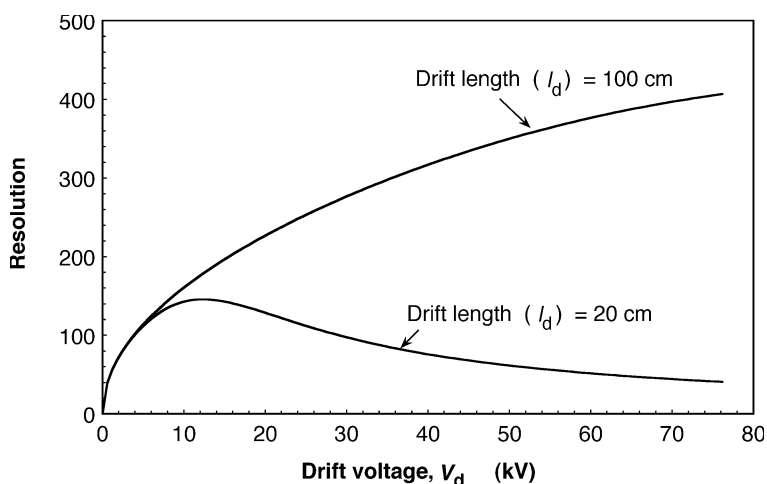


**Fig. 10.8** Theoretical resolution of an IMS at different drift lengths. At short drift lengths, increasing the drift voltage above an optimum does not further improve the resolution. The parameters in this example are: temperature, 130 °C; ion mobility,  $10^{-5} \text{ m}^2 \text{ V}^{-1} \text{ s}^{-1}$ ; initial ion pulse width, 1 ms; shutter pulse voltage, 1000 V; length of the reaction area, 3 mm; distance between aperture grid and Faraday plate, 1 mm; voltage at the aperture grid, 500 V

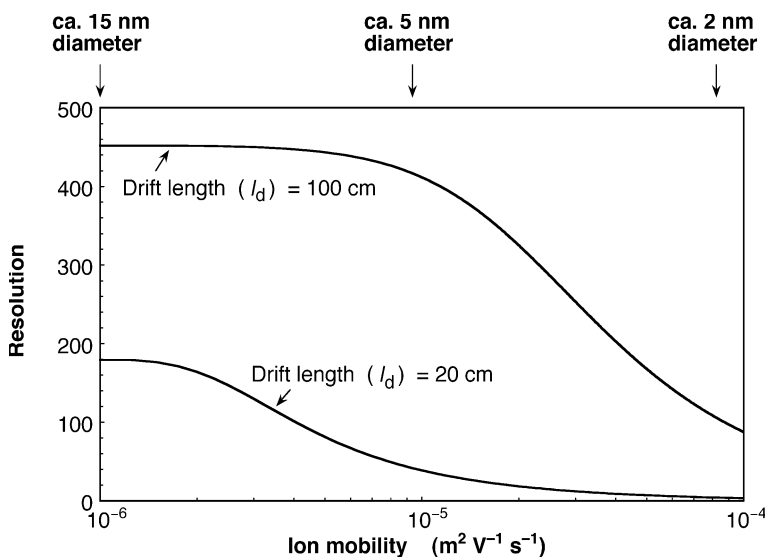


**Fig. 10.9** Theoretical resolution of an IMS at different drift lengths and ion mobilities: long shutter pulses enhance the sensitivity, but limit the resolution for small ions. The parameters in this example are: temperature, 130 °C; drift voltage, 80 kV; initial ion pulse width, 1 ms; shutter pulse voltage, 1000 V; length of the reaction area, 3 mm; distance between aperture grid and Faraday plate, 1 mm; voltage at the aperture grid, 500 V

$R$  is approximately given by Eq. 10.2 (St. Louis and Hill, 1990; Hill et al., 1990; Leonhardt et al., 2001):

$$R = \frac{1}{\sqrt{16 \ln 2 \frac{k_B T}{q V_d} + \frac{K^2 V_d^2}{l_d^4} \left( t_{Pulse} - \frac{s^2}{K V_{Pulse}} \right)^2 + \left( \frac{a^2 V_d}{l_d^2 V_{ap}} \right)^2 + \frac{t_{Pulse}^2 K^2 V_d^2}{l_d^4}}} \quad (10.2)$$

where  $k_B$ , Boltzmann constant ( $1.3807 \times 10^{-23} \text{ J K}^{-1}$ );  $T$ , absolute temperature;  $q$ , ion charge;  $V_d$ , drift voltage;  $l_d$ , drift length;  $K$ , ion mobility;  $t_{Pulse}$ , initial ion pulse width;  $V_{Pulse}$ , shutter pulse voltage;  $s$ , distance between space charge in the reaction area and shutter grid (roughly half the length of the reaction area);  $a$ , distance between aperture grid and Faraday plate;  $V_{ap}$ , voltage at the aperture grid.

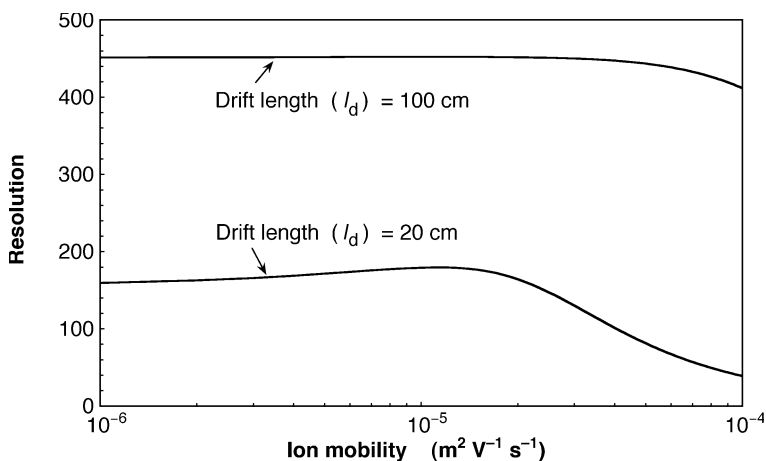


**Fig. 10.10** Theoretical resolution of an IMS at different drift lengths and ion mobilities. Short shutter pulses and long drift lengths allow the high resolution of both medium-sized and as well large molecules. The parameters in this example are: temperature,  $130 \text{ }^\circ\text{C}$ ; drift voltage,  $80 \text{ kV}$ ; initial ion pulse width,  $100 \text{ }\mu\text{s}$ ; shutter pulse voltage,  $1000 \text{ V}$ ; length of the reaction area,  $3 \text{ mm}$ ; distance between aperture grid and Faraday plate,  $1 \text{ mm}$ ; voltage at the aperture grid,  $500 \text{ V}$

The sensitivity of an IMS can be 1000 times greater than that of a good mass spectrometer: with conventional electronics, theoretically down to 1000 ions are still detectable corresponding to  $3 \times 10^{-19} \text{ g TNT}$  or  $2.5 \times 10^{-16} \text{ g botulinum toxin}$  ( $M_w = 150 \text{ kDa}$ ). For comparison, the fingerprint of a person likely contains many billion times more residue of organic compounds. Practical detection limits are

typically on the order of 0.1 to 100 ppbv. One reason for the often superior sensitivity relative to mass spectrometers is the simple and large sample inlet. Many IMS contain a thin large area-polymer membrane inlet or a metal grid inlet with cause only little sample losses (Fig. 10.3; Spangler, 1982; Spangler and Carrico, 1983; Kotiaho et al., 1995). In some IMS, the sample inlet solely consists of a tube with a filter which removes dust particles and in some cases water from the sample prior to sample injection into the IMS.

Short gating pulses and high humidity tend to lower the sensitivity. All means of noise reduction, such as (a) small collector capacity, (b) a highly stabilized voltage of the guard rings, (c) an electric shielding of the whole IMS, and (d) low-noise resistors in the electronics, tend to improve the sensitivity. Further, for a high sensitivity and low memory effects, the IMS must be built from materials which adsorb extremely little if any sample molecules, e.g., special ceramics.

Sensitivity and resolution are also affected by the presence or absence of an aperture grid: The function of the aperture grid is to capacitively decouple the collector (Faraday plate or collector grid) from the approaching ion cloud. Without the aperture grid, the collector senses the approaching ion cloud several millimeter prior to its arrival, resulting in line broadening (St. Louis and Hill, 1990). On the other hand, the aperture grid neutralizes ions which decreases the ion current and sensitivity by a factor of roughly 3.

### 10.3 IMS-based “sniffers”

IMS sniffers (Figs. 10.11 and 10.12) are hand-carried IMS-based devices, mainly manufactured for the detection of dangerous substances. They contain a small IMS and a database of the signatures of substances of interests and interferents. After a few seconds of measurement, the processing unit identifies and signalizes detected agents. The sniffers weighting about 2–10 kg are roughly 25–40 cm long. False alarm rates for the detection of chemicals are quite often 0.01–1%.

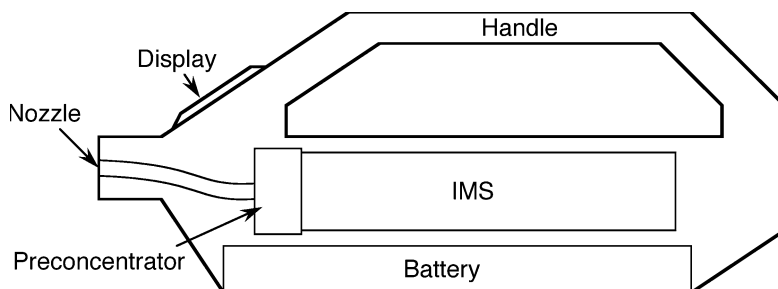


**Fig. 10.11** Hand-carried “sniffers” comprising a chemical preconcentrator and an IMS (made, e.g., by Sandia Corporation, Albuquerque, NM, and Barringer Instruments, Inc., Warren, NJ)

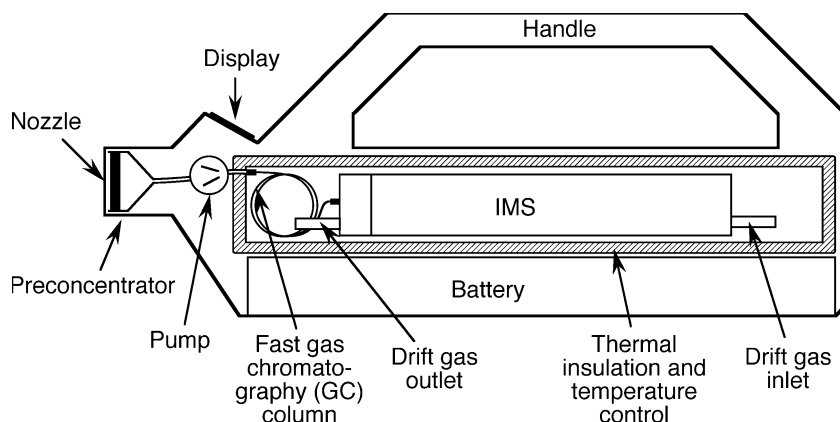


**Fig. 10.12** Hand-carried sniffing detector which further comprises a fast gas chromatography (see, e.g., Snyder et al., 1993). The combination with GC improves the false alarm rate for the detection of dangerous substances by typically one order of magnitude

## 10.4 Design details

Figs. 10.11 and 10.12 show a portable IMS and GC/IMS detector with a preconcentrator, respectively. GC in combination with IMS significantly reduces the false alarm rate for the detection of hazardous compounds. Preconcentrators (Fig. 10.13) can increase the sample concentration and the sensitivity of the method by a factor of more than 1000, and can also reduce the false alarm rate.

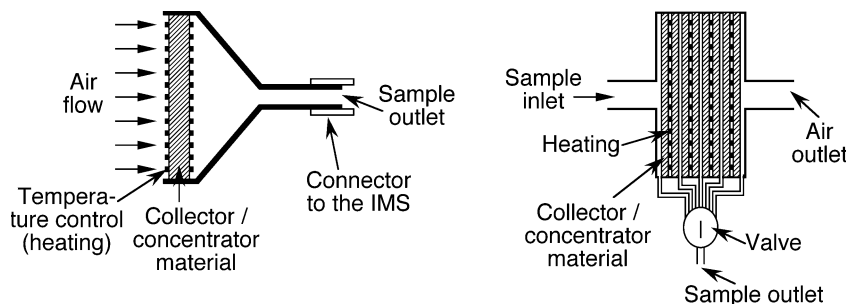


**Fig. 10.13** Two design variants of preconcentrators for ion mobility spectrometry. It draws a large volume of air and collects biological and heavy chemical organic compounds from the air onto the filter. The filter is made from zeolites – a material which is commonly used in molecular sieves (see Fig. 10.7). After several minutes of sample collection, the heater vaporizes the organic material into a small parcel of air which is delivered to the IMS. These preconcentrators increase the sample concentration by a factor of typically 10–1000 (see, e.g., Spangler, 1992a)

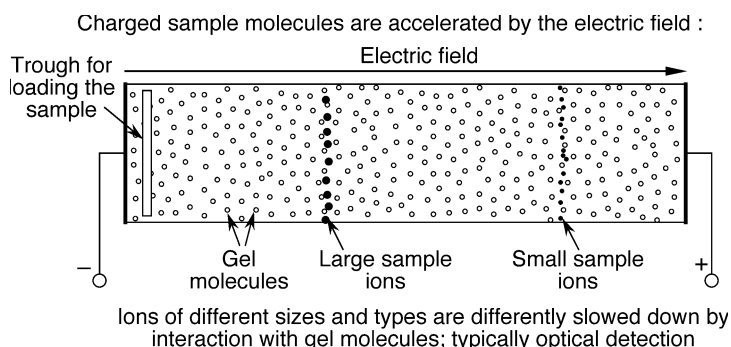


**Fig. 10.14** The typical set-up for electrophoresis shows an analogy to ion mobility spectrometry: in both methods charged molecules are accelerated by an electric field and slowed down by interaction with molecules of a stationary phase. In electrophoresis, the stationary phase is generally a gel, and the movement of the sample molecules is often optically detected. A gas serves as stationary phase in ion mobility spectrometry, and the movement of the sample ions is electrically detected. A small size and high charge of ions correlates with a large speed

Ion mobility spectrometry has some similarities to electrophoresis (Fig. 10.14). Because of the similarities to common chromatography, originally ion mobility spectrometry was called “plasma chromatography”. However, one has to keep in mind that in contrast to common chromatography, ion mobility spectrometers have a narrow linear range due to space charge effects (Bird and Keller, 1976; Blanchard and Bacon, 1989; Spangler, 1992b), and show serious matrix interferences and prolonged memory effects.

**Table 10.1** Common methods of sample ionization in ion mobility spectrometry (Lubman and Kronick, 1982, 1983; Baim et al., 1983; Leasure et al., 1986; Eiceman et al., 1988; Shumate and Hill, 1989; Begley et al., 1991; Phillips and Gormally, 1992; Davies, 1994; Spangler et al., 1994; Carnahan and Tarassov, 1995; Leonhardt, 1996; Lee et al., 1998; Wu et al., 1998a, 1998b, 2000; Budovich et al., 1999; Döring et al., 1999; Borsdorf et al., 2000; Megerle and Cohn, 2000; Schnurpfeil and Klepel, 2000; Borsdorf and Rudolph, 2001)

Method of ionization	Example
Radioactive isotopes	$^3\text{H}$ , $^{241}\text{Am}$ foil, or $^{63}\text{Ni}$ foil; Fig. 10.15
Photoionization	UV and VUV light from a 30-W krypton or hydrogen lamp with a $\text{MgF}_2$ -window, or perpendicular to the drift channel from a frequency-quadrupled Nd:YAG laser at 266 nm (Fig. 10.15). A VUV-absorbing compound may be added for an increased degree of ionization.
Electrospray	Fig. 3.11 in Chap. 3
Laser desorption	Fig. 10.15
Electrical (corona) discharge	Fig. 10.15

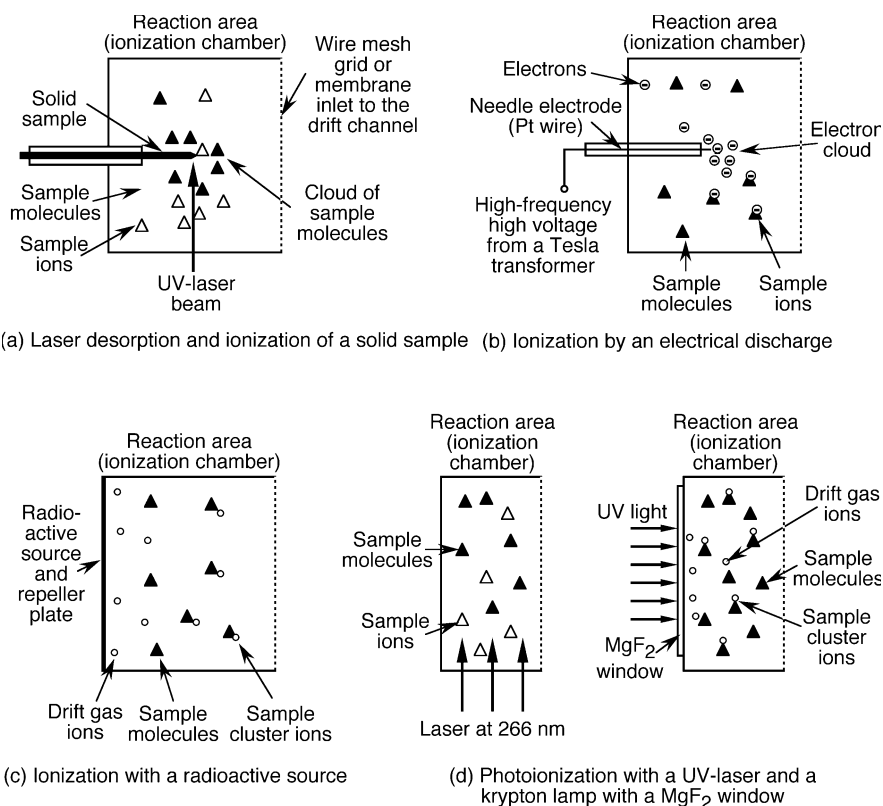


**Fig. 10.15** Examples of ionization methods (see also Table 10.1)

Since most of the interesting chemical and biological substances are not charged, it is necessary to ionize them prior to the drift. Table 10.1 and Figs. 10.15 and 10.16 show methods for ionization in ion mobility spectrometry. Radioactive isotopes and photoionization are the most common methods. When using a  $^{63}\text{Ni}$  foil as the source of ionization and air as the drift gas, the primary ions are mainly short-living  $\text{N}_2^+$ ,  $\text{NO}^+$ , and  $\text{O}_2^-$ . These primary ions rapidly react with traces of water in the drift gas to form clusters of the types  $\text{N}_2^+(\text{H}_2\text{O})_n$ ,  $\text{NO}^+(\text{H}_2\text{O})_m$ , and  $\text{O}_2^-(\text{H}_2\text{O})_k$ . Photoionization with hydrogen plasma discharge lamps and krypton plasma discharge lamps requires a photon flux of about  $10^{12} \text{ cm}^{-2} \text{ s}^{-1}$ . The geometry of the shutter grid is chosen so that most photons cannot enter the drift channel since this would reduce the resolution. Common radioactive sources in IMS have the advantage of relatively long half-lives of several years. For immobilization of  $^3\text{H}$ , it is gettered in a thin titanium layer.

Ion mobility spectrometry has gained significant importance in the context of the detection of ultra-trace chemical and biological contaminants (Snyder et al., 1991a, 1991b, 1996a, 1996b, 1999, 2000; Ogden and Strachan, 1993; Strachan et



al., 1995; Dworzanski et al., 1997; Smith et al., 1997), explosives (e.g., Fetterolf and Clark, 1993; Steinfeld and Wormhoudt, 1998; Fig. 10.17), illicit drugs (e.g., Miki et al., 1997, 1998; Keller et al., 1998), pesticides, the detection of animals and animal activity in jungles, and other environmental monitoring.

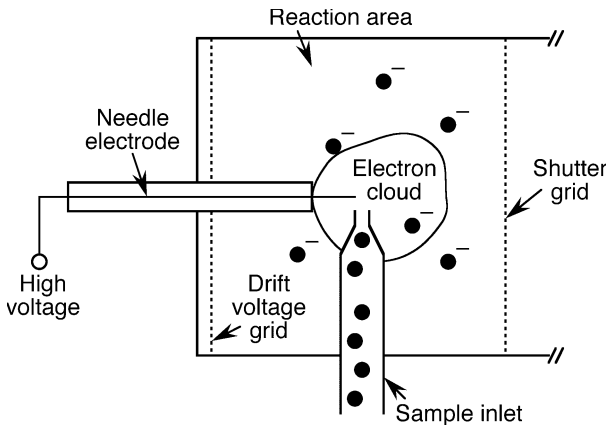


**Fig. 10.16** Gas inlet for electrical-discharge (corona discharge) ionization

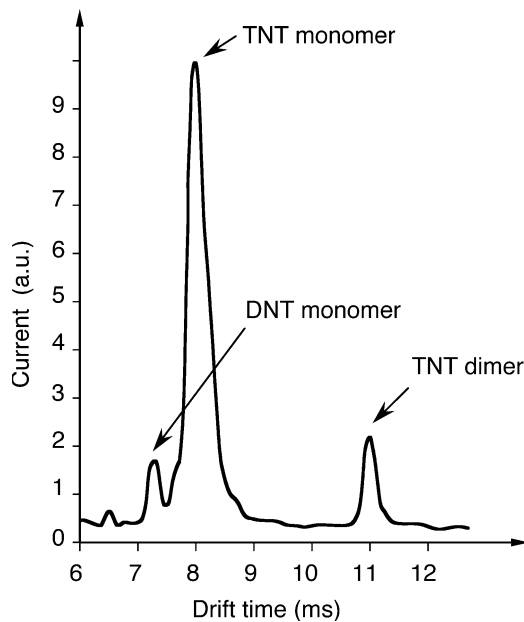


**Fig. 10.17** Ion mobility spectrogram of TNT (trinitrotoluene). From data supplied by the Institute for Environmental Technologies Ltd., Berlin

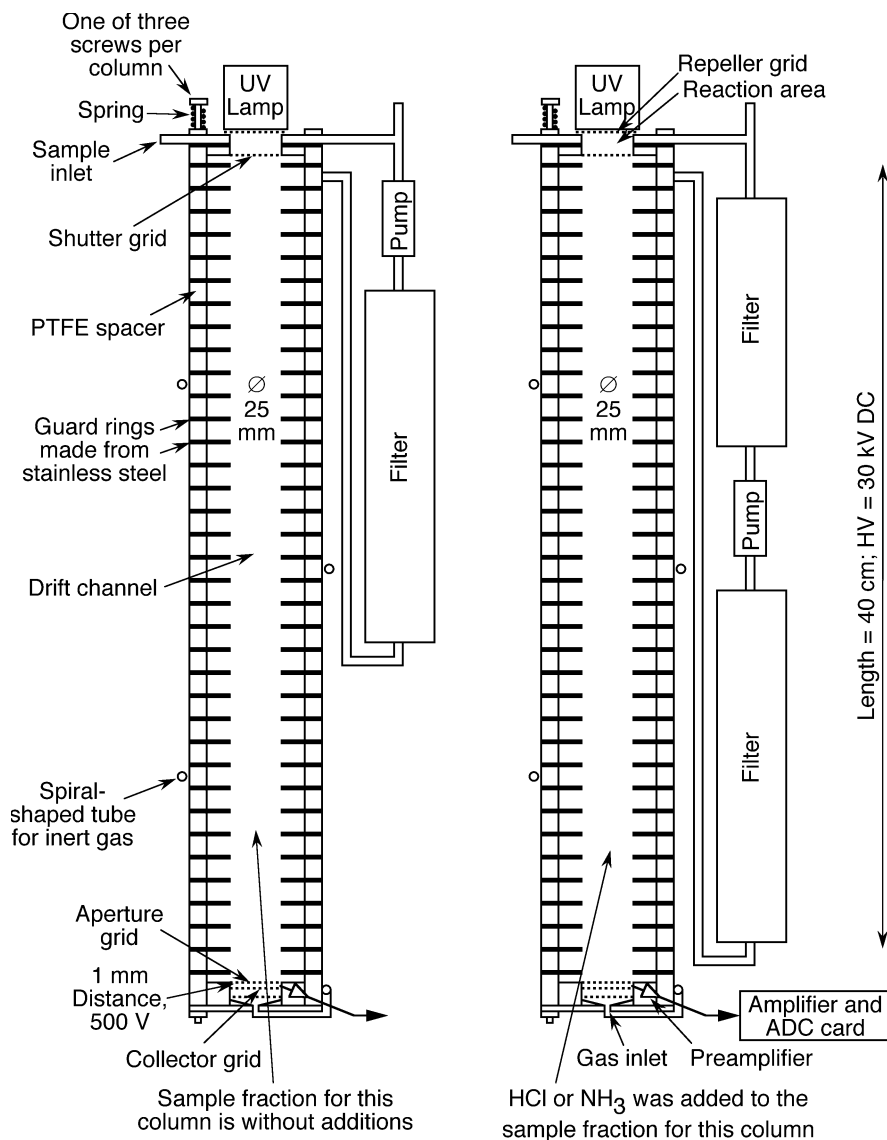


**Fig. 10.18** A high-resolution two-channel ion mobility spectrometer. Here the sample is simultaneously analyzed in two different ways reducing false identifications of agents. In one of the columns, the sample is chemically and/or physically modified by a chemical addition

Fig. 10.18 outlines an IMS-based twochannel detector which was designed within a feasibility study. In this design the differentiation between various

biological and also some chemical substances is improved by utilizing physical and chemical modifications of the sample in one of the two columns, e.g., by adding an acidizing gas: Most proteins display a strong pH-dependency of the charge (see, e.g., Chap. 2 in Nölting, 2005). Thus, by changing the pH, the charge state of the protein-containing biological material is altered and consequently its speed of diffusion in the drift channel is changed. Further, the added gas can cause chemical changes of some chemical and biological agents. This causes specific changes of the IMS spectra and thus contributes to a further improvement of the correct identification of the agents. Multichannel designs are a further option to reduce false detection rates of IMS. The channels may be operated in the same way speeding up the measurement of slowly drifting substances. Alternatively the sample may simultaneously be distributed over different channels which are operated in various different modes which can improve the resolution of the method.

IMS with an oscillating electric field allow the application of large field strengths without need for a very high voltage (Fig. 10.19). Since very large macromolecules have low mobilities, their fast detection with high resolution requires a high electric field strength in the drift channel. In the common design this may cause safety problems and increases the price of the IMS.

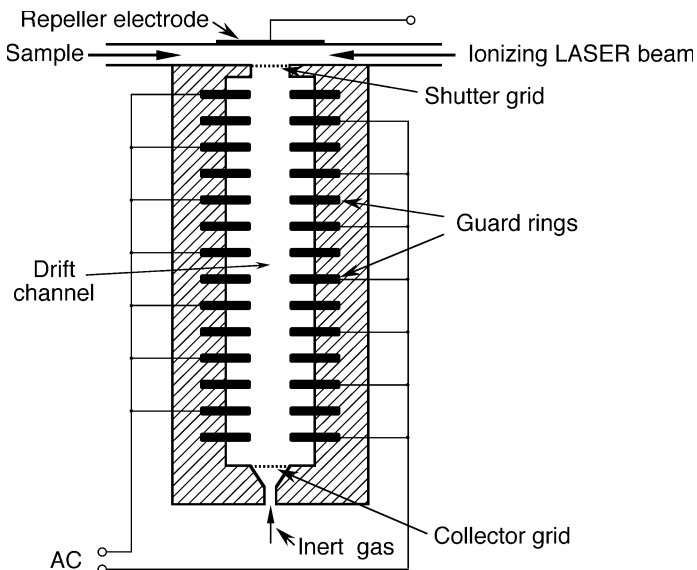


**Fig. 10.19** IMS with an oscillating electric field of the guard rings instead of a constant electrostatic field. Only ions of which the movement is in phase with the oscillating electric field can pass through the drift channel and reach the collector. For further details on frequency-domain IMS see, e.g., Martin et al., 1998

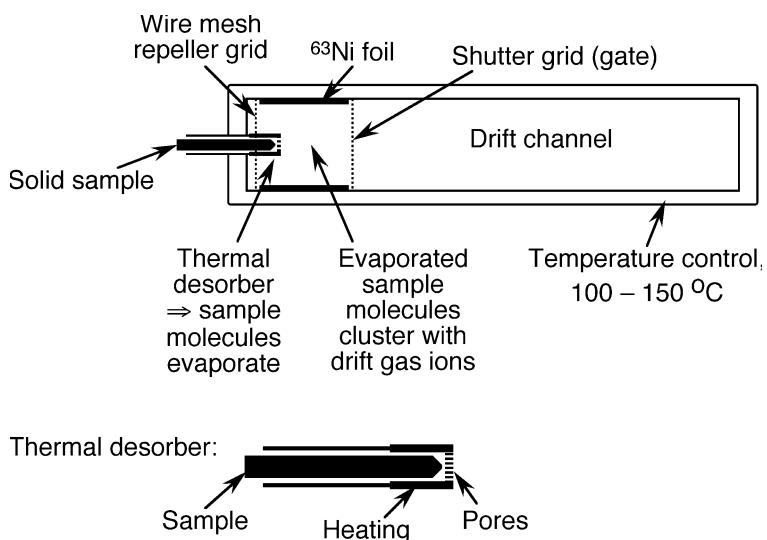


**Fig. 10.20** Modified IMS for the detection of chemicals contained in solid samples and for the identification of different solid materials, e.g., wood (Lawrence et al., 1991; Matz and Schröder, 1997; Schröder et al., 1998)

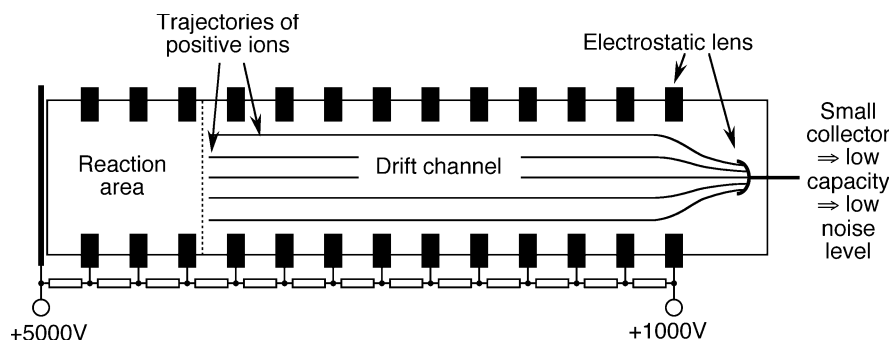


**Fig. 10.21** Noise reduction with a smaller collector grid: The collector and the guard ring in front of the collector act together as an electrostatic lens. The smaller collector causes less noise and, thus, a higher sensitivity

Measurements on solid samples require special sample inlets with a heating and a temperature-resistant porous membrane (see, e.g., Fig. 10.20) and possibly a higher temperature of the IMS.

An electrostatic lens focusing the ions towards the collector can allow the reduction of the collector size and capacity (Fig. 10.21). This decreases noise and can improve the sensitivity.

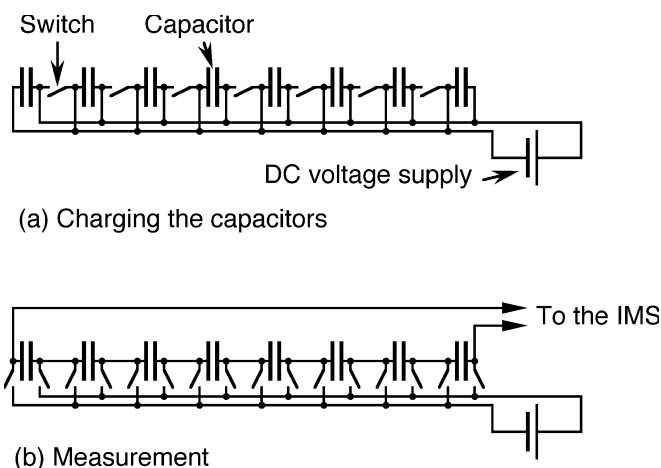


**Fig. 10.22** Generating the high voltage for an IMS (Goebel and Breit, 2000). (a) A set of  $n$  capacitors is charged with the voltage  $V$ . (b) The capacitors are connected together in series for generating the high voltage  $n \cdot V$

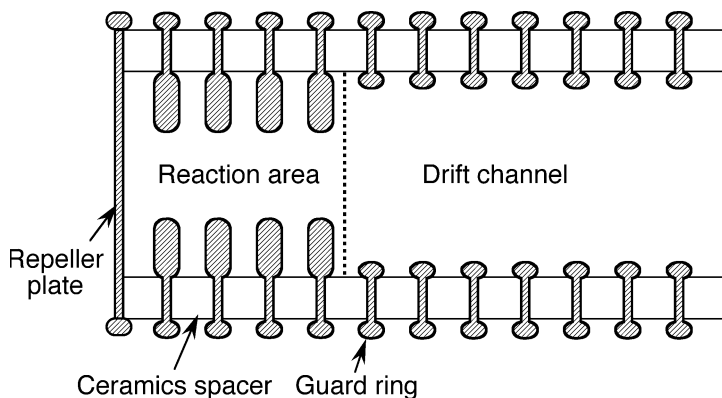


**Fig. 10.23** Improved mechanical stability of the drift channel. For a similar design see also (Karl, 1994)

A technique of high voltage generation which does not necessarily require much weight is illustrated in Fig. 10.22: a set of capacitors is charged in parallel and then connected in series.

Parameters which are important for a high reproducibility of IMS spectra are a constant degree of humidity, constant electric field strength, constant source of ionization, efficient removal of previous samples, mechanical stability. The latter can be improved by a special shape of the guard rings (Fig. 10.23). Figs. 10.24–10.26 display some further important innovations in ion mobility spectrometry.

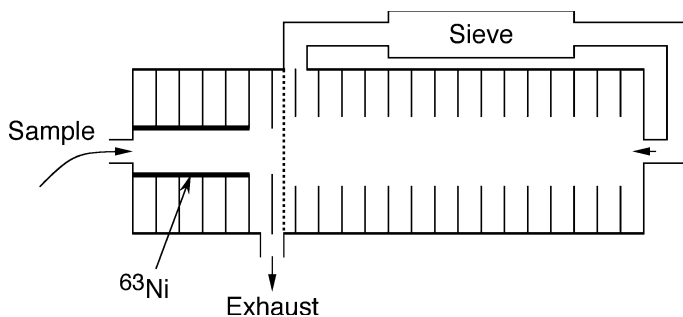


**Fig. 10.24** Improved purgeability of the reaction area (see, e.g., Snyder et al., 1993) and improved homogeneity of the electric field the ions experiencing in the drift channel: the sample outlet is located close to the shutter grid, and the diameter of the reaction area is smaller than that of the drift channel

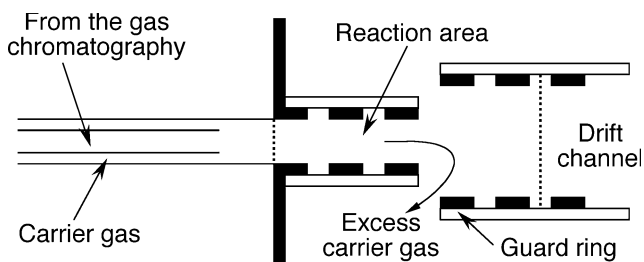


**Fig. 10.25** Injection of the output of a gas chromatograph or of the vapor from a solid sample into the IMS with the help of a gentle stream of carrier gas

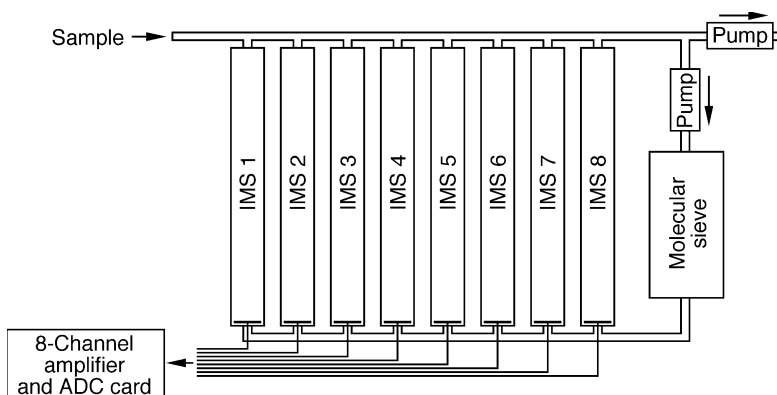


**Fig. 10.26** A multichannel ion mobility spectrometer. For an 8 times higher sampling rate than a single-channel spectrometer, all channels are operated in the same way. For decreased rate of false identifications, one sample may be distributed over different channels that are operated in different modes (see, e.g., Turner, 1993)

## 10.5 Detection of biological agents

Unfortunately, many biological agents are too large to be detected directly: The velocity,  $v$ , of a large spherical particle depends on its charge,  $z$ , its radius,  $r$ , the

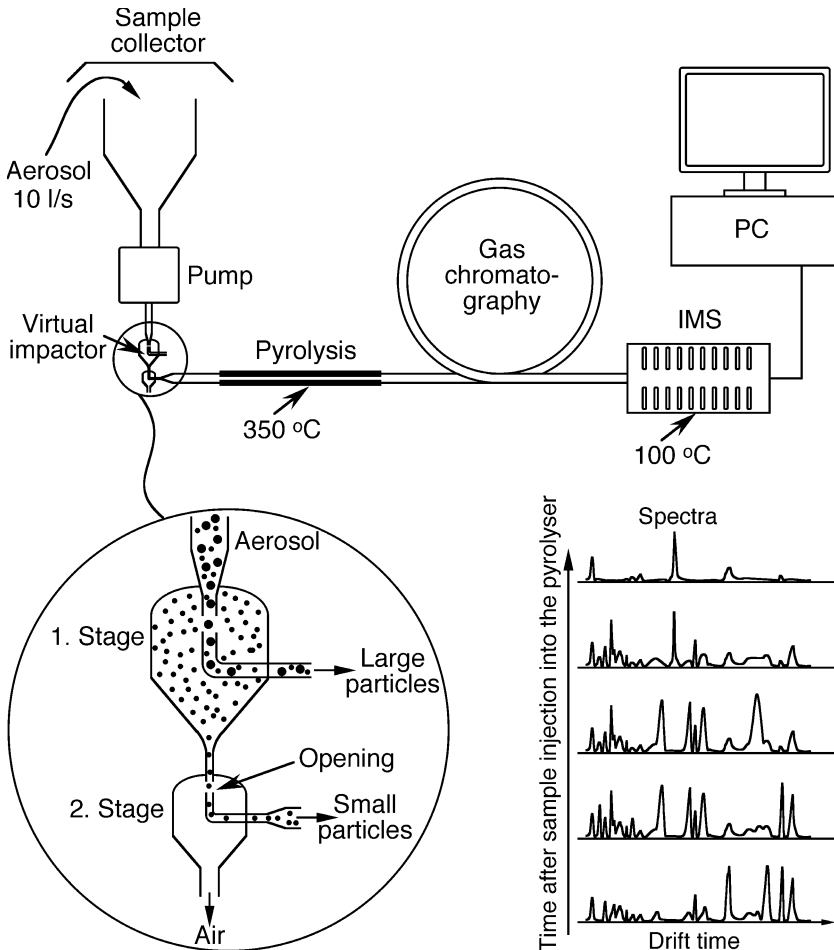


**Fig. 10.27** Setup for IMS-detection of biological agents (see, e.g., Snyder et al., 2000). The virtual impactor selects a certain size range of particles, e.g., 1–10  $\mu\text{m}$ , and transfers the selected particles into the pyrolysis tube. Within a few seconds, particles of biological origin are partially decomposed in the pyrolysis reaction at, e.g., 350 °C. In the subsequent analysis of the pyrolysis reaction products, a short gas chromatography and an IMS are combined for enhanced resolution. The operating temperature of the GC/IMS is typically 80–150 °C. For the principle of operation of the virtual impactor see also Fig. 3.20. Due to the highly dispersed 2D-spectra, Py-GC/IMS can potentially much safer unambiguously identify traces of biological agents than a measurement of particle size distribution alone

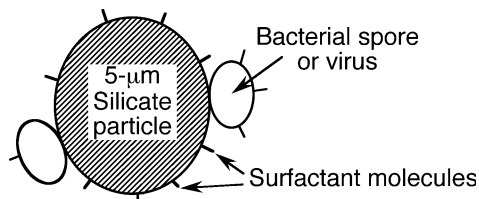


**Fig. 10.28** Example of a particle of a dangerous biological contaminant. Light and fluffy composites of bacterial spores or viruses to dust-forming particles of about 1–5  $\mu\text{m}$  diameter can drift in dry air for 100 miles, and can be sucked into the deepest sacs of the lung (Preston, 1998)

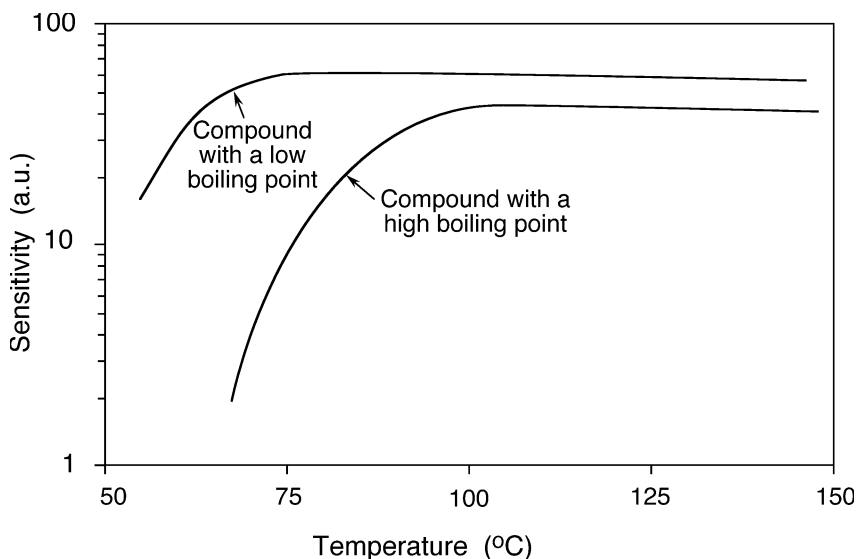


**Fig. 10.29** Typical sensitivity of IMS detection of compounds with different boiling points and vapor pressures

electric field strength,  $E$ , and the viscosity of the medium,  $\eta$ :

$$v = zE (6\pi\eta r)^{-1} \quad (10.3)$$

Small chemical compounds typically travel in an IMS with several  $\text{m s}^{-1}$ , but a single-charged dust particle ( $z = 1.6 \times 10^{-19}\text{C}$ ) with a radius of 1  $\mu\text{m}$  travels in air ( $\eta_{\text{air}} = 1.8 \times 10^{-5} \text{ N s m}^{-2}$ ) at a field strength of  $E = 300 \text{ V mm}^{-1}$  only with about 0.14  $\text{mm s}^{-1}$ . At higher gating frequencies of the IMS, successive spectra of slowly moving agents would superimpose. Also, just average size and size distri-



bution of biological agents offers little information about the precise nature of the agent. That is why biological agents are pyrolyzed prior to analysis in the IMS (Fig. 10.27). Pyrolysis (see also Sect. 3.2) decomposes and vaporizes biological agents and can be applied on bacteria and viruses (Fig. 10.28). The low vapor pressure of most biological compounds requires an operation of the IMS at a sufficiently high temperature (Fig. 10.29). The set-up virtual impactor / pyrolyzer / GC / IMS (Fig. 10.27) is capable to detect a few bacterial spores in a volume of several 1000 liters.

# 11 $\Phi$ -Value analysis

In Chap. 1 some inter-residue contact maps of protein transition states were presented. Here, the method of  $\Phi$ -value analysis underlying such maps and some of its high-resolution applications are presented in more detail: the correlation of inter-residue contacts with  $\Phi$ -values (see Fig. 1.9) is the currently available method with the highest resolution for protein folding transition states (Nölting, 1998, 1999a, b; Nölting and Andert, 2000).

The transition state corresponds to the state with the highest free energy in the course of the reaction. Since it is only extremely short-living, at present its structural resolution can not be carried out with NMR or X-ray crystallographic analysis.  $\Phi$ -Value analysis uses mutants as structural reporters and a combination of equilibrium thermodynamics and kinetics methods (Nölting, 2005).

## 11.1 The method

Fig. 11.1 shows the free energy changes in the folding reaction for a wild-type protein and a mutant of this protein. One can see that in the course of the reaction

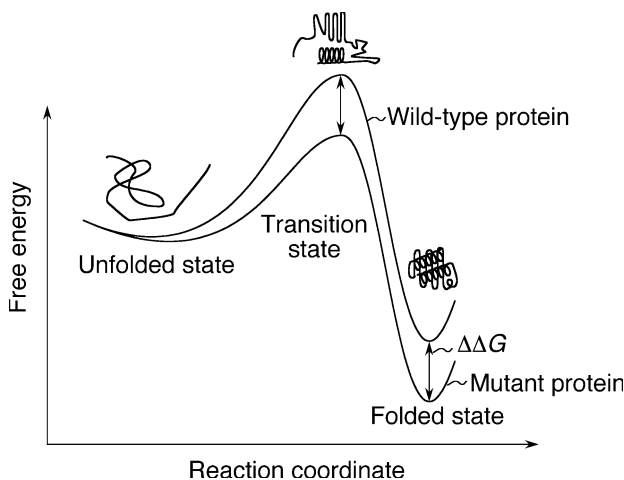


**Fig. 11.1** Energy landscape along the reaction coordinate for the folding reaction of a wild-type protein (top curve) and a mutant of this protein (bottom curve)

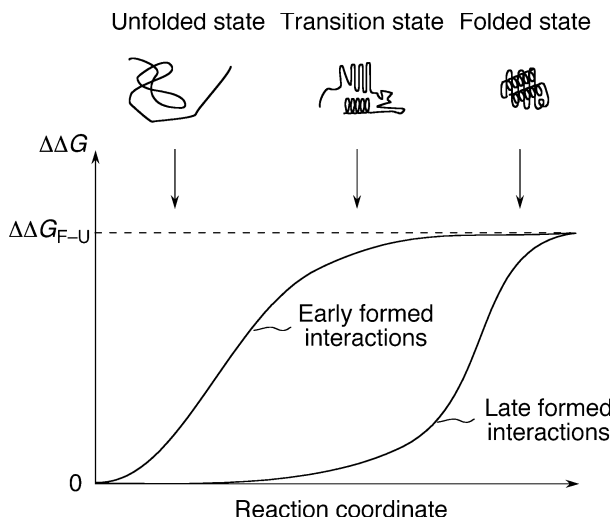


**Fig. 11.2** Built-up of an energy difference,  $\Delta\Delta G$ , between wild-type protein and a mutant in the course of the folding reaction.  $\Delta\Delta G_{F-U}$  is the energy difference between wild-type and mutant protein in the folded state

an energy difference,  $\Delta\Delta G$ , builds up between wild-type and mutant protein. This build-up of  $\Delta\Delta G$  corresponds to the build-up of structure in the molecule. In particular, the time point in the reaction at which  $\Delta\Delta G$  becomes significant depends on the time at which the interactions probed by the mutation build up in the molecule: If the interactions altered by the mutagenesis form early in the folding reaction (left curve in Fig. 11.2), one usually observes an early increase of  $|\Delta\Delta G|$ . In contrast, if the interactions probed by mutagenesis are formed late in the folding reaction, there is usually no significant  $\Delta\Delta G$  till late in the reaction (right curve in Fig. 11.2). So, by measuring  $\Delta\Delta G$  at the different stages of the folding reaction one can find out when certain interactions in the molecule are becoming formed. For the methods of measurement of  $\Delta\Delta G$  see Nölting (2005).

The formation of stable interactions in the molecule is usually expressed by the  $\Phi$ -value which is a measure of the structure consolidation at the position of the mutation on a scale from 0 to 1.  $\Phi$  is defined as  $\Phi = \Delta\Delta G / \Delta\Delta G_{F-U}$ , where  $\Delta\Delta G_{F-U}$  is the  $\Delta\Delta G$  in the folded state (Nölting, 2005). A  $\Phi$  of 0 at a certain stage of the folding reaction suggest the absence of stable structure at the position of the mutation at this time. If structure is completely formed at the position of the mutation at this stage of the reaction, one would expect a  $\Phi$ -value of 1. Possible sources of error in this analysis, e.g., the effect of non-native interactions, can be decreased by using several mutants for the same part of the molecule.

So, in order to obtain information on the structure of a transition state one simply needs to measure  $\Phi$  of the transition state for many mutants and correlate the data with the inter-residue contacts in the molecule (Nölting, 1998, 1999a, b).

## 11.2 High resolution of six protein folding transition states

This section presents the structural characteristics of the main transition states of six proteins obtained by correlation of inter-residue contacts with  $\Phi$ -values (see also Sect. 11.1; Chap. 1; Nölting and Andert, 2000). The first four proteins, barstar, barnase, chymotrypsin inhibitor 2 (CI2), and src SH3 domain are monomeric in the native state. Arc repressor is dimeric, and p53 is a tetramer with the structure of a dimer of dimers. In the first five main transition states (Figs. 11.3–11.7) one can see a very non-uniform consolidation of structure. It has been shown that for all five proteins the most consolidated clusters (highlighted as ribbons in Figs. 11.3–11.7; unconsolidated structure is displayed as wires) contain a relatively higher content of residues which belong to secondary structure elements than the non-consolidated parts of the molecules. On the other hand, all six transition states with the exception of the src SH3 domain (Figs. 11.3–11.5, 11.7, 11.8) contain on average a similar content of secondary and tertiary structure interactions (Nölting and Andert, 2000). This high resolution of folding transition states led to an understanding of the mechanism of protein folding and of its astonishing efficiency: folding of many proteins proceeds similar as the growth of a crystal – largely driven by the propensity of secondary structure formation, but also by the hydrophobic effect and other forces, a folding nucleus forms early in the folding reaction. This nucleus then restricts the number of possible conformations and enables further structure growth around it (Nölting and Andert, 2000; Nölting et al., 2003; Nölting, 2005).

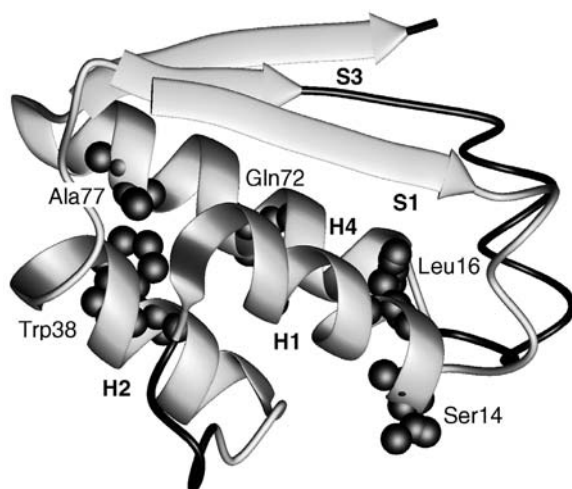


**Fig. 11.3** Main transition state structure of barstar (Nölting and Andert, 2000). Consolidated structure is highlighted as ribbons; unconsolidated parts of the molecule are shown as wires. Amino acid residues with high  $\Phi$ -values are highlighted as spheres. This figure and the following figures in this section were prepared using MOLMOL, Koradi et al., 1996

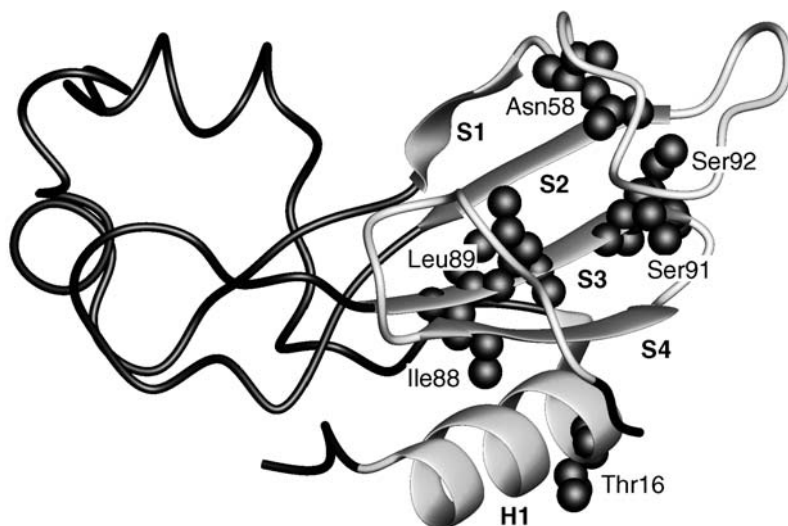


**Fig. 11.4** Main transition state structure of barnase (Nölting and Andert, 2000). Consolidated structure is highlighted as ribbons. For further explanation see Fig. 11.3

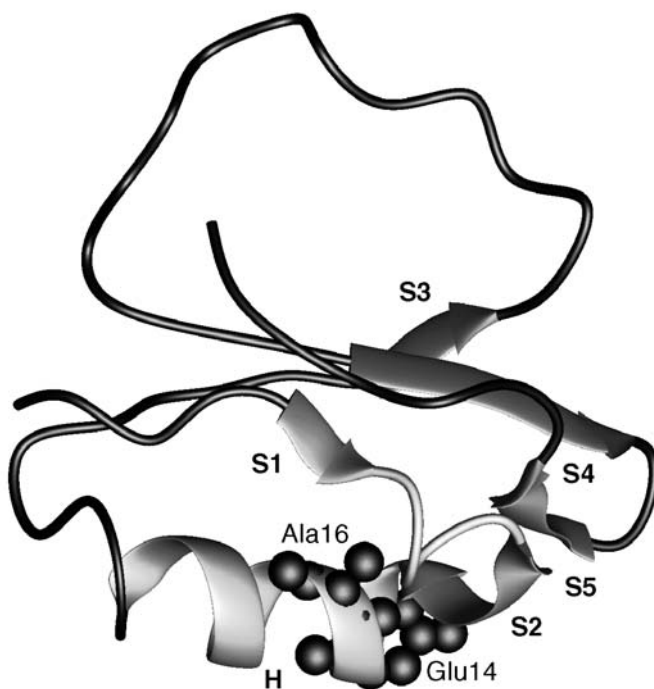


**Fig. 11.5** Transition state structure of CI2 (Nölting and Andert, 2000). Consolidated structure is highlighted as ribbons. For further explanation see Fig. 11.3

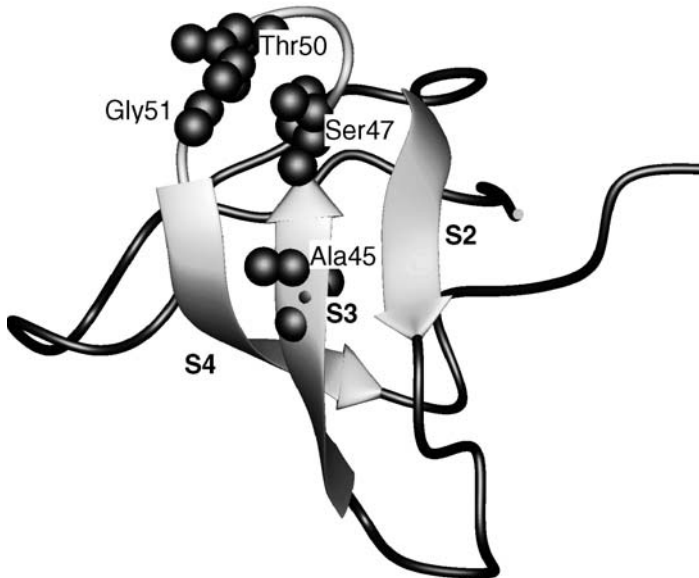


**Fig. 11.6** Transition state structure of the src SH3 domain (Nölting and Andert, 2000). Consolidated structure is highlighted as ribbons. For further explanation see Fig. 11.3

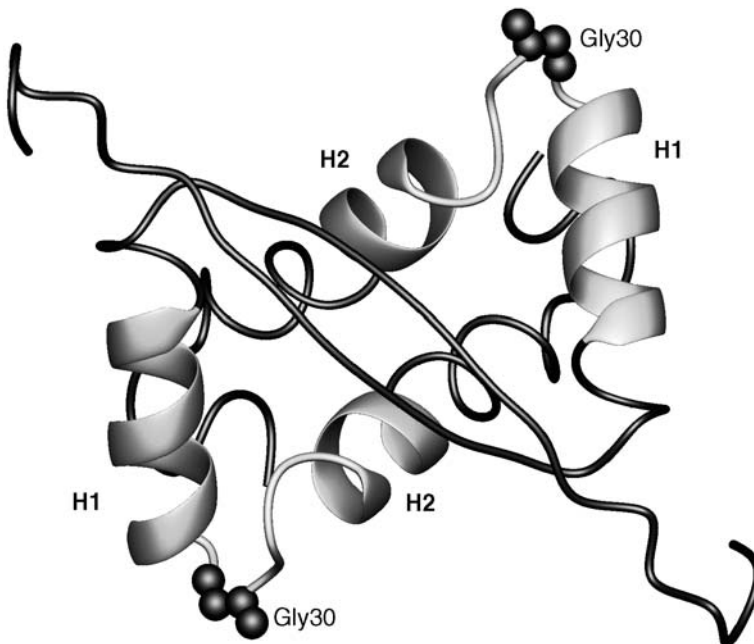


**Fig. 11.7** Transition state structure of Arc repressor (Nölting and Andert, 2000). Consolidated structure is highlighted as ribbons. For further explanation see Fig. 11.3

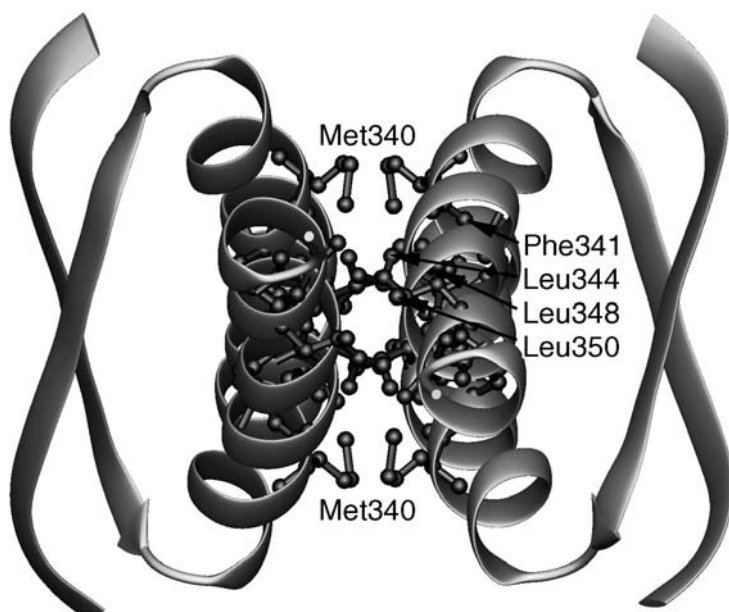


**Fig. 11.8** Main transition state structure of p53 (Nölting and Andert, 2000). In this transition state essentially all parts of the molecule are highly consolidated. Here the residues with low  $\Phi$ -values are highlighted as small spheres

## 12 Evolutionary computer programming

### 12.1 Reasons for the necessity of self-evolving computer programs

Nature offers a tremendous amount of extremely complicated problems which cannot easily be rationalized and resolved. Probably one has to accept that there are scientific and technological problems too complex to be directly rationalized by humans. A well-known example is the non-periodical movement of many gravitationally interacting bodies in space. Since we are not able to imagine their motions with a sufficient degree of perfection, we call it "chaos". Unfortunately, humans obviously have significant intellectual difficulties to find theoretical descriptions or models for phenomena which they do not comprehend. Similarly, as an ape cannot write a mathematical equation beyond its intellectual abilities, humans are not directly able to establish mathematical structures beyond their intellectual limits. However, further progression of science and technology urgently requires to overcome such limits.

One well-known example for a complicated problem is the so-called folding paradox (see, e.g., Nölting, 2005): how can a protein find its unique native conformation among the  $\sim 10^{30}$ – $10^{200}$  possible conformations of an average small protein in the unfolded state? One of the major difficulties of complex phenomena like protein folding is often the lack of an efficient and solvable mathematical description. Often one is able to write down some equations which describe the physics of the system while not being able to solve them.

This chapter describes a method which can potentially provide solutions beyond current human intelligence: in order to overcome the limits of rational design, one lets a computer program evolve itself. The method is exemplarily applied on protein folding and structure predictions (Nölting et al., 2004) and the optimization of optical effects of nanoparticle arrays. In Sect. 12.5 the much wider scope of this method is discussed.

### 12.2 General features of the method

Figs. 12.1 and 12.3 show the principle of operation of the method of self-evolving programs. A so-called wild-type computer program is evolved towards higher efficiency by mutagenesis and selection in a similar way as species evolve in



nature: First a number of mutants of the wild-type program is created. The performance of the mutants is then tested and the best performing program serves

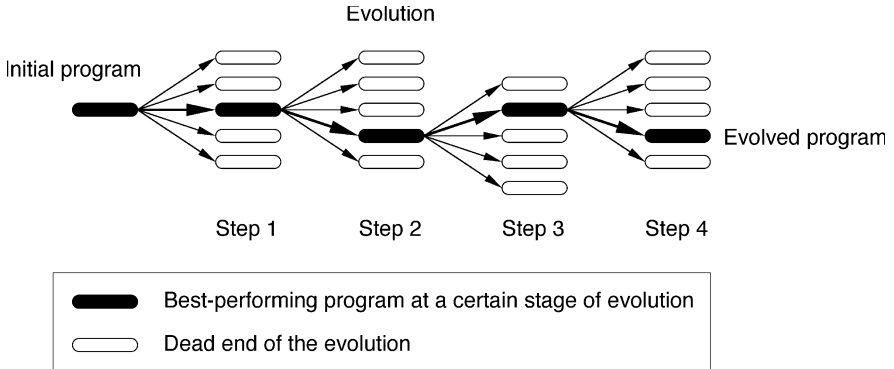


**Fig. 12.1** Scheme of the method of evolutionary computer programming. The best performing program at a certain stage of the evolution is shown as a filled rectangle. Open rectangles indicate less-performing mutants which are usually sorted out. Essentially, the method is based on the mutation and selection of computer programs similarly as for species in the biological evolution. In this way, an initial program which contains mutable parts becomes highly optimized in the course of successive rounds of evolution

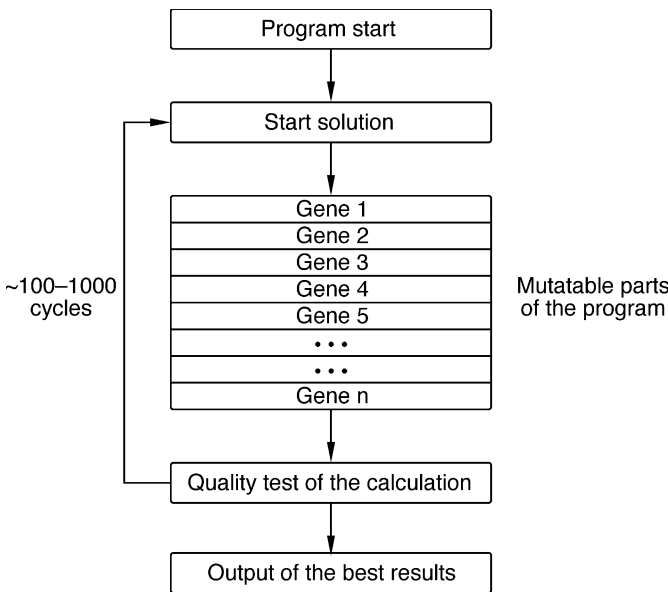


**Fig. 12.2** A suitable structure of a program for self-evolution. The genes are the mutable parts of the program. The genes improve the start solution of the given task

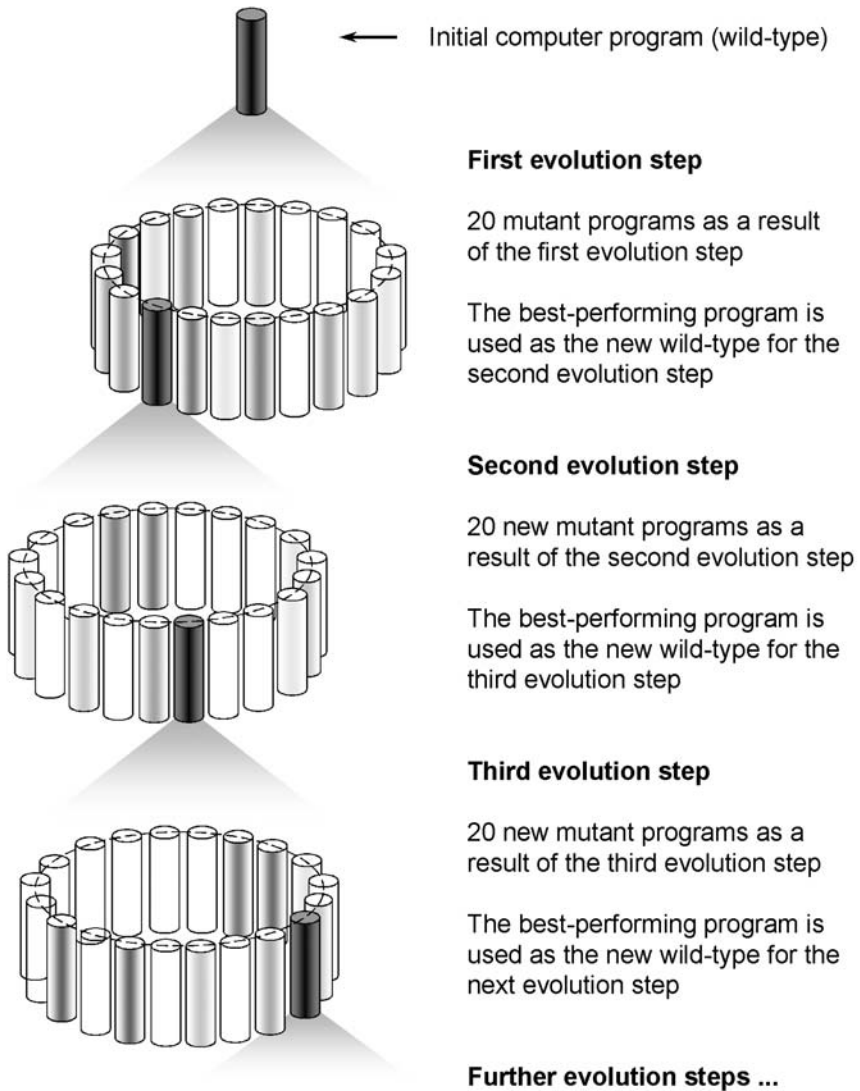


**Fig. 12.3** Example of evolutionary computer programming

as a template for further mutagenesis (the next evolution step). The pathway of evolution is highlighted by filled rectangles in Fig. 12.1. Open rectangles correspond to dead ends of the evolution, e.g., mutants which did not perform best

at a certain stage of evolution. In order to overcome high energy barriers in the evolution, also less well performing mutants may be tried in further evolution steps (not shown).

Fig. 12.2 gives an example for a suitable program structure. The genes are the parts of the program changed in the course of the evolution. Mutation is performed, e.g., by modification of the genes, deletion, addition, or exchange of genes. As nature teaches us, gene shuffling is an efficient method to improve the genome of the program. The specific changes of the genes in the mutagenesis depend on the technological task the program is intended to fulfil (see the next sections). Important in this method is the significant change of the program code in the course of the evolution. Despite significant flexibility, the program stays slim. Completely different, nonlinear program structures are feasible.

### 12.3 Protein folding and structure simulations

Evolution computer methods as described in the previous section were developed to demonstrate a new way of protein folding and structure predictions (Nölting et al., 2004). Folding of proteins has been shown to be an extremely complex, but also surprisingly efficient process (see Chap. 11). For a long time, the origin of the extreme efficiency of protein folding remained unknown. Only recently, the development of new methods for the high resolution of transition states of proteins

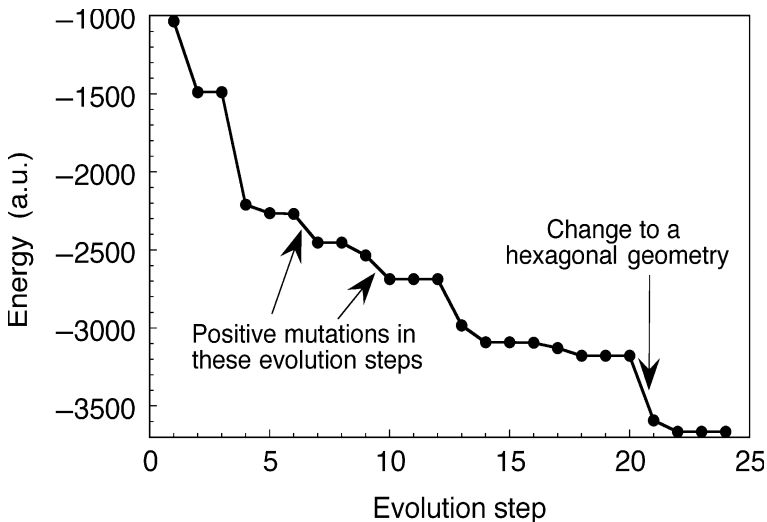


**Fig. 12.4** Evolution of the program for protein structure predictions (Nölting et al., 2004; Nölting, 2005)

provided some insight into the mechanism of folding (see Chap. 11): several small proteins were shown to fold via a nucleation–condensation mechanism where structure grows similar to a crystallization process (Nölting and Andert, 2000; Chap. 11).

Fig. 12.4 shows the improvement of the program in the course of the evolution (Nölting et al., 2004; Nölting, 2005). With the program at evolution step 20 in Fig. 12.4, the loop in chymotrypsin inhibitor 2 (CI2) was correctly predicted (Nölting et al., 2004). Results with the program at step 24 (Fig. 12.4) show that it can predict essential features of the structure of several small proteins within less than 1 hour run on a PC (Nölting, 2005).

## 12.4 Evolution of nanooptical devices made from nanoparticles

A computer method for the creation and optimization of nanooptical devices is introduced. In this method a computer program evolves itself towards a higher efficiency. In contrast to most simple self-learning programs, in the course of the evolution, the program code changes significantly (see Sect. 12.2). The highly evolved program is then used to calculate optimized arrangements of nanooptical elements with the desired optical properties. In applications on complex arrays of nanoparticles and other complex scientific and technological problems, such self-evolving computer programs may be many orders of magnitude more efficient than programs developed solely by rational design.

### 12.4.1 Materials and methods

*Evolution of the computer program.* Figs. 12.1 and 12.3 show the principle of operation of the evolution method (Nölting et al., 2004). The method is based on the mutation and selection of computer programs in successive rounds of evolution (see Sects. 12.2, 12.3 and Nölting et al., 2004). Each evolution step of the computer program on the way from the initial wild-type to the finally evolved mutant program proceeds as follows: a) create different mutants of the computer program, b) test the performance of the mutants, c) take the best-performing program within the set of mutants and wild type-program as a template for further mutations. Mutations are, e.g., omissions, additions, or changes of program lines, or changes of the sequence of lines. Only after a few evolution steps, a program suitably designed for this mutagenesis approach can usually perform more than ten times better than the original wild-type program (Nölting et al., 2004).

In this case, the self-evolving program was written in C++ and run on a PC. Because of the aim to achieve a high speed of the program, the time for testing each mutant was always only about 1 minute.

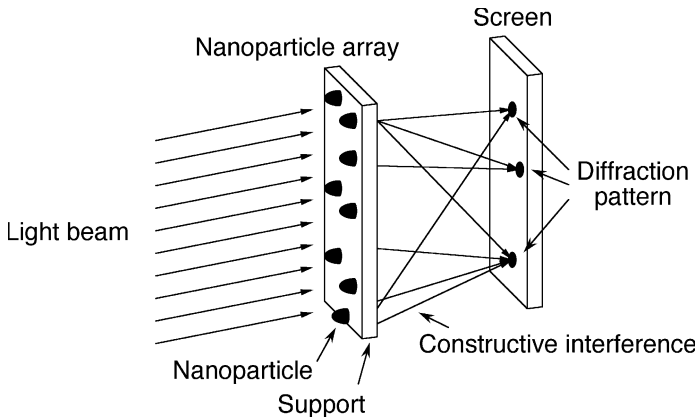


**Fig. 12.5** The optical setup the evolution method is applied on (see the text)

*Optical setup:* The specific optical arrangement investigated with this evolution method is shown in Fig. 12.5. A light beam with the shape of a plane wave with a wavelength of 500 nm is passed through an array of nanoparticles. The diffraction pattern is measured on a screen at a distance of 100 nm.

*Calculation of the diffraction pattern.* The diffraction pattern,  $F(S)$ , of an arrangement of nanoparticles with the diffraction (scattering) power,  $\rho(r) = 1$ , is given by (see Eq. 4.3):

$$F(S) = \int_{-\infty}^{\infty} e^{-2\pi i r S} dr, \quad (12.1)$$

where  $r$  is the position of a scattering particle, and  $S = (s - s_0)/\lambda$  is the scattering vector with  $s_0 =$  vector (direction) of the incident plane wave,  $s =$  vector (direction) of the scattered wave,  $\lambda =$  wavelength of the light.

## 12.4.2 Results and discussion

Fig. 12.6 presents the success of the evolution process. RMSD (root mean square deviation) is a measure of the quality of the match between the desired optical pattern and the optical pattern caused by the nanoparticles after optimization of their position by the program. One can see that there is a rapid improvement in the course of the program evolution. Fig. 12.7 shows a specific example of an optical effect aimed at. The evolved program started with a random distribution of 29 nanoparticles (Fig. 12.7a). It then moved the nanoparticles and compared the generated diffraction pattern with the diffraction pattern aimed at (Fig. 12.7c). Successful moves were accepted, the others were rejected. Figs. 12.7d and 12.7e show the final diffraction pattern and positions of the nanoparticles, respectively. The evolved program found this arrangement of particles within 1 minute on a PC.

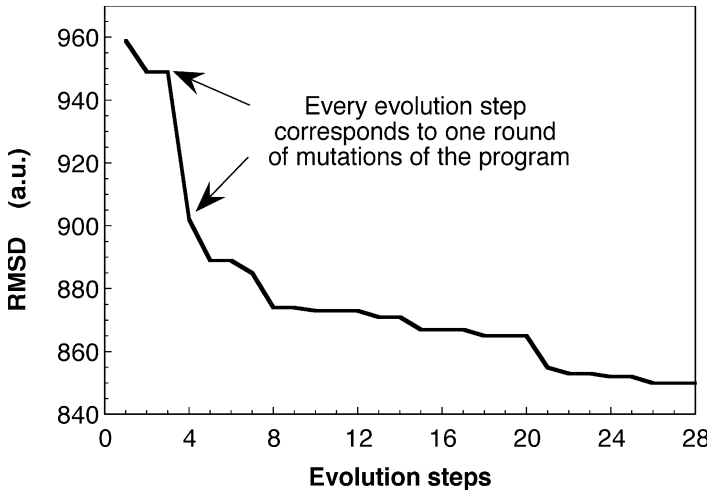


**Fig. 12.6** Evolution of the program for the calculation of complex patterns of nanoparticles with given optical properties. RMSD is the root mean square deviation of the optical pattern generated by the nanoparticle array compared with the demanded pattern. Each evolution step corresponds to one round of mutagenesis and testing

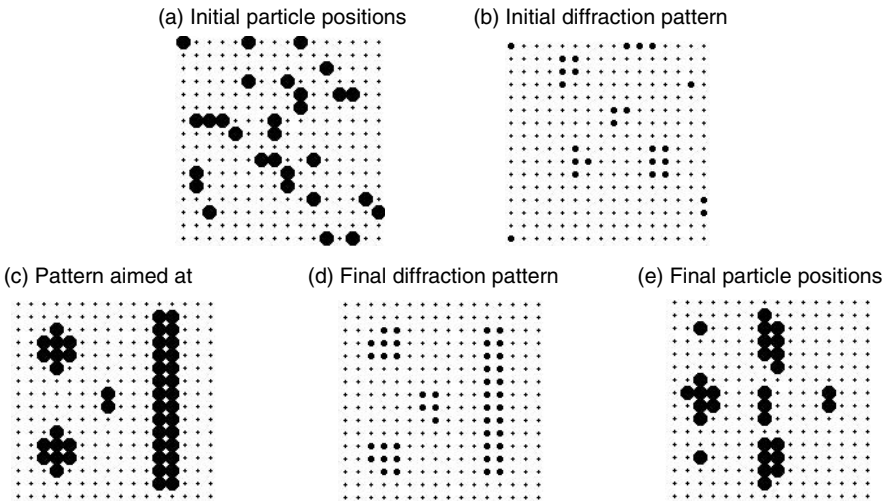


**Fig. 12.7** Optimization of 29 nanoparticles placed on a  $16 \times 16$  pixel array. The size of each pixel is  $100 \times 100 \text{ nm}^2$ , the wavelength of the light is 500 nm, and the distance between the nanoparticles and screen is 100 nm. (a) initial positions of the nanoparticles; (b) initial diffraction pattern resulting from the arrangement of these particles; (c) diffraction pattern aimed at; (d) diffraction pattern of the optimized arrangement of the nanoparticles; (e) optimized arrangement of the nanoparticles. The shown arrangement of nanoparticles was found by the evolved program on a PC within 1 minute among  $\sim 10^{38}$  possibilities

These arrays seem simple, but the number,  $N$ , of possible arrangements of the 29 nanoparticles on the 256 places of the array is:

$$N = \binom{256}{29} = \left( \frac{256!}{29! \times 227!} \right) \approx 10^{38} . \quad (12.2)$$

At the beginning, the evolution progresses quite rapidly and appears to slow down after a certain number of evolution steps (Fig. 12.6). However, even after a relatively long period of evolution, further jumps are possible: see, e.g., the significant progress from evolution step 20 to 21. The progress of evolution appears to depend largely on the degree of freedom which is allowed for the system. Strong restrictions may cause the evolution to end prematurely. On the other hand, very fanciful and severe mutations are often negative mutations, but, if positive, have a higher potential to enable a sustained progress over many evolution steps.

One might argue that the geometry of the scattering array may more easily be found by Fourier-transforming the demanded pattern. This is because the diffraction pattern,  $F(\mathbf{S})$ , has the form of the Fourier transform and so the optical arrangement could be calculated with the inverse Fourier transform of the diffraction pattern (see Chap. 4). However, when recording the diffraction pattern on a screen, the phase information gets lost and so the inverse Fourier transform is not easily done. More importantly, however, none of the solutions might be compatible with a fixed number or density of nanoparticles. Furthermore, some optical effects are difficult to calculate by Fourier transform. For example, the Fourier transform is not easily applicable if one tries to find an arrangement with near-invisibility of the nanoparticle array within a certain spectral region. Also, with this approach one might find completely new approximate solutions.

Here, only a short evolution of a simple program is presented. Significant improvement was achieved by changing the positions of the nanoparticles in the third dimension, i.e., the height above the support layer. Even though there are  $\sim 10^{73}$  possible arrangements of 29 particles in a  $16 \times 16 \times 16$  3D array of nanoparticles, the evolved program provided better results (not shown).

It is expected that the following means will lead to further improvement: (a) the program starts with more different random arrangements of the nanoparticles (start solutions in Fig. 12.2) and searches for the one which yields the best results, (b) the program is passed through further rounds of evolution cycles, (c) the program is given more time for the optimization of the arrays.

## 12.5 Further potential applications

Self-evolving systems have a much wider applicability. In principle such systems should be a powerful way out when the objects of investigation are too compli-

cated and too complex to be easily rationalized (see, e.g., Back, 1996). Adaptive optics (Fig. 12.8), electrical circuits (Fig. 12.9), robots and nanomechanics (Fig. 12.10) are suitable targets.

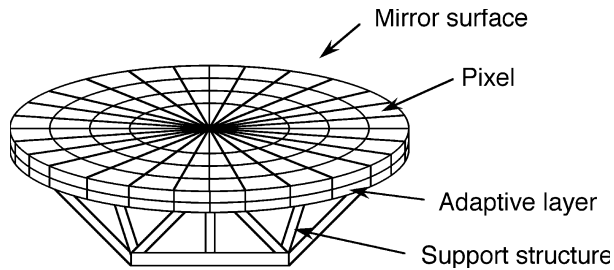


**Fig. 12.8** Adaptive systems are used in optics, e.g., to compensate for bending of the support structures of large mirrors due to its own weight and thermal fluctuations and for the distortion of the image by density fluctuations of the atmosphere

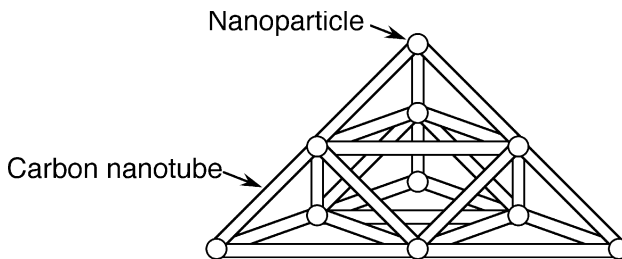


**Fig. 12.9** Macroscopic circuits and nanocircuits made, e.g., from nanoparticles and nanotubes can have an exponential rise of possibilities with the number of structural elements

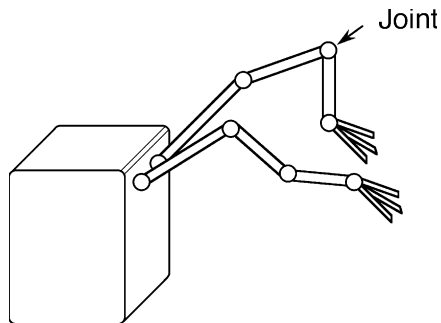


**Fig. 12.10** The calculation of movements of sophisticated robots can be connected with an exponential growth of possibilities with the degree of freedom of the system and accordingly such movements may be difficult to optimize



Self-evolving programs should also be a powerful tool to study the evolution of species (Fig. 12.11): why have species evolved in the way they did. Which parameters have an effect on the evolution? Which evolutionary mechanisms are encoded in the DNA? What causes dead ends in the evolution? What will, in this regard, be the fate of human kind and how can it be affected? These are important yet largely unanswered questions.

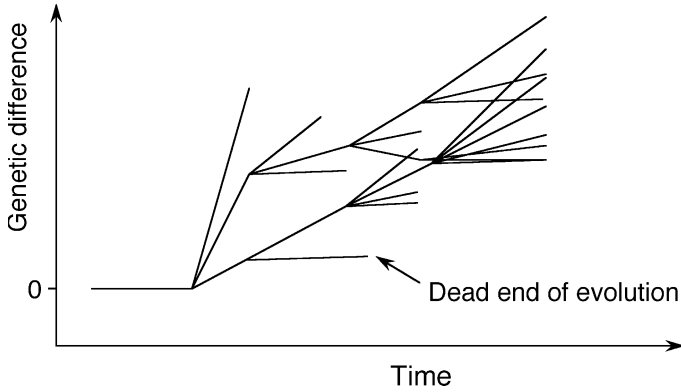


**Fig. 12.11** Scheme of the evolution of species

## 13 Conclusions

Biophysical methods are extremely important for the further understanding of biological processes. Structurally highly resolving methods such as X-ray crystallography and scanning probe microscopy in combination with kinetic methods (see, e.g., Nölting, 2005) give us a true understanding of biological processes at a molecular and cellular level. Proteome maps of healthy and ill individuals are compared for identification of up- or down-regulation in disease states and for individual, highly efficient drug targeting. Biophysical nanotechnology and mass spectrometry open new fascinating ways of studying and influencing complex biological systems. Biophysical nanotechnology takes novel approaches to assemble protein nanoarrays, nanoparticles, and nanowires to well-functioning structures. Mass spectrometry and ion mobility spectrometry have significantly advanced towards the detection of ultra-traces not only of chemical, but also of biological agents.

The biophysical understanding of the living world is crucial to develop rational strategies to influence, in a responsible manner, pathological and non-pathological limitations, stress situations, and disease states. In this way, biophysics can contribute to the understanding of the factors that affect the prosperity and evolution of the human society.

## References

- Abkevich VI, Gutin AM, Shakhnovich EI (1995) Impact of local and nonlocal interactions on the thermodynamics and kinetics of protein folding. *J Mol Biol* 252:460–471
- Abola EE, Sussman JL, Prilusky J, Manning NO (1997) Protein data bank archives of three-dimensional macromolecular structures. *Methods Enzymol* 277:556–571
- Achari A, Hale SP, Howard AJ, Clore GM, Gronenborn AM, Hardman KD, Whitlow M (1992) 1.67 Å X-ray structure of the B2 immunoglobulin-binding domain of streptococcal protein G and comparison to the NMR structure of the B1 domain. *Biochemistry* 31:10449–10457
- Adam GC, Sorensen EJ, Cravatt BF (2002a) Chemical strategies for functional proteomics. *Mol Cell Proteomics* 1:781–790
- Adam GC, Sorensen EJ, Cravatt BF (2002b) Proteomic profiling of mechanistically distinct enzyme classes using a common chemotype. *Nat Biotechnol* 20:805–809
- Aitio H, Laakso T, Pihlajamaa T, Torkkeli M, Kilpelainen I, Drakenberg T, Serimaa R, Annala A (2001) Characterization of apo and partially saturated states of calerythrin, an EF-hand protein from *S. erythraea*: a molten globule when deprived of Ca<sup>2+</sup>. *Protein Sci* 10:74–82
- Aitken A, Learmonth M (2002) Protein identification by in-gel digestion and mass spectrometric analysis. *Mol Biotechnol* 20:95–97
- Allison DP, Hinterdorfer P, Han W (2002) Biomolecular force measurements and the atomic force microscope. *Curr Opin Biotechnol* 13:47–51
- Alm E, Baker D (1999) Matching theory and experiment in protein folding. *Curr Opin Struct Biol* 9:189–196
- Andersen KV, Poulsen FM (1992) Three-dimensional structure in solution of acyl-coenzyme A binding protein from bovine liver. *J Mol Biol* 226:1131–1141
- Anderson RJ, Bendell DJ, Garnett I, Groundwater PW, Lough WJ, Mills MJ, Savery D, Shattock PE (2002) Identification of indolyl-3-acryloylglycine in the urine of people with autism. *J Pharm Pharmacol* 54:295–298
- Andolfi L, Cannistraro S, Canters GW, Facci P, Ficca AG, van Amsterdam IM, Verbeet MP (2002) A poplar plastocyanin mutant suitable for adsorption onto gold surface via disulfide bridge. *Arch Biochem Biophys* 399:81–88
- Andretzky P, Lindner MW, Herrmann JM, Schultz A, Konzog M, Kiesewetter F, Häusler G (1998) Optical coherence tomography by “Spectral radar”. *SPIE* 3567:78–87
- Åqvist J (1999) Long-range electrostatic effects on peptide folding. *FEBS Lett* 457:414–418
- Arai S, Hirai M (1999) Reversibility and hierarchy of thermal transition of hen egg-white lysozyme studied by small angle X-ray scattering. *Biophys J* 76:2192–2197
- Aries RE, Gutteridge CS, Ottley TW (1986) Evaluation of a low-cost, automated pyrolysis mass spectrometer. *J Anal Appl Pyrol* 9:81–98

- Armitage S, Saywell S, Roux C, Lennard C, Greenwood P (2001) The analysis of forensic samples using laser micro-pyrolysis gas chromatography mass spectrometry. *J Forensic Sci* 46:1043–1052
- Asbury GR, Hill HH (2000) Separation of amino acids by ion mobility spectrometry. *J Chromatogr A* 902:433–437
- Ash EA, Nicholls G (1972) Super-resolution aperture scanning microscope. *Nature* 237:510–513
- Astley OM, Donald AM (2001) A small angle X-ray scattering study of the effect of hydration on the microstructure of flax fibers. *Biomacromolecules* 2:672–680
- Avseenko NV, Morozova TY, Ataulkhanov FI, Morozov VN (2001) Immobilization of proteins in immunochemical microarrays fabricated by electrospray deposition. *Anal Chem* 73:6047–6052
- Avseenko NV, Morozova TY, Ataulkhanov FI, Morozov VN (2002) Immunoassay with multicomponent protein microarrays fabricated by electrospray deposition. *Anal Chem* 74:927–933
- Back T (1996) *Evolutionary Algorithms in Theory and Practice: Evolution Strategies, Evolutionary Programming, Genetic Algorithms*. Oxford University Press
- Backmann J, Schäfer G, Wyns L, Bönsch H (1998) Thermodynamics and kinetics of unfolding of the thermostable trimeric adenylate kinase from the archaeon *Sulfolobus acidocaldarius*. *J Mol Biol* 284:817–833
- Bada M, Walther D, Arcangioli B, Doniach S, Delarue M (2000) Solution structural studies and low-resolution model of the *Schizosaccharomyces pombe* sap1 protein. *J Mol Biol* 300:563–574
- Bai YW (1999) Equilibrium amide hydrogen exchange and protein folding kinetics. *J Biomol NMR* 15:65–70
- Bai YW (2000) Kinetic evidence of an on-pathway intermediate in the folding of lysozyme. *Protein Sci* 9:194–196
- Bailey JA, Tomson FL, Mecklenburg SL, MacDonald GM, Katsonouri A, Puustinen A, Gennis RB, Woodruff WH, Dyer RB (2002) Time-resolved step-scan Fourier transform infrared spectroscopy of the CO adducts of bovine cytochrome c oxidase and of cytochrome  $b_0_3$  from *Escherichia coli*. *Biochemistry* 41:2675–2683
- Baim MA, Eatherton RL, Hill HH (1983) Ion mobility detector for gas chromatography with a direct photoionization source. *Anal Chem* 55:1761–1766
- Baker D (2000) A surprising simplicity to protein folding. *Nature* 405:39–42
- Baker D, DeGrado WF (1999) Engineering and design – editorial overview. *Curr Opin Struct Biol* 9:485–486
- Barrera FN, Garzon MT, Gomez J, Neira JL (2002) Equilibrium unfolding of the C-terminal SAM domain of p73. *Biochemistry* 41:5743–5753
- Barshick SA, Wolf DA, Vass AA (1999) Differentiation of microorganisms based on pyrolysis ion trap mass spectrometry using chemical ionization. *Anal Chem* 71:633–641
- Barth A (2002) Selective monitoring of 3 out of 50,000 protein vibrations. *Biopolymers* 67:237–241
- Baumbach JL, Eiceman GA (1999) Ion mobility spectrometry: arriving on site and moving beyond a low profile. *Appl Spectrosc* 53:338A–355A
- Baumbach JI, Stach J (ed) (1998) *Recent Developments in Ion Mobility Spectrometry*. International Society for Ion Mobility Spectrometry, Dortmund, Germany

- Beamer LJ, Pabo CO (1992) Refined 1.8 Å crystal structure of the  $\lambda$ -repressor-DNA complex. *J Mol Biol* 227:177–196
- Beegle LW, Kanik I, Matz L, Hill HH (2001) Electrospray ionization high-resolution ion mobility spectrometry for the detection of organic compounds, 1. Amino acids. *Anal Chem* 73:3028–3034
- Begley P, Corbin R, Foulger BE, Simmonds PG (1991) Photoemissive ionization source for ion mobility detectors. *J Chromatogr* 588:239–249
- Bellotti V, Stoppini M, Mangione P, Sunde M, Robinson C, Asti L, Brancaccio D, Ferri G (1998)  $\beta$ 2-microglobulin can be refolded into a native state from *ex vivo* amyloid fibrils. *Eur J Biochem* 258:61–67
- Benoit M, Gabriel D, Gerisch G, Gaub HE (2000) Discrete interactions in cell adhesion measured by single-molecule force spectroscopy. *Nature Cell Biol* 2:313–317
- Berkeley RCW, Goodacre R, Helyer RJ, Kelley T (1990) Pyrolysis-MS in the identification of micro-organisms. *Lab Pract* 39:81–83
- Berks BC, Sargent F, Palmer T (2000) The Tat protein export pathway. *Mol Microbiol* 35:260–274
- Bernal JD (1939) The structure of proteins. *Nature* 143:663–667
- Bernal JD, Crowfoot D (1934) X-ray photographs of crystalline pepsin. *Nature* 138:133–134
- Betzig E, Harootunian A, Isaacson M, Kratschmer E, Lewis A (1986) Near-field scanning optical microscopy (NSOM): development and biophysical applications. *Biophys J* 49:269–279
- Betzig E, Trautmann JK, Harris TD, Weiner JS, Kostelak RL (1991) Breaking the diffraction barrier: optical microscopy on a nanometric scale. *Science* 251:1468–1470
- Betzig E, Finn PL, Weiner JS (1992) Combined shear force and near-field scanning optical microscopy. *Appl Phys Lett* 60:2484–2486
- Bianco A, Corvaja C, Crisma M, Guldi DM, Maggini M, Sartori E, Toniolo C (2002) A helical peptide receptor for [60]fullerene. *Chemistry* 8:1544–1553
- Binnig G, Rohrer H (1987) Scanning tunneling microscopy – from birth to adolescence. *Rev Mod Phys* 59, No 3, Part I
- Binnig G, Gerber C, Quate CF (1986) Atomic force microscopy. *Phys Rev Lett* 56:930–933
- Binnig G, Rohrer H, Gerber C, Weibel E (1982a) Vacuum tunneling. *Physica* 109 & 110B 2075–2077
- Binnig G, Rohrer H, Gerber C, Weibel E (1982b) Surface studies by scanning tunneling microscopy. *Phys Rev Lett* 49:57–61
- Binnig G, Rohrer H, Gerber C, Weibel E (1983) 7×7 reconstruction on Si(111) resolved in real space. *Phys Rev Lett* 50:120–123
- Bird GM, Keller RA (1976) Vapor concentration dependence of plasmagrams. *J Chromatographic Sci* 14:574–577
- Birolo L, Dal Piaz F, Pucci P, Marino G (2002) Structural characterization of the M\* partly folded intermediate of wild-type and P138A aspartate aminotransferase from *Escherichia coli*. *J Biol Chem* 277:17428–17437
- Biscarini F, Cavallini M, Leigh DA, Leon S, Teat SJ, Wong JK, Zerbetto F (2002) The effect of mechanical interlocking on crystal packing: predictions and testing. *J Am Chem Soc* 124:225–233
- Blanchard WC, Bacon AT (1989) Ion mobility spectrometer. US Patent 4,797,554

- Blomberg A (2002) Use of two-dimensional gels in yeast proteomics. *Methods Enzymol* 350:559–584
- Boettner M, Prinz B, Holz C, Stahl U, Lang C (2002) High-throughput screening for expression of heterologous proteins in the yeast *Pichia pastoris*. *J Biotechnol* 99:51–62
- Boisvert DC, Wang J, Otwinowski Z, Horwich AL, Sigler PB (1996) The 2.4 Å crystal structure of the bacterial chaperonin GroEL complexed with ATP  $\gamma$ S. *Nature Struct Biol* 3:170–177
- Bork P (2002) Comparative analysis of protein interaction networks. *Bioinformatics* 18 Suppl 2:S64
- Borsdorf H, Rudolph M (2001) Gas-phase ion mobility studies of constitutional isomeric hydrocarbons using different ionization techniques. *Int J Mass Spectrom* 208:67–72
- Borsdorf H, Schelhorn H, Flachowsky J, Döring HR, Stach J (2000) Corona discharge ion mobility spectrometry of aliphatic and aromatic hydrocarbons. *Anal Chim Acta* 403:235–242
- Braig K, Otwinowski Z, Hegde R, Boisvert DC, Joachimiak A, Horwich AL, Sigler PB (1994) The crystal structure of the bacterial chaperonin GroEL at 2.8 Å. *Nature* 371:578–586
- Brask J, Jensen KJ (2000) Carbopeptides: chemoselective ligation of peptide aldehydes to an aminoxy-functionalized D-galactose template. *J Pept Sci* 6:290–299
- Brown DR, Wong BS, Haifiz F, Clive C, Haswell SJ, Jones IM (1999) Normal prion protein has an activity like that of superoxide dismutase. *Biochem J* 344:1–5
- Brown DR, Hafiz F, Glasssmith LL, Wong BS, Jones IM, Clive C, Haswell SJ (2000) Consequences of manganese replacement of copper for prion protein function and proteinase resistance. *EMBO J* 19:1180–1186
- Bruckbauer A, Ying L, Rothery AM, Korchev YE, Klenerman D (2002a) Characterization of a novel light source for simultaneous optical and scanning ion conductance microscopy. *Anal Chem* 74:2612–2616
- Bruckbauer A, Ying L, Rothery AM, Zhou D, Shevchuk AI, Abell C, Korchev YE, Klenerman D (2002b) Writing with DNA and protein using a nanopipet for controlled delivery. *J Am Chem Soc* 124:8810–8811
- Bryden WA (1995) Tiny-TOF-MALDI mass spectrometry for particulate drug and explosives detection. 3rd Symposium on Research & Development, Kossiakoff Center, The Johns Hopkins University
- Budovich VL, Mikhailov AA, Arnold G (1999) Ion mobility spectrometer. US Patent 5,969,349
- Burbaum J, Tobal GM (2002) Proteomics in drug discovery. *Curr Opin Chem Biol* 6:427–433
- Burke JR (1992) Ion mobility detector. US Patent 5,162,649
- Burton RE, Huang GS, Daugherty MA, Fullbright PW, Oas TG (1996) Microsecond protein folding through a compact transition state. *J Mol Biol* 263:311–322
- Burton RE, Huang GS, Daugherty MA, Calderone TL, Oas TG (1997) The energy landscape of a fast-folding protein mapped by Ala→Gly substitutions. *Nature Struct Biol* 4:305–310
- Bustamante C, Smith SB, Liphardt J, Smith D (2000) Single-molecule studies of DNA mechanics. *Curr Opin Struct Biol* 10:279–285

- Butler BC, Hanchett RH, Rafailov H, MacDonald G (2002) Investigating structural changes induced by nucleotide binding to RecA using difference FTIR. *Biophys J* 82:2198–2210
- Calvo EJ, Danilowicz C, Wolosiuk A (2002) Molecular “wiring” enzymes in organized nanostructures. *J Am Chem Soc* 124:2452–2453
- Campbell DN, Spangler GE, Davis RC Jr, Fafaul EF, Carrico JP Jr (1991) All ceramic ion mobility spectrometer cell. US Patent 5,021,654
- Canady MA, Tsuruta H, Johnson JE (2001) Analysis of rapid, large-scale protein quaternary structural changes: time-resolved X-ray solution scattering of *Nudaurelia capensis*  $\Omega$  virus (N $\Omega$ V) maturation. *J Mol Biol* 311:803–814
- Canet D, Last AM, Tito P, Sunde M, Spencer A, Archer DB, Redfield C, Robinson CV, Dobson CM (2002) Local cooperativity in the unfolding of an amyloidogenic variant of human lysozyme. *Nature Struct Biol* 9:308–315
- Carnahan BL, Tarassov AS (1995) Ion mobility spectrometer. US Patent 5,420,424
- Carnahan BL, Tarassov AS (1998) Recirculating filtration system for use with a transportable ion mobility spectrometer. US Patent 5,723,861
- Carroll DI (1972) Apparatus and methods for separating, detecting, and measuring trace gases. US Patent 3,668,383
- Carroll DI, Cohen MJ, Wernlund RF (1971) Apparatus and methods for separating, detecting, and measuring trace gases with enhanced resolution. US Patent 3,626,180
- Carrion-Vazquez M, Oberhauser AF, Fowler SB, Marszalek PE, Broedel SE, Clarke J, Fernandez JM (1999) Mechanical and chemical unfolding of a single protein: a comparison. *Proc Natl Acad Sci USA* 96:3694–3699
- Casari G, Sippl MJ (1992) Structure-derived hydrophobic potential – hydrophobic potential derived from X-ray structures of globular proteins is able to identify native folds. *J Mol Biol* 224:725–732
- Castellanos IJ, Cruz G, Crespo R, Griebenow K (2002) Encapsulation-induced aggregation and loss in activity of  $\gamma$ -chymotrypsin and their prevention. *J Control Release* 81:307–319
- Celis JE, Celis P, Palsdottir H, Ostergaard M, Gromov P, Primdahl H, Orntoft TF, Wolf H, Celis A, Gromova I (2002) Proteomic strategies to reveal tumor heterogeneity among urothelial papillomas. *Mol Cell Proteomics* 1:269–279
- Chacon P, Moran F, Diaz JF, Pantos E, Andreu JM (1998) Low-resolution structures of proteins in solution retrieved from X-ray scattering with a genetic algorithm. *Biophys J* 74:2760–2775
- Chambert R, Petit-Glatron MF (1999) Anionic polymers of *Bacillus subtilis* cell wall modulate the folding rate of secreted proteins. *FEMS Microbiol. Lett* 179:43–47
- Chan HS (1998) Protein folding: matching speed and locality. *Nature* 392:761–763
- Chan HS (1999) Folding alphabets. *Nature Struct Biol* 6:994–996
- Chan HS (2000) Modeling protein density of states: additive hydrophobic effects are insufficient for calorimetric two-state cooperativity. *Proteins* 40:543–571
- Chang AM, Hallen HD, Harriott L, Hess HF, Kao HL, Kwo J, Miller RE, Wolfe R, van der Ziel J, Chang TY (1992a) Scanning Hall probe microscopy. *Appl Phys Lett* 61:1974–1976
- Chang AM, Hallen HD, Hess HF, Kao HL, Kwo J, Sudbø A, Chang TY (1992b) Scanning Hall probe microscopy of a vortex and field fluctuations in  $\text{La}_{1.85}\text{Sr}_{0.15}\text{CO}_4$  films. *Europhys Lett* 20:645–650

- Chang JY, Li L, Bulychev A (2000a) The underlying mechanism for the diversity of disulfide folding pathways. *J Biol Chem* 275:8287–8289
- Chang JY, Li L, Canals F, Aviles FX (2000b) The unfolding pathway and conformational stability of potato carboxypeptidase inhibitor. *J Biol Chem* 275:14205–14211
- Charras GT, Horton MA (2002) Single cell mechanotransduction and its modulation analyzed by atomic force microscope indentation. *Biophys J* 82:2970–2981
- Chen SJ, Dill KA (2000) RNA folding energy landscapes. *Proc Natl Acad Sci USA* 97:646–651
- Chen L, Wildegger G, Kiefhaber T, Hodgson KO, Doniach S (1998) Kinetics of lysozyme refolding: structural characterization of a non-specifically collapsed state using time-resolved X-ray scattering. *J Mol Biol* 276:225–237
- Chen J, Chen Y, Gong P, Jiang Y, Li YM, Zhao YF (2002a) Novel phosphoryl derivatization method for peptide sequencing by electrospray ionization mass spectrometry. *Rapid Commun. Mass Spectrom* 16:531–536
- Chen L, Haushalter KA, Lieber CM, Verdine GL (2002b) Direct visualization of a DNA glycosylase searching for damage. *Chem Biol* 9:345–350
- Cheng J, Wu L, Heller MJ, Sheldon E, Diver J, O'Connell JP, Smolko D, Jalali S, Willoughby D (2002) Integrated portable biological detection system. US Patent 6,403,367
- Cherny DI, Jovin TM (2001) Electron and scanning force microscopy studies of alterations in supercoiled DNA tertiary structure. *J Mol Biol* 313:295–307
- Cho SJ, Quinn AS, Stromer MH, Dash S, Cho J, Taatjes DJ, Jena BP (2002) Structure and dynamics of the fusion pore in live cells. *Cell Biol Int* 26:35–42
- Choy WY, Mulder FA, Crowhurst KA, Muhandiram DR, Millett IS, Doniach S, Forman-Kay JD, Kay LE (2002) Distribution of molecular size within an unfolded state ensemble using small angle X-ray scattering and pulse field gradient NMR techniques. *J Mol Biol* 316:101–112
- Christendat D, Yee A, Dharamsi A, Kluger Y, Gerstein M, Arrowsmith CH, Edwards AM (2000) Structural proteomics: prospects for high throughput sample preparation. *Prog Biophys Mol Biol* 73:3393–45
- Clementi C, Jennings PA, Onuchic JN (2000a) How native-state topology affects the folding of dihydrofolate reductase and interleukin-1 $\beta$ . *Proc Natl Acad Sci USA* 97:5871–5876
- Clementi C, Nymeyer H, Onuchic JN (2000b) Topological and energetic factors: what determines the structural details of the transition state ensemble and “en-route” intermediates for protein folding? An investigation for small globular proteins. *J Mol Biol* 298:937–953
- Cobon GS, Verrills N, Papakostopoulos P, Eastwood H, Linnane AW (2002) The proteomics of aging. *Biogerontology* 3:133–136
- Cohen MJ, Karasek FW (1970) Plasma chromatography – a new dimension for gas chromatography and mass spectrometry. *J Chromatographic Sci* 8:330–337
- Cohen MJ, Crowe RW (1973) Apparatus and methods for detecting, separating, concentrating and measuring electronegative trace vapors. US Patent 3,742,213
- Cohen MJ, Carroll DI, Wernlund RF, Kilpatrick WD (1972) Apparatus and methods for separating, concentrating, detecting, and measuring trace gases. US Patent 3,699,333
- Coimbra MA, Goncalves F, Barros AS, Delgadillo I (2002) Fourier transform infrared spectroscopy and chemometric analysis of white wine polysaccharide extracts. *J Agric Food Chem* 50:3405–3411



- Collet J, Vuillaume D (1998) Nano-field effect transistor with an organic self-assembled monolayer as gate insulator. *Appl Phys Lett* 73:2681–2683
- Collet J, Tharaud O, Chapoton A, Vuillaume D (2000) Low voltage, 30 nm channel length, organic transistors with a self-assembled monolayer as gate insulating films. *Appl Phys Lett* 76:1941–1943
- Coligan JE, Dunn BM, Ploegh HL, Speicher DW, Wingfield PT (ed) (1996) *Current protocols in protein science*. Wiley & Sons, New York
- Costantino HR, Griebenow K, Mishra P, Langer R, Klibanov AM (1995) Fourier transform infrared spectroscopic investigation of protein stability in the lyophilized form. *Biochim Biophys Acta* 1253:69–74
- Crawford OH (1999) A fast, stochastic threading algorithm for proteins. *Bioinformatics* 15:66–71
- Csermely P (1999) Chaperone-percolator model: a possible molecular mechanism of Anfinsen-cage-type chaperones. *BioEssays* 21:959–965
- Cui XD, Primak A, Zarate X, Tomfohr J, Sankey OF, Moore AL, Moore TA, Gust D, Harris G, Lindsay SM (2001) Reproducible measurement of single-molecule conductivity. *Science* 294:571–574
- Czaplewski C, Rodziewicz-Motowidlo S, Liwo A, Ripoll DR, Wawak RJ, Scheraga HA (2000) Molecular simulation study of cooperativity in hydrophobic association. *Protein Sci* 9:1235–1245
- D'Alessio G (1999a) Evolution of oligomeric proteins – the unusual case of a dimeric ribonuclease. *Eur J Biochem* 266:699–708
- D'Alessio G (1999b) The evolutionary transition from monomeric to oligomeric proteins: tools, the environment, hypotheses. *Progress Biophys Mol Biol* 72:271–298
- Dammer U, Popescu O, Wagner P, Anselmetti D, Güntherodt HJ, Misevic GN (1995) Binding strength between cell adhesion proteoglycans measured by atomic force microscopy. *Science* 267:1173–1175
- Dammer U, Hegner M, Anselmetti D, Wagner P, Dreier M, Huber W, Güntherodt HJ (1996) Specific antigen/antibody interactions measured by force microscopy. *Biophys J* 70:2437–2441
- Davda J, Labhasetwar V (2002) Characterization of nanoparticle uptake by endothelial cells. *Int J Pharm* 233:51–59
- Davies DK (1994) Pulsed ionization ion mobility sensor. US Patent 5,300,773
- Dawson RMC, Elliott DC, Elliott WH, Jones KM (1969) *Data for biochemical research*. Oxford University Press, 2nd Ed,
- de Cock H, Brandenburg K, Wiese A, Holst O, Seydel U (1999) Non-lamellar structure and negative charges of lipopolysaccharides required for efficient folding of outer membrane protein PhoE of *Escherichia coli*. *J Biol Chem* 274:5114–5119
- Demers LM, Ginger DS, Park SJ, Li Z, Chung SW, Mirkin CA (2002) Direct patterning of modified oligonucleotides on metals and insulators by dip-pen nanolithography. *Science* 296:1836–1838
- Dempsey BR, Economou A, Dunn SD, Shilton BH (2002) The ATPase domain of SecA can form a tetramer in solution. *J Mol Biol* 315:831–843
- de Paris R, Strunz T, Oroszlan K, Güntherodt HJ, Hegner M (2000) Force spectroscopy and dynamics of the biotin-avidin bond studied by scanning force microscopy. *Single Mol* 1:285–290

- Desmeules P, Grandbois M, Bondarenko VA, Yamazaki A, Salesse C (2002) Measurement of membrane binding between recoverin, a calcium-myristoyl switch protein, and lipid bilayers by AFM-based force spectroscopy. *Biophys J* 82:3343–3350
- Dierksen K, Typke D, Hegerl R, Koster AJ, Baumeister W (1992) Towards automatic electron tomography. *Ultramicroscopy* 40:71–87
- Dill KA, Fiebig KM, Chan HS (1993) Cooperativity in protein folding kinetics. *Proc Natl Acad Sci USA* 90:1942–1946
- Ding FX, Schreiber D, VerBerkmoes NC, Becker JM, Naider F (2002) The chain length dependence of helix formation of the second transmembrane domain of a G protein-coupled receptor of *Saccharomyces cerevisiae*. *J Biol Chem* 277:14483–14492
- Djuricic D, Hill HA, Lo KK, Wong LL (2002) A scanning tunneling microscopy (STM) investigation of complex formation between cytochrome P450<sub>cam</sub> and putidaredoxin. *J Inorg Biochem* 88:362–367
- Dong A, Malecki JM, Lee L, Carpenter JF, Lee JC (2002) Ligand-induced conformational and structural dynamics changes in *Escherichia coli* cyclic AMP receptor protein. *Biochemistry* 41:6660–6667
- Döring HR, Arnold G, Adler J, Röbel T, Riemenschneider J (1999) Photo-ionization ion mobility spectrometry. US Patent 5,968,837
- Doyle R, Simons K, Qian H, Baker D (1997) Local interactions and the optimization of protein folding. *Proteins* 29:282–291
- Drablos F (1999) Clustering of non-polar contacts in proteins. *Bioinformatics* 15:501–509
- Duarte IF, Barros A, Delgadillo I, Almeida C, Gil AM (2002) Application of FTIR spectroscopy for the quantification of sugars in mango juice as a function of ripening. *J Agric Food Chem* 50:3104–3111
- Duncan MD, Bashkansky M, Reintjes j (1998) Subsurface defect detection in materials using optical coherence tomography. *Optics Express* 2:540–545
- Durbin SD, Carlson WE (1992) Lysozyme crystal growth studied by atomic force microscopy. *J Cryst Growth* 122:71–79
- Durbin SD, Carson WE, Saros MT (1993) *In situ* studies of protein crystal growth by atomic force microscopy. *J Phys D Appl Phys* 26:B128–B132
- Dwek MV, Rawlings SL (2002) Current perspectives in cancer proteomics. *Mol Biotechnol* 22:139–152
- Dworzanski JP, McClennen WH, Cole PA, Thornton SN, Meuzelaar HLC, Arnold NS, Snyder AP (1997) Field-portable, automated pyrolysis/GC/IMS system for rapid biomarker detection in aerosols: a feasibility study. *Field Anal Chem Technol* 1:295–305
- Dzwolak W, Kato M, Taniguchi Y (2002) Fourier transform infrared spectroscopy in high-pressure studies on proteins. *Biochim Biophys Acta* 1595:131–144
- Edwards AM, Arrowsmith CH, des Pallieres B (2000) Proteomics: New tools for a new era. *Modern Drug Discovery* 5:35–44
- Edwards AM, Kus B, Jansen R, Greenbaum D, Greenblatt J, Gerstein M (2002) Bridging structural biology and genomics: assessing protein interaction data with known complexes. *Trends Genet* 18:529–536
- Efimov AV (1998) A structural tree for protein containing S-like  $\beta$ -sheets. *FEBS Lett* 437:246–250
- Efimov AV (1999) Complementary packing of  $\alpha$ -helices in proteins. *FEBS Lett* 463:3–6
- Egawa A, Chiba N, Homma K, Chinone K, Muramatsu H (1999) High-speed scanning by dual feedback control in SNOM/AFM. *J Microsc* 194:325–328

- Egea PF, Rochel N, Birck C, Vachette P, Timmins PA, Moras D (2001) Effects of ligand binding on the association properties and conformation in solution of retinoic acid receptors RXR and RAR. *J Mol Biol* 307:557–576
- Eiceman GA, Karas Z (1994) *Ion Mobility Spectrometry*. CRC Press, Boca Raton
- Eiceman GA, Ferris MJ, Anderson GK, Danen WC, Tjee JJ (1988) Laser desorption and ionization of solid polycyclic aromatic hydrocarbons in air with analysis by ion mobility spectrometry. *Anal Lett* 21:539–552
- Eiceman GA, Tadjikov B, Krylov E, Nazarov EG, Miller RA, Westbrook J, Funk P (2001) Miniature radio-frequency mobility analyzer as a gas chromatographic detector for oxygen-containing volatile organic compounds, pheromones and other insect attractants. *J Chromatogr A* 917:205–217
- El Khattabi M, Ockhuijsen C, Bitter W, Jaeger KE, Tommassen J (1999) Specificity of the lipase-specific foldases of gram-negative bacteria and the role of the membrane anchor. *Mol Gen Genet* 261:770–776
- Ellis RJ, Hartl FU (1999) Principles of protein folding in the cellular environment. *Curr Opin Struct Biol* 9:102–110
- Eve JK, Patel N, Luk SY, Ebbens SJ, Roberts CJ (2002) A study of single drug particle adhesion interactions using atomic force microscopy. *Int J Pharm* 238:17–27
- Facci P, Alliata D, Cannistraro S (2001) Potential-induced resonant tunneling through a redox metalloprotein investigated by electrochemical scanning probe microscopy. *Ultramicroscopy* 89:291–298
- Fagas G, Cuniberti G, Richter K (2002) Molecular wire-nanotube interfacial effects on electron transport. *Ann N Y Acad Sci* 960:216–224
- Favier AL, Schoehn G, Jaquinod M, Harsi C, Chroboczek J (2002) Structural studies of human enteric adenovirus type 41. *Virology* 293:75–85
- Fermi G, Perutz MF, Shaanan B, Fourme R (1984) The crystal structure of human deoxyhemoglobin at 1.74 Å resolution. *J Mol Biol* 175:159–174
- Fernandez M, Keyrilainen J, Serimaa R, Torkkeli M, Karjalainen-Lindsberg ML, Tenhunen M, Thomlinson W, Urban V, Suortti P (2002) Small angle X-ray scattering studies of human breast tissue samples. *Phys Med Biol* 47:577–592
- Fersht AR (1995a) Characterizing transition states in protein folding – an essential step in the puzzle. *Curr Opin Struct Biol* 5:79–84
- Fersht AR (1995b) Optimization of rates of protein folding – the nucleation-condensation mechanism and its implications. *Proc Natl Acad Sci USA* 92:10869–10873
- Fersht AR, Matouschek A, Serrano L (1992) The folding of an enzyme. 1. Theory of protein engineering analysis of stability and pathway of protein folding. *J Mol Biol* 224:771–782
- Fetler L, Tauc P, Baker DP, Macol CP, Kantrowitz ER, Vachette P (2002) Replacement of Asp-162 by Ala prevents the cooperative transition by the substrates while enhancing the effect of the allosteric activator ATP on *E. coli* aspartate transcarbamoylase. *Protein Sci* 11:1074–1081
- Fetterolf DD, Clark TD (1993) Detection of trace explosive evidence by ion mobility spectrometry. *J Forensic Sci* 38:28–39
- Feughelman M, Lyman DJ, Willis BK (2002) The parallel helices of the intermediate filaments of  $\alpha$ -keratin. *Int J Biol Macromol* 30:95–96
- Figey D (2002a) Proteomics approaches in drug discovery. *Anal Chem* 74:412A–419A
- Figey D (2002b) Adapting arrays and lab-on-a-chip technology for proteomics. *Proteomics* 2:373–382

- Figeys D (2002c) Functional proteomics: mapping protein-protein interactions and pathways. *Curr Opin Mol Ther* 4:210–215
- Florin EL, Moy VT, Gaub HE (1994) Adhesion forces between individual ligand-receptor pairs. *Science* 264:415–417
- Florin EL, Pralle A, Horber JK, Stelzer EH (1997) Photonic force microscope based on optical tweezers and two-photon excitation for biological applications. *J Struct Biol* 119:202–211
- Forge V, Hoshino M, Kuwata K, Arai M, Kuwajima K, Batt CA, Goto Y (2000) Is folding of  $\beta$ -lactoglobulin non-hierarchical? Intermediate with native-like  $\beta$ -sheet and non-native  $\alpha$ -helix. *J Mol Biol* 296:1039–1051
- Freeman R, Goodfellow M, Gould FK, Hudson SJ, Lightfoot NF (1990) Pyrolysis mass spectrometry (Py-MS) for the rapid epidemiological typing of clinically significant bacterial pathogens. *J Med Microbiol* 32:283–286
- Freeman R, Sisson PR, Heatherington CS (1995) Pyrolysis mass spectrometry. *Methods Mol Biol* 46:97–105
- Freeman R, Sisson PR, Barer MR, Ward AC, Lightfoot NF (1997) A highly discriminatory method for the direct comparison of two closely related bacterial populations by pyrolysis mass spectrometry. *Zentralbl Bakteriol* 285:285–290
- Frey TG, Mannella CA (2000) The internal structure of mitochondria. *Trends Biochem Sci* 25:319–324
- Fringeli UP, Goette J, Reiter G, Siam M, Baurecht D (1998) Structural investigation of oriented membrane assemblies by FTIR-ATR spectroscopy. *AIP Conf Proc* 430:729–747
- Fritz J, Baller MK, Lang HP, Rothuizen H, Vettiger P, Meyer E, Güntherodt HJ, Gerber C, Gimzewski JK (2000) Translating biomolecular recognition into nanomechanics. *Science* 288:316–318
- Frolow F, Kalb AJ, Yariv J (1994) Structure of a unique, twofold symmetrical haem-binding site. *Nature Struct Biol* 1:453–460
- Fujita K, Yasuda T, Tsutsui T (2003) Flexible organic field-effect transistors fabricated by the electrode-peeling transfer with an assist of self-assembled monolayer. *Appl Phys Lett* 82:4373–4375
- Furuike S, Ito T, Yamazaki M (2001) Mechanical unfolding of single filamin A (ABP-280) molecules detected by atomic force microscopy. *FEBS Lett* 498:72–75
- Gaietta G, Deerinck TJ, Adams SR, Bouwer J, Tour O, Laird DW, Sosinsky GE, Tsien RY, Ellisman MH (2002) Multicolor and electron microscopic imaging of connexin trafficking. *Science* 296:503–507
- Gagnéaux A, Ruyschaert JM, Goormaghtigh E (2002) Infrared spectroscopy as a tool for discrimination between sensitive and multiresistant K562 cells. *Eur J Biochem* 269:1968–1973
- Gallagher T, Alexander P, Bryan P, Gilliland GL (1994) Two crystal structures of the B1 immunoglobulin-binding domain of streptococcal protein G and comparison with NMR. *Biochemistry* 33:4721–4729
- Gallardo K, Job C, Groot SP, Puype M, Demol H, Vandekerckhove J, Job D (2002) Proteomics of *Arabidopsis* seed germination. A comparative study of wild-type and gibberellin-deficient seeds. *Plant Physiol* 129:823–837
- Galzitskaya OV, Surin AK, Nakamura H (2000) Optimal region of average sidechain entropy for fast protein folding. *Protein Sci* 9:580–586

- Gao H, Oberringer M, Englisch A, Hanselmann RG, Hartmann U (2001) The scanning near-field optical microscope as a tool for proteomics. *Ultramicroscopy* 86:145–150
- Garcia P, Serrano L, Durand D, Rico M, Bruix M (2001) NMR and SAXS characterization of the denatured state of the chemotactic protein CheY: implications for protein folding initiation. *Protein Sci* 10:1100–1112
- Garcia-Hernandez E, Hernandez-Arana A (1999) Structural basis of lectin-carbohydrate affinities: comparison with protein-folding energetics. *Protein Sci* 8:1075–1086
- Gaub HE, Fernandez JM (1998) The molecular elasticity of individual proteins studied by AFM-related techniques. *AvH Magazin* 71:11–18
- Genick UK, Borgstahl GEO, Ng K, Ren Z, Pradervand C, Burke PM, Srajer V, Teng TY, Schildkamp W, McRee DE, Moffat K, Getzoff ED (1997) Structure of a protein photocycle intermediate by millisecond time-resolved crystallography. *Science* 275:1471–1475
- Gera JF, Hazbun TR, Fields S (2002) Array-based methods for identifying protein-protein and protein-nucleic acid interactions. *Methods Enzymol* 350:499–512
- Ghirlanda G, Lear JD, Ogihara NL, Eisenberg D, DeGrado WF (2002) A hierarchic approach to the design of hexameric helical barrels. *J Mol Biol* 319:243–253
- Giessibl FJ, Hembacher S, Bielefeldt H, Mannhart J (2000) Subatomic features on the Silicon(111)-(7x7) surface observed by atomic force microscopy. *Science* 289:422–426
- Gilardi G, Fantuzzi A, Sadeghi SJ (2001) Engineering and design in the bioelectrochemistry of metalloproteins. *Curr Opin Struct Biol* 11:491–499
- Goebel J, Breit U (2000) Ion mobility spectrometer. US Patent 6,049,076
- Goldbeck RA, Thomas YG, Chen E, Esquerra RM, Kliger DS (1999) Multiple pathways on a protein-folding energy landscape: kinetic evidence. *Proc Natl Acad Sci USA* 96:2782–2787
- Goldsbury C, Aebi U, Frey P (2001) Visualizing the growth of Alzheimer's A  $\beta$ -amyloid-like fibrils. *Trends Mol Med* 7:582
- Goodacre R (1994) Characterisation and quantification of microbial systems using pyrolysis mass spectrometry: introducing neural networks to analytical pyrolysis. *Microbiology Europe* 2:16–22
- Goodacre R, Kell DB (1996) Pyrolysis mass spectrometry and its applications in biotechnology. *Curr Opin Biotechnol* 7:20–28
- Goodacre R, Howell SA, Noble WC, Neal MJ (1996) Sub-species discrimination, using pyrolysis mass spectrometry and self-organising neural networks, of *Propionibacterium acnes* isolated from normal human skin. *Zentralbl Bakteriol* 284:501–515
- Goodacre R, Rooney PJ, Kell DB (1998a) Discrimination between methicillin-resistant and methicillin-susceptible *Staphylococcus aureus* using pyrolysis mass spectrometry and artificial neural networks. *J Antimicrob Chemother* 41:27–34
- Goodacre R, Timmins EM, Burton R, Kaderbhai N, Woodward AM, Kell DB, Rooney PJ (1998b) Rapid identification of urinary tract infection bacteria using hyperspectral whole-organism fingerprinting and artificial neural networks. *Microbiology* 144:1157–1170
- Goodacre R, Shann B, Gilbert RJ, Timmins EM, McGovern AC, Alsberg BK, Kell DB, Logan NA (2000) Detection of the dipicolinic acid biomarker in *Bacillus* spores using Curie point pyrolysis mass spectrometry and Fourier transform infrared spectroscopy. *Anal Chem* 72:119–127

- Goodfellow M, Freeman R, Sisson PR (1997) Curie point pyrolysis mass spectrometry as a tool in clinical microbiology. *Zentralbl Bakteriol* 285:133–156
- Gordon L, Mobley PW, Pilpa R, Sherman MA, Waring AJ (2002) Conformational mapping of the N-terminal peptide of HIV-1 gp41 in membrane environments using  $^{13}\text{C}$ -enhanced Fourier transform infrared spectroscopy. *Biochim Biophys Acta* 1559:96–120
- Goto Y, Aimoto S (1991) Anion and pH-dependent conformational transition of an amphiphilic polypeptide. *J Mol Biol* 218:387–396
- Goto Y, Hoshino M, Kuwata K, Batt CA (1999) Folding of  $\beta$ -lactoglobulin, a case of the inconsistency of local and non-local interactions. In: Kuwajima K and Arai M (ed) *Old and New Views of Protein Folding*. Elsevier, Amsterdam, 3–11
- Govindarajan S, Goldstein RA (1995) Optimal local propensities for model proteins. *Proteins* 22:413–418
- Grabner B, Landis WJ, Roschger P, Rinnerthaler S, Peterlik H, Klaushofer K, Fratzl P (2001) Age- and genotype-dependence of bone material properties in the osteogenesis imperfecta murine model (oim). *Bone* 29:453–457
- Grandori R, Matecko I, Müller N (2002) Uncoupled analysis of secondary and tertiary protein structure by circular dichroism and electrospray ionization mass spectrometry. *J Mass Spectrom* 37:191–196
- Grantcharova VP, Riddle DS, Baker D (2000) Long-range order in the src SH3 folding transition state. *Proc Natl Acad Sci USA* 97:7084–7089
- Grayhack EJ, Phizicky EM (2001) Genomic analysis of biochemical function. *Curr Opin Chem Biol* 5:34–39
- Griffin TJ, Goodlett DR, Aebersold R (2001) Advances in proteome analysis by mass spectrometry. *Curr Opin Biotechnol* 12:607–612
- Grigoriev IV, Rakhmaninova AB, Mironov AA (1998) Simulated annealing for  $\alpha$ -helical protein folding: searches in vicinity of the “molten globule” state. *J Biomol Struct Dyn* 16:115–121
- Grigoriev IV, Mironov AA, Rakhmaninova AB (1999) Refinement of helix boundaries in  $\alpha$ -helical globular proteins (in Russian). *Mol Biol (Moscow)* 33:206–214
- Griko YV (2000) Energetic basis of structural stability in the molten globule state of  $\beta$ -lactalbumin. *J Mol Biol* 297:1259–1268
- Gromiha MM, Selvaraj S (1997) Influence of medium and long range interactions in different structural classes of globular proteins. *J Biol Phys* 23:151–162
- Gromiha MM, Selvaraj S (1999) Importance of long-range interactions in protein folding. *Biophys Chem* 77:49–68
- Gross M (1996) Linguistic analysis of protein folding. *FEBS Lett* 390:249–252
- Gruebele M (1999) The fast protein-folding problem. *Annu Rev Phys Chem* 50:485–516
- Gunning AP, Wilde PJ, Clark DC, Morris VJ, Parker ML, Gunning PA (1996) Atomic force microscopy of interfacial protein films. *J Colloid Interface Sci* 183:600–602
- Gursky O (1999) Probing the conformation of a human apolipoprotein C-1 by amino acid substitutions and trimethylamine-N-oxide. *Prot Sci* 8:2055–2064
- Gursky O, Alekhov S (2000) Temperature-dependent  $\beta$ -sheet formation in  $\beta$ -amyloid A $\beta$ (1–40) peptide in water: uncoupling  $\beta$ -structure folding from aggregation. *Biochim Biophys Acta* 1476:93–102
- Gutsche I, Holzinger J, Rößle M, Heumann H, Baumeister W, May RP (2000a) Conformational rearrangements of an archaeal chaperonin upon ATPase cycling. *Curr Biol* 10:405–408

- Gutsche I, Mihalache O, Hegerl R, Typke D, Baumeister W (2000b) ATPase cycle controls the conformation of an archaeal chaperonin as visualized by cryo-electron microscopy. *FEBS Lett* 477:278–282
- Haas J, Lehr CM (2002) Developments in the area of bioadhesive drug delivery systems. *Expert. Opin Biol Ther* 2:287–298
- Haider M, Uhlemann S, Schwan E, Rose H, Kabius B, Urban K (1998) Electron microscopy image enhanced. *Nature* 392:768–769
- Hamada D, Kuroda Y, Tanaka T, Goto Y (1995) High helical propensity of the peptide fragments derived from  $\beta$ -lactoglobulin, a predominantly  $\beta$ -sheet protein. *J Mol Biol* 254:737–746
- Hansma PK, Drake B, Marti O, Gould SAC, Prater CB (1989) The scanning ion-conductance microscope. *Science Reports* 243:641–643
- Hardesty B, Tsalkova T, Kramer G (1999) Co-translational folding. *Curr Opin Struct Biol* 9:111–114
- Häusler G, Lindner MW (1998) “Coherence radar” and “Spectral radar”—New tools for dermatological diagnosis. *J Biomed Opt* 3:21–31
- Heimel J, Fischer UC, Fuchs H (2001) SNOM/STM using a tetrahedral tip and a sensitive current-to-voltage converter. *J Microsc* 202:53–59
- Heinemann U, Frevert J, Hofmann K, Illing G, Maurer C, Oschkinat H, Saenger W (2000) An integrated approach to structural genomics. *Prog Biophys Mol Biol* 73:347–362
- Heinemann U, Illing G, Oschkinat H (2001) High-throughput three-dimensional protein structure determination. *Curr Opin Biotechnol* 12:348–354
- Helyer RJ, Kelley T, Berkeley RC (1997) Pyrolysis mass spectrometry studies on *Bacillus anthracis*, *Bacillus cereus* and their close relatives. *Zentralbl Bakteriol* 285:319–328
- Henderson R (1996) Lecture "Resolution limits of microscopes", Laboratory of Molecular Biology, Cambridge
- Henderson E, Haydon PG, Sakaguchi DS (1992) Actin filament dynamics in living glial cells imaged by atomic force microscopy. *Science* 257:1944–1946
- Hertadi R, Ikai A (2002) Unfolding mechanics of *holo*- and *apocalmodulin* studied by the atomic force microscope. *Protein Sci* 11:1532–1538
- Heyes CD, Wang J, Sanii LS, El-Sayed MA (2002) Fourier transform infrared study of the effect of different cations on bacteriorhodopsin protein thermal stability. *Biophys J* 82:1598–1606
- Hilario J, Kubelka J, Syud FA, Gellman SH, Keiderling TA (2002) Spectroscopic characterization of selected  $\beta$ -sheet hairpin models. *Biopolymers* 67:233–236
- Hildebrand G, Kunze S, Driver M (2001) Blood cell adhesion on sensor materials studied by light, scanning electron, and atomic-force microscopy. *Ann Biomed Eng* 29:1100–1105
- Hill HH, Siems WF, St Louis RW, McMinn DG (1990) Ion mobility spectrometry. *Anal Chem* 62:1201–1209
- Hodneland CD, Lee YS, Min DH, Mrksich M (2002) Selective immobilization of proteins to self-assembled monolayers presenting active site-directed capture ligands. *Proc Natl Acad Sci USA* 99:5048–5052
- Honda S, Kobayashi N, Munekata E, Uedaira H (1999) Fragment reconstitution of a small protein: folding energetics of the reconstituted immunoglobulin binding domain B1 of streptococcal protein G. *Biochemistry* 38:1203–1213
- Honda S, Kobayashi N, Munekata E (2000) Thermodynamics of a  $\beta$ -hairpin structure: evidence for cooperative formation of folding nucleus. *J Mol Biol* 295:269–278

- Hoover DM, Ludwig ML (1997) A flavodoxin that is required for enzyme activation: the structure of oxidized flavodoxin from *Escherichia coli* at 1.8 Å resolution. *Protein Sci* 6:2525–2537
- Horiuchi Y, Yagi K, Hosokawa T, Yamamoto N, Muramatsu H, Fujihira M (1999) Imaging of various surface properties of fluorescently labelled phospholipid Langmuir-Blodgett films with a combined scanning probe microscope. *J Microsc* 194:467–471
- Hornemann S, Glockshuber R (1998) A scrapie-like unfolding intermediate of the prion protein domain PrP(121–231) induced by acidic pH. *Proc Natl Acad Sci USA* 95:6010–6014
- Howald L, Lüthli R, Meyer E, Güntherodt HJ (1995) Atomic-force microscopy on the Si(111)-(7x7) surface. *Phys Rev B Condens Matter* 51:5484–5487
- Huang CY, Getahun Z, Zhu Y, Klemke JW, DeGrado WF, Gai F (2002) Helix formation via conformation diffusion search. *Proc Natl Acad Sci USA* 99:2788–2793
- Hubbard MJ (2002) Functional proteomics: The goalposts are moving. *Proteomics* 2:1069–1078
- Hung K, Sun X, Ding H, Kalafatis M, Simioni P, Guo B (2002) A matrix-assisted laser desorption/ionization time-of-flight based method for screening the 1691 G ← A mutation in the factor V gene. *Blood Coagul Fibrinolysis* 13:117–122
- Igartua M, Saulnier P, Heurtault B, Pech B, Proust JE, Pedraz JL, Benoit JP (2002) Development and characterization of solid lipid nanoparticles loaded with magnetite. *Int J Pharm* 233:149–157
- Ikarashi Y, Itoh K, Maruyama Y (1991) Application of FRIT fast atom bombardment liquid chromatography / mass spectrometry for the determination of acetylcholine levels in rat brain regions. *Biol Mass Spectrom*. 20:21–25
- Ikeda S, Morris VJ (2002) Fine-stranded and particulate aggregates of heat-denatured whey proteins visualized by atomic force microscopy. *Biomacromolecules* 3:382–389
- Irbäck A, Peterson C, Potthast F, Sandelin E (1999) Design of sequences with good folding properties in coarse-grained protein models. *Structure Fold Des* 7:347–360
- Ironside JW (1998) Prion diseases in man. *J Pathol* 186:227–234
- Ishizawa F, Misawa S (1990) Capillary column pyrolysis - gas chromatography of hair: a short study in personal identification. *J Forensic Sci Soc* 30:201–209
- Ito Y, Bleloch AL, Brown LM (1998) Nanofabrication of solid-state Fresnel lenses for electron optics. *Nature* 394:49–52
- Ito T, Ota K, Kubota H, Yamaguchi Y, Chiba T, Sakuraba K, Yoshida M (2002) Roles for the two-hybrid system in exploration of the yeast protein interactome. *Mol Cell Proteomics* 1:561–566
- Itoh H, Ogura M, Komatsuda A, Wakui H, Miura AB, Tashima Y (1999) A novel chaperone-activity-reducing mechanism of the 90-kDa molecular chaperone HSP90. *Biochem J* 343:697–703
- Itzhaki LS, Otzen DE, Fersht AR (1995) The structure of the transition state for folding of chymotrypsin inhibitor 2 analysed by protein engineering methods: evidence for a nucleation-condensation mechanism for protein folding. *J Mol Biol* 254:260–288
- Iverson TM, Luna-Chavez C, Cecchini G, Rees DC (1999) Structure of the *E. coli* fumarate reductase respiratory complex. *Science* 284:1961–1966
- Jackson SE (1998) How do small single-domain proteins fold? *Fold Des* 3:R81–R91
- Jäger D, Jungblut PR, Müller-Werdan U (2002) Separation and identification of human heart proteins. *J Chromatogr B Analyt Technol Biomed Life Sci* 771:131–153



- Jain KK (2002) Recent advances in oncoproteomics. *Curr Opin Mol Ther* 4:203–209
- Jeney S, Florin EL, Horber JK (2001) Use of photonic force microscopy to study single-motor-molecule mechanics. *Methods Mol Biol* 164:91–108
- Jésior JC, Filhol A, Tranqui D (1994) FoldIt (light) – an interactive program for Macintosh computers to analyze and display Protein Data Bank coordinate files. *J Appl Cryst* 27:1075
- Jésior JC (2000) Hydrophilic frameworks in proteins? *J Protein Chem* 19:93–103
- Jiang M, Nölting B, Stayton PS, Sligar SG (1996) Surface-linked molecular monolayers of an engineered myoglobin: structure, stability, and function. *Langmuir* 12:1278–1283
- Jiao Y, Cherny DI, Heim G, Jovin TM, Schaffer TE (2001) Dynamic interactions of p53 with DNA in solution by time-lapse atomic force microscopy. *J Mol Biol* 314:233–243
- Jimenez CR, Eyman M, Lavina ZS, Gioio A, Li KW, van der Schors RC, Geraerts WP, Giuditta A, Kaplan BB, van Minnen J (2002) Protein synthesis in synaptosomes: a proteomics analysis. *J Neurochem* 81:735–744
- Kaji N, Ueda M, Baba Y (2001) Direct measurement of conformational changes on DNA molecule intercalating with a fluorescence dye in an electrophoretic buffer solution by means of atomic force microscopy. *Electrophoresis* 22:3357–3364
- Kamatari YO, Ohji S, Konno T, Seki Y, Soda K, Kataoka M, Akasaka K (1999) The compact and expanded denatured conformations of apomyoglobin in the methanol-water solvent. *Protein Sci* 8:873–882
- Kandori H, Shimono K, Shichida Y, Kamo N (2002) Interaction of Asn105 with the retinal chromophore during photoisomerization of pharaonis phoborhodopsin. *Biochemistry* 41:4554–4559
- Karasek FW (1970) Plasma chromatograph. *Research/Development* 21:34–37
- Karl M (1994) Ion mobility spectrometer drift chamber. US Patent 5,280,175
- Karplus M, Weaver DL (1994) Protein folding dynamics: the diffusion-collision model and experimental data. *Protein Sci* 3:650–668
- Katakuse I, Matsuo T, Matsuda H, Shimonishi Y, Hong YM, Izumi Y (1982) Sequence determination of a peptide with 55 amino acid residues by Edman degradation and field desorption mass spectrometry. *Biomed Mass Spectrom* 9:64–68
- Katou H, Hoshino M, Kamikubo H, Batt CA, Goto Y (2001) Native-like  $\beta$ -hairpin retained in the cold-denatured state of bovine  $\beta$ -lactoglobulin. *J Mol Biol* 310:471–484
- Kawata Y, Kawagoe M, Hongo K, Mikuya T, Higurashi T, Mizobata T, Nagai J (1999) Functional communications between the apical and equatorial domains of GroEL through the intermediate domain. *Biochemistry* 38:15731–15740
- Keller RA (1975) Plasma chromatograph, an atmospheric pressure chemical ionization drift-time spectrometer. *Am Lab* 7:35–44
- Keller T, Miki P, Regenscheit P, Dirnhofer R, Schneider A, Tsuchihashi H (1998) Detection of designer drugs in human hair by ion mobility spectrometry. *Forensic Sci Int* 94:55–63
- Kellermayer MS, Smith SB, Bustamante C, Granzier HL (2001) Mechanical fatigue in repetitively stretched single molecules of titin. *Biophys J* 80:852–863
- Kendrew JC, Dickerson RE, Strandberg BE, Hart RJ, Davies DR, Phillips DC, Shore VC (1960) Structure of myoglobin: a three-dimensional Fourier synthesis at 2 Å resolution. *Nature* 185:422–427
- Kenyon RG, Ferguson EV, Ward AC (1997) Application of neural networks to the analysis of pyrolysis mass spectra. *Zentralbl Bakteriol* 285:267–277

- Kersten B, Burkle L, Kuhn EJ, Giavalisco P, Konthur Z, Lueking A, Walter G, Eickhoff H, Schneider U (2002) Large-scale plant proteomics. *Plant Mol Biol* 48:133–141
- Kharakoz DP (1989) Volumetric properties of proteins and their analogs in diluted water solutions. 1. Partial volumes of amino acids at 15–55 °C. *Biophys Chem* 34:115–125
- Kharakoz DP (1991) Volumetric properties of proteins and their analogs in diluted water solutions. 2. Partial adiabatic compressibilities of amino acids at 15–70 °C. *J Phys Chem* 95:5634–5642
- Kharakoz DP (1997) Partial volumes and compressibilities of extended polypeptide chains in aqueous solution: additivity scheme and implication of protein unfolding at normal and high pressure. *Biochemistry* 36:10276–10285
- Khomutov GB, Belovolova LV, Gubin SP, Khanin VV, Obydenov AY, Sergeev-Cherenkov AN, Soldatov ES, Trifonov AS (2002) STM study of morphology and electron transport features in cytochrome c and nanocluster molecule monolayers. *Bioelectrochemistry* 55:177–181
- Kienzl E, Jellinger K, Stachelberger H, Linert W (1999) Iron as catalyst for oxidative stress in the pathogenesis of Parkinson's disease? *Life Sci* 65:1973–1976
- Kim Y, Prestegard JH (1990) Refinement of the NMR structures for acyl carrier protein with scalar coupling data. *Proteins* 8:377–385
- Kim JM, Ohtani T, Sugiyama S, Hirose T, Muramatsu H (2001) Simultaneous topographic and fluorescence imaging of single DNA molecules for DNA analysis with a scanning near-field optical/atomic force microscope. *Anal Chem* 73:5984–5991
- Kinney JH, Pople JA, Marshall GW, Marshall SJ (2001) Collagen orientation and crystallite size in human dentin: a small angle X-ray scattering study. *Calcif Tissue Int* 69:31–37
- Kintz P, Cirimele V, Sengler C, Mangin P (1995) Testing human hair and urine for anhydroecgonine methyl ester, a pyrolysis product of cocaine. *J Anal Toxicol* 19:479–482
- Kizil R, Irudayaraj J, Seetharaman K (2002) Characterization of irradiated starches by using FT-Raman and FTIR spectroscopy. *J Agric Food Chem* 50:3912–3918
- Klade CS (2002) Proteomics approaches towards antigen discovery and vaccine development. *Curr Opin Mol Ther* 4:216–223
- Kline AD, Braun W, Wüthrich K (1988) Determination of the complete three-dimensional structure of the  $\alpha$ -amylase inhibitor tendamistat in aqueous solution by nuclear magnetic resonance and distance geometry. *J Mol Biol* 204:675–724
- Kneipp J, Beekes M, Lasch P, Naumann D (2002) Molecular changes of preclinical scrapie can be detected by infrared spectroscopy. *J Neurosci* 22:2989–2997
- Koga N, Takada S (2001) Roles of native topology and chain-length scaling in protein folding: a simulation study with a Go-like model. *J Mol Biol* 313:171–180
- Kohno M, Enatsu M, Yoshiizumi M, Kugimiya W (1999) High-level expression of *Rhizopus niveus* lipase in the yeast *Saccharomyces cerevisiae* and structural properties of the expressed enzyme. *Protein Expr Purif* 15:327–335
- Kojima M, Tanokura M, Maeda M, Kimura K, Amemiya Y, Kihara H, Takahashi K (2000) pH-dependent unfolding of aspergillopepsin II studied by small angle X-ray scattering. *Biochemistry* 39:1364–1372
- Konan YN, Gurny R, Allemann E (2002) Preparation and characterization of sterile and freeze-dried sub-200 nm nanoparticles. *Int J Pharm* 233:239–252
- Koradi R, Billeter M, Wüthrich K (1996) MOLMOL: a program for display and analysis of macromolecular structures. *J Mol Graphics* 14:51–55

- Korchev YE, Bashford CL, Milovanovic M, Vodyanoy I, Lab MJ (1997) Scanning ion conductance microscopy of living cells. *Biophys J* 73:653–658
- Korchev YE, Gorelik J, Lab MJ, Sviderskaya EV, Johnston CL, Coombes CR, Vodyanoy I, Edwards CR (2000a) Cell volume measurement using scanning ion conductance microscopy. *Biophys J* 78:451–457
- Korchev YE, Raval M, Lab MJ, Gorelik J, Edwards CR, Rayment T, Klenerman D (2000b) Hybrid scanning ion conductance and scanning near-field optical microscopy for the study of living cells. *Biophys J* 78:2675–2679
- Koshland DE Jr, Hamadani K (2002) Proteomics and models for enzyme cooperativity. *J Biol Chem* 277:46841–46844
- Köster H (2001a) DNA sequencing by mass spectrometry. US Patent 6,194,144
- Köster H (2001b) DNA sequencing by mass spectrometry. US Patent 6,225,450
- Kotiaho T, Lauritsen FR, Degn H, Paakkanen H (1995) Membrane inlet ion mobility spectrometer for on-line measurement of ethanol in beer and in yeast fermentation. *Anal Chim Acta* 309:317–325
- Kramer G, Kudlicki W, McCarthy D, Tsalkova T, Simmons D, Hardesty B (1999) N-terminal and C-terminal modifications affect folding, release from the ribosomes and stability of *in vitro* synthesised proteins. *Int J Biochem Cell Biol* 31:231–241
- Kraulis PJ (1991) MOLSRCIPT – a program to produce both detailed and schematic plots of protein structures. *J Appl Crystallogr* 24:946–950
- Krautbauer R, Pope LH, Schrader TE, Allen S, Gaub H (2002) Discriminating small molecule DNA binding modes by single molecule force spectroscopy. *FEBS Lett* 510:154–158
- Kukar T, Eckenrode S, Gu Y, Lian W, Megginson M, She JX, Wu D (2002) Protein microarrays to detect protein-protein interactions using red and green fluorescent proteins. *Anal Biochem* 306:50–54
- Kuwajima K, Yamaya H, Sugai S (1996) The burst-phase intermediate in the refolding of  $\beta$ -lactoglobulin studied by stopped-flow circular dichroism and absorption spectroscopy. *J Mol Biol* 264:806–822
- Kuznetsov YG, Malkin AJ, Lucas RW, McPherson A (2000) Atomic force microscopy studies of icosahedral virus crystal growth. *Colloids Surf B Biointerfaces* 19:333–346
- Lasch P, Pacifico A, Diem M (2002) Spatially resolved IR microspectroscopy of single cells. *Biopolymers* 67:335–338
- Laurell T, Marko-Varga G (2002) Miniaturisation is mandatory unravelling the human proteome. *Proteomics* 2:345–351
- Lawrence AH, Barbour RJ, Sutcliffe R (1991) Identification of wood species by ion mobility spectrometry. *Anal Chem* 63:1217–1221
- Leahy DJ, Hendrickson WA, Aukhil I, Erickson HP (1992) Structure of a fibronectin type III domain from tenascin phased by MAD analysis of the selenomethionyl protein. *Science* 258:987–991
- Leasure CS, Fleischer ME, Anderson GK, Eiceman GA (1986) Photoionization in air with ion mobility spectrometry using a hydrogen discharge lamp. *Anal Chem* 58:2142–2147
- Leaves NI, Sisson PR, Freeman R, Jordens JZ (1997) Pyrolysis mass spectrometry in epidemiological and population genetic studies of *Haemophilus influenzae*. *J Med Microbiol* 46:204–207

- Lee DS, Wu C, Hill HH (1998) Detection of carbohydrates by electrospray ionization / ion mobility spectrometry following microbore high-performance liquid chromatography. *J Chromatogr* 822:1–9
- Lee KA, Craven KB, Niemi GA, Hurley JB (2002a) Mass spectrometric analysis of the kinetics of in vivo rhodopsin phosphorylation. *Protein Sci* 11:862–874
- Lee KB, Park SJ, Mirkin CA, Smith JC, Mrksich M (2002b) Protein nanoarrays generated by dip-pen nanolithography. *Science* 295:1702–1705
- Lee SW, Mao CB, Flynn CE, Belcher AM (2002c) Ordering of quantum dots using genetically engineered viruses. *Science* 296:892–895
- Leonhardt JW (1996) New detectors in environmental monitoring using tritium sources. *J Radioanal Nucl Chem* 206:333–339
- Leonhardt JW, Rohrbeck W, Bensch H (2001) A high resolution IMS for environmental studies. Supplement to the catalogue for the IMS supplied by the IUT Institute for Environmental Technologies Ltd, Berlin
- Li T, Talvenheimo J, Zeni L, Rosenfeld R, Stearns G, Arakawa T (2002) Changes in protein conformation and dynamics upon complex formation of brain-derived neurotrophic factor and its receptor: investigation by isotope-edited Fourier transform IR spectroscopy. *Biopolymers* 67:10–19
- Lim SO, Park SJ, Kim W, Park SG, Kim HJ, Kim YI, Sohn TS, Noh JH, Jung G (2002) Proteome analysis of hepatocellular carcinoma. *Biochem Biophys Res Commun* 291:1031–1037
- Lin H, Cornish VW (2002) Screening and selection methods for large-scale analysis of protein function. *Angew Chem Int Ed Engl* 2002 41:4402–4425
- Linderoth NA, Simon MN, Russel M (1997) The filamentous phage pIV multimer visualized by scanning transmission electron microscopy. *Science* 278:1635–1638
- Lindqvist M, Graslund A (2001) An FTIR and CD study of the structural effects of G-tract length and sequence context on DNA conformation in solution. *J Mol Biol* 314:423–432
- Lindsay SM, Thundat T, Nagahara L, Knipping U, Rill RL (1989) Images of DNA double helix in water. *Science* 244:1063–1064
- Liphardt J, Onoa B, Smith SB, Tinoco I Jr, Bustamante C (2001) Reversible unfolding of single RNA molecules by mechanical force. *Science* 292:733–737
- Liu M, Barth A (2002) Mapping nucleotide binding site of calcium ATPase with IR spectroscopy: effects of ATP  $\gamma$ -phosphate binding. *Biopolymers* 67:267–270
- Liu H, Berger SJ, Chakraborty AB, Plumb RS, Cohen SA (2002) Multidimensional chromatography coupled to electrospray ionization time-of-flight mass spectrometry as an alternative to two-dimensional gels for the identification and analysis of complex mixtures of intact proteins. *J Chromatogr B Analyt Technol Biomed Life Sci* 782:267–289
- Lubman DM, Kronick MN (1982) Plasma chromatography with laser-produced ions. *Anal Chem* 54:1546–1551
- Lubman DM, Kronick MN (1983) Multiwavelength-selective ionization of organic compounds in an ion mobility spectrometer. *Anal Chem* 55:867–873
- MacBeath G (2002) Protein microarrays and proteomics. *Nat Genet* 32 Suppl 2:526–532
- Magee JG, Goodfellow M, Sisson PR, Freeman R, Lightfoot NF (1997) Differentiation of *Mycobacterium senegalense* from related non-chromogenic mycobacteria using pyrolysis mass spectrometry. *Zentralbl Bakteriol* 285:278–284

- Malins DC, Hellstrom KE, Anderson KM, Johnson PM, Vinson MA (2002) Antioxidant-induced changes in oxidized DNA. *Proc Natl Acad Sci USA* 99:5937–5941
- Malkin AJ, Land TA, Kuznetsov YG, McPherson A, DeYoreo JJ (1995) Investigation of virus crystal growth mechanisms by *in situ* atomic force microscopy. *Phys Rev Lett* 75:2778–2781
- Malkin AJ, Plomp M, McPherson A (2002) Application of atomic force microscopy to studies of surface processes in virus crystallization and structural biology. *Acta Crystallogr D Biol Crystallogr* 58:1617–1621
- Man WJ, White IR, Bryant D, Bugelski P, Camilleri P, Cutler P, Heald G, Lord PG, Wood J, Kramer K (2002) Protein expression analysis of drug-mediated hepatotoxicity in the *Sprague-Dawley* rat. *Proteomics* 2:1577–1585
- Maret W, Heffron G, Hill HA, Djuricic D, Jiang LJ, Vallee BL (2002) The ATP/metallothionein interaction: NMR and STM. *Biochemistry* 41:1689–1694
- Marple VA, Chein CM (1980) Virtual impactors: a theoretical study. *Environmental Sci Technol* 14:976–985
- Marple VA, Olson BA, Miller NC (1998) The role of inertial particle collectors in evaluating pharmaceutical aerosol delivery systems. *J Aerosol Med* 11 Suppl 1:S139–S153
- Martin SJ, Butler MA, Frye GC, Schubert WK (1998) Ion mobility spectrometer using frequency-domain separation. US Patent 5,789,745
- Martzen MR, McCraith SM, Spinelli SL, Torres FM, Fields S, Grayhack EJ, Phizicky EM (1999) A biochemical genomics approach for identifying genes by the activity of their products. *Science* 286:1153–1155
- Maruyama T, Nakajima M, Ichikawa S, Sano Y, Nabetani H, Furusaki S, Seki M (2001) Small angle X-ray scattering analysis of stearic acid modified lipase. *Biosci Biotechnol Biochem* 65:1003–1006
- Mathur AB, Collinworth AM, Reichert WM, Kraus WE, Truskey GA (2001) Endothelial, cardiac muscle and skeletal muscle exhibit different viscous and elastic properties as determined by atomic force microscopy. *J Biomech* 34:1545–1553
- Matsko N, Klinov D, Manykin A, Demin V, Klimenko S (2001) Atomic force microscopy analysis of bacteriophages  $\Phi$ KZ and T4. *J Electron Microscop (Tokyo)* 50:417–422
- Matsuda H (1976) Double focusing mass spectrometers of second order. *Atomic Masses and Fundamental Constants* 5:185–191
- Matsuda H (1981) Mass spectrometers of high transmission and high resolving power. *Nucl Instr Meth* 187:127–136
- Matsuda H, Naito M, Takeuchi M (1974) Advanced virtual image double focussing mass spectrometer. *Adv Mass Spectrom* 6:407–412
- Matz G, Schröder W (1996) Fast GC/MS field screening for excavation and bioremediation of contaminated soil. *Field Anal Chem Technol* 1:77–85
- Matz G, Schröder W (1997) Fast detection of wood preservatives on waste wood with GC/MS, GC/ECD and ion mobility spectrometry. Conference “Field analytical methods for hazardous wastes and toxic chemicals”, Las Vegas
- Matz LM, Hill HH (2001) Evaluation of opiate separation by high-resolution electrospray ionization-ion mobility spectrometry / mass spectrometry. *Anal Chem* 73:1664–1669
- Mayor U, Johnson CM, Daggett V, Fersht AR (2000) Protein folding and unfolding in microseconds to nanoseconds by experiment and simulation. *Proc Natl Acad Sci USA* 97:13518–13522

- McCraith S, Holtzman T, Moss B, Fields S (2000) Genome-wide analysis of vaccinia virus protein-protein interactions. *Proc Natl Acad Sci USA* 97:4879–4884
- McPherson A, Malkin AJ, Kuznetsov YG (2000) Atomic force microscopy in the study of macromolecular crystal growth. *Annu Rev Biophys Biomol Struct* 29:361–410
- McPherson A, Malkin AJ, Kuznetsov YG, Plomp M (2001) Atomic force microscopy applications in macromolecular crystallography. *Acta Crystallogr D Biol Crystallogr* 57:1053–1060
- Megerle CA, Cohn DB (2000) Ion mobility sensors and spectrometers having a corona discharge ionization source. US Patent 6,100,698
- Meixner AJ, Knepe H (1998) Scanning near-field optical microscopy in cell biology and microbiology. *Cell Mol Biol* 44:673–688
- Merkel R, Nassoy P, Leung A, Ritchie K, Evans E (1999) Energy landscapes of receptor-ligand bonds explored with dynamic force spectroscopy. *Nature* 397:50–53
- Mezzetti A, Nabedryk E, Breton J, Okamura MY, Paddock ML, Giacometti G, Leibl W (2002) Rapid-scan Fourier transform infrared spectroscopy shows coupling of Glu-L212 protonation and electron transfer to Q(B) in *Rhodobacter sphaeroides* reaction centers. *Biochim Biophys Acta* 1553:320–330
- Michener CM, Ardekani AM, Petricoin EF 3rd, Liotta LA, Kohn EC (2002) Genomics and proteomics: application of novel technology to early detection and prevention of cancer. *Cancer Detect Prev* 26:249–255
- Miki A, Keller T, Regenscheit P, Dirnhöfer R, Tatsuno M, Katagi M, Nishikawa M, Tsuchihashi H (1997) Application of ion mobility spectrometry to the rapid screening of methamphetamine incorporated in hair. *J Chromatogr B* 692:319–328
- Miki A, Tatsuno M, Katagi M, Nishikawa M, Tsuchihashi H (1998) Analysis of illicit drugs by ion mobility spectrometry. *J Toxicol - Toxin Rev* 17:93–93
- Miller LD, Putthanarat S, Eby RK, Adams WW (1999) Investigation of the nanofibrillar morphology in silk fibers by small angle X-ray scattering and atomic force microscopy. *Int J Biol Macromol* 24:159–165
- Mills G, Zhou H, Midha A, Donaldson L, Weaver JMR (1998) Scanning thermal microscopy using batch fabricated thermocouple probes. *Appl Phys Lett* 72:2900–2902
- Mills G, Weaver JMR, Harris G, Chen W, Carrejo J, Johnson L, Rogers B (1999) Detection of subsurface voids using scanning thermal microscopy. *Ultramicroscopy* 80:7–11
- Mirny L, Shakhnovich E (2001) Protein folding theory: from lattice to all-atom models. *Annu Rev Biophys Biomol Struct* 30:361–396
- Mitsuoka Y, Niwa T, Ichihara S, Kato K, Muramatsu H, Nakajima K, Shikida M, Sato K (2001) Microfabricated silicon dioxide cantilever with subwavelength aperture. *J Microsc* 202:12–15
- Mo W, Karger BL (2002) Analytical aspects of mass spectrometry and proteomics. *Curr Opin Chem Biol* 6:666–675
- Mollica V, Borassi A, Relini A, Cavalleri O, Bolognesi M, Rolandi R, Gliozzi A (2001) An atomic force microscopy investigation of protein crystal surface topography. *Eur Biophys J* 30:313–318
- Moritz R, Reinstadler D, Fabian H, Naumann D (2002) Time-resolved FTIR difference spectroscopy as tool for investigating refolding reactions of ribonuclease T1 synchronized with *trans* → *cis* prolyl isomerization. *Biopolymers* 67:145–155

- Morris VJ, Kirby AR, Gunning AP (1999) Using atomic force microscopy to probe food biopolymer functionality. *Scanning* 21:287–292
- Morrison RS, Kinoshita Y, Johnson MD, Uo T, Ho JT, McBee JK, Conrads TP, Veenstra TD (2002) Proteomic analysis in the neurosciences. *Mol Cell Proteomics* 1:553–560
- Morton CJ, Pugh DJR, Brown ELJ, Kahmann JD, Renzoni DAC, Campbell ID (1996) Solution structure and peptide binding of the SH3 domain from human Fyn. *Structure* 4:705–714
- Mui C, Han JH, Wang GT, Musgrave CB, Bent SF (2002) Proton transfer reactions on semiconductor surfaces. *J Am Chem Soc* 124:4027–4038
- Muñoz V, Eaton WA (1999) A simple model for calculating the kinetics of protein folding from three-dimensional structures. *Proc Natl Acad Sci USA* 96:11311–11316
- Muramatsu H, Homma K, Chiba N, Yamamoto N, Egawa A (1999) Dynamic etching method for fabricating a variety of tip shapes in the optical fiber probe of a scanning near-field optical microscope. *J Microsc* 194:383–387
- Muroga Y (2001) Derivation of the small angle X-ray scattering functions for local conformations of polypeptide chains in solution. *Biopolymers* 59:320–329
- Natsume T, Yamauchi Y, Nakayama H, Shinkawa T, Yanagida M, Takahashi N, Isobe T (2002) A direct nanoflow liquid chromatography-tandem mass spectrometry system for interaction proteomics. *Anal Chem* 74:4725–4733
- Nemeth-Cawley JF, Rouse JC (2002) Identification and sequencing analysis of intact proteins via collision-induced dissociation and quadrupole time-of-flight mass spectrometry. *J Mass Spectrom* 37:270–282
- Niggemann M, Steipl B (2000) Exploring local and nonlocal interactions for protein stability by structural motif engineering. *J Mol Biol* 296:181–195
- Nilges M, Macias MJ, O'Donoghue SI, Oschkinat H (1997) Automated NOESY interpretation with ambiguous distance restraints: the refined NMR solution structure of the pleckstrin homology domain from beta-spectrin. *J Mol Biol* 269:408–422
- Nilsson CL (2002) Bacterial proteomics and vaccine development. *Am J Pharmacogenomics* 2:59–65
- Nilsson T, Bassani MR, Larsen TO, Montanarella L (1996) Classification of species in the genus *Penicillium* by Curie point pyrolysis / mass spectrometry followed by multivariate analysis and artificial neural networks. *J Mass Spectrom* 31:1422–1428
- Noinville S, Revault M, Baron MH (2002) Conformational changes of enzymes adsorbed at liquid-solid interface: relevance to enzymatic activity. *Biopolymers* 67:323–326
- Nölting B (1991) Development of a novel spectrometer for the simultaneous measurement of absorption and circular dichroism (in German). PhD thesis, University of Bochum.
- Nölting B (1998) Structural resolution of the folding pathway of a protein by correlation of  $\Phi$ -values with inter-residue contacts. *J Theor Biol* 194:419–428
- Nölting B (1999a) Analysis of the folding pathway of chymotrypsin inhibitor by correlation of  $\Phi$ -values with inter-residue contacts. *J Theor Biol* 197:113–121
- Nölting B (1999b, 2005) *Protein Folding Kinetics: Biophysical Methods*. Springer, Berlin Heidelberg New York
- Nölting B, Andert K (2000) Mechanism of protein folding. *Proteins* 41:288–298
- Nölting B, Golbik R, Fersht AR (1995) Submillisecond events in protein folding. *Proc Natl Acad Sci USA* 92:10668–10672
- Nölting B, Golbik R, Neira JL, Soler-Gonzalez AS, Schreiber G, Fersht AR (1997a) The folding pathway of a protein at high resolution from microseconds to seconds. *Proc Natl Acad Sci USA* 94:826–830

- Nölting B, Golbik R, Soler-González AS, Fersht AR (1997b) Circular dichroism of denatured barstar shows residual structure. *Biochemistry* 36:9899–9905
- Nölting B, Schälke W, Hampel P, Grundig F, Gantert S, Sips N, Bandlow W, Qi PX (2003) Structural determinants of the rate of protein folding. *J Theor Biol* 223:299–307
- Nölting B, Jülich D, Vonau W, Andert K (2004) Evolutionary computer programming of protein folding and structure predictions. *J theor Biol* 229:13–18
- Norledge B, Mayr EM, Glockshuber R, Bateman OA, Slingsby C, Jaenicke R, Driessen HPC (1996) The X-ray structures of two mutant crystallin domains shed light on the evolution of multi-domain proteins. *Nature Struct Biol* 3:267–274
- Nyman TA (2001) The role of mass spectrometry in proteome studies. *Biomol Eng* 18:221–227
- Odom TW, Huang JL, Lieber CM (2002) Single-walled carbon nanotubes: from fundamental studies to new device concepts. *Ann N Y Acad Sci* 960:203–215
- Oesterhelt F, Oesterhelt D, Pfeiffer M, Engel A, Gaub HE, Müller DJ (2000) Unfolding pathways of individual bacteriorhodopsins. *Science* 288:143–146
- Ogden ID, Strachan NJC (1993) Enumeration of *Escherichia coli* in cooked and raw meats by ion mobility spectrometry. *J Applied Bacteriology* 74:402–405
- Orengo CA, Jones DT, Thornton JM (1994) Protein superfamilies and domain superfolds. *Nature* 372:631–634
- Oroudjev E, Soares J, Arcidiacono S, Thompson JB, Fossey SA, Hansma HG (2002) Segmented nanofibers of spider dragline silk: atomic force microscopy and single-molecule force spectroscopy. *Proc Natl Acad Sci USA* 99:6460–6465
- Oubridge C, Ito N, Evans PR, Teo CH, Nagai K (1994) Crystal structure at 1.92 Å resolution of the RNA-binding domain of the U1A spliceosomal protein complexed with an RNA hairpin. *Nature* 372:432–438
- Panick G, Malessa R, Winter R, Rapp G, Frye KJ, Royer CA (1998) Structural characterization of the pressure-denatured state and unfolding/refolding kinetics of staphylococcal nuclease by synchrotron small angle X-ray scattering and Fourier transform infrared spectroscopy. *J Mol Biol* 275:389–402
- Panick G, Malessa R, Winter R (1999a) Differences between the pressure- and temperature-induced denaturation and aggregation of  $\beta$ -lactoglobulin A, B, and AB monitored by FTIR spectroscopy and small angle X-ray scattering. *Biochemistry* 38:6512–6519
- Panick G, Vidugiris GJ, Malessa R, Rapp G, Winter R, Royer CA (1999b) Exploring the temperature-pressure phase diagram of staphylococcal nuclease. *Biochemistry* 38:4157–4164
- Park SJ, Taton TA, Mirkin CA (2002) Array-based electrical detection of DNA with nanoparticle probes. *Science* 295:1503–1506
- Pastore A, Saudek V, Ramponi G, Williams RJP (1992) Three-dimensional structure of acylphosphatase refinement and structure analysis. *J Mol Biol* 224:427–440
- Pereira RS (2001) Atomic force microscopy as a novel pharmacological tool. *Biochem Pharmacol* 62:975–983
- Perez J, Defrenne S, Witz J, Vachette P (2000) Detection and characterization of an intermediate conformation during the divalent ion-dependent swelling of tomato bushy stunt virus. *Cell Mol Biol* 46:937–948
- Perkins WD (1986) Fourier transform infrared spectroscopy. *J Chem Education* 63:A5–A10



- Perkins G, Renken C, Martone ME, Young SJ, Ellisman M, Frey TG (1997a) Electron tomography of neuronal mitochondria: three-dimensional structure and organization of cristae and neuronal contacts. *J Struct Biol* 119:260–272
- Perkins G, Renken CW, Song JY, Frey TG, Young SJ, Lamont S, Martone ME, Lindsey S, Ellisman MH (1997b) Electron tomography of large, multicomponent biological structures. *J Struct Biol* 120:219–227
- Perutz MF, Rossmann MG, Cullis AF, Muirhead G, Will G, North AT (1960) Structure of haemoglobin: a three-dimensional Fourier synthesis at 5.5 Å resolution, obtained by X-ray analysis. *Nature* 185:416–422
- Petsko GA, Ringe D (2000) Observation of unstable species in enzyme-catalyzed transformations using protein crystallography. *Curr Opin Chem Biol* 4:89–94
- Philippson A, Im W, Engel A, Schirmer T, Roux B, Müller DJ (2002) Imaging the electrostatic potential of transmembrane channels: atomic probe microscopy of OmpF porin. *Biophys J* 82:1667–1676
- Phillips J, Gormally J (1992) The laser desorption of organic molecules in ion mobility spectrometry. *Int J Mass Spectrom Ion Processes* 112:205–214
- Phillips GN Jr, Arduini RM, Springer BA, Sligar SG (1990) Crystal structure of myoglobin from a synthetic gene. *Proteins* 7:358–365
- Phizicky EM, Martzen MR, McCraith SM, Spinelli SL, Xing F, Shull NP, Van Slyke C, Montagne RK, Torres FM, Fields S, Grayhack EJ (2002) Biochemical genomics approach to map activities to genes. *Methods Enzymol* 350:546–559
- Pillutla RC, Goldstein NI, Blume AJ, Fisher PB (2002) Target validation and drug discovery using genomic and protein-protein interaction technologies. *Expert Opin Ther Targets* 6:517–531
- Plaxco KW, Simons KT, Baker D (1998) Contact order, transition state placement and the refolding rates of single-domain proteins. *J Mol Biol* 277:985–994
- Pohl DW, Denk W, Lanz M (1984) Optical stethoscopy: image recording with resolution  $\lambda/20$ . *Appl Phys Lett* 44:651–653
- Powell KD, Wales TE, Fitzgerald MC (2002) Thermodynamic stability measurements on multimeric proteins using a new H/D exchange- and matrix-assisted laser desorption/ionization (MALDI) mass spectrometry-based method. *Protein Sci* 11:841–851
- Pralle A, Florin EL (2002) Cellular membranes studied by photonic force microscopy. *Methods Cell Biol* 68:193–212
- Prechtel K, Bausch AR, Marchi-Artzner V, Kantlehner M, Kessler H, Merkel R (2002) Dynamic force spectroscopy to probe adhesion strength of living cells. *Phys Rev Lett* 89:028101-1–4
- Preston R (1998) The bioweaponers. *The New Yorker*, March 9:52–65
- Prokop A, Holland CA, Kozlov E, Moore B, Tanner RD (2001) Water-based nanoparticulate polymeric system for protein delivery. *Biotechnol Bioeng* 75:228–232
- Prusiner SB (ed) (1999) Prion Biology and Diseases. Cold Spring Harbor Monograph Series, No 38.
- Purves RW, Barnett DA, Ells B, Guevremont R (2000) Investigation of bovine ubiquitin conformers separated by high-field asymmetric waveform ion mobility spectrometry: cross section measurements using energy-loss experiments with a triple quadrupole mass spectrometer. *J Am Soc Mass Spectrom* 11:738–745
- Ranson NA, White HE, Saibil HR (1998) Chaperonins. *Biochem J* 333:233–242



- Sandhu KK, McIntosh CM, Simard JM, Smith S, Rotello VM (2002) Gold nanoparticle-mediated transfection of mammalian cells. *Bioconjug Chem* 13:3–6
- Sanger F (1988) Sequences, sequences, and sequences. *Annu Rev Biochem* 57:1–28
- Sanger F, Nicklen S, Coulson AR (1977) DNA sequencing with chain-terminating inhibitors. *Proc Natl Acad Sci USA* 74:5463–5467
- Sano Y, Inoue H, Hiragi Y (1999) Differences of reconstitution process between tobacco mosaic virus and cucumber green mottle mosaic virus by synchrotron small angle X-ray scattering using low-temperature quenching. *J Protein Chem* 18:801–805
- Sato M, Hida M, Nagase H (2001) Analysis of pyrolysis products of dimethylamphetamine. *J Anal Toxicol* 25:304–309
- Saurina J, Hernandez-Cassou S (1999) Flow-injection and stopped-flow completely continuous flow spectrometric determination of aniline and cyclohexylamine. *Anal Chim Acta* 396:151–159
- Scheuring S, Stahlberg H, Chami M, Houssin C, Rigaud JL, Engel A (2002) Charting and unzipping the surface layer of *Corynebacterium glutamicum* with the atomic force microscope. *Mol Microbiol* 44:675–684
- Schindelin H, Marahiel MA, Heinemann U (1993) Universal nucleic acid-binding domain revealed by crystal structure of the *B. subtilis* major cold-shock protein. *Nature* 364:164–168
- Schlichting I, Berendzen J, Chu K, Stock AM, Maves SA, Benson DE, Sweet RM, Ringe D, Petsko GA, Sligar SG (2000) The catalytic pathway of cytochrome P450<sub>cam</sub> at atomic resolution. *Science* 287:1615–1622
- Schmid MB (2002) Structural proteomics: the potential of high-throughput structure determination. *Trends Microbiol.* 10(Suppl):S27–31
- Schmitke JL, Stern LJ, Klivanov AM (1997) The crystal structure of subtilisin Carlsberg in anhydrous dioxane and its comparison with those in water and acetonitrile. *Proc Natl Acad Sci USA* 94:4250–4255
- Schmitke JL, Stern LJ, Klivanov AM (1998) Comparison of X-ray crystal structures of an acyl-enzyme intermediate of subtilisin Carlsberg formed in anhydrous acetonitrile and in water. *Proc Natl Acad Sci USA* 95:12918–12923
- Schnurpfeil R, Klepel S (2000) Radioactivity ion sources for miniaturized ion mobility spectrometers. US Patent 6,064,070
- Schönbrunn E, Svergun DI, Amrhein N, Koch MH (1998) Studies on the conformational changes in the bacterial cell wall biosynthetic enzyme UDP-N-acetylglucosamine enolpyruvyltransferase (MurA). *Eur J Biochem* 15:406–412
- Schröder W, Matz G, Kubler J (1998) Fast detection of preservatives on waste wood with GC/MS, GC-ECD and ion-mobility spectrometry. *Field Anal Chem Technol* 2:287–297
- Schurmann G, Noell W, Stauffer U, de Rooij NF (2000) Microfabrication of a combined AFM-SNOM sensor. *Ultramicroscopy* 82:33–38
- Schwartz DE, Mancinelli RL, White MR (1995) Search for life on Mars: evaluation of techniques. *Adv Space Res* 15:193–197
- Schweitzer-Stenner R (2002) Dihedral angles of tripeptides in solution directly determined by polarized Raman and FTIR spectroscopy. *Biophys J* 83:523–532
- Schwesinger F, Ros R, Strunz T, Anselmetti D, Güntherodt HJ, Honegger A, Jermutus L, Tiefenauer L, Plückthun A (2000) Unbinding forces of single antibody-antigen complexes correlate with their thermal dissociation rates. *Proc Natl Acad Sci USA* 97:9972–9977

- Scott DJ, Grossmann JG, Tame JR, Byron O, Wilson KS, Otto BR (2002) Low resolution solution structure of the Apo form of *Escherichia coli* haemoglobin protease Hbp. *J Mol Biol* 315:1179–1187
- Seeman NC, Belcher AM (2002) Emulating biology: building nanostructures from the bottom up. *Proc Natl Acad Sci USA* 99:6451–6455
- Segel DJ, Eliezer D, Uversky V, Fink AL, Hodgson KO, Doniach S (1999) Transient dimer in the refolding kinetics of cytochrome c characterized by small angle X-ray scattering. *Biochemistry* 38:15352–15359
- Sekatskii SK, Dietler G (1999) Near-field optical excitation as a dipole-dipole energy transfer process. *J Microsc* 194:255–259
- Seong GH, Kobatake E, Miura K, Nakazawa A, Aizawa M (2002) Direct atomic force microscopy visualization of integration host factor-induced DNA bending structure of the promoter regulatory region on the *Pseudomonas* TOL plasmid. *Biochem Biophys Res Commun* 291:361–366
- Service RF (2001) Breakthrough of the year. Molecules get wired. *Science* 294:2442–2443
- Service RF (2002) Analytical chemistry – new test could speed bioweapon detection. *Science* 295:1447–1447
- Shakhnovich EI (1997) Theoretical studies of protein-folding thermodynamics and kinetics. *Curr Opin Struct Biol* 7:29–40
- Shakhnovich E, Abkevich V, Ptitsyn O (1996) Conserved residues and the mechanism of protein folding. *Nature* 379:96–98
- Shevchenko A, Chernushevich I, Shevchenko A, Wilm M, Mann M (2002) “De novo” sequencing of peptides recovered from in-gel digested proteins by nano-electrospray tandem mass spectrometry. *Mol Biotechnol* 20:107–118
- Shilton B, Svergun DI, Volkov VV, Koch MH, Cusack S, Economou A (1998) *Escherichia coli* SecA shape and dimensions. *FEBS Lett* 436:277–282
- Shimonishi Y, Hong YM, Kitagishi T, Matsuo T, Matsuda H, Katakuse I (1980) Sequencing of peptide mixtures by Edman degradation and field-desorption mass spectrometry. *Eur J Biochem* 112:251–264
- Shumate CB, Hill HH (1989) Coronaspray nebulization and ionization of liquid samples for ion mobility spectrometry. *Anal Chem* 61:601–606
- Simpson AA, Tao YZ, Leiman PG, Badasso MO, He Y, Jardine PJ, Olson NH, Morais MC, Grimes S, Anderson DL, Baker TS, Rossmann MG (2000) Structure of the bacteriophage  $\Phi$ 29 DNA packaging motor. *Nature* 408:745–750
- Sisson PR, Freeman R, Magee JG, Lightfoot NF (1991) Differentiation between mycobacteria of the *Mycobacterium tuberculosis* complex by pyrolysis mass spectrometry. *Tubercle* 72:206–209
- Smith DE, Tans SJ, Smith SB, Grimes S, Anderson DL, Bustamante C (2001) The bacteriophage straight  $\Phi$ 29 portal motor can package DNA against a large internal force. *Nature* 413:748–752
- Smith SB, Cui Y, Bustamante C (1996) Overstretching B-DNA: the elastic response of individual double-stranded and single-stranded DNA molecules. *Science* 271:795–799
- Smith GB, Eiceman GA, Walsh MK, Critz SA, Andazola E, Ortega E, Cadena F (1997) Detection of *Salmonella typhimurium* by hand-held ion mobility spectrometer: a quantitative assessment of response characteristics. *Field Anal Chem Technol* 1:213–226

- Snabe T, Petersen SB (2002) Application of infrared spectroscopy (attenuated total reflection) for monitoring enzymatic activity on substrate films. *J Biotechnol* 95:145–155
- Snow CD, Nguyen H, Pande VS, Gruebele M (2002) Absolute comparison of simulated and experimental protein-folding dynamics. *Nature* 420:102–106
- Snyder AP, McClennen WH, Dworzanski JP, Meuzelaar HL (1990) Characterization of underivatized lipid biomarkers from microorganisms with pyrolysis short-column gas chromatography / ion trap mass spectrometry. *Anal Chem* 62:2565–2573
- Snyder AP, Miller M, Shoff DB, Eiceman GA, Blyth DA, Parsons JA (1991a) Enzyme-substrate assay for the qualitative detection of microorganisms by ion mobility spectrometry. *J Microbiol Methods* 14:21–32
- Snyder AP, Shoff DB, Eiceman GA, Blyth DA, Parsons JA (1991b) Detection of bacteria by ion mobility spectrometry. *Anal Chem* 63:526–529
- Snyder AP, Harden CS, Brittain AH, Kim MG, Arnold NS, Meuzelaar HLC (1993) Portable hand-held gas chromatography / ion mobility spectrometry device. *Anal Chem* 65:299–306
- Snyder AP, Blyth DA, Parsons JA (1996a) Ion mobility spectrometry as an immunoassay detection technique. *J Microbiol Methods* 27:81–88
- Snyder AP, Thornton SN, Dworzanski JP, Meuzelaar HLC (1996b) Detection of picolinic acid biomarker in *Bacillus* spores using a potentially field-portable pyrolysis gas chromatography / ion mobility spectrometer. *Field Anal Chem Technol* 1:49–59
- Snyder AP, Maswadeh WM, Parson JP, Tripathi A, Meuzelaar HLC, Dworzanski J, Kim MG (1999) Field detection of *Bacillus* spore aerosols with stand-alone pyrolysis gas chromatography / ion mobility spectrometry. *Field Anal Chem Technol* 3:315–326
- Snyder AP, Maswadeh WM, Tripathi A, Dworzanski JP (2000) Detection of gram-negative *Erwinia herbicola* outdoor aerosols with pyrolysis gas chromatography / ion mobility spectrometry. *Field Anal Chem Technol* 4:111–126
- Snyder AP, Tripathi A, Maswadeh WM, Ho J, Spence M (2001) Field detection and identification of a bioaerosol suite by pyrolysis / gas chromatography / ion mobility spectrometry. *Field Anal Chem Technol* 5:190–204
- Spangler GE (1982) Membrane interface for ion mobility detector cells. US Patent 4,311,669
- Spangler GE (1992a) Preconcentrator for ion mobility spectrometer. US Patent 5,083,019
- Spangler GE (1992b) Space charge effects in ion mobility spectrometry. *Anal Chem* 64:1312–1312
- Spangler GE, Carrico JP (1983) Membrane inlet for ion mobility spectrometry (plasma chromatography). *Int J Mass Spectrom Ion Phys* 52:267–287
- Spangler GE, Roehl JE, Patel GB, Dorman A (1994) Photoionization ion mobility spectrometer. US Patent 5,338,931
- Srajer V, Teng TY, Ursby T, Pradervand C, Ren Z, Adachi SI, Schildkamp W, Bourgeois D, Wulff M, Moffat K (1996) Photolysis of the carbon monoxide complex of myoglobin: nanosecond time-resolved crystallography. *Science* 274:1726–1729
- Stachelberger H (2001) personal communication.
- Stagljar I, Fields S (2002) Analysis of membrane protein interactions using yeast-based technologies. *Trends Biochem Sci* 27:559–63
- Steinfeldt JI, Wormhoudt J (1998) Explosives detection: a challenge for physical chemistry. *Annu Rev Phys Chem* 49:203–232

- Stephenson JL, McLuckey SA, Reid GE, Wells JM, Bundy JL (2002) Ion/ion chemistry as a top-down approach for protein analysis. *Curr Opin Biotechnol* 13:57–64
- St Louis RH, Hill HH (1990) Ion mobility spectrometry in analytical chemistry. *CRC Crit Rev Anal Chem* 21:321–355
- Stöckle RM, Fokas C, Deckert V, Zenobi R, Sick B, Hecht B, Wild UP (1999a) High quality near-field optical probes by tube etching. *Appl Phys Lett* 75:160–162
- Stöckle RM, Schaller N, Deckert V, Fokas C, Zenobi R (1999b) Brighter near-field optical probes by means of improving the optical destruction threshold. *J Microsc* 194:378–382
- Stoeva S, Idakieva K, Betzel C, Genov N, Voelter W (2002) Amino acid sequence and glycosylation of functional unit RtH2-e from *Rapana thomasiana* (gastropod) hemocyanin. *Arch Biochem Biophys* 399:149–158
- Stone E, Gillig KJ, Ruotolo B, Fuhrer K, Gonin M, Schultz A, Russell DH (2001) Surface-induced dissociation on a MALDI ion mobility / orthogonal time-of-flight mass spectrometer: sequencing peptides from an “in-solution” protein digest. *Anal Chem* 73:2233–2238
- Strachan NJC, Nicholson FJ, Ogden ID (1995) An automated sampling system using ion mobility spectrometry for the rapid detection of bacteria. *Anal Chim Acta* 313:63–67
- Strunz T, Oroszlan K, Schäfer R, Güntherodt HJ (1999) Dynamic force spectroscopy of single DNA molecules. *Proc Natl Acad Sci USA* 96:11277–11282
- Sultana S, Magee JT, Duerden B (1995) Analysis of *Bacteroides* species by pyrolysis mass spectrometry. *Clin Infect Dis* 20 Suppl 2:S122–S127
- Swedberg SA, Kaltenbach P, Witt KE, Bek F, Mittelstadt LS (1996) Fully integrated miniaturized planar liquid sample handling and analysis device. US Patent 5,571,410
- Swedberg SA, Brennen RA (2001) Device for high throughput sample processing, analysis and collection, and methods of use thereof. US Patent 6,240,790
- Synge EH (1928) A suggested method for extending microscopic resolution into the ultra-microscopic region. *Phil Mag* 6:356–362
- Talapatra A, Rouse R, Hardiman G (2002) Protein microarrays: challenges and promises. *Pharmacogenomics* 3:527–536
- Tanaka S, Scheraga HA (1975) Model of protein folding: Inclusion of short-, medium-, and long-range interactions. *Proc Natl Acad Sci USA* 72:3802–3806
- Tanaka S, Scheraga HA (1977) Hypothesis about the mechanism of protein folding. *Macromolecules* 10:291–304
- Taylor J, Goodacre R, Wade WG, Rowland JJ, Kell DB (1998) The deconvolution of pyrolysis mass spectra using genetic programming: application to the identification of some *Eubacterium* species. *FEMS Microbiol Lett* 160:237–246
- Taylor SJ (1996) Introduction of samples into an ion mobility spectrometer. US Patent 5,574,277
- Taylor SJ, Turner RB (1999) Ion mobility spectrometers. US Patent 5,952,652
- Tcherkasskaya O, Uversky VN (2001) Denatured collapsed states in protein folding: example of apomyoglobin. *Proteins* 44:244–254
- Tilleman K, Van den Haute C, Geerts H, van Leuven F, Esmans EL, Moens L (2002) Proteomics analysis of the neurodegeneration in the brain of tau transgenic mice. *Proteomics* 2:656–665
- Timmins EM, Goodacre R (1997) Rapid quantitative analysis of binary mixtures of *Escherichia coli* strains using pyrolysis mass spectrometry with multivariate calibration and artificial neural networks. *J Appl Microbiol* 83:208–218

- Tiner WJS, Potaman VN, Sinden RR, Lyubchenko YL (2001) The structure of intramolecular triplex DNA: atomic force microscopy study. *J Mol Biol* 314:353–357
- Toledo-Crow R, Yang PC, Chen Y, Vaez-Iravani M (1992) Near-field differential scanning optical microscope with atomic force regulation. *Appl Phys Lett* 60:2957–2959
- Torres J, Briggs JA, Arkin IT (2002) Multiple site-specific infrared dichroism of CD3-zeta, a transmembrane helix bundle. *J Mol Biol* 316:365–374
- Tripathi A, Maswadeh WM, Snyder AP (2001) Optimization of quartz tube pyrolysis atmospheric pressure ionization mass spectrometry for the generation of bacterial biomarkers. *Rapid Commun Mass Spectrom* 15:1672–1680
- Trudel E, Gallant J, Mons S, Mioskowski C, Lebeau L, Jeuris K, Foubert P, De Schryver F, Salesse C (2001) Design of functionalized lipids and evidence for their binding to photosystem II core complex by oxygen evolution measurements, atomic force microscopy, and scanning near-field optical microscopy. *Biophys J* 81:563–571
- Turner DR (1983) Etch procedure for optical fibers. US Patent 4,469,554
- Turner BR (1993) Ion mobility detector. US Patent 5,227,628
- Unger R, Moulton J (1996) Local interactions dominate folding in a simple protein model. *J Mol Biol* 259:988–994
- Valle F, Dietler G, Londei P (2001) Single-molecule imaging by atomic force microscopy of the native chaperonin complex of the thermophilic archaeon *Sulfolobus solfataricus*. *Biochem. Biophys Res Commun* 288:258–262
- van den Berg B, Wain R, Dobson CM, Ellis RJ (2000) Macromolecular crowding perturbs protein refolding kinetics: implications for folding inside the cell. *EMBO J* 19:3870–3875
- van Duyn GD, Standaert RF, Karplus PA, Schreiber SL, Clardy J (1991) Atomic structure of FKBP-FK506, an immunophilin-immunosuppressant complex. *Science* 252:839–842
- van Kempen TA, Powers WJ, Sutton AL (2002) Technical note: Fourier transform infrared (FTIR) spectroscopy as an optical nose for predicting odor sensation. *J Anim Sci* 80:1524–1527
- van Nuland NAJ, Hangyi IW, van Schaik RC, Berendsen HJC, van Gunsteren WF, Scheek RM, Robillard GT (1994) The high-resolution structure of the histidine-containing phosphocarrier protein HPr from *Escherichia coli* determined by restrained molecular dynamics from nuclear magnetic resonance nuclear Overhauser effect data. *J Mol Biol* 237:544–559
- Veerman JA, Otter AM, Kuipers L, van Hulst NF (1998) High definition aperture probes for near-field optical microscopy fabricated by focused ion beam milling. *Appl Phys Lett* 72:3115–3117
- Vendrell J, Billeter M, Wider G, Aviles FX, Wüthrich K (1991) The NMR structure of the activation domain isolated from porcine procarboxypeptidase B. *EMBO J* 10:11–15
- Vijay-Kumar S, Bugg CE, Cook WJ (1987) Structure of ubiquitin refined at 1.8 Å resolution. *J Mol Biol* 194:531–544
- Voigt J, Schrötter T (1999) Phonon assisted exciton transitions on LHC-II complexes – a long wavelength absorption mechanism by cooperative action of photons and protein vibrations. *Zeitschrift Phys Chem* 211:181–191
- Volz K, Matsumura P (1991) Crystal structure of *Escherichia coli* CheY refined at 1.7 Å resolution. *J Biol Chem* 266:15511–15519
- von Ardenne M (1940) *Elektronen-Übermikroskopie*, Springer, Berlin

- Vora KN, Carrico JP Sr, Spangler GE, Campbell DN, Martin CE (1987) Ion mobility spectrometer. US Patent 4,712,008
- Vytvytska O, Nagy E, Bluggel M, Meyer HE, Kurzbauer R, Huber LA, Klade CS (2002) Identification of vaccine candidate antigens of *Staphylococcus aureus* by serological proteome analysis. *Proteomics* 2:580–590
- White HE, Chen S, Roseman AM, Yifrach O, Horovitz A, Saibil H (1997) Structural basis of allosteric changes in the GroEL mutant Arg197→Ala. *Nature Struct Biol* 4:690–694
- Whitelegge JP, le Coutre J (2002) Proteomics. Making sense of genomic information for drug discovery. *Am J Pharmacogenomics* 1:29–35
- Wikström M, Sjöbring U, Drakenberg T, Forsén S, Björck L (1995) Mapping of the immunoglobulin light chain-binding site of protein L. *J Mol Biol* 250:128–133
- Williams S, Causgrove TP, Gilmanshin R, Fang KS, Callender RH, Woodruff WH, Dyer RB (1996) Fast events in protein folding: helix melting and formation in a small peptide. *Biochemistry* 35:691–697
- Williams JC, Zeelen JP, Neubauer G, Vriend G, Backmann J, Michels PA, Lambeir AM, Wierenga RK (1999) Structural and mutagenesis studies of leishmania triosephosphate isomerase: a point mutation can convert a mesophilic enzyme into a superstable enzyme without losing catalytic power. *Protein Eng* 12:243–250
- Williams BH, Hathout Y, Fenselau C (2002) Structural characterization of lipopeptide biomarkers isolated from *Bacillus globigii*. *J Mass Spectrom* 37:259–264
- Williamson RL, Miles MJ (1996) Melt-drawn scanning near-field optical microscopy probe profiles. *J Appl Phys* 80:4804–4812
- Williamson RL, Brereton LJ, Antognozzi M, Miles MJ (1998) Are artefacts in scanning near-field optical microscopy related to the misuse of shear force? *Ultramicroscopy* 71:165–175
- Wilmot CM, Pearson AR (2002) Cryocrystallography of metalloprotein reaction intermediates. *Curr Opin Chem Biol* 6:202–207
- Wolynes PG, Luthey-Schulten Z, Onuchic JN (1996) Fast folding experiments and the topography of protein-folding energy landscapes. *Chem Biol* 3:425–432
- Wu C, Hill HH, Gamerdinger AP (1998a) Electrospray ionization / ion mobility spectrometry as a field monitoring method for the detection of atrazine in natural water. *Field Anal Chem Technol* 2:155–161
- Wu C, Siems WF, Asbury GR, Hill HH (1998b) Electrospray ionization high-resolution ion mobility spectrometry / mass spectrometry. *Anal Chem* 70:4929–4938
- Wu C, Siems WF, Klasmeier J, Hill HH (2000) Separation of isomeric peptides using electrospray ionization/high-resolution ion mobility spectrometry. *Anal Chem* 72:391–395
- Wuite GJL, Smith SB, Young M, Keller D, Bustamante C (2000) Single-molecule studies of the effect of template tension on T7 DNA polymerase activity. *Nature* 404:103–106
- Wynne SA, Crowther RA, Leslie AGW (1999) The crystal structure of the human hepatitis B virus capsid. *Mol Cell* 3:771–780
- Xu L, Frederik P, Pirollo KF, Tang WH, Rait A, Xiang LM, Huang W, Cruz I, Yin Y, Chang EH (2002) Self-assembly of a virus-mimicking nanostructure system for efficient tumor-targeted gene delivery. *Hum Gene Ther* 13:469–481
- Yamasaki R, Hoshino M, Wazawa T, Ishii Y, Yanagida T, Kawata Y, Higurashi T, Sakai K, Nagai J, Goto Y (1999) Single molecular observations of the interaction of GroEL with substrate proteins. *J Mol Biol* 292:965–972



- Yarmush ML, Jayaraman A (2002) Advances in proteomic technologies. *Annu Rev Biomed Eng* 4:349–373
- Ying LM, Bruckbauer A, Rothery AM, Korchev YE, Klenerman D (2002) Programmable delivery of DNA through a nanopipet. *Anal Chem* 74:1380–1385
- Yip CM (2001) Atomic force microscopy of macromolecular interactions. *Curr Opin Struct Biol* 11:567–572
- Zal F, Chausson F, Leize E, van Dorsselaer A, Lallier FH, Green BN (2002) Quadrupole time-of-flight mass spectrometry of the native hemocyanin of the deep-sea crab *Bythograea thermydron*. *Biomacromolecules* 3:229–231
- Zhang J, Oettmeier W, Gennis RB, Hellwig P (2002a) FTIR spectroscopic evidence for the involvement of an acidic residue in quinone binding in cytochrome bd from *Escherichia coli*. *Biochemistry* 41:4612–4617
- Zhang ZL, Pang DW, Zhang RY, Yan JW, Mao BW, Qi YP (2002b) Investigation of DNA orientation on gold by EC-STM. *Bioconjug Chem* 13:104–109
- Zheng W, Doniach S (2002) Protein structure prediction constrained by solution X-ray scattering data and structural homology identification. *J Mol Biol* 316:173–187
- Zheng PP, Kros JM, Sillevius-Smitt PA, Theo M, Luider Fm FM (2003) Proteomics in primary brain tumors. *Front Biosci* 8:D451–463
- Zhou Y, Karplus M (1999) Interpreting the folding kinetics of helical proteins. *Nature* 401:400–403
- Zhou H, Midha A, Mills G, Thoms S, Murad SK, Weaver JMR (1998) Generic scanned-probe microscope sensors by combined micromachining and electron-beam lithography. *J Vacuum Sci Technol B* 16:54–58
- Zhou H, Mills G, Chong BK, Midha A, Donaldson L, Weaver JMR (1999) Recent progress in the functionalization of atomic force microscope probes using electron-beam nanolithography. *J Vacuum Sci Technol A* 17:2233–2239
- Zocchi G (2001) Force measurements on single molecular contacts through evanescent wave microscopy. *Biophys J* 81:2946–2953

# Index

- Abbe's limit of diffraction IX, 135
- Aberration
  - chromatic 41, 114, 115
  - spherical 113, 114
- Acyl carrier protein 5, 6
- Acyl-coenzyme A binding protein 5, 6
- ADC (analog-to-digital converter) 176, 181, 188, 192
- Affinity chromatography 31–33
- AFM – *see* atomic force microscope
- Alanine 3, 4, 19
- Alzheimer's disease 131
- Amine 26
- $\alpha$ -Amylase inhibitor 7
- Analog-to-digital converter (ADC) 176, 181, 188, 192
- Analysis of  $\Phi$ -values 9–12, 197–202
- Anion exchanger 23, 25, 26
- Antibodies 32, 152, 161
- Antigen 32, 152, 165
- Aperture
  - grid 176, 178, 179–183
  - subwavelength 138–142
- apo*-Calmodulin 149
- Arc repressor 11, 199
- Arginine 3, 4
- Artifacts in atomic force microscopy 125
- Asparagine 3, 4, 16
- Aspartic acid 3, 4
- Atomic force microscope 121–132, 142, 143, 145, 147–150, 152, 154, 155, 158, 159
- ATP (adenosine triphosphate) 135
- Attenuated total reflection (ATR) 100, 101
  
- Bacillus subtilis* 7
- Bacterial membrane 88, 147, 149, 154, 159
- Bacterioferritin 5
  
- Bacteriophage
  - $\Phi$ 29 117
  - $\Phi$ KZ and T4 131
  - crystal 158
- Bacteriorhodopsin 104, 147, 149
- Barnase 11, 12, 48, 199, 200
- Barstar 11, 48, 56, 199
- BESSY (Berlin Electron Synchrotron Storage Ring) 75
- Bioagents detection 49–54, 96, 97, 153, 177, 178, 186, 188, 189, 193–195
- Bioelectronic structures 156
- Biological agents detection 49–54, 96, 97, 153, 177, 178, 186, 188, 189, 193–195
- Biomarkers 166
- Biophysical nanotechnology X, 147–163
- Botulinum toxin 182
- Bovine serum albumin (BSA) 131, 132
- Bovine spongiform encephalopathy (BSE) 3
- Breakaway forces between different biomolecules 152
- Bright field detection 119
- Brookhaven National Laboratory Protein Data Bank 2, 5, 7, 8, 14, 18, 19
- BSA (bovine serum albumin) 131, 132
- BSE (bovine spongiform encephalopathy) 3
  
- C++ 207
- Cantilever 121–135, 143–145, 152, 154
- Capacity of ion exchanger 26
- Carbon
  - fiber AFM tip 127
  - monoxide 84
  - nanotube 156, 157, 211
- Carboxylic acid 26
- Cardiac cells 131

- Cation exchanger 23, 25, 26  
CBMS (chemical-biological mass spectrometer) 49  
CCD (charge coupled device)  
  area detectors 71–74  
  camera 107  
CD (circular dichroism) 91  
cDNA 167  
Cell  
  adhesion 130, 131, 147, 150  
  lysis 170  
Chain topology parameter (*CTP*) 13–16,  
  19, 20  
Chaperone 20, 33, 131  
Chaperonin – *see* chaperone  
Charge interaction 5, 19, 23–28, 41–44,  
  48, 131, 175  
Chemical  
  -biological mass spectrometer (CBMS)  
    49  
  ionization 44  
  linkers 2, 152, 155, 168  
  proteomics 172  
CheY 8  
Chromatic aberration 41, 114, 115  
Chromatography  
  affinity 31–33  
  gel filtration 28–31, 171  
  gel permeation – *see* gel filtration  
  ion exchange 23–28  
  of a crude cell extract 47  
  plasma 185  
  resolution 27, 28  
  size exclusion 28–31, 171  
  two-dimensional 169, 170  
Chymotrypsin inhibitor 2 (CI2) 10, 11,  
  199, 200, 207  
Circular dichroism (CD) 91  
CJD (Creutzfeldt-Jacob disease) 3  
CNS disorders 3, 131, 165  
CO (carbon monoxide) 84  
Cold shock protein 7  
Collagen fibrils 86, 88  
Collector for  
  IMS 176, 178–182, 189  
  MS 38, 40–42  
  protein fractions 26, 28  
Collision chamber 45  
Compound lens 113, 114  
Concentrating protein solutions 34, 35  
Contact  
  angle measurement 156  
  mode 128, 129  
  order 13, 15  
Continuous-flow method 162  
Convolution 66, 67  
Convolution theorem 67  
Coulomb repulsion 123, 181  
Craig counter-current distribution  
  apparatus 33, 34  
Creutzfeldt-Jacob disease (CJD) 3  
Cryocrystallography 84, 85  
Crystallization robot 70  
Crystallography 59–85  
Crystal production 69–71, 158, 159  
Crystals suitable for crystallography 69,  
  158, 159  
*CTP* (chain topology parameter) 13–16,  
  19, 20  
Curie point pyrolyzer 49, 51, 193, 195  
Cysteine 3, 135, 148  
Cytochrome  
  b<sub>1</sub> 5, 6  
  c 135  
  P450 135  
2D-chromatography 169, 170  
2D-electrophoresis 166, 169, 170  
Dark field image 119, 120  
DEAE (diethyl-amino-ethyl) 23, 25, 26  
de Broglie relation 109  
Dentin 88  
Detection of  
  animal activity in jungles 187  
  camouflaged organic material 89  
  changes in forest structure 97  
  chemical activity of proteins 172  
  chemicals in solid samples 190  
  crystal growth mechanism 158, 159  
  drug-protein interactions 154,  
    165–167, 170, 171  
  environmental pollutants 97, 187  
  illicit drugs 187  
  intermolecular interactions 152–154,  
    168–171  
  mass-to-charge ratio 37–57

- membrane pores 144, 154
- non-proteinaceous interaction partners 165
- organic compounds 175–195
- pesticides 187
- protein-protein interactions 165, 168–171
- size-to-charge ratio 175
- surface composition 133
- tumor marker 165
- ultra-trace chemical and biological agents 49–54, 153, 175–195
- Detectors for
  - electrons 44–46
  - ions 37–46, 178, 180–183
  - IR radiation 96, 105
  - X-rays 72–74, 85, 87, 88
- Deuterated triglycine sulfate (DTGS) pyroelectric detectors 96
- Dichroism
  - circular (CD) 91
  - linear (LD) 102
- Diethyl-amino-ethyl (DEAE) 23, 25, 26
- Differentiation between different species of bacteria and viruses 52, 53
- Diffraction 64–79, 83, 84, 86, 103
- Diffraction pattern 64–67, 69, 71–73, 76, 77, 86, 208–210
- Discovery of new gene functions 172
- Diseases IX, 1, 3, 17, 50, 88, 131, 165–167
- Dispersion of electron energy 115
- Dissecting bacterial surface layers 159
- Distribution of conductivity within a biomolecule 134
- DNA 14, 16, 18, 23, 50, 55, 103, 130, 131, 135, 150, 151, 153, 154, 160–162, 166, 167, 169, 173, 174
  - microarray 165, 167, 173, 174
  - sensor 153, 154
  - sequencing 50, 55
- Doppler-shift 151
- Drift
  - channel of an IMS 175–182, 185, 186, 189
  - tube 175, 176, 178–180
  - velocity 194
- Drug-protein interactions 154, 165–167, 170, 171
- Dynamic force mode 128, 129
- Efficiency of folding 17
- Elastic dark field image 119
- Elastically scattered electrons 115–117, 119
- Elastic modulus 131
- Electron
  - bombardment 44, 51
  - density 68, 83–85
  - elastically scattered 115–117, 119
  - flashes, ultrashort 117
  - inelastically scattered 108, 115–117, 119, 120
  - microscopy (EM) IX, 107–120
  - multiplier 44–46
  - nanolithography 141
  - tomography 117
  - transport 135
- Electrophoresis 55, 166, 169, 170, 185
  - two-dimensional 166, 169, 170
- Electrospray
  - deposition 161
  - ionization 44, 46, 185
- Electrostatic energy analyzer 38, 45, 46, 115, 116, 120
- Electrostatic lens 44, 111–114, 119, 190
- EM (electron microscope and microscopy) IX, 107–120
- Energy filter for
  - electrons 115, 116, 119, 120
  - ions (sector filter) 38, 39, 45, 46
- Engineered tags 31, 71, 135
- Environmental monitoring 97, 187
- Escherichia coli* 2, 5
- Etched tungsten tip for STM 134
- Etching a SNOM probe 138–140
- Evolution of computer programs VII, 203–211
- Explosives detection 89, 183, 187
- False alarm rate 183, 184
- Faraday plate 178, 180–183
- Fast performance liquid chromatography (FPLC), 26, 28, 46, 48

- Feedback loop  
  STM 133  
  SNOM 136
- Fibronectin 7
- Field-effect transistor 163
- $\Omega$ -Filter 116
- Flavodoxin 2
- Folding  
  chaperonin – *see* chaperone  
  high resolution 9–20, 197–202  
  mechanism 4, 10, 12, 16, 19, 132, 149,  
    199, 206, 207  
  rate constant 12–20  
  -related diseases 3  
  transition state X, 9–20, 84, 103, 104,  
    197–202  
  -unfolding forces within single  
    protein molecules 132, 147–149
- Force  
  -extension curve 149  
  measurements in single DNA molecules  
    150, 151  
  measurements in single protein  
    molecules 132, 147–149
- Forest structure and terrain survey 97
- Fourier transform  
  infrared (FTIR) spectroscopy 91–96,  
    103–105  
  inverse 59  
  mass spectrometer (FTMS) 37, 43, 44  
  mathematical method 59–68, 79–83
- Fourier transformation  
  – *see* Fourier transform
- FPLC (fast performance liquid  
  chromatography) 26, 28, 46, 48
- FPLC/MS connector 48
- Fragmentation of pyrolysates 51, 53
- Friction force microscope 143
- FTIR (Fourier transform infrared)  
  sample cell 96  
  isotope-edited 102–104  
  spectroscopy 91–96, 103–105
- FTMS (Fourier transform mass  
  spectrometer) 37, 43, 44
- Fumarate reductase 5, 6
- Gas chromatography (GC) 46, 47, 184,  
  192, 193
- GC/IMS (gas chromatography ion mobility  
  spectrometry) 184, 193
- GC/MS (gas chromatography mass  
  spectrometry) 47
- Gel  
  chromatography – *see* gel filtration  
  chromatography  
  filtration chromatography 28–31, 171  
  permeation chromatography – *see* gel  
    filtration chromatography  
  polyacrylamide 55, 166
- Generation of  
  amplitude contrast in electron  
    microscopy 116  
  high voltage 191
- Gene therapy 162
- Genetically engineered virus 155
- Global positioning system (GPS) 96, 97
- Glutamic acid 3, 4
- Glutamine 3, 4
- Glycine XV, XVI, 3, 96
- Glycoprotein 147
- Gold nanoparticle 153
- GroEL 4, 118
- Guard rings 178, 179, 189–191
- Hall probe microscope 143
- Hanging drop method 70
- Heating effects in biological tissue 144
- Heavy atom  
  replacement 66, 76–83  
  salt 76
- $\alpha$ -Helix 1, 4, 15, 22, 56, 130, 149, 157
- Hemoglobin 5, 6
- High pressure  
  IR spectroscopy 103  
  liquid chromatography – *see* HPLC
- High resolution mass spectrometer 43, 45
- High resolution of protein folding  
  197–202
- High voltage generation 191
- Histidine 3, 8, 31, 32, 71, 135
- Histidine tags 31, 32, 71, 135
- holo*-Calmodulin 149
- HPLC (high pressure liquid  
  chromatography) 26, 46
- Hybridized DNA 153, 167
- Hydrofluoric acid 140

- Hydrogen lamp 185, 186
- Hydrophilic amino acid sidechains 4, 5, 19, 156
- Hydrophobic amino acid sidechains 1, 4, 5, 19, 22, 23, 157
- Immobilized
- DNA 135, 152, 153, 167
  - proteins 135, 152, 168, 170, 172
- Impactor 49, 50, 193, 195
- IMS (ion mobility spectrometer) 175–195
- inert gas 179
  - operating temperature 178
  - sample inlet 177
- Inelastically scattered electrons 108, 115–117, 119, 120
- Inelastic dark field image 119, 120
- Inertial measurement unit (IMU) 97
- Infrared
- beam splitter 96
  - detectors 96, 105
  - isotope-edited spectroscopy 102–104
  - LIDAR (light detection and ranging) 91, 96, 97
  - microscope 101, 102
  - sample cell 96
  - source 92
  - spectroscopy 91–105
- Ink-jet printing protein spots 168
- Insulin 30
- Integration host factor (IHF) 130
- Interaction proteomics 168–171
- Interferogram 93–95
- Interferometer 92, 93, 136, 137
- Intermolecular
- forces 150–152
  - individual interactions 152–154
  - interactions 152–154, 168–171
- Inter-residue contacts in protein molecules 9–17
- Ion
- bombardment 44
  - exchange chromatography 23–28
  - extractor 174
  - fragmentation 45, 51, 53, 54
  - guide 44, 48
  - mobility spectrometry 175–195
  - trap mass spectrometer 37, 39, 44, 53, 54
- Ionization
- chemical 44
  - electron bombardment 44, 51
  - electrospray 44, 46, 185
  - ion bombardment 44
  - MALDI 40, 44
- IR
- beam splitter 96
  - detectors 96, 105
  - LIDAR (light detection and ranging) 91, 96, 97
  - microscope 101, 102
  - sample cell 96
  - spectrometer 92, 93
- Isoleucine 3, 4
- Krypton lamp 185, 186
- Lab-on-a-chip technology 165, 173
- $\beta$ -Lactoglobulin 130
- Langmuier-Blodgett film 142
- Latex beads 143
- Lens
- electrostatic 44, 111–114, 119, 190
  - Fresnel 116
  - magnetic 109, 112–114, 116, 119
  - optical 65, 135
  - X-ray 77
- Leucine 3, 4
- LIDAR (light detection and ranging) 91, 96, 97
- Linear dichroism (LD) 102
- Liquid chromatography 23–34
- Loop,
- feedback 133, 136
  - in proteins 1, 207
- Lysine 3, 4
- Macromolecular crowding 17
- Magnetic
- lens 109, 112–114, 116, 119
  - sector mass spectrometer 37, 38, 46
- MALDI (matrix-assisted laser desorption ionization) 40, 44

- Manipulation of  
DNA 150, 151  
macromolecules 132, 147–157  
protein crystal growth 158, 159
- Mars mobile 57
- Mass spectrometry 37–57, 165, 166, 170, 171, 174  
Fourier transform 37, 43, 44  
high resolution 43, 45  
ion trap 37, 39, 44, 53, 54  
magnetic sector 37, 38, 46  
quadrupole filter 37, 39  
time-of-flight (TOF) 37, 40–42
- Matrix-assisted laser desorption ionization (MALDI) 40, 44
- MCT (mercury cadmium telluride)  
detectors 96
- Mechanism of protein folding 4, 10, 12, 16, 19, 132, 149, 199, 206, 207
- Melt-drawing a SNOM probe 139
- Membrane  
pore detection 144  
proteins 4, 5, 101, 130, 131, 147, 149, 154  
sample inlet 177
- Mercury cadmium telluride (MCT)  
detectors 96
- Methionine 3, 56
- Michelson interferometer 92, 93, 136, 137
- Microarray  
scanner 173  
technology 165–174
- Microchannels 173
- Microchips 165–174
- Microfluid technique 172, 173
- Microscope and microscopy  
atomic force (AFM) 121–132, 142, 143, 145, 147–150, 152, 154, 155, 158, 159  
bright field 119  
dark field 119, 120  
electron IX, 107–120  
infrared 101, 102  
neutron 116  
scanning ion conductance (SICM) 122, 144  
scanning probe (SPM) 121–145  
scanning thermal (SThM) 144  
scanning transmission electron (STEM) 118–120  
scanning tunneling (STM) 122, 126, 133–135  
X-ray 77
- Miller indices 67
- Misfolded protein 3, 4, 33, 71
- $m^n$  Mass spectrometry 54
- Molecular  
exclusion chromatography – *see*  
gel filtration chromatography  
redox relays 156  
sieve 179, 180, 184  
weight determination  
chromatographic 31  
mass-spectrometric 37–57  
X-ray spectrometric 89  
wires 155, 156, 157
- MOLSCRIPT 2, 4, 5, 7, 8, 18, 118
- Molten globule 21, 22
- Monochromatic  
electrons 115  
radiation 75, 92, 94, 102, 115
- mRNA 167
- Myoglobin 5, 6, 30, 105
- Nanobiosensor 154
- Nanobiotechnology 154, 156, 157, 159
- Nanocrystals 155, 158, 160
- Nanodissector 159
- Nanoelectrodes 160
- Nanofabrication 141, 142, 155, 156, 159–163
- Nanolithography 141, 155, 156
- Nanometer-sized light source 136–142
- Nanooptical devices 207
- Nanoparticles 162, 207–211, 213
- Nanopipette 144, 159, 160
- Nanotechnology IX, 136–142, 144, 147–163, 207–210
- Nanotransistors 163
- Nanotubes 156, 157
- Nanowires 157
- Near-field scanning optical microscope (NSOM) – *see* SNOM
- Negative  
ion mode 177  
stain 116, 117

- Neurodegeneration 165  
 Neuronal network method 53, 54  
 Neutron microscope 116  
 Neutron scattering 88  
 NMR (nuclear magnetic resonance) 4, 174  
 Nobel prize 109, 134  
 Noise reduction 59, 183, 190  
 Non-contact mode 129  
 Non-proteinaceous interaction partners 165  
 NSOM (near-field scanning optical microscope) – *see* SNOM  
 Nuclear magnetic resonance (NMR) 4, 174
- OCT (optical coherence tomography) 98, 99  
 Octopole ion guide 44  
 Open reading frame (ORF) 172  
 Optical  
   coherence tomography (OCT) 98, 99  
   far-field 141  
   near-field 141  
   pattern 208, 209  
   tweezers 151  
   waveguide 100, 101  
 Optics, limit of classical IX, 135, 136  
 Overcoming the classical limits of optics IX, 135–142
- p53, 199, 202  
 Particle analysis 49, 50, 193  
 Pattern, optical 208, 209  
 Peptide sequencing 50, 56, 57  
 Pesticide detection 187  
 Phase difference – *see* phases  
 Phases and phase differences  
   crystallographic 59–61, 64–66, 76–83  
   determination 66, 76–83  
   in optical coherence tomography 99  
   in the Fourier transform of a function 59–61, 64–66  
   of an electric field 189  
   of electrons in an EM 109, 115–117  
   of light in a SNOM shear force interferometer 137  
   of light in FTIR spectrometers 93, 94  
 Phenylalanine 3, 4, 157
- Phi-value analysis – *see*  $\Phi$ -value analysis  
 Phosphocarrier protein 8  
 Photoionization 185, 186  
 Photon  
   detection 73, 74  
   flux 186  
   shot noise 93  
 Photosystem 142  
 Physisorption of protein 168  
 Piezoelectric scanner 121–125, 133, 137, 138  
 Plasma  
   chromatography 185  
   discharge lamps 186  
 Plastocyanin 135  
 Pohlshuh lens 112, 113  
 Polyacrylamide gel electrophoresis 55, 166  
 Polychromatic interferogram 94, 95  
 Polychromator 99  
 Polymerase 32, 150, 151  
 Porin 130, 131  
 Positive ion mode 177  
 Post-translational changes 50  
 Preconcentrator 184  
 Prediction,  
   protein folding 19, 203, 206, 207  
   protein folding rate 19  
   protein structure 20, 88, 174, 203, 206, 207  
 Primary  
   amine 26  
   structure 1  
 Prion 3, 4  
 “Prion-only” hypothesis 3  
 Procarboxypeptidase B 8  
 Profilometer 122  
 Proline 3  
 Propagation of light in a SNOM tip 140  
 Protein  
   crystallography 59–85  
   crystal production 69–71  
   Data Bank 2, 5, 7, 8, 14, 18, 19  
   DNA-binding 169  
   -drug interactions 154, 165–167, 170, 171  
   engineering 155–158  
   folding mechanism 4, 10, 12, 16, 19, 132, 149, 199, 206, 207



- folding and structure simulations
  - 20–22, 206, 207
- folding transition states X, 9–20, 84,
  - 103, 104, 197–202
- G 14, 17, 18
- high level expression 27
- high throughput assays 166
- immobilization 135, 152, 168, 170, 172
- L 7
- microarrays 161, 165, 168, 170, 174
- nanoarrays 155, 156, 161
- physisorption 168
- polymer nanoparticles 162
- protein interactions 50, 152, 154, 165,
  - 168–171
- stability 3, 17, 21, 71
- subunits 1, 2, 5
- three-dimensional structure 1–22, 118
- X-ray crystallography IX, 59–85
- Proteomics
  - chemical 172
  - interaction 167–171
  - large scale 165–174
  - structural 174
  - target discovery 166, 167
- PTFE (polytetrafluoroethylene) 96, 177
- PyMS (pyrolysis mass spectrometry) 49,
  - 51–54
- Pyroelectric detectors 96, 105
- Pyrolysis 49, 51–53, 193, 195
- Pyrolyzer 49, 51, 193, 195
  
- Quadrupole
  - filter mass spectrometer – *see*
    - quadrupole mass spectrometer
  - ion trap mass spectrometer
    - *see* ion trap mass spectrometer
  - mass spectrometer 37, 39
- Quaternary
  - amine 26
  - structure 2, 86
  
- Radiation damage by
  - electrons 117, 118
  - X-rays 65, 71–73, 77
- Random coil 1, 22, 105
- Reconstitution of
  - misfolded protein 33
  - molecular sieves 179
- Recoverin 149
- Refinement 83
- Reflectron time-of-flight mass spectrometer 40–42
- Repeller plate for
  - IMS 177
  - MS 40, 42
- Resolution of
  - AFM 122, 128, 129, 131
  - chromatography 24, 47
  - classical optical microscope 135
  - electron microscope 109, 110, 117–119
  - FTIR and IR 91–93, 101, 102, 104
  - IMS 180–183, 186, 188, 189, 193
  - MS 37, 40, 41, 43, 47
  - near-field optical microscope IX, 135,
    - 136, 138, 142, 143
  - SAXS 88
  - SICM 144
  - STM 134
  - $\Phi$ -value analysis 9–12, 197–202
  - X-ray crystallography 76
  - X-ray microscope 65
- Reverse transcriptase 167
- RNA 8, 20, 167
- Rotating anode generator 71, 74
- Rotational evaporation 139
- Rupture force for molecular complexes 152, 154
  - subunits 147
  
- Sanger sequencing method 55
- SAXS (small angle X-ray scattering) 85–88
- Scanning
  - force microscope – *see* atomic force microscope (AFM)
  - friction force microscope 143
  - Hall probe microscope 143
  - infrared microscope 101, 102
  - ion conductance microscope (SICM) 122, 144
  - IR spectrometer 92
  - near-field optical microscope (SNOM) 122, 131, 135–143
  - probe microscopy (SPM) 121–145
  - thermal microscope (SThM) 144

- transmission electron microscope (STEM) 118–120  
 tunneling microscope (STM) 122, 126, 133–135  
 Scattering,  
   Abbe's (diffraction) limit IX, 135  
   electron 115, 117  
   infrared 99, 102  
   neutron 88  
   visible spectral region 109, 151, 208, 210  
   X-ray 64, 65, 76, 85, 88, 89  
 SDOCT (spectral domain optical coherence tomography) 99  
 Secondary structure 1, 4, 5, 7, 9–11, 15, 16, 22, 56, 91, 105  
 Self-evolving computer programs VII, 203–211  
 Self-learning programs VII, 207  
 Sequencing method  
   DNA 50, 55  
   peptides 50, 56, 57  
 Serine 3  
 SH3 domain 7, 9, 11, 199, 201  
 Shear force 136, 137  
 $\beta$ -Sheets 1, 4, 7–9, 15, 16, 22, 105, 126  
 Shot noise 93  
 Shutter  
   electrode 40, 41  
   grid 176–179, 186, 193  
   mechanical 92  
 SICM (scanning ion conductance microscope) 122, 144  
 Silicon nitride  
   AFM tips 126, 128  
   EM grid 112  
   SNOM probe 141  
   SThM tip support 144  
 Silicon wafer IR sample cell 96  
 Single  
   bacteria detection 49–54, 153, 193–195  
   DNA molecule force measurements 130, 150, 151, 153  
   protein molecule force measurements 147–154  
 Size exclusion chromatography – *see* gel filtration chromatography  
 Size-to-charge ratios 175  
 Skeletal muscle cells 131  
 Skimmer 46  
 Small angle X-ray scattering (SAXS) 85–88  
 Sniffers 183, 184  
 SNOM (scanning near-field optical microscope) 122, 131, 135–143  
   pulling a probe 138, 139  
 Source-gate channel 163  
 Spectral domain optical coherence tomography (SDOCT) 99  
 Spectrometry – *see* spectroscopy  
 Spectroscopy  
   electron 115, 116  
   infrared (IR) and Fourier transform infrared (FTIR) 91–105  
   ion mobility 175–195  
   mass 37–57, 165, 166, 170, 171, 174  
   molecular force 130, 147  
 Speed of  
   electrons in an EM 110, 115  
   ions in an IMS 194  
   ions in an MS 41  
 Spherical aberration 113, 114  
 SPM (scanning probe microscopy) 121–145  
   src SH3 domain 199, 201  
 STEM (scanning transmission electron microscope) 118–120  
 SThM (scanning thermal microscope) 144  
 STM (scanning tunneling microscope) 122, 126, 133–135  
 Streptavidin-biotin complex 154  
 Stretch-activated ion channels 159  
 Structural  
   characterization by FTIR spectroscopy 102–105  
   characterization of biomolecules by scanning probe microscopy 131, 132, 134, 147–152, 154, 158, 159  
   determinants of folding rate constants 12–20  
   high resolution of folding 197–202  
   proteomics 174  
   resolution of proteins by X-ray crystallography 59–85

- Structure  
  characterization by FTIR spectroscopy 102–105  
  determination by a charged AFM tip 131  
  determination by X-ray crystallography 59–85  
  of the native state of proteins 1–8, 118  
  prediction 20–22, 88, 174, 203, 206, 207
- Stylus profilometer 122
- Subwavelength aperture 138–142
- Sulfonic acid 26
- Synchrotron 71, 75
- T7 polymerase 150, 151
- Tags 31, 71, 135
- Target discovery in proteomics 166, 167
- TEM (transmission electron microscope) 107–118
- Tendamistat 7
- Tertiary  
  amine 26  
  structure 1, 4, 9–11, 91
- TGS (triglycine sulfate) detector 105
- Therapeutics development 162, 165, 166
- Thermocouple probe 144
- Thermostable proteins 17–19
- Threonine 3
- Time-of-flight mass spectrometer 37, 40–42
- Titin 1, 147–149
- TIR (total internal reflection) 100, 101, 139
- TOF (time-of-flight mass spectrometer) 37, 40–42
- Total internal reflection (TIR) 100, 101, 139
- Transformation of cells 169
- Transgenic mice 165
- Transition state for protein folding X, 9–20, 84, 103, 104, 197–202
- Transistor 163
- Translation products 165
- Transmembrane channel 131, 154
- Transmission electron microscope (TEM) 107–118
- Trap, optical 151
- Triglycine sulfate (TGS) detector 105
- Tryptophan 3, 4, 157
- Tumor marker 165
- Tunneling current 133, 134
- Turnip yellow mosaic virus 158
- Turns 1
- Tweezers, optical 151
- Two-hybrid system 168, 169
- Tyrosine 3, 7
- Tyrosine kinase 7
- U1A spliceosomal protein 8
- Ubiquitin 8
- Ultrafiltration 34, 35
- Ultra-trace detection 49–54, 153, 175–195
- Unfolding of single protein molecules 147–149
- $\Phi$ -Value analysis 9–12, 197–202
- van-der-Waals radii 1, 123, 129, 132
- Valine 3, 4
- Vector 169
- Velocity of  
  electrons in an EM 110, 115  
  ions in an IMS 194  
  ions in an MS 41
- Vibrational isolation of an AFM 123, 129, 130
- Viral capsid protein 5, 6
- Virtual impactor 49, 50, 193, 195
- Virus  
  crystallographic analysis 69–71, 77, 158, 159  
  crystals 69–71, 77, 158, 159
- Waveguide, optical 100, 101
- Wavenumber 91, 93, 94
- Wide angle X-ray scattering analysis 85
- X-ray  
  backscattering 88, 89  
  cryogenic system 72  
  crystallography 59–85  
  detectors 72–74, 85, 87, 88  
  diffraction 69–85  
  microscope 77  
  mirrors 77, 79

molecular weight determination 89  
poorly scattering crystal 76  
scattering 69–89  
small angle scattering 85–88  
sources 71, 74, 75, 87  
wide angle scattering 85

Yeast  
  strains 172  
  two-hybrid system 168, 169

Zeolite 179, 184